POLITECHNIKA RZESZOWSKA
im. Ignacego Łukasiewicza
WYDZIAŁ CHEMICZNY

PRACA DOKTORSKA

SYNTEZA I BADANIA NANOSTRUKTUR WSPOMAGAJĄCYCH LASEROWĄ SPEKTROMETRIĘ MAS

mgr inż. Artur Kołodziej

Opiekun:
prof. dr hab. inż. Tomasz Ruman

Rzeszów, 2023

NARODOWE CENTRUM NAUKI

Część badań została zrealizowana w ramach grantu SONATA 14 nr UMO-2018/31/ST4/00109
finansowanego przez Narodowe Centrum Nauki

Pragnę serdecznie podziękować mojemu promotorowi
Panu Profesorowi Tomaszowi Rumanowi
za cenne rady i pomysły, przekazanie ogromnej ilości wiedzy
oraz inspirowanie do pracy i naukowego rozwoju.

Dziękuję pracownikom i doktorantom,
z którymi miałem możliwość współpracować
w trakcie mojego doktoratu, a w szczególności
Pani Anecie Płaza-Altamer oraz Pani dr hab. Joannie Nizioł, prof. PRz
za setki godzin spędzonych w laboratorium w miłej atmosferze
oraz okazaną mi życzliwość i pomoc.

Dziękuję Pani Doktor ***Małgorzacie Walczak***
za pomoc w wykonaniu pomiarów DLS.

Dziękuję moim przyjaciołom
Panu Wojciechowi Kośkowi oraz Panu Piotrowi Orzechowskiemu
za dodawanie otuchy w chwilach zwątpienia
oraz za pomoc w zachowaniu równowagi
między pracą, a życiem prywatnym.

Dziękuje moim ***Rodzicom oraz Siostrze***
za wsparcie, wiarę we mnie oraz
dopingowanie moich działań.

SPIS TREŚCI

1. WYKAZ PUBLIKACJI WCHODZĄCYCH W SKŁAD CYKLU

1) **Kołodziej A**, Ruman T, Nizioł J. *Gold and silver nanoparticles-based laser desorption/ionization mass spectrometry method for detection and quantification of carboxylic acids*. Journal of Mass Spectrometry **2020**;55:e4604. DOI: 10.1002/jms.4604

   Impact Factor (2022): 2,394
   Punktacja MNiSW: 70

2) Szulc, J.; **Kołodziej, A**.; Ruman, T. *Silver-109/Silver/Gold Nanoparticle-Enhanced Target Surface-Assisted Laser Desorption/Ionisation Mass Spectrometry—The New Methods for an Assessment of Mycotoxin Concentration on Building Materials*. Toxins **2021**, 13, 45. https://doi.org/10.3390/toxins13010045

   Impact Factor (2022): 5,075
   Punktacja MNiSW: 100

3) Aneta Płaza, **Artur Kołodziej**, Joanna Nizioł, and Tomasz Ruman, *Laser Ablation Synthesis in Solution and Nebulization of Silver-109 Nanoparticles for Mass Spectrometry and Mass Spectrometry Imaging*, ACS Measurement Science Au, 2022, 2, 1, 14–22. DOI: 10.1021/acsmeasuresciau.1c00020

   Czasopismo utworzone w 2021 roku
   Impact Factor: -
   Punktacja MNiSW: -

4) Płaza-Altamer, **A., Kołodziej**, A., Nizioł, J., Ruman, T. *Laser generated gold nanoparticles for mass spectrometry of low molecular weight compounds*, Chemical Technology and Biotechnology, **2022**, ISSN 2720-6793

   Impact Factor: -
   Punktacja MNiSW: -

5) **Artur Kołodziej**, Aneta Płaza-Altamer, Joanna Nizioł, Tomasz Ruman, *Infrared pulsed fiber laser-produced silver-109-nanoparticles for laser desorption/ionization mass spectrometry of carboxylic acids*, International Journal of Mass Spectrometry, **2022**, 474, 116816. DOI: 10.1016/j.ijms.2022.116816

Impact Factor (2022): 1,986

Punktacja MNiSW: 70

6) **Artur Kołodziej**, Aneta Płaza-Altamer, Joanna Nizioł, Tomasz Ruman, *Infrared pulsed fiber laser-produced silver-109 nanoparticles for laser desorption/ionization mass spectrometry of 3-hydroxycarboxylic acids*, Rapid Communications in Mass Spectrometry, **2022**, 36, 21, e9375. DOI: 10.1002/rcm.9375

   Impact Factor (2022): 2,586

   Punktacja MNiSW: 70

7) Aneta Płaza-Altamer, **Artur Kołodziej**, Joanna Nizioł, and Tomasz Ruman, *Infrared pulsed fiber laser-produced silver-109-nanoparticles for laser desorption/ionization mass spectrometry of amino acids,* Journal of Mass Spectrometry, **2022**, 57:e4815. https://doi.org/10.1002/jms.4815

   Impact Factor (2022): 2,394

   Punktacja MNiSW: 70

8) Krzysztof Ossoliński, Tomasz Ruman, Tadeusz Ossoliński, Anna Ossolińska, Adrian Arendowski, **Artur Kołodziej,** Aneta Płaza-Altamer, Joanna Nizioł, *Monoisotopic silver nanoparticles-based mass spectrometry imaging of human bladder cancer tissue: Biomarker discovery,* Advances in Medical Sciences, **2023**, 68(1), 38-45, https://doi.org/10.1016/j.advms.2022.12.002

   Impact Factor (2022) 3,287

   Punktacja MNiSW: 100

9) Krzysztof Ossoliński, Tomasz Ruman, Valérie Copié, Brian P. Tripet, Leonardo B. Nogueira, Katiane O.P.C. Nogueira, **Artur Kołodziej**, Aneta Płaza-Altamer, Anna Ossolińska, Tadeusz Ossoliński, Joanna Nizioł, *Metabolomic and elemental profiling of blood serum in bladder cancer,* Journal of Pharmaceutical Analysis, **2022**, ISSN 2095-1779. https://doi.org/10.1016/j.jpha.2022.08.004

   Impact Factor (2022): 14,026

   Punktacja MNiSW: 140

10) Nizioł J., Ossoliński K., Płaza-Altamer A., **Kołodziej A.** *i wsp. Untargeted ultra-high-resolution mass spectrometry metabolomic profiling of blood serum in bladder cancer.* Scientific Reports, 12, 15156 (**2022**). https://doi.org/10.1038/s41598-022-19576-9

Impact Factor (2022): 4,996
Punktacja MNiSW: 140

Sumaryczny współczynnik Impact Factor: 36,744
Sumaryczna punktacja Ministerstwa Nauki i Szkolnictwa Wyższego: 760

2. STRESZCZENIE

Spektrometria mas z laserową desorpcją/jonizacją jest jedną z najszybciej rozwijających się metod analizy instrumentalnej w obecnych czasach. Na jej popularność wpływa łatwość przygotowania próbek oraz szybkość pomiarów, co pozwala na przeprowadzenie pomiarów bardzo dużej ilości próbek w relatywnie krótkim czasie. Rozwój tej techniki przyczynił się do znacznych postępów w dziedzinie badań omicznych: proteomice, lipidomice oraz metabolomice.

Kilkanaście ostatnich lat znacząco wpłynęło na postęp w syntezie nanostruktur, które zaczęto wykorzystywać dla matryc organicznych w laserowej spektrometrii mas. Charakterystyczne właściwości nanocząstek pozwoliły na uzyskiwanie większej czułości pomiarów, przy jednoczesnym zachowaniu bardzo wysokiej powtarzalności, co spopularyzowało ich wykorzystanie w tej rodzinie metod analitycznych. Dodatkowo, obniżenie intensywności tła chemicznego na widmach pozwoliło na badanie bardziej skomplikowanych próbek, takich jak obiekty biologiczne. Dzięki temu możliwe stało się śledzenie rozmieszczenia oraz stężenia metabolitów w tkankach, a to z kolei przekłada się na lepsze poznanie biochemii organizmów żywych.

Na przygotowaną rozprawę doktorską składa się cykl dziesięciu publikacji, w których zaprezentowane zostały oryginalne badania z wykorzystaniem nanocząstek metalicznych (złota i srebra) zastępujących typowe dla MALDI matryce organiczne do laserowej spektrometrii mas.

W pierwszej części pracy przygotowany został krótki wstęp teoretyczny zawierający opis dotychczasowego stanu wiedzy w zakresie wykorzystania nanostruktur w laserowej spektrometrii mas oraz mechanizmach desorpcji i jonizacji.

W kolejnych rozdziałach omówione zostały kolejne publikacje wchodzące w skład cyklu, wraz z uzasadnieniem połączenia ich w jeden cykl. Przedstawiono w nich wyniki badań przeprowadzonych w trakcie całych studiów doktoranckich oraz w sposób zwięzły omówiono wyniki uzyskane w trakcie analiz.

ABSTRACT

Laser desorption/ionization mass spectrometry is one of the fastest developing methods of instrumental analysis nowadays. Its popularity is influenced by the ease of sample preparation and the speed of measurements, which allows you to measure a large number of samples in a relatively short time. The development of this technique has contributed to significant advances in the fields of proteomics, lipidomics and metabolomics.

The last dozen or so years have significantly influenced the progress in the synthesis of nanostructures, which began to be used as a substitute for organic matrices in laser mass spectrometry. The characteristic properties of nanoparticles allowed for greater sensitivity of measurements, while maintaining very high repeatability, which popularized their use in this family of analytical methods. In addition, lowering the intensity of the chemical background in the spectra allowed for the study of more complex samples such as biological objects. Thanks to this, it became possible to track the distribution and concentration of metabolites in tissues, which in turn contributes to a better understanding of the biochemistry of living organisms.

The prepared doctoral dissertation consists of a series of ten publications in which original research using metallic nanoparticles (gold and silver) replacing typical MALDI organic matrices for laser mass spectrometry was presented.

In the first part of the work, a short theoretical introduction was prepared describing the current state of knowledge in the field of the use of nanostructures in laser mass spectrometry and mechanisms of desorption and ionization, with particular emphasis on laser ablation.

In the following chapters, subsequent publications included in the series are discussed, together with the justification for combining them into one series. They present the research that has been carried out and concisely discuss the results obtained during the analyses.

3. WYKAZ STOSOWANYCH SKRÓTÓW

^{109}AgLGN – laserowo wytwarzane nanocząstki srebra-109

^{109}AgNPET - target wzbogacony o nanocząstki srebra-109

AgLGN – laserowo wytwarzane nanocząstki srebra

AgNPET – target wzbogacony o nanocząstki srebra

AuLGN – laserowo wytwarzane nanocząstki złota

AuNPET – target wzbogacony o nanocząstki złota

BC – nowotwór pęcherza moczowego

CHCA – kwas α-cyjano-4-hydroksycynamonowy

DHB – kwas 2,5-dihydroksybenzoesowy

DIOS - desorpcja/jonizacja na krzemie

DLS – dynamiczne rozpraszanie światła

ESI-QTOF MS – spektrometr masowy z jonizacją w elektrospreju wyposażony w kwadrupol i analizator czasu przelotu

ICP-OES – spektrometria atomowa emisyjna z indukcyjnie sprzężoną plazmą

LASiS – synteza w roztworze poprzez laserową ablację

LDI – laserowa desorpcja/jonizacja

LGN – laserowo wytwarzane nanocząstki

LIAD - desorpcja akustyczna indukowana laserem

LIMS - spektrometria mas z jonizacją laserową

LIP – laserowo indukowana plazma

LLOQ – dolna granica oznaczalności

LOD – granica wykrywalności

MALDI – wspomagana matrycą laserowa desorpcja/jonizacja

MS – spektrometria mas

MSI – obrazowanie spektrometrią mas

NMR – spektroskopia magnetycznego rezonansu jądrowego

NPs - nanocząstki

SA – kwas synapinowy

SALDI – wspomagana strukturami laserowa desorpcja/jonizacja

SEM – skaningowy mikroskop elektronowy

SPR - powierzchniowy rezonans plazmonowy

ToF – analizator czasu przelotu

UHPLC – ultra-wysokosprawny chromatograf cieczowy

4. CEL I ZAKRES PRACY

Celem pracy było opracowanie nowej metody syntezy nanocząstek do laserowej spektrometrii mas, badanie ich właściwości oraz wykorzystanie ich do modyfikacji powierzchni płytek ze stali nierdzewnej. Otrzymane płytki, pokryte nanocząstkami, wykorzystano następnie do analizy różnych związków chemicznych oraz mieszanin, w tym biologicznych z wykorzystaniem spektrometru masowego z laserową desorpcją/jonizacją.

Zakres pracy obejmował:

- badania literaturowe w tematyce metod stosowanych w laserowej spektrometrii mas ze szczególnym uwzględnieniem metod bezmatrycowych;
- opracowanie nowej metody syntezy nanocząstek wykorzystując metodę laserowej ablacji;
- analizę efektywności desorpcji/jonizacji związków testowych za pomocą płytek pokrytych zawiesiną nowo wytworzonych nanocząstek ^{109}Ag;
- określenie limitów wykrywalności związków biologicznych z wykorzystaniem układów ^{109}AgNPET, AuNPET oraz ^{109}AgLGN;
- wykorzystanie układów ^{109}AgNPET, AuNPET oraz ^{109}AgLGN do obrazowania spektrometrią mas;
- analizę płynów biologicznych z wykorzystanie układów pokrytych nanocząstkami metalicznymi;
- badania metabolomiczne z zastosowaniem nowo wytworzonych targetów (płytek ze stali nierdzewnej) pokrytych nanocząstkami.

5. Wstęp teoretyczny

5.1. Nanocząstki stosowane w laserowej spektrometrii mas

Metoda laserowej desorpcji/jonizacji wspomaganej matrycą (MALDI), jest jedną z najpopularniejszych metod analizy próbek z wykorzystaniem spektrometrii mas. Próbka analitu mieszana z matrycą jest nakładana na płytkę i po odparowaniu rozpuszczalników umieszczana jest w źródle jonów instrumentu.

Najpopularniejszymi matrycami organicznymi stosowanymi w metodzie MALDI są: kwas α-cyjano-4-hydroksycynamonowy (CHCA), kwas 2,5-dihydroksybenzoesowy (DHB) oraz kwas synapinowy (SA). Jednak ich zastosowanie nie pozwala na skuteczną analizę ilościową ze względu na ograniczenia. Pierwszym z nich jest konieczność znalezienia matrycy w której analit rozpuszcza się, a następnie wspólnie z matrycą krystalizują na powierzchni płytki. Selekcja matryc odbywa się na zasadzie prób i błędów, co zajmuje sporo czasu w trakcie przygotowania próbek. Kolejnym problemem jest niehomogeniczna krystalizacja na powierzchni plamki, co powoduje powstawanie na płytce „sweet spotów”. Prowadzi to z kolei do niskiej powtarzalności pomiarów typu strzał do strzału (ang. *shoot-to-shoot*) oraz próbka do próbki (ang. *sample-to-sample*) i bardzo utrudnia porównywanie wyników pomiędzy pomiarami. Ponadto metoda MALDI nie pozwala na osiągnięcie wysokiej czułości pomiaru analitu w zakresie *m/z* <1000 ze względu na liczne sygnały matrycy o bardzo wysokiej intensywności. Do tej pory prezentowane były podejścia, w których do analizy związków małocząsteczkowych wykorzystywano matryce polimerowe o dużej masie cząsteczkowej, jednak trudność we wdrażaniu tego podejścia polegała na tym, że matryce te często nie współkrystalizowały z analitem [1]. Innym problemem wartym wymienienia jest niewiarygodna kalibracja, która może się zmieniać w zależności od warunków przygotowania próbki, co prowadzi następnie do niskiej dokładności wartości *m/z* ze względu na konieczność zastosowania kalibracji zewnętrznej. Bardzo często dla obojętnych związków chemicznych uzyskiwana jest niska wydajność jonizacji [2]. Ze względu na ograniczenia metody MALDI skupiono się na modyfikacji matrycy lub jej całkowitym zastąpieniu.

Po raz pierwszy w historii nanocząstki metaliczne w laserowej spektrometrii mas zostały wykorzystane przez zespół Koichiego Tanaki już w 1988 roku. W badaniach zastosowano proszek kobaltowy o średnicy ok. 300 Å, który został zmieszany z glicerolem [3]. Analiza próbek wykazała, że zastosowanie tej metody pozwoliło na detekcję jonów o dużej masie molekularnej, rzędu tysięcy daltonów, których detekcja nie była możliwa przy zastosowania klasycznej metody MALDI [3].

W roku 1995 kolejny zespół badawczy pod przewodnictwem Jana Sunnera analizował możliwość stosowania modyfikowanej matrycy do analizy MS. W badaniach wykorzystano glicerol, który mieszano z cząstkami grafitu o średnicy ok. 10-150 μm. Tak przygotowaną matrycę wykorzystano do analizy białek, a wyniki zaprezentowane przez ten zespół badawczy jasno wskazywały, że zastosowanie wzbogaconej cząstkami grafitu matrycy poprawia czułość oraz rozdzielczość na widmach [4].

Z biegiem lat tworzenie nowych matryc poprzez dodawanie rożnego rodzaju cząstek stało się coraz popularniejsze, zwłaszcza w momencie ogromnego rozwoju w nanotechnologii. Produkcja nanocząstek o różnych rozmiarach, kształtach, oraz składzie przyczyniła się do znacznego przyspieszenia opisywanego procesu [5].

Tabela 1. Przykłady stosowanych nanocząstek w spektrometrii mas.

Rodzaj nanomateriału	Typ nanocząstek	Analizowane próbki	Literatura
Nanocząstki metaliczne	Co	chymotrypsyna	[3]
	Ag	aminokwasy, kwasy tłuszczowe, nukleozydy, ekstrakty roślinne, ekstrakty płynów fizjologicznych, tkanki	[6–10]
	Au	aminokwasy, nukleozydy, ekstrakty roślinne, ekstrakty płynów fizjologicznych, tkanki	[11–14]
	Pd	kwasy tłuszczowe, triacylglicerydy, metale w próbkach biologicznych	[15,16]
	Pt	peptydy, fosfolipidy	[17]
Tlenki metali	porowaty tlenek glinu	peptydy	[18]

	TiO_2	fosfopeptydy, katechiny	[19,20]
	MnO_2 i Mn_2O_3	peptydy, białka, leki	[21]
	ZnO	leki	[22]
	ZrO_2	cyklodekstryny, peptydy	[23]
	Fe_3O_4	peptydy, białka	[24,25]
Nanostruktury na bazie krzemu	nanostrukturalne podłoża krzemowe	ektrakty roślinne, białka,	[26–28]
	nanocząstki azotku krzemu	leki	[29]
Kropki kwantowe (ang. *qauntum dots*)	GeNDs	angiotensyna-I	[30]
	FePtCuNPs	oligopeptydy	[31]
	GaPNPs	poli(glikole etylenowe)	[32]
Nanomateriały na bazie węgla	diament (proszek, nanodruty)	białka, leki	[33,34]
	nanorurki węglowe	cyklodekstryny, peptydy, białka, ekstrakty roślinne	[35,36]
Materiał porowaty	-	surfaktanty, leki	[37,38]

Wraz z rozwojem metod syntezy nanocząstek zaczęto zastępować matryce organiczne tymi nanostrukturami. Opracowanie metod bezmatrycowych pozwoliło na zintensyfikowanie badań związków małocząsteczkowych z wykorzystaniem spektrometrii mas typu LDI. Wynika to z usunięcia wad, które występowały w przypadku stosowania matryc organicznych.

Najpopularniejszymi nanostrukturami stosowanymi w analizie związków małocząsteczkowych stały się nanocząstki metaliczne. Opracowana przez Sunnera i wsp. metoda należąca do rodziny metod wspomaganej strukturami laserowej desorpcji/jonizacji (SALDI) wykazała kilka zalet takich jak: łatwość przygotowania próbki do pomiaru, bardzo krótki czas pomiaru próbek oraz niska intensywność tła chemicznego na widmie [39].

Zastosowanie nanocząstek srebra lub złota zapewnia dodatkowe korzyści, bowiem nanocząstki te wykazują stosunkowo dużą tolerancję na sole znajdujących w się w analizowanej próbce. Ich zastosowanie pozwala na wytwarzanie sygnałów o dużej powtarzalności, eliminowanie potencjalnych interferencji jonów matrycy z jonami analitu oraz istnieje możliwość wewnętrznej kalibracji z wykorzystaniem sygnałów jonów srebra lub złota [6].

Wykorzystanie monoizotopowego srebra-109 w laserowej spektrometrii mas wiąże się z dodatkowymi korzyściami w porównaniu do mieszaniny izotopów ^{107}Ag i ^{109}Ag. Jest to na przykład około dwukrotnie większa intensywność sygnałów w porównaniu do srebra naturalnego, co przekłada się na zwiększoną czułość pomiarową. Ponadto obserwuje się najprostszy z możliwych rozkład sygnałów, pozwalający na badanie bardziej skomplikowanych próbek zawierających dużą liczbę różnorodnych związków, a dodatkowo znacznie prostszy rozkład izotopowy [2]. Wśród innych zalet jest również dobra zdolności do jonizacji związków o niskiej polarności, np. lipidów oraz właściwości przeciwbakteryjne i przeciwgrzybicze nanocząstek srebra. Umożliwia to zabezpieczenie próbki przed wzrostem tych organizmów na powierzchni próbki, co z kolei mogłoby wpływać na wyniki uzyskiwane w czasie pomiarów. Łącząc wszystkie te zalety, nanocząstki ^{109}Ag mają znacznie korzystniejsze zastosowanie w analizie złożonych mieszanin biologicznych.

5.2. Mechanizmy desorpcji/jonizacji próbek w SALDI MS

Proces laserowej desorpcji/jonizacji jest badany od wielu lat, jednak naukowcom nadal nie udało się jednoznacznie określić dokładnego mechanizmu przebiegu tego procesu. Z biegiem lat powstało wiele teorii, które coraz bardziej szczegółowo opisują zjawiska zachodzące w trakcie tego procesu. Mechanizmy desorpcji/jonizacji podzielono na dwa typy: termiczny oraz nietermiczny.

Mechanizm termiczny zakłada, że transfer energii cieplnej z NPs do analitu powoduje wydajną desorpcję próbki badanej. Chociaż istnieje wiele dowodów na to, że inicjacja jonizacji nie zachodzi poprzez proces termiczny, wiele badań odnosiło się do niego jako źródła wzmocnienia sygnału [40]. Przykładem mogą być wyniki badań Tanaki *i wsp.* w których sugerowali, że główny mechanizm wykrywania jonów w ich początkowym badaniu LDI-MS można wyprowadzić z mechanizmu termicznego, odnosząc się do właściwości termicznych ultra drobnych cząstek, takich jak niska pojemność cieplna, wysoki współczynnik absorpcji światła oraz duża powierzchnia właściwa na jednostkę objętości. Podobne wnioski zostały wysunięte przez zespoły Wei *i wsp.* oraz Shen *i wsp.* co oznacza, że procesy termiczne dominują w metodach wykorzystujących porowaty krzem (np. metoda DIOS) [41]. Arakawa *i wsp.* dokonali przeglądu różnych możliwych mechanizmów wzmacniania sygnału w procesie SALDI. Ich wnioski sugerują, że wywołany laserem szybki wzrost temperatury nanocząstek może być najbardziej prawdopodobną przyczyną termicznej desorpcji cząsteczek analitu bez rozkładu w SALDI-MS

[42]. Jeśli jednak mechanizm termiczny przeważałby jako główny mechanizm desorpcji/jonizacji w metodzie SALDI, to wydajność desorpcji powinna rosnąć wraz ze wzrostem wewnętrznego transferu energii. W raporcie Tanga *i wsp.* dotyczącego badania efektywności desorpcji w odniesieniu do zewnętrznego transferu energii wykazano odwrotny wynik. Nie zaobserwowano wzrostu wydajności desorpcji, mimo że zwiększył się zakres wewnętrznego transferu energii [43]. Proces jonizacji musi być zatem zainicjowany w innym mechanizmie.

Lim *i wsp.* zaproponowali dwuetapowy mechanizm, w którym w pierwszym etapie następuje interakcja między analitem i materiałem SALDI i tworzy się kompleks analit-matryca, a następnie zachodzi drugi etap transferu energii z NPs do cząsteczek analitów [44]. Zaproponowano kilka innych propozycji dotyczących nietermicznego mechanizmu jonizacji SALDI, a pośród nich bardziej szczegółowo zbadano dwa: desorpcję akustyczną indukowaną laserem (LIAD) i powierzchniowy rezonans plazmonowy (SPR). Hsu *i wsp.* zaproponowali LIAD jako jeden z głównych mechanizmów jonizacji w SALDI-MS. Ich zdaniem procesy termicznego przenoszenia energii są powolne i nie pozwoliłyby na uzyskiwanie widm masowych w tak krótkim czasie, w jakim zachodzi proces jonizacji. Jednakże w trakcie procesu desorpcji akustycznej analit desorbowany jest z płytki po przeciwnej stronie do powierzchni napromieniowanej laserem, a nie z tej samej strony powierzchni płytki pokrytej nanocząstkami na którą pada promień lasera, jak ma to miejsce w przypadku procesu SALDI [45]. Dodatkowo pęd fotonów lasera (rozumiany jako iloraz stałej Plancka i długości fali fotonu) nie jest przenoszony na zdesorbowane cząstki, w wyniku czego powstają głównie obojętne produkty, które nie mogą być analizowane w LDI. Peng *i wsp.* przedstawili wyniki, w których zastosowali LIAD do analizy wstępnie naładowanych cząstek. W wyniku zastosowania lasera o wysokiej fluencji udało im się zarejestrować widma dla badanych związków [46]. Nie udało się im jednak wyjaśnić w jaki sposób badane związki zostały wstępnie naładowane. Z tego względu proces desorpcji akustycznej indukowanej laserem nie może być głównym mechanizmem desorpcji/jonizacji w MALDI MS. Powierzchniowy rezonans plazmonowy występuje, gdy foton padającego światła uderza w metalową powierzchnię. Przy pewnym kącie padania część energii świetlnej przechodzi przez metalową powłokę z elektronami w metalowej warstwie powierzchniowej, które następnie poruszają się w wyniku wzbudzenia. Ruchy elektronów są teraz nazywane plazmonami i rozchodzą się równolegle do powierzchni metalu. Z kolei oscylacja plazmonu generuje pole elektryczne, którego zasięg wynosi około 300 nm od granicy między powierzchnią metalu a próbką [47]. Nagoshi *i wsp.* zaproponowali, że transfer ładunku oparty na wzbudzeniu plazmonu może przyczynić się do procesu laserowej desorpcji/jonizacji, przy zastosowaniu nanomateriałów jako substratów [48]. W badaniach stwierdzono, że wzbudzenie plazmonów powierzchniowych może generować duże gęstości ładunków, które z kolei mogą przenosić się z powierzchni metalu na analit, co znacznie zwiększa wydajność desorpcji/jonizacji próbek w SALDI. Mimo to desorpcja metodą SPR zachodzi zazwyczaj poprzez wzbudzanie nanomateriału falą o odpowiedniej, a nie o dowolnej długości,. Ponadto kąt padania wiązki laserowej jest niezwykle ważny dla generowania plazmonu powierzchniowego [49].

Podsumowując dotychchczasowe rozważania można wysunąć kilka wniosków. Po pierwsze, przenoszenie energii cieplnej z matrycy do analitu pozwala na zwiększenie efektywności procesu desorpcji, nie wpływa jednak na proces jonizacji próbki badanej i nie może go zainicjować. Po drugie, proces desorpcji akustycznej z wykorzystaniem lasera również nie może być decydującym procesem w jonizacji, natomiast jest skuteczny w desorpcji próbki. Proces SPR również nie jest głównym procesem jonizacji ze względu na występowanie tylko pod wpływem oddziaływania światła laserowego pod odpowiednim kątem na powierzchnię oraz nie pozwala na wykorzystanie lasera o dowolnej długości fali. [40].

5.3. Omówienie publikacji wchodzących w skład pracy doktorskiej

W skład pracy doktorskiej wchodzi dziesięć prac oryginalnych opublikowanych w recenzowanych czasopismach naukowych. W dwóch pierwszych artykułach zaprezentowano wykorzystanie metod ^{109}AgNPET, AuNPET oraz AgNPET do analiz kwasów karboksylowych, w tym kwasów tłuszczowych oraz mykotoksyn. Trzecia i czwarta publikacja oryginalna przedstawiają nowe metody laserowego wytwarzania nanocząstek srebra-109 oraz złota z wykorzystaniem impulsowego lasera światłowodowego. Przedstawiono charakterystykę otrzymanych nanostruktur z wykorzystaniem UV-Vis, DLS oraz mikroskopii SEM. W pracy pokazane zostały również rezultaty badań związków testowych z wykorzystaniem MALDI-ToF MS oraz obrazowanie spektrometrią mas (MSI) odcisku palca na targetach pokrytych nanocząstkami wytwarzanymi nowo opracowaną metodą. Publikacje 5 – 7 prezentują wyniki analizy jakościowej różnych grup związków, np. aminokwasów i kwasów tłuszczowych z zastosowaniem nowo uzyskanych układów pokrytych nanocząstkami otrzymanymi metodą laserowo wytwarzanych nanocząstek LGN oraz zastosowanie obrazowania spektrometrią mas w analizie ilościowej. Trzy ostatnie publikacje przedstawiają wyniki analiz metabolomicznych próbek pobranych od grup osób zdrowych oraz pacjentów lokalnego szpitala ze zdiagnozowanym nowotworem pęcherza moczowego. Publikacje przedstawione w pracy doktorskiej prezentują cały dorobek badań przeprowadzonych w trakcie studiów doktoranckich.

5.3.1. Detekcja i analiza ilościowa wzorców związków z wykorzystaniem układów ^{109}AgNPET oraz AuNPET (Publikacje 1 – 2)

Celem pierwszej pracy pt. ***Gold and silver nanoparticles-based laser desorption/ionization mass spectrometry method for detection and quantification of carboxylic acids*** opublikowanej w Journal of Mass Spectrometry było porównanie efektywności opracowanych metod do detekcji kwasów karboksylowych z wykorzystaniem nanocząstek złota oraz srebra monoizotopowego. Dodatkowo wyznaczone zostały limity wykrywalności i oznaczalności tych kwasów dla metod AuNPET oraz ^{109}AgNPET.

Do analizy wykorzystano wzorce dziesięciu kwasów karboksylowych, włączając w to kwasy tłuszczowe. Były to kwasy: jabłkowy, pimelinowy, azelainowy, 3-metylohipurowy, palmitynowy, linoleinowy, oleinowy, arachidonowy, arachidowy oraz erukowy. Związki badano w zakresie stężeń od 1 mg/ml do 10 ng/ml, co odpowiada 1 000 000 – krotnej zmianie stężenia. .

Kolejnym etapem było przygotowanie modyfikowanych płytek ze stali nierdzewnej pokrytych srebrem-109 oraz złotem. Płytki poddano czyszczeniu w celu usunięcia zanieczyszczeń, które mogły osadzić się na ich powierzchni w procesie ich wytwarzania.

W celu uzyskania zawiesiny nanocząstek ^{109}Ag przeprowadzono redukcję soli trifluorooctanu srebra-109 za pomocą kwasu 2,5-dihydroksybenzoesowego z wykorzystaniem metody opisanej w artykule Nizioł *i wsp.* [2].

Nanocząstki złota przygotowane zostały z wykorzystaniem procedury opisanej w artykule Sekuła *i wsp.* [12].

Następnie przygotowane roztwory kwasów naniesiono na płytki pokryte nanocząstkami z wykorzystaniem metody wysychającej kropli (ang. *dried droplet*), a płytki po wyschnięciu próbek wprowadzono do spektrometru masowego typu MALDI-ToF.

W wyniku analizy na płytce wzbogaconej nanocząstkami złota udało się oznaczyć pięć z dziesięciu badanych związków, z kolei na płytce wzbogaconej nanocząstkami srebra-109 wszystkie badane związki. Dla ^{109}AgNPET badane związki można było odnaleźć na widmie głownie w postaci adduktów ze srebrem-109, a ich intensywność była znacznie wyższa niż intensywność odpowiadających związków dla AuNPET. Ponadto dla wszystkich badanych kwasów najwyższe intensywności otrzymywano dla stężenia próbki wynoszącego 100 µg/ml. Po przeprowadzeniu analizy ilościowej po raz pierwszy przedstawione zostały limity detekcji oraz oznaczalności dla sześciu z dziesięciu analizowanych kwasów karboksylowych dla laserowej spektrometrii mas.

W drugiej publikacji pt. ***Silver-109/Silver/Gold Nanoparticle-Enhanced Target Surface-Assisted Laser Desorption/Ionisation Mass Spectrometry—The New Methods for an Assessment of Mycotoxin Concentration on Building Materials*** opublikowanej w czasopiśmie Toxins przeprowadzono analizę ilościową oraz jakościową mykotoksyn na materiałach budowlanych z wykorzystaniem płytek ^{109}AgNPET, AgNPET oraz AuNPET w porównaniu do metody MALDI. Próbką badaną była mieszanina siedmiu wzorców mykotoksyn pleśni. Stężenie początkowe wzorców w mieszaninie wynosiło 100 mg/ml dla patuliny, cytryniny, kwasu 3-nitropropionowego, alternariolu, natomiast dla sterygmatocystyny, kwasu cyklopiazonowego, roquefortyny C - 20 µg/ml. Wykonano także badania oznaczania wymienionych wcześniej wzorców mykotoksyn po ekstrakcji z płyty gipsowo-kartonowej. Dodatkowo, dla porównania, analizowane związki poddano badaniu z wykorzystaniem metody MALDI, które pozwoliło na zaobserwowanie bardzo wysokiego powinowactwa tych związków do jonów srebra, co sugerowało, że metoda MALDI nie jest najlepszym wyborem, ponieważ jonizacja tych związków może nie być tak efektywna w przypadku zastosowania matrycy organicznej. Porównując wyniki uzyskane za pomocą układu typu MALDI, najniższe intensywności uzyskano przy użyciu nanocząstek złota, a najwyższe dla nanocząstek srebra i ^{109}AgNPs. Wyniki otrzymane po ekstrakcji badanych mykotoksyn z materiału budowlanego wskazały na możliwość zastosowania metod ^{109}AgNPET/AgNPET jako alternatywy do obecnie istniejących metod identyfikacji, jednak niezbędne są do tego dalsze badania.

5.3.2. Nowe metody syntezy nanocząstek ^{109}Ag oraz Au z wykorzystaniem laserowej ablacji w rozpuszczalniku (Publikacje 3-4)

Kolejnym etapem badań w obrębie niniejszej rozprawy doktorskiej było opracowanie nowej techniki syntezy nanocząstek srebra monoizotopowego oraz złota z wykorzystaniem metody laserowej ablacji w rozpuszczalniku (LASiS). Wyniki zaprezentowano w publikacjach pt. ***Laser Ablation Synthesis in Solution and Nebulization of Silver-109 Nanoparticles for Mass Spectrometry and Mass Spectrometry Imaging*** w czasopiśmie ACS Measurement Science Au oraz ***Laser generated gold nanoparticles for mass spectrometry of low molecular weight compounds*** w Chemical Technology and Biotechnology. Główną motywacją poszukiwania nowych metod syntezy było przyspieszenie procesu syntezy w porównaniu do metody opierającej się o redukcję soli srebra-109 oraz złota, zmniejszenie ilości zużywanego materiału, obniżenie kosztów wytwarzania oraz uzyskanie czystszych chemicznie nanocząstek. W trakcie badań opracowano również metodę aplikacji zawiesiny nanocząstek za pomocą nebulizacji na powierzchni targetów i obiektów badanych, dzięki której możliwe było bardziej jednorodne rozmieszczenie nanocząstek na całej powierzchni.

Blaszkę wykonaną ze srebra-109 zanurzono w acetonitrylu i poddano ablacji laserowej do momentu zmiany barwy roztworu na zielono-brązowy. Podobnie został przeprowadzony proces wytwarzania nanocząstek złota - rozpuszczalnikiem stosowanym do ich wytworzenia była mieszanina woda/izopropanol.

Moim zadaniem było znalezienie optymalne parametrów syntezy nanocząstek srebra oraz pomiary związków testowych z zastosowaniem tych nanocząstek oraz analiza widm LDI MS, natomiast Pani mgr inż. Aneta Płaza-Altamer, doktorantka w Szkole Doktorskiej Nauk Inżynieryjno-Technicznych na Politechnice Rzeszowskiej, skupiła się na optymalizacji parametrów syntezy nanocząstek złota oraz sposobu ich zastosowania do analizy związków testowych. Optymalizacja została przeprowadzona w wyniku eksperymentów, w czasie których każdy z poszczególnych parametrów ulegał modyfikacji. Płytki poddawano analizie z wykorzystaniem MALDI-ToF MS, w czasie której badano intensywność sygnałów ^{109}Ag i jego adduktów oraz obliczano stosunek intensywności sygnałów zanieczyszczeń do sygnałów srebra-109. Po tym etapie naniesione zostały związki testowe, które poddano badaniom MS.

Zawiesina zawierająca nanocząstki była nanoszona poprzez nebulizację na płytki ze stali nierdzewnej. Płytka umieszczona została na systemie translacyjnym ze stolikiem sterowanego precyzyjnymi serwonapędami.

Kolejnym etapem po uzyskaniu najbardziej odpowiedniej zawiesiny nanocząstek srebra-109 i złota do laserowej spektrometrii mas było określenie właściwości uzyskanych nanocząstek. W tym celu poddane zostały one badaniom z wykorzystaniem spektrofotometrii UV-Vis, DLS oraz obrazowania z wykorzystaniem mikroskopii SEM. Badania UV-Vis oraz DLS przeprowadziła Pani mgr inż. Aneta Płaza-Altamer. Badania te wykazały, że wielkości nanocząstek mieściła się w granicach 20 do 100 nm. Obrazowanie SEM zostało wykonane w Centrum Mikro i Nanotechnologii Uniwersytetu Rzeszowskiego. Obrazy mikroskopowe również potwierdzają uzyskanie po syntezie nanocząstek o średnicy około 20-40 nm.

Nanocząstki wytworzone w opracowanym przeze mnie procesie LGN nazwano „^{109}AgLGN” (ang. *silver-109 laser generated nanomaterial*) oraz AuLGN (*gold laser generated nanomaterial)* i tak będą określane w późniejszych rozdziałach. W kolejnych etapach badań analizie poddano jonowe i niejonowe związki wzorcowe takie jak: ryboza, histydyna i tymidyna oraz próbkę poli(tlenku etylenu) (PEG). Badania wykazały, że zastosowanie płytek z ^{109}AgLGN pozwala na kilkudziesięciokrotne zmniejszenie błędu $m/z_{\text{eksperymentalne}} - m/z_{\text{teoretyczne}}$ w stosunku do metody MALDI, natomiast porównując je z wytworzonymi za pomocą metody ^{109}AgNPET, intensywność sygnałów srebra i jego adduktów jest kilkukrotnie wyższa przy zachowaniu średniej intensywności tła chemicznego na podobnym poziomie. Podobne efekty zostały uzyskane dla układów AuLGN.

Płytki pokryte nanocząstkami ^{109}AgLGN wykorzystano także do obrazowania odcisku palca w celu sprawdzenia możliwości ich zastosowania w MSI. Na stalowej płytce wykonano odcisk palca, a następnie wcześniej przygotowaną zawiesinę ^{109}AgLGN napylono na powierzchnię. Wykorzystując płytki pokryte ^{109}AgLGN udało się zidentyfikować ponad 30 różnych związków w badanym odcisku palca, które należały do różnych grup, takich jak sole nieorganiczne (np. NaCl, KCl), proste związki organiczne (np. mocznik, aminokwasy, kwasy karboksylowe o krótkim łańcuchu węglowym), kwasy tłuszczowe i lipidy.

5.3.3. Analiza związków małocząsteczkowych z wykorzystaniem ^{109}AgLGN (Publikacje 5-7)

W piątej pracy oryginalnej pt. ***Infrared pulsed fiber laser-produced silver-109-nanoparticles for laser desorption/ionization mass spectrometry of carboxylic acids*** opublikowanej w czasopiśmie International Journal of Mass Spectrometry zaprezentowano wyniki porównania metod LDI MS oraz MSI w analizie ilościowej sześciu wybranych kwasów karboksylowych.

Badanymi kwasami były kwas azelainowy, 3-metylohipurowy, oleinowy, linoleinowy, arachidowy oraz erukowy. Do badań wykorzystano roztwory badanych kwasów w zakresie stężeń od 1 mg/ml do 1 ng/ml. Roztwory nanoszone były na płytkę pokrytą ^{109}AgLGN, pomiar odbywał się z wykorzystaniem aparatu MALDI-ToF w dwóch trybach: ręcznego pomiaru 4 punktów na plamce oraz obrazowania całej plamki z substancją badaną. Dodatkowo przeprowadzone zostało badanie, którego celem było określenie wpływu oddziaływania innych substancji znajdujących się w próbce na analizę badanych kwasów karboksylowych, tzw. efekt matrycy. W tym celu do próbki surowicy krwi dodano roztworu wzorca kwasu, a następnie poddano badaniu spektrometrem mas.

W publikacji zaprezentowano wyniki dotyczące wartości LOD i LLOQ dla badanych kwasów. Dzięki zastosowaniu płytek pokrytych nanocząstkami wytwarzanymi metodą LGN udało się uzyskać dwu- do pięciokrotnie niższe wartości LOD oraz LLOQ niż w przypadku wyników dla metody ^{109}AgNPET opisanych w Publikacji 1, gdzie zastosowane były nanocząstki syntezowane chemicznie.

Analiza ilościowa pozwoliła na wyznaczenie równań linii trendu na wykresach przedstawiających logarytm stężenia *vs* logarytm intensywności. Dla czterech z sześciu badanych kwasów dopasowanie linii trendu wynosiło nie mniej niż 0,96 w zakresie tysiąckrotnej zmiany stężenia, natomiast w przypadku kwasu azelainowego uzyskano linię trendu z dopasowaniem powyżej 0,99 dla wszystkich siedmiu badanych stężeń, co odpowiadało 1 000 000-krotnej zmianie stężenia tego kwasu. Dodatkowo przeprowadzona analiza *shoot-to-shoot* oraz *spot-to-spot* wykazały bardzo dużą powtarzalność wyników pomiarów dzięki zastosowaniu ^{109}AgLGN.

Badania te wykazały również możliwość stosowania MSI w analizie ilościowej z wykorzystaniem spektrometrii mas. Zaletą tej metody jest możliwość automatyzacji procesu pomiaru całej powierzchni plamki, która w zależności od wielkości obszaru badanego może wymagać przeprowadzania od kilkunastu do kilkuset pomiarów. Wykorzystując MSI w takich analizach generowane są również obrazy jonowe badanych próbek, które jasno wskazują na niejednorodne rozmieszczenie analitu na całej powierzchni plamki.

Szósta praca oryginalna pt. ***Infrared pulsed fiber laser-produced silver-109 nanoparticles for laser desorption/ionization mass spectrometry of 3-hydroxycarboxylic acids*** zaprezentowana w Rapid Communications in Mass Spectrometry przedstawia wyniki analizy ilościowej dla roztworów kwasów 3-hydroksykarboksylowych. Związki te wybrano do analizy ze względu na fakt, występowania ich w endotoksynach bakterii, a dokładniej są one głównym komponentem lipidu A, czyli lipidowej części tych toksyn [50]. Dodatkową motywacją był fakt że nigdzie wcześniej w literaturze nie zostały przeprowadzone badania tych substancji z wykorzystaniem laserowej spektrometrii mas.

W publikacji zostały zaprezentowane wartości LOD i LLOQ obliczone na podstawie wyników uzyskanych podczas pomiarów MS. W przypadku zastosowania metody MSI udało się uzyskać znacząco niższe wartości LOD i LLOQ dla 4 badanych kwasów 3-hydroksykarboksylowych. Dane z analizy ilościowej pokazały, że zastosowanie metody MSI w przypadku analizy tych kwasów pozwoliło na uzyskanie lepszego dopasowania linii trendu dla pięciu z sześciu badanych kwasów, a wartość R^2 wynosiła nie mniej niż 0.95 w przypadku najgorszego dopasowania dla kwasu 3-hydroksyheksadekanowego w zakresie stężeń od 0,1 mg/ml do 10 ng/ml, co odpowiada 10 000 – krotnej zmianie rozcieńczenia roztworu tego kwasu.

W siódmej publikacji pt. ***Infrared pulsed fiber laser-produced silver-109-nanoparticles for laser desorption/ionization mass spectrometry of amino acids*** wydanej w Journal of Mass Spectrometry zaprezentowano wyniki MSI czterech aminokwasów, lizyny, fenyloalaniny, izoleucyny i alaniny. Wzorce aminokwasów badano w zakresie stężeń od 1 mg/ml do 1 ng/ml, co odpowiadało 1 000 000-krotnej zmianie stężenia. Dla każdego badanego związku przygotowano wykresy z dopasowaniem czterech rodzajów linii trendu: liniowej, ekspotencjalnej, potęgowej oraz wielomianowej. Na podstawie współczynnika R^2 wskazane zostało najlepsze dopasowanie, którym w przypadku analizowanych aminokwasów była regresja wielomianowa. W publikacji zaprezentowano również wyniki oznaczania stężenia badanych aminokwasów w próbce surowicy krwi, wykorzystując do tego metodę obrazowania spektrometrią mas.

5.3.4. Analizy metabolomiczne próbek nowotworu pęcherza moczowego (Publikacje 8-10)

W ósmej publikacji pt. ***Monoisotopic silver nanoparticles-based mass spectrometry imaging of human bladder cancer tissue: Biomarker discovery*** wydanej w czasopiśmie Advances in Medical Sciences zaprezentowano porównanie wyników MSI obszarów zdrowych i nowotworowych tkanek pacjentów chorujących na nowotwór pęcherza moczowego (BC *ang. bladder cancer*) z wykorzystaniem układów ^{109}AgNPET. Dodatkowo wykonana została jedno- i wielowymiarowa analiza statystyczna analizowanych tkanek.

Pierwszym etapem było przygotowanie ekstraktów badanych tkanek zgodnie z procedurą zaprezentowaną w publikacji zawierającej etapy ekstrahowania mieszaniną metanol/chloroform oraz metanol/woda. Uzyskane po ekstrakcji dwie fazy poddano odrębnie analizie z wykorzystaniem płytki ^{109}AgNPET w spektrometrze typu MALDI-ToF/ToF. W trakcie badań udało się zidentyfikować 28 związków o najwyższej różnicy intensywności pomiędzy uśrednionymi obszarami zdrowym oraz nowotworowymi. Zastosowaniu analiz statystycznych pozwoliło na wyodrębnienie 10 metabolitów jako nowych potencjalnych biomarkerów tego nowotworu. Analizę statystyczną przeprowadziła dr hab. Joanna Nizioł, prof. PRz.

Kolejnym etapem badań było przeprowadzenie analizy MSI wytypowanych metabolitów. W tym celu wykorzystano tkanki pobrane przez dr Krzysztofa Ossolińskiego od 6 pacjentów chorujących na nowotwór pęcherza moczowego. W trakcie operacji wycięto cały guz oraz niewielki fragment przylegającego do niego zdrowego nabłonka dróg moczowych (tkanka kontrolna). Wykonano odciski (imprinty) tkanek nowotworowych i kontrolnych na płytkach ze stali nierdzewnej a następnie za pomocą zestawu do nebulizacji napylono wytworzone w reakcji redukcji nanocząstki srebra-109. Przygotowane w ten sposób próbki wprowadzono do aparatu, gdzie wykonano analizę MSI. Uzyskane obrazy jonowe potwierdziły potencjalną możliwość zastosowania tej metody jako narzędzia diagnostycznego dzięki temu, że zastosowanie MSI pozwala nie tylko na identyfikację potencjalnych biomarkerów nowotworowych, ale także na określenie ich lokalizacji na powierzchni badanej tkanki.

Dziewiąta publikacja pt. ***Metabolomic and elemental profiling of blood serum in bladder cancer*** wydana w czasopiśmie Journal of Pharmaceutical Analysis przedstawia wyniki analizy metabolomicznej celowanej i niecelowanej z wykorzystaniem trzech metod analitycznych NMR, LDI-MS oraz ICP-OES dwustu próbek ludzkiej surowicy krwi. Próbki surowicy krwi (100 próbek pochodzących od pacjentów chorujących na BC oraz 100 od zdrowych ochotników) zostały zebrane w Szpitalu Powiatowym im. Jana Pawła II w Kolbuszowej. Do analizy LDI-MS wykonano rozcieńczenie 500-krotne metanolem próbki surowicy krwi. Następnie pakiet 100 próbek kontrolnych oraz 100 BC naniesiono na płytki ^{109}AgLGN oraz AuLGN i poddano analizie z wykorzystaniem spektrometru masowego typu MALDI-ToF/ToF. Do analiz NMR oraz ICP-OES wykorzystano wcześniej przygotowane ekstrakty surowicy, które zostały przygotowane we współpracy z mgr inż. Anetą Płazą oraz dr. hab. Joanną Nizioł, prof. PRz. Analiza NMR uzyskanych ekstraktów została przeprowadzona w Montana State University, Bozeman w USA, z kolei analizę ICP-OES wykonano w Federal University of Ouro Preto, Ouro Preto w Brazylii.

Wyniki uzyskane w trakcie analiz poddano wielowymiarowej analizie statystycznej, w której udało się wskazać 4 potencjalne biomarkery znalezione za pomocą metody NMR. Analiza ICP-OES wskazała 2 pierwiastki: Li oraz Fe odróżniające próbki kontrolne od nowotworowych, natomiast wykorzystując metodę LDI-MS udało się wskazać 25 związków różnicujących badane próbki. Analiza statystyczna została przeprowadzona przez dr hab. Joannę Nizioł, prof. PRz. Dodatkowo dzięki zastosowaniu opisanych metod możliwe było rozróżnienie stopni zaawansowania nowotworu pęcherza moczowego

Ostatnia praca pt. ***Untargeted ultra-high-resolution mass spectrometry metabolomic profiling of blood serum in bladder cancer,*** opublikowana w czasopiśmie Scientific Reports prezentuje wyniki analizy ekstraktów 100 próbek surowicy krwi pacjentów chorujących na nowotwór oraz 100 kontrolnych pobranych od zdrowych ochotników z wykorzystaniem UHPLC sprzężonego z ESI-UHR-QTOF-MS+MS/MS.

Pierwszym etapem było przygotowanie ekstraktów zebranych surowic. W tym celu zastosowano metodę ekstrakcji ciecz-ciecz, co umożliwiło uzyskanie dwóch faz: górną zawierającą głównie związki polarne oraz dolną, w skład której wchodziły głównie lipidy. Bezpośrednio przed pomiarami UHPLC próbki rozpuszczono w metanolu i wprowadzono do autosamplera. Pomiary UHPLC ESI-UHR-QTOF-MS+MS/MS przeprowadziła mgr inż. Aneta Płaza-Altamer.

Po uzyskaniu wyników otrzymane dane poddano analizie składowych głównych oraz analizie dyskryminacyjnej ortogonalnych cząstkowych najmniejszych kwadratów. Dzięki tym analizom z 5498 cech zidentyfikowanych w każdej próbce surowicy udało się wyodrębnić 27 metabolitów, które różnicowały próbki kontrolne od próbek pacjentów BC. Stwierdzono również, że dwadzieścia trzy metabolity w surowicy rozróżniają pacjentów z BC o niskim i wysokim stopniu złośliwości oraz grupę kontrolną. W trakcie analizy udało się również znaleźć trzydzieści siedem metabolitów surowicy krwi różnicujących różne etapy nowotworu pęcherza moczowego. Analiza statystyczna została przeprowadzona przez dr hab. Joannę Nizioł, prof. PRz.

6. PODSUMOWANIE I WNIOSKI

Metody oparte o nanocząstki srebra i złota (^{109}AgNPET, AuNPET, ^{109}AgLGN) pozwalają na analizę różnorodnych związków zarówno o wysokiej polarności np. aminokwasy, cukry oraz związków o niskiej polarności , takich jak kwasy tłuszczowe lub lipidy w LDI MS.

Nanocząstki srebra znacznie lepiej sprawdzają się w procesie jonizacji związków o niskiej polarności, z kolei nanocząstki złota znakomicie jonizują związki o wysokiej polarności. Układy ^{109}AgNPET oraz AuNPET mogą być z powodzeniem stosowane zarówno w analizach jakościowych jak i ilościowych, w badaniach czystych roztworów wzorców lub do analizy skomplikowanych mieszanin dla przykładu, moczu, surowicy krwi czy ekstraktów roślinnych.

Opracowanie nowej metody wytwarzania nanocząstek srebra-109 i złota z wykorzystaniem impulsowego lasera światłowodowego wyposażonego w głowicę galwanometryczną pozwoliło na uzyskiwanie chemicznie czystych zawiesin nanocząstek, które mogły być wykorzystane do przygotowania targetów pokrytych nanocząstkami znacznie taniej i szybciej. Analizy związków testowych wykazały, że płytki pokryte nanocząstkami wytworzonymi nową metodą skutecznie sprawdzają się w jonizacji różnego rodzaju związków małocząsteczkowych, jednocześnie zachowując poziom tła chemicznego na bardzo niskim poziomie. Wytworzone płytki pokryte nanocząstkami syntezowanymi tą metodą mogą również być wykorzystane w obrazowaniu spektrometrią mas.

Badania przedstawione w niniejszej rozprawie doktorskiej wykazały również, że obrazowanie spektrometrią mas może być wykorzystywane w analizie ilościowej. Zastosowanie układów ^{109}AgNPET, ^{109}AgLGN oraz AuLGN pozwala na prowadzenie bardzo rozległych badań metabolomicznych, w których wykorzystywane mogą być dziesiątki lub setki próbek, co z kolei pozwala na uzyskiwanie istotnych statystycznie wyników. W połączeniu z innymi metodami analitycznymi takimi jak na przykład NMR, ICP-OES lub HPLC-ESI-QTOF MS umożliwiają poszukiwanie nowych biomarkerów, które mają ogromne znaczenie w diagnostyce chorób nowotworowych

Podsumowując wyniki zaprezentowane w niniejszej pracy doktorskiej można stwierdzić, że otrzymane i badane nanostruktury w znaczący sposób zwiększają możliwości wykorzystania laserowej spektrometrii mas zarówno w analizach jakościowych (głównie związków o niskiej masie cząsteczkowej) oraz w analizach ilościowych wzorców jak i skomplikowanych mieszanin biologicznych.

7. BIBLIOGRAFIA

[1] D.S. Peterson, Matrix-free methods for laser desorption/ionization mass spectrometry, Mass Spectrometry Reviews. 26 (2007) 19–34. https://doi.org/10.1002/mas.20104.

[2] J. Nizioł, W. Rode, B. Laskowska, T. Ruman, Novel Monoisotopic 109AgNPET for Laser Desorption/Ionization Mass Spectrometry, Anal. Chem. 85 (2013) 1926–1931. https://doi.org/10.1021/ac303770y.

[3] K. Tanaka, H. Waki, Y. Ido, S. Akita, Y. Yoshida, T. Yoshida, T. Matsuo, Protein and polymer analyses up to m/z 100 000 by laser ionization time-of-flight mass spectrometry, Rapid Communications in Mass Spectrometry. 2 (1988) 151–153. https://doi.org/10.1002/rcm.1290020802.

[4] Jan. Sunner, Edward. Dratz, Y.-Chie. Chen, Graphite surface-assisted laser desorption/ionization time-of-flight mass spectrometry of peptides and proteins from liquid solutions, Anal. Chem. 67 (1995) 4335–4342. https://doi.org/10.1021/ac00119a021.

[5] C.-K. Chiang, W.-T. Chen, H.-T. Chang, Nanoparticle-based mass spectrometry for the analysis of biomolecules, Chem. Soc. Rev. 40 (2011) 1269–1281. https://doi.org/10.1039/C0CS00050G.

[6] J. Sekuła, J. Nizioł, W. Rode, T. Ruman, Silver nanostructures in laser desorption/ionization mass spectrometry and mass spectrometry imaging, Analyst. 140 (2015) 6195–6209. https://doi.org/10.1039/C5AN00943J.

[7] A. Kołodziej, T. Ruman, J. Nizioł, Gold and silver nanoparticles-based laser desorption/ionization mass spectrometry method for detection and quantification of carboxylic acids, J Mass Spectrom. 55 (2020) e4604. https://doi.org/10.1002/jms.4604.

[8] A. Arendowski, J. Nizioł, T. Ruman, Silver-109-based laser desorption/ionization mass spectrometry method for detection and quantification of amino acids, J. Mass Spectrom. 53 (2018) 369–378. https://doi.org/10.1002/jms.4068.

[9] J. Nizioł, M. Misiorek, T. Ruman, Mass spectrometry imaging of low molecular weight metabolites in strawberry fruit (Fragaria x ananassa Duch.) cv. Primoris with 109Ag nanoparticle enhanced target, Phytochemistry. 159 (2019) 11–19. https://doi.org/10.1016/j.phytochem.2018.11.014.

[10] J. Nizioł, K. Ossoliński, A. Płaza-Altamer, A. Kołodziej, A. Ossolińska, T. Ossoliński, T. Ruman, Untargeted ultra-high-resolution mass spectrometry metabolomic profiling of blood serum in bladder cancer, Sci Rep. 12 (2022) 15156. https://doi.org/10.1038/s41598-022-19576-9.

[11] A. Arendowski, T. Ruman, Lysine detection and quantification by laser desorption/ionization mass spectrometry on gold nanoparticle-enhanced target, Anal. Methods. 10 (2018) 5398–5405. https://doi.org/10.1039/C8AY01677A.

[12] J. Sekuła, J. Nizioł, W. Rode, T. Ruman, Gold nanoparticle-enhanced target (AuNPET) as universal solution for laser desorption/ionization mass spectrometry analysis and imaging of low molecular weight compounds, Analytica Chimica Acta. 875 (2015) 61–72. https://doi.org/10.1016/j.aca.2015.01.046.

[13] A. Arendowski, T. Ruman, Laser Desorption/Ionisation Mass Spectrometry Imaging of European Yew (Taxus baccata) on Gold Nanoparticle-enhanced Target, Phytochemical Analysis. 28 (2017) 448–453. https://doi.org/10.1002/pca.2693.

[14] J. Sekuła, J. Nizioł, M. Misiorek, P. Dec, A. Wrona, A. Arendowski, T. Ruman, Gold nanoparticle-enhanced target for MS analysis and imaging of harmful compounds in plant, animal tissue and on fingerprint, Analytica Chimica Acta. 895 (2015) 45–53. https://doi.org/10.1016/j.aca.2015.09.003.

[15] Y.E. Silina, C. Fink-Straube, H. Hayen, D.A. Volmer, Analysis of fatty acids and triacylglycerides by Pd nanoparticle-assisted laser desorption/ionization mass spectrometry, Anal. Methods. 7 (2015) 3701–3707. https://doi.org/10.1039/C5AY00705D.

[16] Y.-Z. Yi, S.-J. Jiang, A.C. Sahayam, Palladium nanoparticles as the modifier for the determination of Zn, As, Cd, Sb, Hg and Pb in biological samples by ultrasonic slurry sampling electrothermal vaporization inductively coupled plasma mass spectrometry, J. Anal. At. Spectrom. 27 (2012) 426–431. https://doi.org/10.1039/C2JA10314A.

[17] H. Kawasaki, T. Yonezawa, T. Watanabe, R. Arakawa, Platinum Nanoflowers for Surface-Assisted Laser Desorption/Ionization Mass Spectrometry of Biomolecules, J. Phys. Chem. C. 111 (2007) 16278–16283. https://doi.org/10.1021/jp075159d.

[18] R. Nayak, D.R. Knapp, Effects of Thin-Film Structural Parameters on Laser Desorption/Ionization from Porous Alumina, Anal. Chem. 79 (2007) 4950–4956. https://doi.org/10.1021/ac062289u.

[19] M.-L. Niklew, U. Hochkirch, A. Melikyan, T. Moritz, S. Kurzawski, H. Schlüter, I. Ebner, M.W. Linscheid, Phosphopeptide Screening Using Nanocrystalline Titanium Dioxide Films as Affinity Matrix-Assisted Laser Desorption Ionization Targets in Mass Spectrometry, Anal. Chem. 82 (2010) 1047–1053. https://doi.org/10.1021/ac902403m.

[20] K.-H. Lee, C.-K. Chiang, Z.-H. Lin, H.-T. Chang, Determining enediol compounds in tea using surface-assisted laser desorption/ionization mass spectrometry with titanium dioxide nanoparticle matrices, Rapid Communications in Mass Spectrometry. 21 (2007) 2023–2030. https://doi.org/10.1002/rcm.3058.

[21] S. Taira, K. Kitajima, H. Katayanagi, E. Ichiishi, Y. Ichiyanagi, Manganese oxide nanoparticle-assisted laser desorption/ionization mass spectrometry for medical applications, Science and Technology of Advanced Materials. 10 (2009) 034602. https://doi.org/10.1088/1468-6996/10/3/034602.

[22] M.-J. Kang, J.-C. Pyun, J.-C. Lee, Y.-J. Choi, J.-H. Park, J.-G. Park, J.-G. Lee, H.-J. Choi, Nanowire-assisted laser desorption and ionization mass spectrometry for quantitative analysis of small molecules, Rapid Communications in Mass Spectrometry. 19 (2005) 3166–3170. https://doi.org/10.1002/rcm.2187.

[23] S.K. Kailasa, H.-F. Wu, Multifunctional ZrO2 nanoparticles and ZrO2-SiO2 nanorods for improved MALDI-MS analysis of cyclodextrins, peptides, and phosphoproteins, Anal Bioanal Chem. 396 (2010) 1115–1125. https://doi.org/10.1007/s00216-009-3330-7.

[24] W.-Y. Chen, Y.-C. Chen, Affinity-based mass spectrometry using magnetic iron oxide particles as the matrix and concentrating probes for SALDI MS analysis of peptides and proteins, Anal Bioanal Chem. 386 (2006) 699–704. https://doi.org/10.1007/s00216-006-0427-0.

[25] C.-T. Chen, Y.-C. Chen, Fe3O4/TiO2 Core/Shell Nanoparticles as Affinity Probes for the Analysis of Phosphopeptides Using TiO2 Surface-Assisted Laser Desorption/Ionization Mass Spectrometry, Anal. Chem. 77 (2005) 5912–5919. https://doi.org/10.1021/ac050831t.

[26] N.H. Finkel, B.G. Prevo, O.D. Velev, L. He, Ordered Silicon Nanocavity Arrays in Surface-Assisted Desorption/Ionization Mass Spectrometry, Anal. Chem. 77 (2005) 1088–1095. https://doi.org/10.1021/ac048645v.

[27] M. Dupré, Y. Coffinier, R. Boukherroub, S. Cantel, J. Martinez, C. Enjalbal, Laser desorption ionization mass spectrometry of protein tryptic digests on nanostructured silicon plates, Journal of Proteomics. 75 (2012) 1973–1990. https://doi.org/10.1016/j.jprot.2011.12.039.

[28] G. Piret, H. Drobecq, Y. Coffinier, O. Melnyk, R. Boukherroub, Matrix-Free Laser Desorption/Ionization Mass Spectrometry on Silicon Nanowire Arrays Prepared by Chemical Etching of Crystalline Silicon, Langmuir. 26 (2010) 1354–1361. https://doi.org/10.1021/la902266x.

[29] M. Shariatgorji, N. Amini, L.L. Ilag, Silicon nitride nanoparticles for surface-assisted laser desorption/ionization of small molecules, J Nanopart Res. 11 (2009) 1509–1512. https://doi.org/10.1007/s11051-009-9601-6.

[30] T. Seino, H. Sato, A. Yamamoto, A. Nemoto, M. Torimura, H. Tao, Matrix-Free Laser Desorption/Ionization-Mass Spectrometry Using Self-Assembled Germanium Nanodots, Anal. Chem. 79 (2007) 4827–4832. https://doi.org/10.1021/ac062216a.

[31] H. Kawasaki, T. Akira, T. Watanabe, K. Nozaki, T. Yonezawa, R. Arakawa, Sulfonate group-modified FePtCu nanoparticles as a selective probe for LDI-MS analysis of oligopeptides from a peptide mixture and human serum proteins, Anal Bioanal Chem. 395 (2009) 1423. https://doi.org/10.1007/s00216-009-3122-0.

[32] T. Yonezawa, H. Tsukamoto, S. Hayashi, Y. Myojin, H. Kawasaki, R. Arakawa, Suitability of GaP nanoparticles as a surface-assisted laser desorption/ionization mass spectroscopy inorganic matrix and their soft ionization ability, Analyst. 138 (2013) 995–999. https://doi.org/10.1039/C2AN36738F.

[33] I. Feuerstein, M. Najam-ul-Haq, M. Rainer, L. Trojer, R. Bakry, N.H. Aprilita, G. Stecher, C.W. Huck, G.K. Bonn, H. Klocker, G. Bartsch, A. Guttman, Material-Enhanced Laser Desorption/Ionization (MELDI)—A New Protein Profiling Tool Utilizing Specific Carrier Materials for Time of Flight Mass Spectrometric Analysis, Journal of the American Society for Mass Spectrometry. 17 (2006) 1203–1208. https://doi.org/10.1016/j.jasms.2006.04.032.

[34] Y. Coffinier, S. Szunerits, H. Drobecq, O. Melnyk, R. Boukherroub, Diamond nanowires for highly sensitive matrix-free mass spectrometry analysis of small molecules, Nanoscale. 4 (2011) 231–238. https://doi.org/10.1039/C1NR11274K.

[35] S. Xu, Y. Li, H. Zou, J. Qiu, Z. Guo, B. Guo, Carbon Nanotubes as Assisted Matrix for Laser Desorption/Ionization Time-of-Flight Mass Spectrometry, Anal. Chem. 75 (2003) 6191–6195. https://doi.org/10.1021/ac0345695.

[36] L. Hu, S. Xu, C. Pan, C. Yuan, H. Zou, G. Jiang, Matrix-Assisted Laser Desorption/Ionization Time-of-Flight Mass Spectrometry with a Matrix of Carbon Nanotubes for the Analysis of Low-Mass Compounds in Environmental Samples, Environ. Sci. Technol. 39 (2005) 8442–8447. https://doi.org/10.1021/es0508572.

[37] H. Nasser Abdelhamid, B.-S. Wu, H.-F. Wu, Graphene coated silica applied for high ionization matrix assisted laser desorption/ionization mass spectrometry: A novel approach for environmental and biomolecule analysis, Talanta. 126 (2014) 27–37. https://doi.org/10.1016/j.talanta.2014.03.016.

[38] Y.E. Silina, D.A. Volmer, Nanostructured solid substrates for efficient laser desorption/ionization mass spectrometry (LDI-MS) of low molecular weight compounds, Analyst. 138 (2013) 7053–7065. https://doi.org/10.1039/C3AN01120H.

[39] K.P. Law, J.R. Larkin, Recent advances in SALDI-MS techniques and their chemical and bioanalytical applications, Anal Bioanal Chem. 399 (2011) 2597–2622. https://doi.org/10.1007/s00216-010-4063-3.

[40] K. Song, Q. Cheng, Desorption and ionization mechanisms and signal enhancement in surface assisted laser desorption ionization mass spectrometry (SALDI-MS), Applied Spectroscopy Reviews. 55 (2020) 220–242. https://doi.org/10.1080/05704928.2019.1570519.

[41] J. Wei, J.M. Buriak, G. Siuzdak, Desorption–ionization mass spectrometry on porous silicon, Nature. 399 (1999) 243–246. https://doi.org/10.1038/20400.

[42] R. Arakawa, H. Kawasaki, Functionalized Nanoparticles and Nanostructured Surfaces for Surface-Assisted Laser Desorption/Ionization Mass Spectrometry, Analytical Sciences. 26 (2010) 1229–1240. https://doi.org/10.2116/analsci.26.1229.

[43] H.-W. Tang, K.-M. Ng, W. Lu, C.-M. Che, Ion Desorption Efficiency and Internal Energy Transfer in Carbon-Based Surface-Assisted Laser Desorption/Ionization Mass Spectrometry: Desorption Mechanism(s) and the Design of SALDI Substrates, Anal. Chem. 81 (2009) 4720–4729. https://doi.org/10.1021/ac8026367.

[44] A.Y. Lim, F. Gu, Z. Ma, J. Ma, F. Rowell, Doped amorphous silica nanoparticles as enhancing agents for surface-assisted time-of-flight mass spectrometry, Analyst. 136 (2011) 2775–2785. https://doi.org/10.1039/C1AN15172J.

[45] U. Sezer, L. Wörner, J. Horak, L. Felix, J. Tüxen, C. Götz, A. Vaziri, M. Mayor, M. Arndt, Laser-Induced Acoustic Desorption of Natural and Functionalized Biochromophores, Anal. Chem. 87 (2015) 5614–5619. https://doi.org/10.1021/acs.analchem.5b00601.

[46] W.-P. Peng, Y.-C. Yang, M.-W. Kang, Y.-K. Tzeng, Z. Nie, H.-C. Chang, W. Chang, C.-H. Chen, Laser-Induced Acoustic Desorption Mass Spectrometry of Single Bioparticles, Angewandte Chemie International Edition. 45 (2006) 1423–1426. https://doi.org/10.1002/anie.200503271.

[47] J. Homola, S.S. Yee, G. Gauglitz, Surface plasmon resonance sensors: review, Sensors and Actuators B: Chemical. 54 (1999) 3–15. https://doi.org/10.1016/S0925-4005(98)00321-9.

[48] K. Nagoshi, K. Sakata, K. Shibamoto, T. Korenaga, Ionization Mechanism in Surface Plasmon Enhanced Laser Desorption/Ionization, E-Journal of Surface Science and Nanotechnology. 7 (2009) 93–96. https://doi.org/10.1380/ejssnt.2009.93.

[49] T. Mieno, Plasma Science and Technology: Progress in Physical States and Chemical Reactions, BoD – Books on Demand, 2016.

[50] A. Steimle, I.B. Autenrieth, J.-S. Frick, Structure and function: Lipid A modifications in commensals and pathogens, International Journal of Medical Microbiology. 306 (2016) 290–301. https://doi.org/10.1016/j.ijmm.2016.03.001.

8. DOROBEK NAUKOWY

Publikacje w recenzji:

- J. Nizioł, K. Ossoliński, A. Płaza-Altamer, A. Kołodziej, A. Ossolińska, T. Ossoliński, A. Nieczaj, T. Ruman, Untargeted urinary metabolomics for bladder cancer biomarker screening with ultrahigh-resolution mass spectrometry, Scientific Reports, 2023
- K. Ossoliński, T. Ruman, V. Copié, B. P. Tripet, A. Kołodziej, A. Płaza-Altamer, A. Ossolińska, T. Ossoliński, A. Nieczaj, J. Nizioł, Urinary metabolic profiling of bladder cancer, 2023

Materiały pokonferencyjne:

- Joanna Nizioł, Aneta Płaza-Altamer, **Artur Kołodziej**, Tomasz Ruman, *Obrazowanie tkanek za pomocą spektrometrii mas z laserową desorpcją/jonizacją* - (NAUKA I PRZEMYSŁ metody spektroskopowe w praktyce nowe wyzwania i możliwości, Lublin 2022)
- J. Nizioł, K. Ossoliński, A. Płaza-Altamer, **A. Kołodziej**, A. Nieczaj, T. Ruman, *Analiza metabolomiczna surowicy krwi w poszukiwaniu biomarkerów raka pęcherza moczowego,* Nauka i Przemysł metody spektroskopowe w praktyce nowe wyzwania i możliwości, Wydawnictwo UMCS, Lublin, 2023

Konferencje naukowe:

- International Students' Conference ISC-ADAMAS 2020 "Education: Creating Future Today. Going Beyond the Pandemic" 05.12.2020; Kolkata, Indie
- XIII Ogólnopolska Konferencja „Flawonoidy i ich zastosowanie", 08-09.09.2022; Łańcut

Projekty naukowe:

- Wykonawca w grancie pt. „Poszukiwanie oraz charakterystyka biomarkerów raka pęcherza" o nr umowy UMO-2018/31/D/ST4/00109
- Wykonawca w projekcie pt. „Dwu i trójskładnikowe kompleksy jonów srebra z kwasem N-fenyloantranilowym, niflumowym oraz mefenamowym jako nowa alternatywa dla antybiotyków"

Szkolenia:

- Seminarium pt. „Innowacyjne rozwiązania do hodowli komórek ssaczych"; organizator Merck Sp. z o. o. 16.10.2019, Rzeszów

Artykuły popularnonaukowe:

- **Artur Kołodziej**, Wojciech Kosiek, Piotr Orzechowski, *Hodowle 3D – nowy kierunek w badaniach in vitro*, Gazeta Politechniki, 1-3/2019

Działalność organizacyjna:

- Udział w wydarzeniach organizowanych przez Wydział Chemiczny Politechniki Rzeszowskiej („Noc Odkrywców" Nocne Spotkania z Nauką, Wybrane Problemy Chemii)
- Wyjazdy do szkół średnich w ramach promocji nowych kierunków studiów na Wydziale Chemicznym
- Aktywne członkostwo w Kole Naukowym Studentów Biotechnologii „INSERT"
- Członek Uczelnianej Rady Samorządu Doktorantów (2019-2020)

9. KOPIE OŚWIADCZEŃ WSPÓŁAUTORÓW ARTYKUŁÓW NAUKOWYCH

POLITECHNIKA
RZESZOWSKA
im. IGNACEGO ŁUKASIEWICZA

al. Powstańców Warszawy 12, 35-959 Rzeszów
tel.: +48 17 865 1100, e-mail: kancelaria@prz.edu.pl
www.prz.edu.pl

Mgr inż. Artur Kołodziej
Wydział Chemiczny, Politechnika Rzeszowska
Katedra Chemii Nieorganicznej i Analitycznej
al. Powstańców Warszawy 6, 35-959 Rzeszów
e-mail: a.kolodziej@prz.edu.pl

Rzeszów, 05.04.2023

OŚWIADCZENIE

Oświadczam, że w niżej wymienionych pracach mój udział merytoryczny oraz procentowy był następujący:

Lp.	**Tytuł publikacji oraz informacje bibliograficzne**	**Udział merytoryczny**	**Udział %**
1	Kołodziej A, Ruman T, Nizioł J. *Gold and silver nanoparticles-based laser desorption/ionization mass spectrometry method for detection and quantification of carboxylic acids.* Journal of Mass Spectrometry 2020;55:e4604. DOI: 10.1002/jms.4604	- przeprowadzenie analizy wzorców za pomocą spektrometru mas typu MALDI, - analiza i wizualizacja wyników	33%
2	Szulc, J.; Kołodziej, A.; Ruman, T. *Silver-109/Silver/Gold Nanoparticle-Enhanced Target Surface-Assisted Laser Desorption/Ionisation Mass Spectrometry—The New Methods for an Assessment of Mycotoxin Concentration on Building Materials. Toxins* 2021, *13*, 45. https://doi.org/10.3390/toxins13010045	- przeprowadzenie analiz badanych związków, - analiza uzyskanych wyników	10%

3	Aneta Płaza, Artur Kołodziej, Joanna Nizioł, and Tomasz Ruman, *Laser Ablation Synthesis in Solution and Nebulization of Silver-109 Nanoparticles for Mass Spectrometry and Mass Spectrometry Imaging, ACS Measurement Science Au,* 2022, 2, 1, 14–22. DOI: 10.1021/acsmeasuresciau.1c00020	- prowadzenie eksperymentów (synteza nanocząstek, obrazowanie SEM, badanie związków testowych), - analiza i wizualizacja uzyskanych wyników, - odniesienie się do uwag recenzentów i współopracowanie końcowej formy pracy	25%
4	Płaza-Altamer, A., Kołodziej, A., Nizioł, J., Ruman, T. *Laser generated gold nanoparticles for mass spectrometry of low molecular weight compounds*, Chemical Technology and Biotechnology, 2022, ISSN 2720-6793	- prowadzenie eksperymentów (synteza nanocząstek, obrazowanie SEM, badanie związków testowych), - analiza i wizualizacja uzyskanych wyników,	25%
5	Artur Kołodziej, Aneta Płaza-Altamer, Joanna Nizioł, Tomasz Ruman, *Infrared pulsed fiber laser-produced silver-109-nanoparticles for laser desorption/ionization mass spectrometry of carboxylic acids,* International Journal of Mass Spectrometry, 2022, 474, 116816. DOI: 10.1016/j.ijms.2022.116816	- przeprowadzenie eksperymentów, - analiza, wizualizacja i opracowanie statystyczne wyników, - zredagowanie i edycja treści manuskryptu, - odniesienie się do uwag recenzentów i zredagowanie końcowej formy publikacji, - pełnienie funkcji autora korespondencyjnego	25%
6	Artur Kołodziej, Aneta Płaza-Altamer, Joanna Nizioł, Tomasz Ruman, *Infrared pulsed fiber*	- przeprowadzenie eksperymentów,	25%

	laser-produced silver-109 nanoparticles for laser desorption/ionization mass spectrometry of 3-hydroxycarboxylic acids, Rapid Communications in Mass Spectrometry, 2022, 36, 21, e9375. DOI: 10.1002/rcm.9375	- analiza, wizualizacja i opracowanie statystyczne wyników, - zredagowanie i edycja treści manuskryptu, - odniesienie się do uwag recenzentów i zredagowanie końcowej formy publikacji, - pełnienie funkcji autora korespondencyjnego	
7	Aneta Płaza-Altamer, Artur Kołodziej, Joanna Nizioł, and Tomasz Ruman, *Infrared pulsed fiber laser-produced silver-109-nanoparticles for laser desorption/ionization mass spectrometry of amino acids*, Journal of Mass Spectrometry, 2022, 57:e4815. https://doi.org/10.1002/jms.4815	- wytworzenie płytek ^{109}AgLGN do analizy związków, - współtworzenie i edycja manuskryptu	25%
8	Krzysztof Ossoliński, Tomasz Ruman, Tadeusz Ossoliński, Anna Ossolińska, Adrian Arendowski, Artur Kołodziej, Aneta Płaza-Altamer, Joanna Nizioł, *Monoisotopic silver nanoparticles-based mass spectrometry imaging of human bladder cancer tissue: Biomarker discovery*, Advances in Medical Sciences, 2023, 68(1), 38-45, https://doi.org/10.1016/j.advms.2022.12.002	- prowadzenie eksperymentów (analiza tkanek metodą ^{109}AgNPET), - przygotowanie manuskryptu	14%
9	Krzysztof Ossoliński, Tomasz Ruman, Valérie Copié, Brian P. Tripet, Leonardo B. Nogueira, Katiane O.P.C. Nogueira, Artur Kołodziej, Aneta Płaza-Altamer, Anna Ossolińska, Tadeusz	- przeprowadzenie eksperymentów (analiza próbek z wykorzystaniem spektrometru mas typu MALDI),	9%

	Ossoliński, Joanna Nizioł, *Metabolomic and elemental profiling of blood serum in bladder cancer,* Journal of Pharmaceutical Analysis, 2022, ISSN 2095-1779. https://doi.org/10.1016/j.jpha.2022.08.004	- analiza danych uzyskanych po eksperymentach	
10	Nizioł J., Ossoliński K., Płaza-Altamer A., Kołodziej A. *i wsp. Untargeted ultra-high-resolution mass spectrometry metabolomic profiling of blood serum in bladder cancer.* Scientific Reports, 12, 15156 (2022). https://doi.org/10.1038/s41598-022-19576-9	- przygotowanie próbek do analizy	14%

Kołodziej Artur
Podpis

Mgr inż. Aneta Płaza-Altamer
Wydział Chemiczny, Politechnika Rzeszowska
Katedra Chemii Nieorganicznej i Analitycznej
al. Powstańców Warszawy 6, 35-959 Rzeszów
e-mail: a.plaza@prz.edu.pl

Rzeszów, 05.04.2023

OŚWIADCZENIE

Oświadczam, że w niżej wymienionych pracach mój udział merytoryczny oraz procentowy był następujący:

Lp.	Tytuł publikacji oraz informacje bibliograficzne	Udział merytoryczny	Udział %
3	Aneta Płaza, Artur Kołodziej, Joanna Nizioł, and Tomasz Ruman, *Laser Ablation Synthesis in Solution and Nebulization of Silver-109 Nanoparticles for Mass Spectrometry and Mass Spectrometry Imaging, ACS Measurement Science Au,* 2022, 2, 1, 14–22. DOI: 10.1021/acsmeasuresciau.1c00020	- przeprowadzenie eksperymentów (synteza nanocząstek, badania UV-vis, DLS, obrazowanie MS) - analiza, wizualizacja i opracowanie wyników, - zredagowanie i edycja treści manuskryptu, - odniesienie się do uwag recenzentów i zredagowanie końcowej formy publikacji	25%
4	Płaza-Altamer, A., Kołodziej, A., Nizioł, J., Ruman, T. *Laser generated gold nanoparticles for mass spectrometry of low molecular weight compounds*, Chemical	- przeprowadzenie eksperymentów (synteza nanocząstek, badania UV-vis, DLS, pomiary LDI MS), - analiza, wizualizacja i opracowanie statystyczne wyników,	25%

	Technology and Biotechnology, 2022, ISSN 2720-6793	- zredagowanie i edycja treści manuskryptu, - odniesienie się do uwag recenzentów i zredagowanie końcowej formy publikacji, - pełnienie funkcji autora korespondencyjnego	
5	Artur Kołodziej, Aneta Płaza-Altamer, Joanna Nizioł, Tomasz Ruman, *Infrared pulsed fiber laser-produced silver-109-nanoparticles for laser desorption/ionization mass spectrometry of carboxylic acids*, International Journal of Mass Spectrometry, 2022, 474, 116816. DOI: 10.1016/j.ijms.2022.116816	- wytworzenie płytek ^{109}AgLGN do analizy związków, - współtworzenie i edycja manuskryptu	25%
6	Artur Kołodziej, Aneta Płaza-Altamer, Joanna Nizioł, Tomasz Ruman, *Infrared pulsed fiber laser-produced silver-109 nanoparticles for laser desorption/ionization mass spectrometry of 3-hydroxycarboxylic acids*, Rapid Communications in Mass Spectrometry, 2022, 36, 21, e9375. DOI: 10.1002/rcm.9375	- wytworzenie płytek ^{109}AgLGN do analizy związków,	25%
7	Aneta Płaza-Altamer, Artur Kołodziej, Joanna Nizioł, and Tomasz Ruman, *Infrared pulsed fiber laser-produced silver-109-nanoparticles for laser desorption/ionization mass spectrometry of amino acids*, Journal of	- przeprowadzenie eksperymentów, - analiza, wizualizacja i opracowanie statystyczne wyników, - zredagowanie i edycja treści manuskryptu,	25%

	Mass Spectrometry, 2022, 57:e4815. https://doi.org/10.1002/jms.4815	- odniesienie się do uwag recenzentów i zredagowanie końcowej formy publikacji, - pełnienie funkcji autora korespondencyjnego	
8	Krzysztof Ossoliński, Tomasz Ruman, Tadeusz Ossoliński, Anna Ossolińska, Adrian Arendowski, Artur Kołodziej, Aneta Płaza-Altamer, Joanna Nizioł. *Monoisotopic silver nanoparticles-based mass spectrometry imaging of human bladder cancer tissue: Biomarker discovery,* Advances in Medical Sciences, 2023, 68(1), 38-45, https://doi.org/10.1016/j.advms.2022.12.002	- analiza i wizualizacja uzyskanych wyników, - odniesienie się do uwag recenzentów i współopracowanie końcowej formy pracy	14%
9	Krzysztof Ossoliński, Tomasz Ruman, Valérie Copié, Brian P. Tripet, Leonardo B. Nogueira, Katiane O.P.C. Nogueira, Artur Kołodziej, Aneta Płaza-Altamer, Anna Ossolińska, Tadeusz Ossoliński, Joanna Nizioł, *Metabolomic and elemental profiling of blood serum in bladder cancer,* Journal of Pharmaceutical Analysis, 2022, ISSN 2095-1779. https://doi.org/10.1016/j.jpha.2022.08.004	- przygotowanie próbek do analizy	9%
10	Nizioł J., Ossoliński K., Płaza-Altamer A., Kołodziej A. *i wsp. Untargeted ultra-high-resolution mass spectrometry metabolomic*	- przygotowanie próbek do analizy - przeprowadzenie pomiarów UHPLC-ESI-UHRMS+MS/MS	14%

	profiling of blood serum in bladder cancer. Scientific Reports, 12, 15156 (2022). https://doi.org/10.1038/s41598-022-19576-9		

Aneta Okaro-Altomer
....
Podpis

POLITECHNIKA RZESZOWSKA
im. IGNACEGO ŁUKASIEWICZA

al. Powstańców Warszawy 12, 35-959 Rzeszów
tel.: +48 17 865 1100, e-mail: kancelaria@prz.edu.pl
www.prz.edu.pl

Prof. dr hab. inż. Tomasz Ruman
Wydział Chemiczny, Politechnika Rzeszowska
Katedra Chemii Nieorganicznej i Analitycznej
al. Powstańców Warszawy 6, 35-959 Rzeszów
e-mail: tomruman@prz.edu.pl

Rzeszów, 05.04.2023

OŚWIADCZENIE

Oświadczam, że w niżej wymienionych pracach mój udział merytoryczny oraz procentowy był następujący:

Lp.	Tytul publikacji oraz informacje bibliograficzne	Udział merytoryczny	Udział %
1	Kołodziej A, Ruman T, Nizioł J. *Gold and silver nanoparticles-based laser desorption/ionization mass spectrometry method for detection and quantification of carboxylic acids.* Journal of Mass Spectrometry 2020;55:e4604. DOI: 10.1002/jms.4604	- tworzenie koncepcji badań, - korekta treści manuskryptu, - odniesienie się do uwag recenzentów i współopracowanie końcowej formy pracy, - nadzór naukowy nad badaniami	33%
2	Szulc, J.; Kołodziej, A.; Ruman, T. *Silver-109/Silver/Gold Nanoparticle-Enhanced Target Surface-Assisted Laser Desorption/Ionisation Mass Spectrometry—The New Methods for an Assessment of Mycotoxin Concentration on Building Materials.* Toxins 2021, *13,* 45. https://doi.org/10.3390/toxins13010045	- wybór metodologii badawczej, - analiza i wizualizacja uzyskanych wyników, - zredagowanie i edycja treści manuskryptu, - odniesienie się do uwag recenzentów i zredagowanie końcowej formy publikacji, - pozyskanie środków na badania	40%

3	Aneta Płaza, Artur Kołodziej, Joanna Nizioł, and Tomasz Ruman, *Laser Ablation Synthesis in Solution and Nebulization of Silver-109 Nanoparticles for Mass Spectrometry and Mass Spectrometry Imaging, ACS Measurement Science Au,* 2022, 2, 1, 14–22. DOI: 10.1021/acsmeasuresciau.1c00020	- wybór metodologii prowadzenia badań, - korekta treści manuskryptu, - odniesienie się do uwag recenzentów i współopracowanie końcowej formy pracy, - nadzór naukowy nad badaniami	25%
4	Płaza-Altamer, A., Kołodziej, A., Nizioł, J., Ruman, T. *Laser generated gold nanoparticles for mass spectrometry of low molecular weight compounds*, Chemical Technology and Biotechnology, 2022, ISSN 2720-6793	- wybór metodologii prowadzenia badań, - korekta treści manuskryptu, - odniesienie się do uwag recenzentów i współopracowanie końcowej formy pracy, - nadzór naukowy nad badaniami	25%
5	Artur Kołodziej, Aneta Płaza-Altamer, Joanna Nizioł, Tomasz Ruman, *Infrared pulsed fiber laser-produced silver-109-nanoparticles for laser desorption/ionization mass spectrometry of carboxylic acids,* International Journal of Mass Spectrometry, 2022, 474, 116816. DOI: 10.1016/j.ijms.2022.116816	- wybór metodologii prowadzenia badań, - korekta treści manuskryptu, - odniesienie się do uwag recenzentów i współopracowanie końcowej formy pracy, - nadzór naukowy nad badaniami	25%
6	Artur Kołodziej, Aneta Płaza-Altamer, Joanna Nizioł, Tomasz Ruman, *Infrared pulsed fiber laser-produced silver-109 nanoparticles for laser desorption/ionization mass spectrometry of 3-hydroxycarboxylic acids*, Rapid Communications in Mass Spectrometry, 2022, 36, 21, e9375. DOI: 10.1002/rcm.9375	- wybór metodologii prowadzenia badań, - korekta treści manuskryptu, - odniesienie się do uwag recenzentów i współopracowanie końcowej formy pracy, - nadzór naukowy nad badaniami	25%

7	Aneta Płaza-Altamer, Artur Kołodziej, Joanna Nizioł, and Tomasz Ruman, *Infrared pulsed fiber laser-produced silver-109-nanoparticles for laser desorption/ionization mass spectrometry of amino acids*, Journal of Mass Spectrometry, 2022, 57:e4815. https://doi.org/10.1002/jms.4815	- wybór metodologii prowadzenia badań , - korekta treści manuskryptu, - odniesienie się do uwag recenzentów i współopracowanie końcowej formy pracy, - nadzór naukowy nad badaniami	25%
8	Krzysztof Ossoliński, Tomasz Ruman, Tadeusz Ossoliński, Anna Ossolińska, Adrian Arendowski, Artur Kołodziej, Aneta Płaza-Altamer, Joanna Nizioł, *Monoisotopic silver nanoparticles-based mass spectrometry imaging of human bladder cancer tissue: Biomarker discovery*, Advances in Medical Sciences, 2023, 68(1), 38-45, https://doi.org/10.1016/j.advms.2022.12.002	- tworzenie koncepcji badań, - analiza uzyskanych wyników, - korekta treści manuskryptu, - odniesienie się do uwag recenzentów i współopracowanie końcowej formy pracy, - nadzór naukowy nad badaniami	30%
9	Krzysztof Ossoliński, Tomasz Ruman, Valérie Copié, Brian P. Tripet, Leonardo B. Nogueira, Katiane O.P.C. Nogueira, Artur Kołodziej, Aneta Płaza-Altamer, Anna Ossolińska, Tadeusz Ossoliński, Joanna Nizioł, *Metabolomic and elemental profiling of blood serum in bladder cancer*, Journal of Pharmaceutical Analysis, 2022, ISSN 2095-1779. https://doi.org/10.1016/j.jpha.2022.08.004	- wybór metodologii badań, - analiza uzyskanych danych, - przygotowanie treści manuskryptu, - odniesienie się do uwag recenzentów i współopracowanie końcowej formy pracy, - nadzór naukowy nad badaniami	9%
10	Nizioł J., Ossoliński K., Płaza-Altamer A., Kołodziej A. *i wsp. Untargeted ultra-high-*	- wybór metodologii badań, - analiza uzyskanych danych,	14%

	resolution mass spectrometry metabolomic profiling of blood serum in bladder cancer. Scientific Reports, 12, 15156 (2022). https://doi.org/10.1038/s41598-022-19576-9	- przygotowanie treści manuskryptu, - odniesienie się do uwag recenzentów i współopracowanie końcowej formy pracy, - nadzór naukowy nad badaniami	

KIEROWNIK
KATEDRY CHEMII
NIEORGANICZNEJ I ANALITYCZNEJ
WYDZIAŁ CHEMICZNY PRz
prof. dr hab. inż. Tomasz Ruman

....
Podpis

Dr hab. Joanna Nizioł, prof. PRz
Wydział Chemiczny, Politechnika Rzeszowska
Katedra Chemii Nieorganicznej i Analitycznej
al. Powstańców Warszawy 6, 35-959 Rzeszów
e-mail: jniziol@prz.edu.pl

Rzeszów, 05.04.2023

OŚWIADCZENIE

Oświadczam, że w niżej wymienionych pracach mój udział merytoryczny oraz procentowy był następujący:

Lp.	Tytuł publikacji oraz informacje bibliograficzne	Udział merytoryczny	Udział %
1	Kołodziej A, Ruman T, Nizioł J. *Gold and silver nanoparticles-based laser desorption/ionization mass spectrometry method for detection and quantification of carboxylic acids.* Journal of Mass Spectrometry 2020;55:e4604. DOI: 10.1002/jms.4604	- przygotowanie treści manuskryptu, - odniesienie się do uwag recenzentów i współopracowanie końcowej formy pracy, - pozyskanie środków na badania, - pełnienie funkcji autora korespondencyjnego	33%
3	Aneta Płaza, Artur Kołodziej, Joanna Nizioł, and Tomasz Ruman, *Laser Ablation Synthesis in Solution and Nebulization of Silver-109 Nanoparticles for Mass Spectrometry and Mass Spectrometry Imaging, ACS Measurement Science Au*, 2022, 2, 1, 14–22. DOI: 10.1021/acsmeasuresciau.1c00020	- pozyskanie środków na badania	25%

4	Płaza-Altamer, A., Kołodziej, A., Nizioł, J., Ruman, T. *Laser generated gold nanoparticles for mass spectrometry of low molecular weight compounds*, Chemical Technology and Biotechnology, 2022, ISSN 2720-6793	- pozyskanie środków na badania	25%
5	Artur Kołodziej, Aneta Płaza-Altamer, Joanna Nizioł, Tomasz Ruman, *Infrared pulsed fiber laser-produced silver-109-nanoparticles for laser desorption/ionization mass spectrometry of carboxylic acids*, International Journal of Mass Spectrometry, 2022, 474, 116816. DOI: 10.1016/j.ijms.2022.116816	- pozyskanie środków na badania	25%
6	Artur Kołodziej, Aneta Płaza-Altamer, Joanna Nizioł, Tomasz Ruman, *Infrared pulsed fiber laser-produced silver-109 nanoparticles for laser desorption/ionization mass spectrometry of 3-hydroxycarboxylic acids*, Rapid Communications in Mass Spectrometry, 2022, 36, 21, e9375. DOI: 10.1002/rcm.9375	- pozyskanie środków na badania	25%
7	Aneta Płaza-Altamer, Artur Kołodziej, Joanna Nizioł, and Tomasz Ruman, *Infrared pulsed fiber laser-produced silver-109-nanoparticles for laser desorption/ionization mass spectrometry of amino acids*, Journal of Mass Spectrometry, 2022, 57:e4815. https://doi.org/10.1002/jms.4815	- pozyskanie środków na badania	25%
8	Krzysztof Ossoliński, Tomasz Ruman, Tadeusz Ossoliński, Anna Ossolińska, Adrian	- współtworzenie koncepcji badań,	30%

	Arendowski, Artur Kołodziej, Aneta Płaza-Altamer, Joanna Nizioł, *Monoisotopic silver nanoparticles-based mass spectrometry imaging of human bladder cancer tissue: Biomarker discovery*, Advances in Medical Sciences, 2023, 68(1), 38-45, https://doi.org/10.1016/j.advms.2022.12.002	- analiza statystyczna i wizualizacja uzyskanych wyników, - przygotowanie manuskryptu, - pozyskanie środków na badania	
9	Krzysztof Ossoliński, Tomasz Ruman, Valérie Copié, Brian P. Tripet, Leonardo B. Nogueira, Katiane O.P.C. Nogueira, Artur Kołodziej, Aneta Płaza-Altamer, Anna Ossolińska, Tadeusz Ossoliński, Joanna Nizioł, *Metabolomic and elemental profiling of blood serum in bladder cancer*, Journal of Pharmaceutical Analysis, 2022, ISSN 2095-1779. https://doi.org/10.1016/j.jpha.2022.08.004	- współtworzenie koncepcji badań, - analiza statystyczna i wizualizacja uzyskanych wyników, - przygotowanie manuskryptu, - odniesienie się do uwag recenzentów i współopracowanie końcowej formy pracy, - pozyskanie środków na badania	9%
10	Nizioł J., Ossoliński K., Płaza-Altamer A., Kołodziej A. *i wsp. Untargeted ultra-high-resolution mass spectrometry metabolomic profiling of blood serum in bladder cancer*. Scientific Reports, 12, 15156 (2022). https://doi.org/10.1038/s41598-022-19576-9	- współtworzenie koncepcji badań, - analiza statystyczna i wizualizacja uzyskanych wyników, - przygotowanie manuskryptu, - odniesienie się do uwag recenzentów i współopracowanie końcowej formy pracy, - pozyskanie środków na badania	14%

Wydział Chemiczny PRz
dr hab. Joanna Nizioł, prof. PRz
....
Podpis

Dr hab. inż. Justyna Szulc
Wydział Biotechnologii i Nauk o Żywności, Politechnika Łódzka
Katedra Biotechnologii Środowiskowej
ul. Wólczańska 171/173, 90-530 Łódź
e-mail: justyna.szulc@p.lodz.pl

Rzeszów, 05.04.2023

OŚWIADCZENIE

Oświadczam, że w niżej wymienionych pracach mój udział merytoryczny oraz procentowy był następujący:

Lp.	**Tytuł publikacji oraz informacje bibliograficzne**	**Udział merytoryczny**	**Udział %**
2	Szulc, J.; Kołodziej, A.; Ruman, T. *Silver-109/Silver/Gold Nanoparticle-Enhanced Target Surface-Assisted Laser Desorption/Ionisation Mass Spectrometry—The New Methods for an Assessment of Mycotoxin Concentration on Building Materials. Toxins* 2021, *13,* 45. https://doi.org/10.3390/toxins13010045	- tworzenie koncepcji publikacji, - zredagowanie i edycja treści manuskryptu, - odniesienie się do uwag recenzentów i zredagowanie końcowej formy publikacji, - zarządzanie projektem w ramach, którego stworzono publikację - pozyskanie środków na badania	50%

Justyna Szulc
Podpis

Received: 17 March 2020 | Revised: 15 June 2020 | Accepted: 24 June 2020

DOI: 10.1002/jms.4604

RESEARCH ARTICLE

Journal of MASS SPECTROMETRY WILEY

Gold and silver nanoparticles-based laser desorption/ionization mass spectrometry method for detection and quantification of carboxylic acids

Artur Kołodziej[1] | **Tomasz Ruman**[2] | **Joanna Nizioł**[2]

[1]Doctoral School of Engineering and Technical Sciences, Rzeszów University of Technology, 8 Powstańców Warszawy Ave., Rzeszów, 35-959, Poland

[2]Faculty of Chemistry, Rzeszów University of Technology, 6 Powstańców Warszawy Ave., Rzeszów, 35-959, Poland

Correspondence
Joanna Nizioł, Faculty of Chemistry, Rzeszów University of Technology, 6 Powstańców Warszawy Ave., Rzeszów 35-959, Poland.
Email: jniziol@prz.edu.pl

Funding information
National Science Centre, Poland, Grant/Award Number: 2016/23/B/ST4/00062

Abstract

A comparison of ionization efficiency for gold and silver nanoparticles used as an active media of matrix-less laser desorption/ionization (LDI) mass spectrometry (MS) methods was made for carboxylic acids including fatty acids. The matrix-assisted laser desorption/ionization (MALDI)-type targets containing monoisotopic cationic ^{109}Ag nanoparticles (^{109}AgNPs) and Au nanoparticles (AuNPs) were used for rapid MS measurements of 10 carboxylic acids of different chemical properties. Carboxylic acids were directly quantified in experiments with 10 000-fold concentration change conditions ranging from 1 mg/ml to 100 ng/ml which equates to 1 μg to 100 pg of carboxylic acids per measurement spot.

KEYWORDS

carboxylic acids, fatty acids, low molecular weight compounds, MALDI, matrix-free LDI, monoisotopic silver, nanoparticles, SALDI

1 | INTRODUCTION

Matrix-assisted laser desorption/ionization mass spectrometry (MALDI-MS), one of the most sensitive and efficient MS methods, was developed by Tanaka et al. in 1988.[1] Usually, it is not applied for detection of low molecular weight (LMW) compounds (MW < 1000 Da), because common MALDI matrices, which are LMW organic compounds, produce variety of matrix-related ions during desorption/ionization process. Signals from matrix ions make spectrum analysis difficult in the low mass region.[2] The presented problem has been partly solved by the development of surface-assisted desorption/ionization (SALDI) techniques. In this family of methods, target plates are coated with diverse nanostructures.[3–9] We have recently shown new method of preparation of modified MALDI target by covering it with cationic, monoisotopic silver-109 nanoparticles (silver-109 nanoparticle-enhanced target [^{109}AgNPET]). Another method for LMW compounds analysis was using gold nanoparticle-enhanced target (AuNPET).[8,9] In both cases, the elimination of the standard matrix used in MALDI significantly facilitates LMW analysis. Application of silver-109 nanoparticles (^{109}AgNPs) and gold nanoparticles (AuNPs) for detection of various low mass compounds in laser desorption/ionization (LDI) MS was shown in our recent papers proving that targets are useful in rapid determination of pure compounds as well as analysis of complicated biological mixtures such as blood plasma or plant tissue with very high mass accuracy.[8–11] What is more, LDI methods are especially important as they are directly compatible with MS imaging (MSI) and thus allow analyses of spatial distribution of analytes within solid objects such as animal or plant tissues.[12]

Dicarboxylic acids control the activity of many enzymatic receptors and several biosynthetic processes.[13] Fatty acids are connected to various diseases, for example, inflammatory bowel disease and cardiovascular disease, or they can be new biomarkers for diseases.[14–16] What is more, in 2016, research results on the consumption of oils containing erucic acid were published and suggested that eating these oils could eventually lead to a heart disease called myocardial lipidosis.[15] Dicarboxylic and fatty acids are generally detected with the use of liquid chromatography-MS (LC-MS) approach.[18–21] However, there are only few publications presenting LDI approaches to detect these compounds.[17,22,23] In this work, we present for the first time results aimed at detection and quantification of carboxylic acids with the use of surface-assisted LDI MS based on two nanoparticle systems: ^{109}AgNPs and AuNPs.

2 | EXPERIMENTAL SECTION

2.1 | Materials

Silver-109 (min. 99.75% of ^{109}Ag) isotope was purchased from BuyIsotope (Sweden) and transformed to trifluoroacetate salt by commonly known methods (involving dissolving in HNO_3, followed by ^{109}AgOH formation and reaction with trifluoroacetic acid) and recrystallized from THF/hexane system. 2,5-Dihydroxybenzoic acid (DHB) was purchased from Sigma-Aldrich (Poland). Chloro(trimethylophosphite)gold(I) used for nanoparticle synthesis was of 97+% purity (Sigma-Aldrich). The pyridine–borane complex used was at ~8 M borane concentration (Sigma-Aldrich). Steel targets were machined from stainless steel. The surface of targets was polished to mirror-like appearance with P150 to P2000 grit (ISO/FEPA Grit designation). All acid standards and other chemicals were purchased from Sigma-Aldrich (97–99% purity). All solvents were of HPLC quality, except for water (18 MΩ-cm water was produced locally).

2.1.1 | Preparation of ^{109}AgNPET target

The ^{109}AgNP-covered target was prepared similarly to the one described in our recent publication.[8] Silver-109 trifluoroacetate (10 mg) was dissolved in anhydrous, inhibitor-free THF (50 ml) and the solution poured into a beaker containing a target plate (custom made, stainless steel target of 35 × 45 mm size). Solid DHB (35 mg) was added, and following stirring, the solution was left for 24 h. The target plate was then washed with THF and deionized water (three times), very gentle cleaned with cotton wool ball, and again washed three times with THF, then water and acetonitrile. Characterization of nanoparticles on the surface of the target was shown in our recent work.[11]

2.1.2 | Preparation of AuNPET surface

Chloro(trimethylophosphite)gold(I) (8 mg) was dissolved in 15-ml acetonitrile and the solution poured into a beaker containing a target plate (custom made, stainless steel target of 35 × 45 mm size). The pyridine–borane complex (52 μl) was added, and following stirring, the solution was left for 24 h. The target plate was then washed with acetonitrile and deionized water (three times), very gentle cleaned with cotton wool ball, and again washed three times with acetonitrile and water. Characterization of nanoparticles on the surface of the target was shown in our recent work.[9]

TABLE 1 Limits of detection and lower limit of quantification for studied carboxylic acids

	^{109}AgNPs		AuNPs	
Carboxylic acid	LOD[a] ± SD (ng/ml) (μM)	**LLOQ[b] ± SD (ng/ml)**	LOD[a] ± SD (ng/ml) (μM)	**LLOQ[b] ± SD[c] (ng/ml)**
Malic	4204 ± 1013 31.4	7007 ± 1688	3914 ± 1350 48.6	6523 ± 2249
Pimelic	4447 ± 99 27.8	7411 ± 165	7312 ± 3364 76.1	12 186 ± 5607
Azelaic	3166 ± 1279 16.8	5276 ± 2131	9424 ± 5139 83.5	15 707 ± 8564
3-Methylhippuric	1437 ± 735 7.4	2396 ± 1225	1625 ± 672 14.0	2708 ± 1121
Palmitic	13 056 ± 1944 50.9	21 759 ± 3241	-	-
Linoleic	2168 ± 157 7.7	3614 ± 262	-	-
Oleic	3073 ± 298 10.9	5122 ± 469	-	-
Arachidonic	883 ± 180 2.9	1471 ± 300	-	-
Arachidic	5957 ± 3537 19.1	9928 ± 5895	19 562 ± 16 153 104.3	32 603 ± 26 921
Erucic	804 ± 603 2.4	1341 ± 1005	-	-

Abbreviations: ^{109}AgNP, ^{109}Ag nanoparticle; AuNP, Au nanoparticle; LLOQ, lower limit of quantification; LOD, limits of detection; S/N, signal-to-noise.

[a] Based on S/N ratio of 3.

[b] Based on S/N ratio of 5.

[c] SD, standard deviation based on triplicates.

2.1.3 | Sample preparation and handling

All acid standards (malic acid, pimelic acid, azelaic acid, 3-methylhippuric acid, palmitic acid, linoleic acid, oleic acid, arachidonic acid, arachidic acid, and erucic acid) were weighed and dissolved in 2-propanol to give a final concentration of each acid 1 mg/ml in mixture. Lower concentration solutions were prepared by diluting of 10 times higher concentration ones. Volumes of 1 μl of acids solution

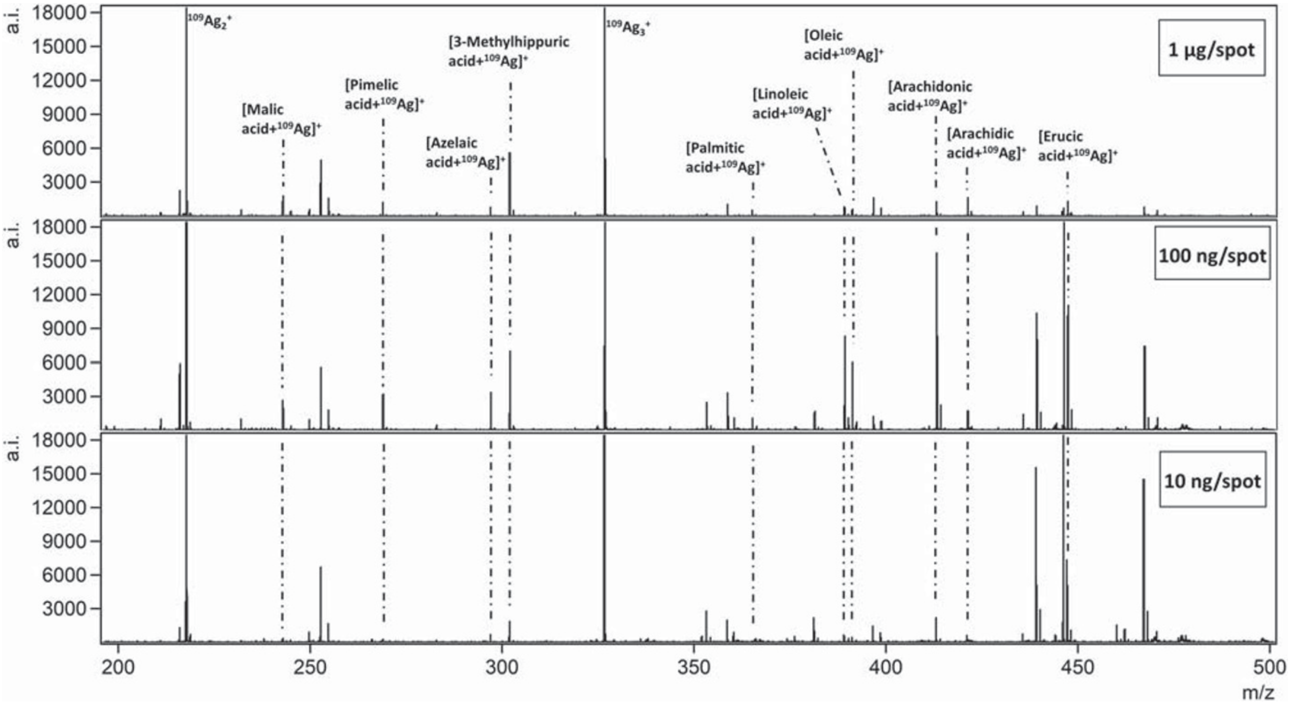

FIGURE 1 Spectra presenting laser desorption/ionization (LDI) mass spectrometry (MS) measurement results for carboxylic acids mixture with ^{109}Ag nanoparticles (^{109}AgNPs)

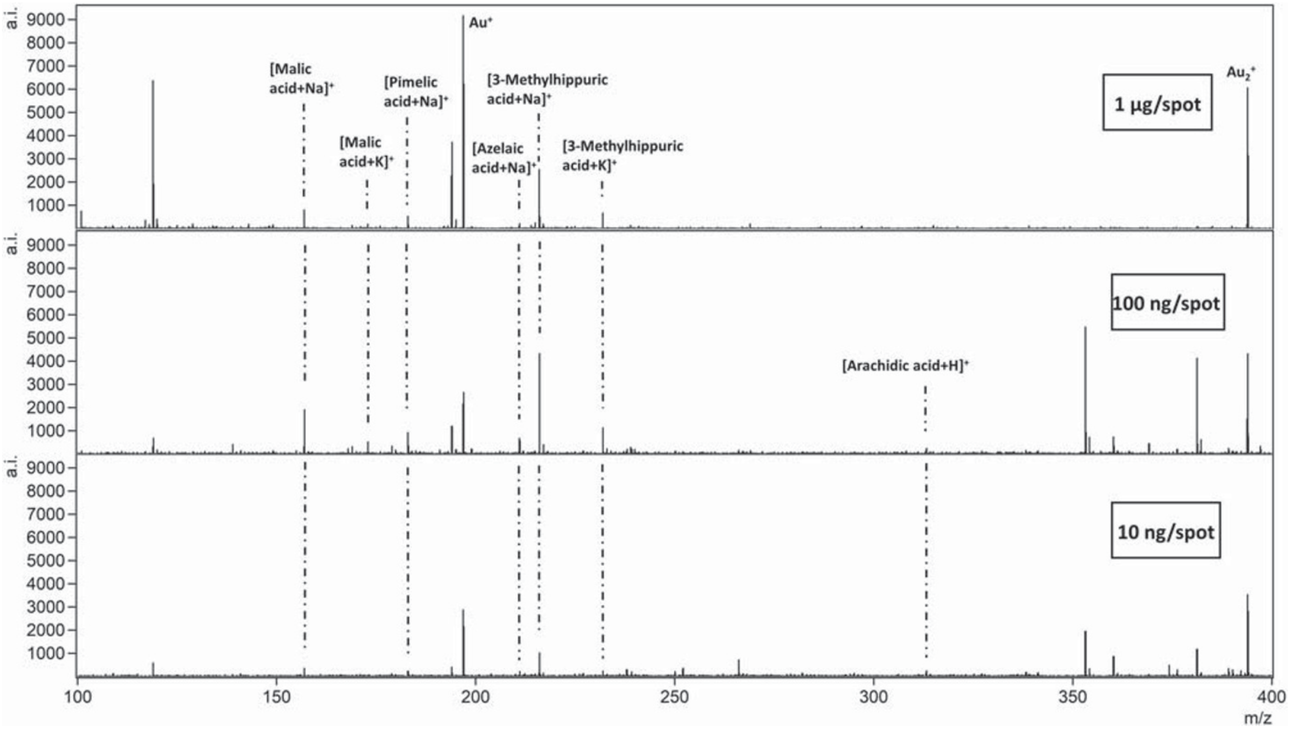

FIGURE 2 Spectra presenting laser desorption/ionization (LDI) mass spectrometry (MS) measurement results for carboxylic acids mixture with Au nanoparticles (AuNPs)

were placed directly on both ^{109}AgNPET or AuNPET plate, air dried, and targets were inserted into MS apparatus for measurements.

2.1.4 | Laser desorption/ionization mass spectrometry

LDI-TOF-MS experiments were performed in reflectron mode using Bruker Autoflex Speed time-of-flight mass spectrometer equipped with a SmartBeam II laser (355 nm). Laser impulse energy was approximately 100–150 μJ, and laser repetition rate was 1000 Hz. The total number of laser shots was 10 000 for each spot. This amount of laser shots was divided into 4 points symmetrically placed around spot center. At each point, 2500 laser shots were made with default random walk applied (random points with 50 laser shots). Measurement range was *m/z* 80–600. Suppression was turned on typically for ions of *m/z* lower than 80. The first accelerating voltage was held at 19 kV and the second ion source voltage at 16.7 kV. Reflector voltages used were 21 (the first) and 9.55 kV (the second). The data were calibrated and analyzed with FlexAnalysis (version 3.3) using centroid calibration model. Mass calibration for ^{109}AgNPET (enhanced cubic calibration typically based on 5 calibration points) was performed using internal standards (silver-109 ions and cluster from $^{109}Ag^+$ to $^{109}Ag_3^+$ and $^{109}Ag_5^+$) and for AuNPET (enhanced cubic calibration) was performed using gold ions and cluster from Au^+ to Au_3^+.

3 | RESULTS AND DISCUSSION

Carboxylic acids chosen for this study—malic, pimelic, azelaic, 3-methylhippuric, palmitic, linoleic, oleic, arachidonic, arachidic, and erucic acid—represent many different groups of compounds. Palmitic and arachidic acid belong to saturated fatty acids; linoleic, oleic, arachidonic, and erucic are unsaturated fatty acids. Malic, pimelic, and

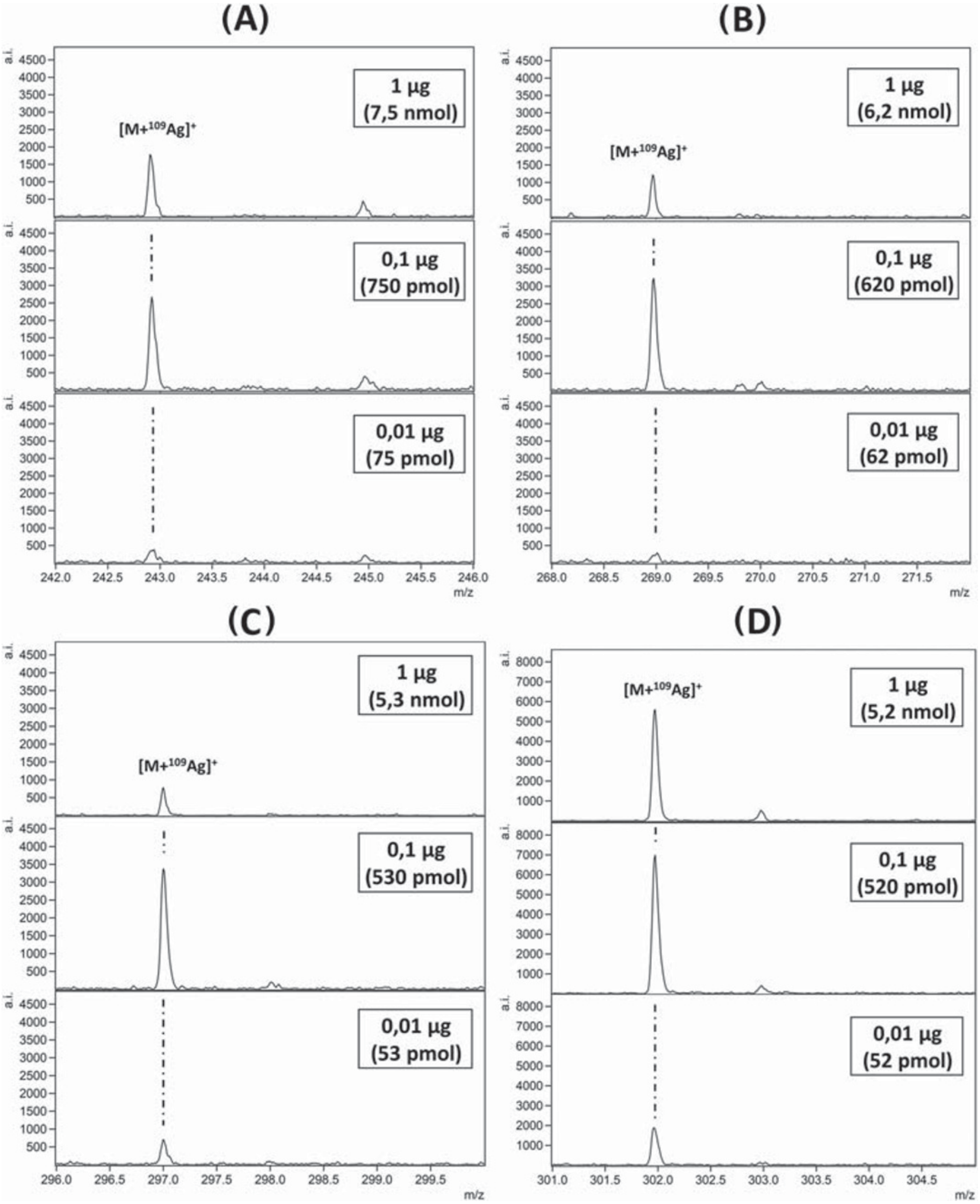

FIGURE 3 Spectra presenting laser desorption/ionization (LDI) mass spectrometry (MS) measurement results on ^{109}Ag nanoparticles (^{109}AgNPs) for (A) malic acid, (B) pimelic acid, (C) azelaic acid, and (D) 3-methylhippuric acid. Spectra panel contains magnified view on silver-109-carboxylic acid adduct signals. Text in boxes provides information on carboxylic acid amount per spot

azelaic acids all are dicarboxylic acids. Mixture of all listed acids was directly measured in concentrations ranging from 1 mg/ml to 100 ng/ml which equates to 10 000-fold concentration change. Limits of detection (LOD) values were calculated for signal-to-noise (S/N) value of 3 for lowest concentration samples. Every sample was placed on target plate in 1-μl volume equating to 1 μg to 10 pg of acids per measurement spot which is approximately 3 nmol to 300 fmol, respectively, calculated, for example, for erucic acid molar mass.

3.1 | Quantification results

Signals of all carboxylic acids on ^{109}AgNPs plate were found in spectra as silver-109 adducts with significantly smaller sodium, potassium, and proton adduct signals. As an example, sum of signal intensities of potassium, sodium, and proton adducts was approximately 1.5% of the signal intensity of silver-109 adduct of linoleic acid. Only five out of 10 of studied acids were found in spectra while using with AuNPs. Signals of these acids were found as sodium, potassium, and proton adducts where the latter ones were of significantly lower intensity. All missing acids contained long, low-polar hydrocarbon chain. LOD and lower limit of quantification (LLOQ) values for carboxylic acids are shown in Table 1.

Intensity-concentration data was used for generation of calibration curves with linear trend lines as shown in the Supporting Information. Most of trend lines were found to have very good r^2 values above 0.99, which is a very good result considering very large concentration range. Figures 1 and 2 contain spectra for target plates coated with ^{109}AgNPs and AuNPs, respectively. Silver-109 adducts for ^{109}AgNPs and sodium, potassium, and proton adducts for AuNPs of carboxylic acids were found in spectra of mixtures at concentrations of 10 ng to 1 μg of each acid per spot. For both nanoparticle solutions used in experiment, the highest intensities for all adducts of carboxylic acids were found at 100-μg/ml concentration samples which equals to 100 ng per measurement spot of each carboxylic acid. Comparing our previous results of quantification of amino acids with ^{109}AgNPET where LOD values of 0.3 to 77 nm/ml were obtained,[24] with data in Table 1, an interesting observation can be made that LOD values for

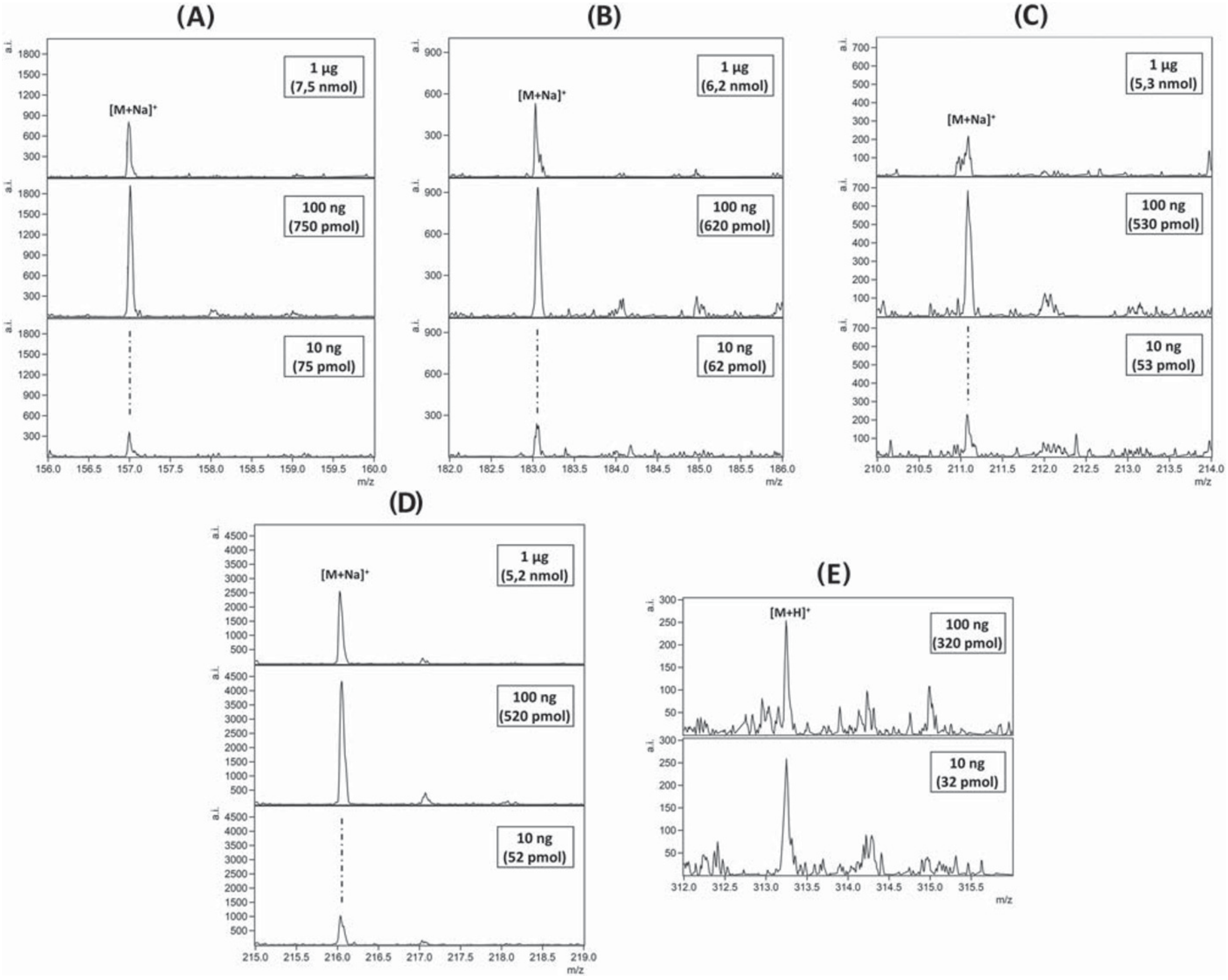

FIGURE 4 Spectra presenting laser desorption/ionization (LDI) mass spectrometry (MS) measurement results on Au nanoparticles (AuNPs) for (A) malic acid, (B) pimelic acid, (C) azelaic acid, (D) 3-methylhippuric acid, and (E) arachidic acid. Spectra panel contains magnified view on potassium, sodium, and proton-carboxylic acid adduct signals. Text in boxes provides information on carboxylic acid amount per spot

carboxylic acids are much higher (approximately 100 to over 1000 times) than for amino acids. It is certainly an effect of effective neutralization of cationic structures of nanoparticles by acids deprotonated anions.

Figures 3 and 4A–D show results for malic, pimelic, azelaic, and 3-methylhippuric acids obtained with the use of ^{109}AgNPs and AuNPs, respectively. LOD based on S/N ratio of 3 were found to be 3.2 μg/ml or 3.2 ng (24 pmol) of malic acid per measurement point in mixture analyzed with ^{109}AgNPs or 2.6 μg/ml (2.6 ng or 19 pmol per spot) for AuNPs. Intensities of strongest adducts are presented in Figure 6. LOD of pimelic acid was found to be 4.3 μg/ml (4.3 ng/spot = 27 pmol/spot) for ^{109}AgNP method and 4.0 μg/ml (4.0 ng/spot = 25 pmol/spot) for AuNPs.

Intensity of silver-109 adduct of azelaic acid for the highest concentration sample was found to be at lower level compared with previously discussed acids; however, it was higher than intensity of dominating sodium adduct for AuNPs. LOD of azelaic acid was found to be 1.9 μg/ml or 1.9 ng/spot (10 pmol/spot) for ^{109}AgNPs and 4.3 μg/ml or 4.3 ng/spot (23 pmol/spot) for AuNPs. It should be noted that there are no published results for malic, pimelic, and azelaic acids regarding LOD for LDI MS. Intensity of sodium adduct of 3-methylhippuric acid for AuNPs at concentration 10 μg/ml was found higher than silver-109 adduct for ^{109}AgNPs. LOD for this carboxylic acid for ^{109}AgNPs plate was found to be 0.7 μg/ml (0.7 ng/spot = 3.6 pmol/spot) and 1.0 μg/ml (1.0 ng/spot = 4.9 pmol/spot) for AuNPs. Despite the lack of information about LOD determined by laser MS, Gagne provided LOD value of 89 nM for 3-methylhippuric acid using UPLC coupled with tandem MS.[18]

Figure 5 presents results for fatty acids analysis for ^{109}AgNPs. Intensities for four of them were higher than for previously analyzed acids except for palmitic acid. Signals of fatty acids could not be found for AuNPs with small exception of very small signal of proton adduct of arachidic acid (Figure 4E).

Signal of silver-109 adduct of palmitic acid was found only at two concentrations and was significantly lower than for any other acids. LOD for palmitic acid was found to be 11 μg/ml

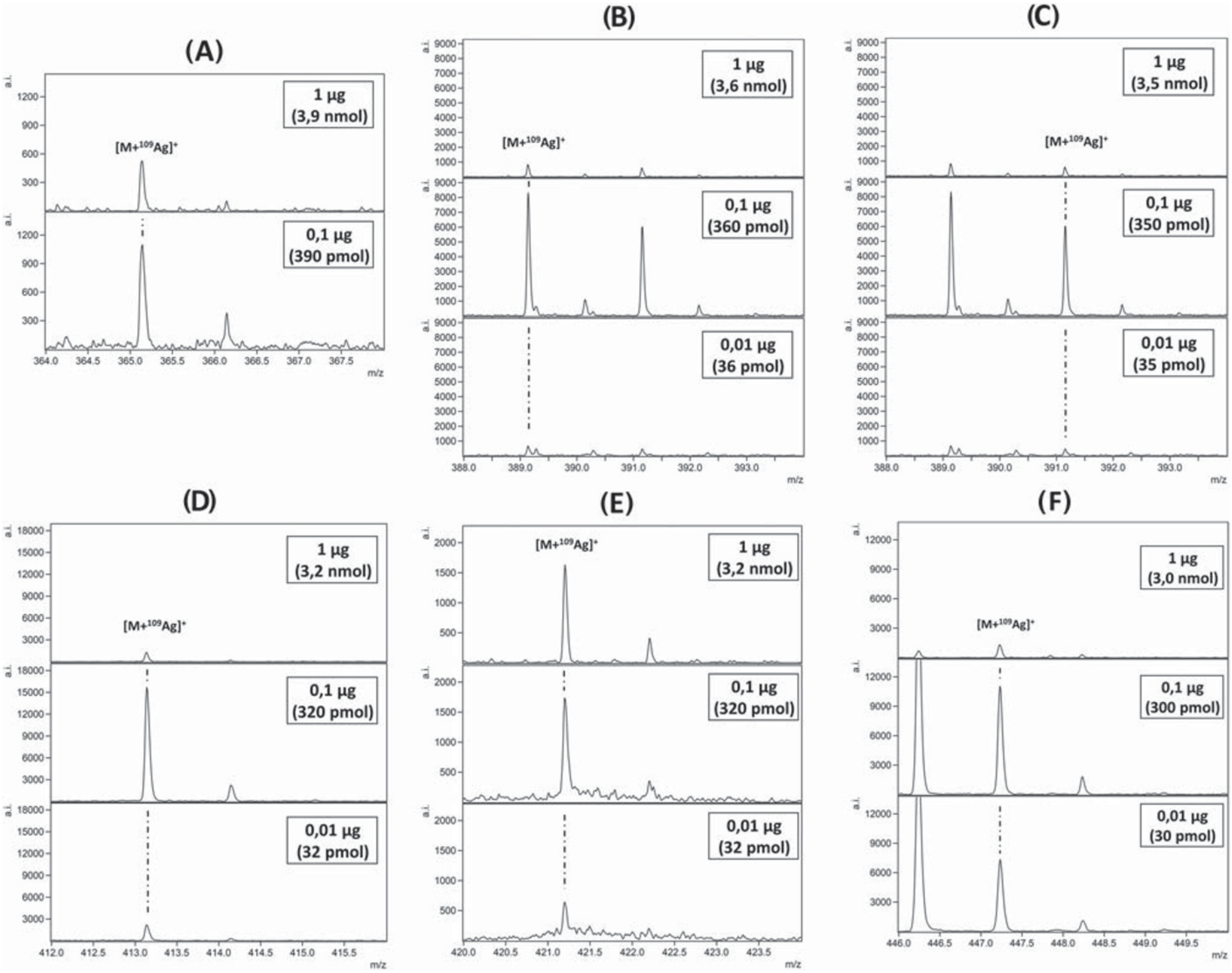

FIGURE 5 Spectra presenting laser desorption/ionization (LDI) mass spectrometry (MS) measurement results on silver-109 nanoparticle-enhanced target (^{109}AgNPET) for (A) palmitic acid, (B) linoleic acid, (C) oleic acid, (D) arachidonic acid, (E) arachidic acid, and (F) erucic acid. Spectra panel contains magnified view on silver-109-carboxylic acid adduct signals. Text in boxes provides information on carboxylic acid amount per spot

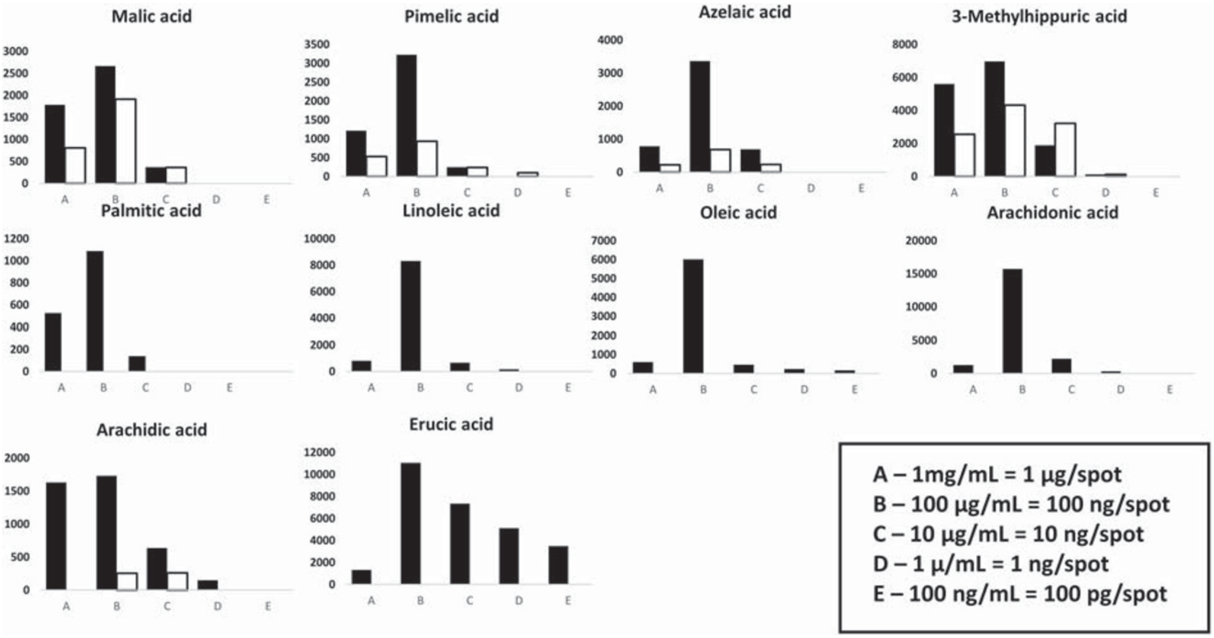

FIGURE 6 Column charts presenting intensity values for silver-109 adducts (black) and highest intensity adduct for gold nanoparticle-enhanced target (AuNPET) plate (gray) of carboxylic acids for different concentrations

(11 ng/spot = 43 pmol/spot). MALDI method with paper array as a target used by Ren et al. provided LOD for palmitic acid of 8.6 μM.[22] However, Ahmed et al. was able to obtain LOD value for palmitic acid of 0.8 nM using MALDI-FTICR MS.[16]

LOD value for linoleic acid was found to be 2.3 μg/ml (2.3 ng/spot = 8 pmol/spot) and for oleic acid 3.4 μg/ml (3.4 ng/spot = 12 pmol/spot). Literature contains reports of LOD values for mentioned acids as 26 μM for linoleic acid and 104.2 μM for oleic with the use of MALDI-paper array method and also 0.3 μM and 1 nM for linoleic acid and oleic acid, respectively, with the use of MALDI-FTICR MS.[16,22]

Intensity for arachidonic acid silver-109 adduct in concentration of 100 ng/spot was the highest of all acids measured with the use of ^{109}AgNPs. LOD for this case was found to be 1.2 μg/ml (1.2 ng/spot = 2.3 pmol/spot). LOD obtained with paper array MALDI method for arachidonic acid was 26 μM. The use of MALDI-FTICR MS LOD value was calculated as 80 nM.[16,22] Arachidic acid was the only fatty acid detected with the use of AuNPs (Figure 4E). Proton adduct of arachidic acid was found only in two concentrations: 10 and 100 μg/ml. LOD for arachidic acid was found to be 4.0 μg/ml or 4.0 ng/spot (7.7 pmol/spot) for ^{109}AgNPs and 3.4 μg/ml (3.4 ng/spot = 11 pmol/spot) for AuNPs. There are no published results for that acid regarding LOD for LDI MS; however, UPLC-Q/TOF-MS^E analysis provided LOD of arachidic acid of 1.8 ng/ml which equates to 4.3 nmol/ml.[25]

Last detected fatty acid was erucic acid. LOD for erucic acid was found to be lowest of all studied acids: 0.3 μg/ml (0.3 ng/spot = 0.6 pmol/spot). As in previous case, no results for LOD were presented in literature for this acid for LDI MS method. LOD value described by Gao et al. with the use of UPLC-Q/TOF-MS was of much lower value: 0.2 ng/ml, which is approximately 0.48 fmol/ml.[25]

Intensity-concentration plots (Figures 3–6) for most of studied compounds present lower intensities for the highest concentrations of acids compared with samples of lower concentrations. This phenomenon suggests that nanoparticles are overloaded with analyte molecules for concentrations as high as 1 μg per spot.

Summarizing, carboxylic acids were ionized more efficiently with ^{109}AgNPs compared with AuNPs as judged by higher intensities of signals. It is most noticeable in the case of fatty acids, target containing AuNPs contained no signals from palmitic, linoleic, oleic, arachidonic, and erucic acids. This may be due to inefficiency of AuNPs of ionizing low-polarity compounds. In case of ^{109}AgNPs, mainly silver-109 adducts are formed, whereas for AuNPs, sodium, potassium, and proton adducts were found. It is known from literature that AgNPs form strong interactions with low-polarity compounds and can be used to concentrate various compounds such as low-polar drugs, polyaromatic hydrocarbons, or olefinic compounds.[26–29] For example, Hidalgo et al. used discussed properties presenting effective nonsteroidal anti-inflammatory drugs extraction method with AgNP-containing agar film.[27] Vasil'eva et al. presented the possibility of using silver nanoparticles to preconcentrate pyrene, which is an aromatic compound of very low polarity.[28] Sherrod et al. studies showed selective binding of AgNPs with olefins, a carbon–carbon double bond-containing group very close in structure with unsaturated fatty acids studied in this work.[29] As silver forms relatively stable complexes with π-electron compounds which is crucial for detection of these adducts, for saturated compounds, most likely the ion–dipole interaction mechanism is responsible for the stability of formed silver adducts. High intensities of signals for fatty acids in case of ^{109}AgNPs may be also related to the fact that longer chain lengths of fatty acid cause to have larger contact areas with nanoparticles; hence, more stable adducts may be formed in ionization processes. On the other hand, publications showed that AuNPs are commonly used for sensing polar compounds, for example, proteins, urea, or amino acids.[30–32] Considering all of these factors, higher intensity values for ^{109}AgNPET were expected compared with gold-based method. Our results suggest that gold nanoparticles are not suitable for detection of traces of low-polar acids.

4 | CONCLUSION

Silver-109- and gold-based nanoparticle-enhanced surfaces allowed detection and quantification of carboxylic acids in large concentration range. For ^{109}AgNPs, signals for all tested acids were found but only smaller and polar carboxylic acids were detected with the use of AuNPs. LOD values for ^{109}AgNPs were found to be in range from 703 for 3-methulhippuric and arachidonic acids to 11 111 ng/ml for palmitic acid. For AuNPs, LOD values were in range from 952 ng/ml for 3-methylhippuric acid to 4286 ng/ml for azelaic acid. Results suggest that silver nanoparticles are better suited for detection of traces of low-polar acids. LOD values obtained for both nanoparticle systems are very good compared with other laser methods. Lower LOD values were reported previously for LC-MS/MS systems, but speed of measurements and compatibility with MSI makes laser methods presented here highly useful.

ACKNOWLEDGEMENT

The work was supported by Grant 2016/23/B/ST4/00062 from the National Science Centre, Poland.

CONFLICT OF INTEREST

The authors declare no competing and financial interest.

ORCID

Artur Kołodziej https://orcid.org/0000-0002-9222-0937
Tomasz Ruman https://orcid.org/0000-0002-9899-8627
Joanna Nizioł https://orcid.org/0000-0002-4783-8615

REFERENCES

1. Tanaka K, Waki H, Ido Y, et al. Protein and polymer analyses up to *m/z* 100 000 by laser ionization time-of-flight mass spectrometry. *Rapid Commun Mass Spectrom*. 1988;2:151-153. https://doi.org/10.1002/rcm.1290020802
2. Rzagalinski I, Volmer DA. Quantification of low molecular weight compounds by MALDI imaging mass spectrometry—a tutorial review. *Biochim Biophys Acta - Proteins Proteomics*. 2017;1865(7):726-739. https://doi.org/10.1016/j.bbapap.2016.12.011
3. Ha M-S, Seo H, Bae D-H, Yeo W-S. Detection of enrofloxacin and its metabolite ciprofloxacin using gold nanoparticles and laser desorption/ionization time-of-flight mass spectrometry. *Anal Sci*. 2014;30:451-455. https://doi.org/10.2116/analsci.30.451
4. López De Laorden C, Beloqui A, Yate L, et al. Nanostructured indium tin oxide slides for small-molecule profiling and imaging mass spectrometry of metabolites by surface-assisted laser desorption ionization MS. *Anal Chem*. 2015;87:431-440. https://doi.org/10.1021/ac5025864
5. Lin Z, Wu J, Qiao W, et al. Precisely controlled delivery of magnesium ions thru sponge-like monodisperse PLGA/nano-MgO-alginate core-shell microsphere device to enable in-situ bone regeneration. *Biomaterials*. 2018;174:1-16. https://doi.org/10.1016/j.biomaterials.2018.05.011
6. Abdelhamid HN. Nanoparticle assisted laser desorption/ionization mass spectrometry for small molecule analytes. *Microchim Acta*. 2018;185(3):1-16. https://doi.org/10.1007/s00604-018-2687-8
7. Chu HW, Unnikrishnan B, Anand A, Mao JY, Huang CC. Nanoparticle-based laser desorption/ionization mass spectrometric analysis of drugs and metabolites. *J Food Drug Anal*. 2018;26(4):1215-1228. https://doi.org/10.1016/j.jfda.2018.07.001
8. Nizioł J, Rode W, Laskowska B, Ruman T. Novel monoisotopic ^{109}AgNPET for laser desorption/ionization mass spectrometry. *Anal Chem*. 2013;85(3):1926-1931. https://doi.org/10.1021/ac303770y
9. Sekuła J, Nizioł J, Rode W, Ruman T. Gold nanoparticle-enhanced target (AuNPET) as universal solution for laser desorption/ionization mass spectrometry analysis and imaging of low molecular weight compounds. *Anal Chim Acta*. 2015;875:61-72. https://doi.org/10.1016/J.ACA.2015.01.046
10. Sekuła J, Nizioł J, Misiorek M, et al. Gold nanoparticle-enhanced target for MS analysis and imaging of harmful compounds in plant, animal tissue and on fingerprint. *Anal Chim Acta*. 2015;895:45-53. https://doi.org/10.1016/j.aca.2015.09.003
11. Nizioł J, Ruman T. Silver ^{109}Ag nanoparticles for matrix-less mass spectrometry of nucleosides and nucleic bases. *Int J Chem Eng Appl*. 2013;46-49. https://doi.org/10.7763/ijcea.2013.v4.259
12. Baker TC, Han J, Borchers CH. Recent advancements in matrix-assisted laser desorption/ionization mass spectrometry imaging. *Curr Opin Biotechnol*. 2017;43:62-69. https://doi.org/10.1016/J.COPBIO.2016.09.003
13. Curiel D, Más-Montoya M, Sánchez G. Complexation and sensing of dicarboxylate anions and dicarboxylic acids. *Coord Chem Rev*. 2015;284:19-66. https://doi.org/10.1016/j.ccr.2014.09.010
14. Bartoszek A, Von Moo E, Binienda A, et al. Free fatty acid receptors as new potential therapeutic target in inflammatory bowel diseases. *Pharmacol Res*. 2020;152:1–11. https://doi.org/10.1016/j.phrs.2019.104604
15. Nestel P, Clifton P, Colquhoun D, et al. Indications for omega-3 long chain polyunsaturated fatty acid in the prevention and treatment of cardiovascular disease. *Hear Lung Circ*. 2015;24:769-779. https://doi.org/10.1016/j.hlc.2015.03.020
16. Ahmed SH, Koubaa N, Kharroubi W, et al. Identification of long and very long chain fatty acids, plasmalogen-C16:0 and phytanic acid as new lipid biomarkers in Tunisian coronary artery disease patients. *Prostaglandins Other Lipid Mediat*. 2017;131:49-58. https://doi.org/10.1016/j.prostaglandins.2017.08.001
17. Volný M, Sadílek M, Jackson KE, Diener M, Elam WT, Tureček F. Matrix-free laser desorption/ionization of ions landed on plasma-treated metal surfaces. *J Mass Spectrom*. 2008;43(9):1265-1273. https://doi.org/10.1002/jms.1402
18. Gagné S. Achieving greater selectivity for the analysis of *o*-, *m*-, *p*-methylhippuric acids in workers' urine by ultra performance liquid chromatography coupled with tandem mass spectrometry. *J Chromatogr B Anal Technol Biomed Life Sci*. 2013;931:42-49. https://doi.org/10.1016/j.jchromb.2013.05.015
19. Dei Cas M, Paroni R, Saccardo A, et al. LC-MS/MS analysis to study serum profile of short and medium chain fatty acids. *J Chromatogr B*. 2020:1–14. https://doi.org/10.1016/j.jchromb.2020.121982
20. Hewawasam E, Liu G, Jeffery DW, Muhlhausler BS, Gibson RA. A validated method for analyzing polyunsaturated free fatty acids from dried blood spots using LC–MS/MS. *Prostaglandins Leukot Essent Fat Acids*. 2017;125:1-7. https://doi.org/10.1016/j.plefa.2017.08.010
21. Pérez-Navarro J, Da Ros A, Masuero D, et al. LC-MS/MS analysis of free fatty acid composition and other lipids in skins and seeds of *Vitis*

vinifera grape cultivars. *Food Res Int*. 2019;125:1–9. https://doi.org/10.1016/j.foodres.2019.108556

22. Ren H, Chen W, Wang H, et al. Quantitative analysis of free fatty acids in gout by disposable paper-array plate based MALDI MS. *Anal Biochem*. 2019;579:38-43. https://doi.org/10.1016/j.ab.2019.05.013
23. Li N, Qiu Y, Wu Y, et al. Association of serum total fatty acids with type 2 diabetes. *Clin Chim Acta*. 2020;500:59-68. https://doi.org/10.1016/j.cca.2019.09.018
24. Arendowski A, Nizioł J, Ruman T. Silver-109-based laser desorption/-ionization mass spectrometry method for detection and quantification of amino acids. *J. Mass Spectrom.* 2018;53(4):369-378. https://doi.org/10.1002/jms.4068
25. Gao Y, Wu S, Feng L. Rapid and direct determination of fatty acids and glycerides profiles in *Schisandra chinensis* oil by using UPLC-Q/TOF-MSE. *J. Chromatogr. B Anal. Technol. Biomed. Life Sci.* 2019;1104:157-167. https://doi.org/10.1016/j.jchromb.2018.11.022
26. Dastafkan K, Khajeh M, Ghaffari-Moghaddam M, Bohlooli M. Silver nanoparticles for separation and preconcentration processes. *TrAC - Trends Anal Chem*. 2015;64:118-126. https://doi.org/10.1016/j.trac.2014.08.017
27. Hidalgo CR, Ramos-Payán M, Ocaña-González JA, Martín-Valero MJ, Bello-López MÁ. Agar films containing silver nanoparticles as new supports for electromembrane extraction. *Anal Bioanal Chem*. 2015;407(5):1519-1525. https://doi.org/10.1007/s00216-014-8375-6
28. Vasil'eva SY, Olenin AY, Romanovskaya GI, et al. Adsorption preconcentration of pyrene by silver nanoparticles and its determination in aqueous solutions. *J Anal Chem*. 2009;64(12):1214-1220. https://doi.org/10.1134/S106193480912003X
29. Sherrod SD, Diaz AJ, Russell WK, Cremer PS, Russell DH. Silver nanoparticles as selective ionization probes for analysis of olefins by mass spectrometry. *Anal Chem*. 2008;80:6796-6799. https://doi.org/10.1021/ac800904g
30. Deng HH, Hong GL, Lin FL, Liu AL, Xia XH, Chen W. Colorimetric detection of urea, urease, and urease inhibitor based on the peroxidase-like activity of gold nanoparticles. *Anal Chim Acta*. 2016;915:74-80. https://doi.org/10.1016/j.aca.2016.02.008
31. Chang CC, Chen CP, Chen CY, Lin CW. DNA base-stacking assay utilizing catalytic hairpin assembly-induced gold nanoparticle aggregation for colorimetric protein sensing. *Chem Commun*. 2016;52(22):4167-4170. https://doi.org/10.1039/c6cc01238h
32. Song G, Zhou F, Xu C, Li B. A universal strategy for visual chiral recognition of α-amino acids with L-tartaric acid-capped gold nanoparticles as colorimetric probes. *Analyst*. 2016;141:1257-1265. https://doi.org/10.1039/c5an02434j

SUPPORTING INFORMATION

Additional supporting information may be found online in the Supporting Information section at the end of this article.

How to cite this article: Kołodziej A, Ruman T, Nizioł J. Gold and silver nanoparticles-based laser desorption/ionization mass spectrometry method for detection and quantification of carboxylic acids. *J Mass Spectrom*. 2020;55:e4604. https://doi.org/10.1002/jms.4604

toxins

MDPI

Communication

Silver-109/Silver/Gold Nanoparticle-Enhanced Target Surface-Assisted Laser Desorption/Ionisation Mass Spectrometry—The New Methods for an Assessment of Mycotoxin Concentration on Building Materials

Justyna Szulc [1,*], Artur Kołodziej [2] and Tomasz Ruman [3]

[1] Department of Environmental Biotechnology, Lodz University of Technology, Wólczańska 171/173, Łódź 90-924, Poland
[2] Doctoral School of Engineering and Technical Sciences at the Rzeszow University of Technology, 8 Powstańców Warszawy Ave., 35-959 Rzeszów, Poland; d497@stud.prz.edu.pl
[3] Faculty of Chemistry, Rzeszów University of Technology, 6 Powstańców Warszawy Ave., 35-959 Rzeszów, Poland; tomruman@prz.edu.pl
* Correspondence: justyna.szulc@p.lodz.pl

Abstract: This study aimed to detect and quantify mycotoxins on building materials using innovative laser mass spectroscopy methods—silver-109/silver/gold nanoparticle-enhanced target surface-assisted laser desorption/ionisation mass spectrometry (^{109}AgNPs, AgNPs and AuNPs SALDI). Results from SALDI-type methods were also compared with commonly used matrix-assisted laser desorption/ionization (MALDI) mass spectrometry. Standards of seven moulds mycotoxin in a final concentration of 100 µg/mL for patulin, citrinin, 3-nitropropionic acid, alternariol and 20 µg/mL for sterigmatocystin, cyclopiazonic acid, roquefortine C in the mixture were tested in pure solutions and after extraction from the plasterboards. Among the studied SALDI-type method, the lowest detection limits and the highest signal intensity of the mycotoxins tested were obtained with the use of ^{109}AgNPs SALDI MS. The ^{109}AgNPs method may be considered as an alternative to the currently most frequently used method MALDI MS and also liquid chromatography tandem mass spectrometry LC-MS/MS for mycotoxin determination. Future studies should attempt to use these methods for mass spectrometry imaging (MSI) to evaluate spatial distribution and depth of mycotoxin penetration into building materials.

Keywords: mycotoxins; building materials; laser desorption/ionisation mass spectrometry; metabolomics method; nanoparticles

Key Contribution: The study provided preliminary results of analysis of mycotoxins on building material using innovative laser mass spectroscopy methods—^{109}AgNPs; AgNPs and AuNPs SALDI. Among these methods, ^{109}AgNPs showed the lowest detection limits and the highest signal intensity in model conditions. Therefore, the ^{109}AgNPs method should be considered as an alternative to other methods of mycotoxin analysis, especially MALDI MS and LC-MS/MS.

Citation: Szulc, J.; Kołodziej, A.; Ruman, T. Silver-109/Silver/Gold Nanoparticle-Enhanced Target Surface-Assisted Laser Desorption/Ionisation Mass Spectrometry—The New Methods for an Assessment of Mycotoxin Concentration on Building Materials. *Toxins* **2021**, *13*, 45. https://doi.org/10.3390/toxins13010045

Received: 16 December 2020
Accepted: 6 January 2021
Published: 9 January 2021

1. Introduction

Mycotoxins (approximately 400, low-molecular-weight substances, produced by more than 200 mould species), are compounds exhibiting a great structural diversity as well as chemical and thermal stability [1,2]. In the literature, the greatest attention is paid to the occurrence of toxic mould's compounds in food products and feed. Mycotoxins may pose a potential threat to human and animal health, and exposure to them may result in acute and chronic diseases [3,4]. However, there has been a growing body of scientific literature indicating that exposure to mycotoxins and toxigenic moulds adversely affect the health of people working and living in water-damaged buildings (homes, offices, schools and public facilities) [5]. Dampness and moulds growth on building materials occurs in 10–50% of buildings located in Europe, Asia, Australia, and North America [6,7]. Fungi, including moulds from genera *Alternaria* (*A. alternata*), *Aspergillus* (*A. flavus, A. niger* and *A. versicolor*), *Penicillium* (*P. aurantiogriseum, P. chrysogenum, P. expansum, and P. viridicatum*), *Stachybotrys* (*S. chartarum*) and many others, are able to grow on all common types of building materials including wallpaper, plasterboards, wooden elements, emulsion paints, materials for insulation, and finishing [6,8–10].

People staying in mouldy buildings have an increased risk of airways infections and other health problems including asthma, and respiratory symptoms [11,12]. Recently a new term, dampness, and mould hypersensitivity syndrome (DMHS), was introduced for disease previously described as biotoxin-related illness, mould-related illness, and chronic inflammatory response syndrome etc. [5,13,14].

It was proven that mycotoxins inhalation might be even ten times more toxic than other routes of entry (via ingestion and skin); therefore, the emission of mycotoxins into the air from building materials is dangerous [15]. The most frequently identified mycotoxins on building materials are trichothecenes, ochratoxin A, sterigmatocystin. Mycotoxins have also been detected in dust from ventilation systems and in the indoor air where residents have complained of health problems potentially caused by the presence of moulds in the buildings [16–19].

Although the problem of the presence of mycotoxins on building materials is not new, its study still poses many difficulties. Among mould genera such us *Alternaria, Aspergillus, Penicillium,* only a few experienced microbiologists are able to identify environmental isolates to the level of species [20,21]. It should also be noted that many inappropriate sequences (from misidentified strains) can be found, as well as misidentified mycotoxins from a wide variety of mould species which can be found in databases [22]. Moreover, unidentified and masked mycotoxins and synergistic effects of metabolites can be discovered in the extracts of fungi, which have been detailed and analysed for metabolites production [7,21,23].

Immunochemical-based and chromatographic-based methods are two groups of the methods for mycotoxins analysis [4,24]. Enzyme-linked immunoassay (ELISA) is primarily used for the detection of mycotoxins in cereals. Aflatoxin B1, the deoxynivalenol (DON), ochratoxin A and zearalenone were determined by ELISA. Monoclonal antibodies have also been developed for the diacetoxyscirpentriol, 3- and 15-acetyl-DON, sporidesmin A, roridin, and other mycotoxins [25].

Nowadays the liquid chromatography with tandem mass spectrometry (MS/MS) methods, including multi-mycotoxin methods, are accurate, highly selective and sensitive methods of mycotoxin determination. The aim of the LC-MS/MS multi-mycotoxin methods is to avoid cumbersome and complicated cleaning methods and the use of many analytical techniques [1,2,26,27]. Multi-mycotoxin methods are validated for many types of matrices i.e., cereals, spices, fruit, oilseed and others plant and food products [26,28,29].

An alternative for LC-MS/MS methods in the determination of secondary metabolites of fungi are the soft-ionisation, laser-based family of techniques—laser desorption/ionisation mass spectrometry (LDI MS) methods including matrix-assisted laser desorption/ionisation (MALDI) and surface-assisted laser desorption/ionisation (SALDI).

MALDI analyses of the medium–high molecular mass of compounds (mainly proteins and lipids) are a valuable tool in identification of species of fungi with clinical significance [30,31]. However, classical MALDI is characterized by some limitations which include: a high level of chemical background (in the low-mass region—m/z 1000), the effect of the sweet spot and in the case of low-polarity compounds, low ionisation efficiency. These disadvantages do not occur in laser desorption–ionisation methods that use a steel target covered with silver or gold nanoparticles instead of the matrix, i.e., the surface-assisted laser desorption ionisation method (SALDI) such as silver-109/silver/gold nanoparticle-enhanced target surface-assisted laser desorption/ionisation mass spectrometry, respectively: ^{109}AgNPET, AgNPET, and AuNPET SALDI methods [32,33].

Kuo et al., (2017) used Langmuir–Blodgett films with silver nanocrystals (cube, cuboctahedron and octahedron) for glucose detection in SALDI MS. The authors obtained significantly improved parameters of analysis (the intensity of the signal, signal-to-noise ratio, noise reproducibility) compared to MALDI with α-cyano-4-hydroxycinnamic acid and 2,5-dihydroxybenzoic acid matrices [34]. AuNPET (gold nanoparticle-enhanced target) and gold nanoparticle multilayers (AuNPs-ML) were used recently for mass spectral analysis of compounds with different polarities, over a wide range of m/z values. Amino acids, glycosides, lipids, saccharides, nucleosidesand others were successfully studied using these methods [35–37]. Pan et al. (2019) used gold nanoparticles in form of two-dimensional multilayered AuNPs thin film (MTF-AuNPs) for direct analysis of bone biomarker (hydroxyproline) in the research of osteoporosis detection [38]. SALDI AuNPET, in contrast with conventional MALDI, allows the analysis of low molecular weight compounds. The other advantages include a reduction in the background level, a high signal-to-noise (S/N) ratio, and a precise internal spectral calibration [35,36].

In the recent studies, SALDI methods were used for c analysis of metabolites of microbial origin in objects of cultural heritage. AuNPET SALDI allows the detection of microbial metabolites, including tocopherols, 2-methyl-6-phytylquinol and 3-hydroxy-L-kynurenine, which may be responsible for foxing formation [39].

The ^{109}AgNPET allows the discovery of mycotoxins (aflatoxins B1, and B2, ochratoxin B andT2-toxin), and organic acids on the surfaces of historical photographs [40]. Szulc et al. (2020) using the same method proved the presence of *Aspergillus* and *Penicillium* metabolites including micotoxins and their derivatives (e.g., aflatoxin M2, 3-*O*-methylviridicatin, dihydroaflatoxin G1 and dihydrohydroxyaflatoxin B1) and antibiotics (penicillin K) in beeswax seal samples [41].

Based on the above, the suitability of NPET SALDI with silver and gold nanoparticles methods in mycotoxins analysis should be further investigated.

This study aimed to detect and quantify mycotoxins for building materials using innovative laser mass spectroscopy methods—silver/silver-109/gold nanoparticle-enhanced target surface-assisted laser desorption/ionisation mass spectrometry.

2. Results

The presented data (Table 1) contain the first presentation of detection limits for mycotoxin detection using silver, silver-109 and gold nanoparticle-enhanced targets used in surface-assisted laser desorption/ionisation mass spectrometry. The commonly used MALDI and LC-MS/MS method quoted different detection limits, depending on the matrix. Still, foodstuffs were the most commonly employed products (np. apple puree, hazelnut, sweetcorn, and green pepper) with the limits of detection (LOD) ranging from 0.2 to 134.6 µg/kg [1,26,27]. Tuomi et al. (2000) analysed 79 samples of mouldy building materials, mainly interior finishes containing paper, wood and plastic, (e.g., wallpaper, plywood, plasterboards, mineral wool) and others. The authors obtained the LOD value for sterigmatocistin and citrinin amounting to 2 and 20 ng, respectively [42]. Concerning different methods of LOD and and lower limits of quantification (LLOQ) presentation in the literature and a very limited scope of studies involving building materials, it is hard to compare the obtained results.

Table 1. Limits of detection and lower limits of quantification for studied mycotoxins.

Toxin	^{109}AgNPs		AgNPs		AuNPs		MALDI	
	LOD ^{a} (ng/mL) (μM)	**LLOQ ^{b} (ng/mL)**	**LOD ^{a} (ng/mL) (μM)**	**LLOQ ^{b} (ng/mL)**	**LOD ^{a} (ng/mL) (μM)**	**LLOQ ^{b} (ng/mL)**	**LOD ^{a} (ng/mL) (μM)**	**LLOQ ^{b} (ng/mL)**
Patulin	4271 27.7	7118	5565 36.1	9276	30,000 194.7	50,000	nd	nd
Citrinin	6830 27.3	11,384	6905 27.6	11,508	5405 21.6	9009	nd	nd
Citrinin (Cation Radical Adduct) Extracted from Plasterboards	561 2.24	935	nd	nd	96,774 248.5	161,290	nd	nd
Citrinin (^{109}Ag Adduct) Extracted from PlasterBoards	396 1.58	660	58,824 151.0	98,039	nd	nd	nd	nd
Sterigmatocystin	15,272 47.1	25,453	19,990 61.6	33,317	nd	nd	nd	nd
Cyclopiazonic Acid	2756 8.19	4594	17,298 51.4	28,830	17,143 51.0	28,571	nd	nd
Roquefortine C	7935 20.4	13,225	27,883 71.6	46,471	93,750 240.7	156,250	nd	nd
Alternariol	8092 31.3	13,487	5367 13.8	8945	3834 14.8	6390	1939 4.98	3232
3-Nitropropionic Acid	4088 34.3	6814	62,500 160.5	104,167	nd	nd	nd	nd

^{a} based on a signal-to-noise (S/N) ratio of 3; ^{b} based on an S/N ratio of 5; LOD—limit of detection; LLOQ—lower limit of quantification; "nd"—signal not detected.

MALDI mass spectrometry is commonly used for biomolecule detection as shown by the very large amount of publications in last fifteen years. In case of mycotoxin mixtures studied in this work, only alternariol was found as a proton adduct (Figure 4D). The possible explanation is that relatively poor, linear internal calibration performed on two signals emitted by the 2,5-dihydroxybenzoic acid (DHB) matrix is producing too many m/z matching errors over 5 ppm forcing us to reject possible peak assignment. This kind of problem is virtually absent with our methods based on nanoparticles, which, after laser pulse irradiation, are emitting a series of well-defined ions used for enhanced cubic calibration. Examples of spectra presenting LDI MS-obtained results on different SALDI for tested mycotoxins are given in Figures 1–4. All the studied compounds were found in LDI MS spectra in the form of adducts, mostly with metal ions, which is expected behaviour for compounds of medium-to-low polarity. The most intense ions found for citrinin, sterigmatocystin, cyclopiazonic acid, roquefortine C, 3-nitropropionic acid and alternariol were silver adducts. Much more polar patulin was found mostly in the form of proton adduct for all targets: ^{109}AgNPET, AgNPET and AuNPET. The observed very high affinity of the studied compounds toward silver ions suggests strongly that the methods used typically for ionisation of these compounds—electrospray ionisation and MALDI are not the best choices as the studied ions are usually proton adducts. Intensity values on different MALDI-type targets for different concentrations of mycotoxins standards are presented in Figure 5. Intensity values depend on mycotoxin type and its concentration for particular MALDI-type targets. The highest intensity in the case of each tested standard concentration was obtained for AgNPET for citrinin. For patulin, sterigmatocystin, cyclopiazonic acid and roquefortine, the greatest intensity was obtained for the highest tested concentrations using ^{109}AgNPET; the greater intensity characterised the AgNPET method in the case of lower standard concentrations. Comparing the MALDI type targets, the lowest intensities were obtained with the use of gold nanoparticles, and the highest for silver nanoparticles and ^{109}AgNPs.

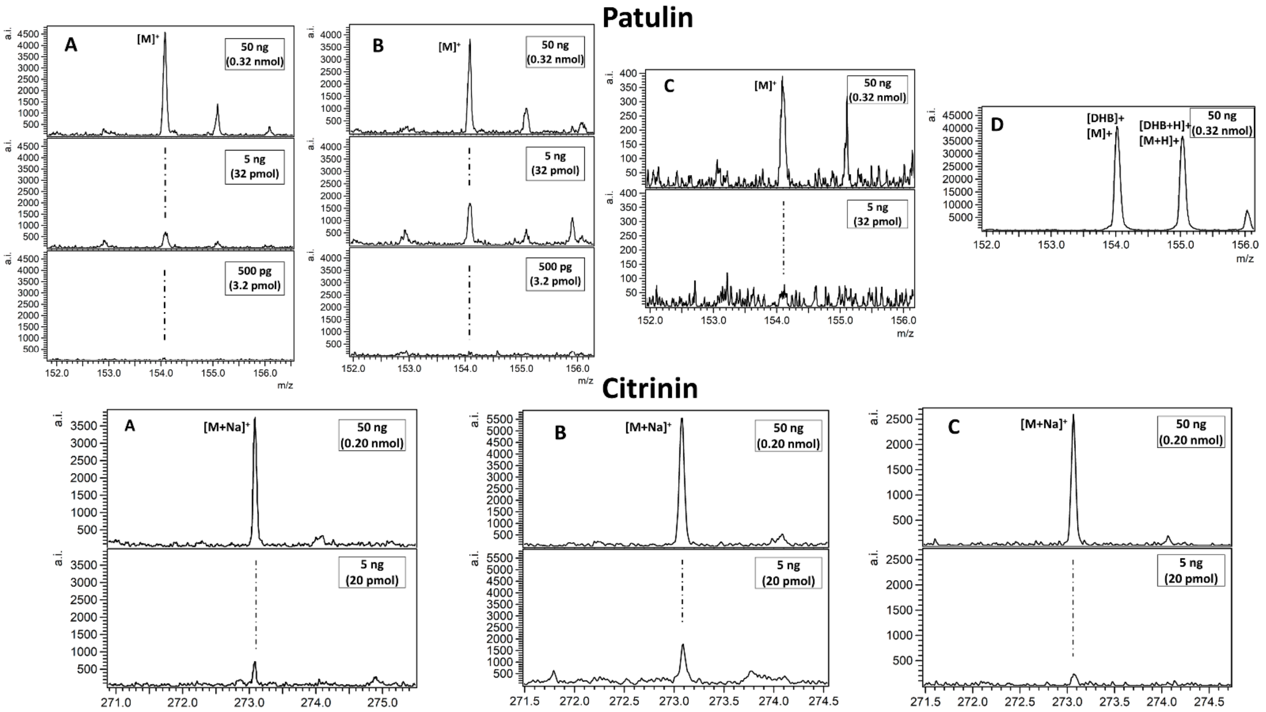

Figure 1. Spectra presenting laser desorption/ionisation mass spectrometry (LDI MS) obtained results on different targets ((**A**) ^{109}AgNPET; (**B**) AgNPET; (**C**) AuNPET; (**D**) MALDI with the 2,5-dihydroxybenzoic acid (DHB) matrix) for patulin and citrinin. The spectra panel contains a magnified view on most intense adduct signals. Text in boxes provides information on a compound amount per spot.

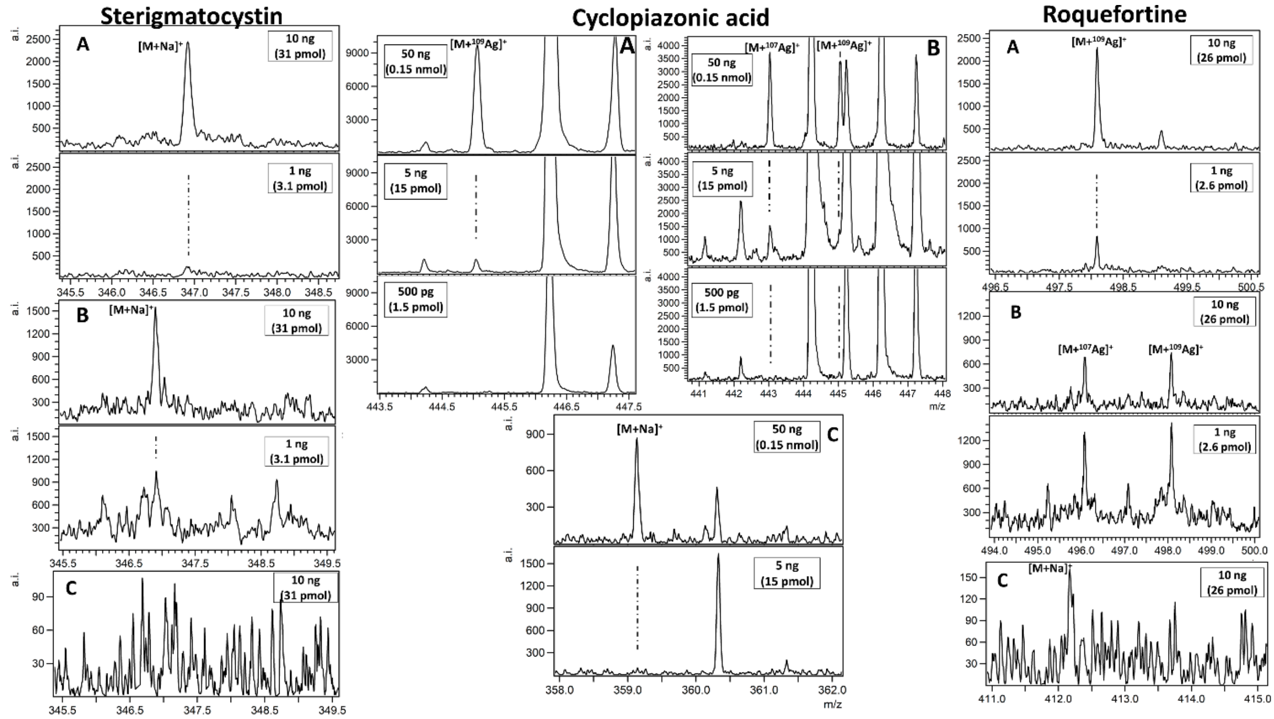

Figure 2. Spectra presenting LDI MS obtained results on different targets ((**A**) ^{109}AgNPET; (**B**) AgNPET; (C) AuNPET; (**D**) MALDI with the DHB matrix) for sterigmatocystin, cyclopiazonic acid and roquefortine C. The spectra panel contains a magnified view of the most intense adduct signals. Text in boxes provides information on a compound amount per spot.

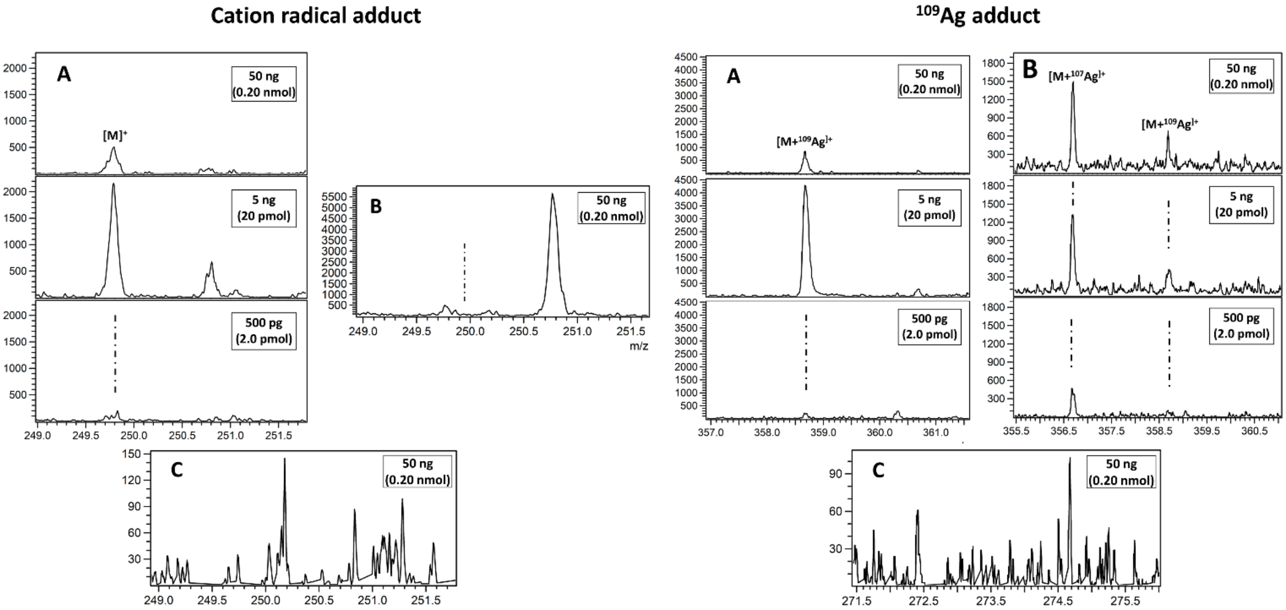

Figure 3. Spectra presenting LDI MS obtained results for citrinin after extraction from plasterboard ((**A**) ^{109}AgNPET; (**B**) AgNPET; (**C**) AuNPET; (**D**) MALDI with the DHB matrix). Text in boxes provides information on a compound amount per spot.

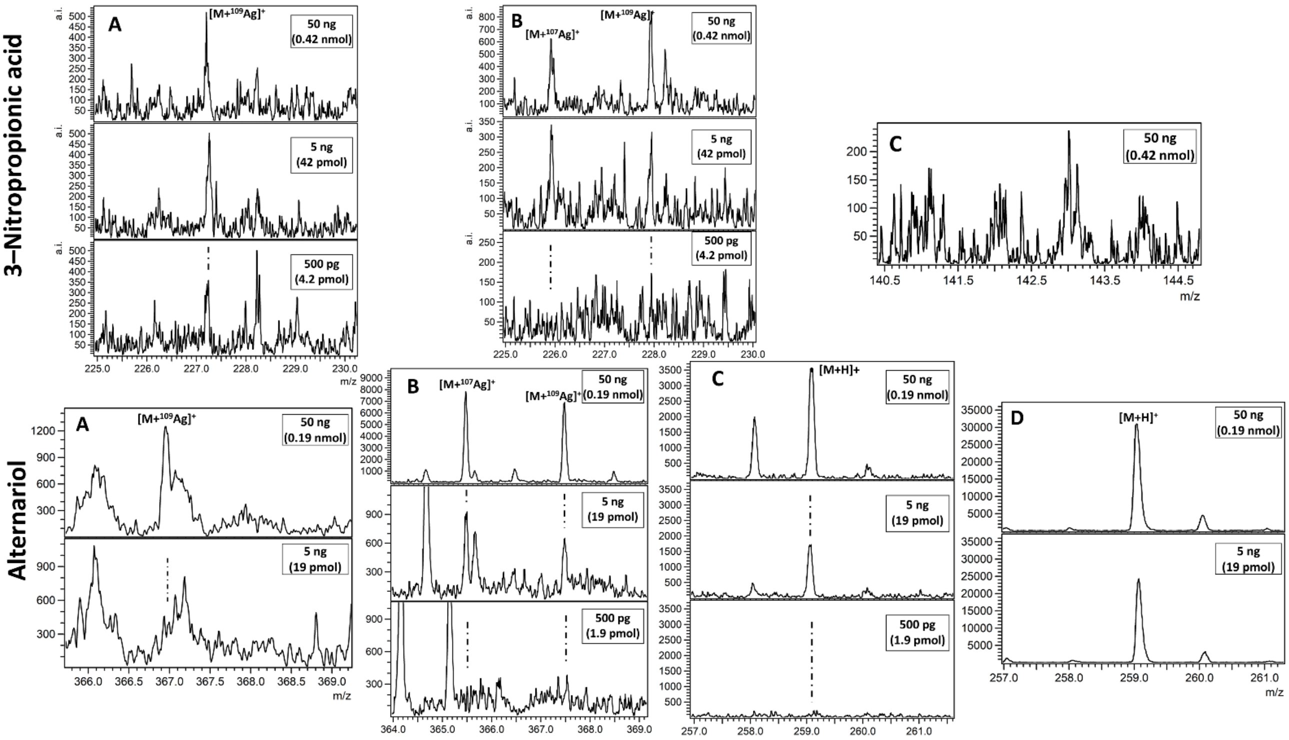

Figure 4. Spectra presenting LDI MS obtained results of 3-nitropropionic acid and alternariol on (**A**) ^{109}AgNPET, (**B**) AgNPET and (**C**) AuNPET; (**D**) MALDI with the DHB matrix. Insets contain a magnified view of the most intense adduct signals. Text in boxes provides information on a compound amount per spot.

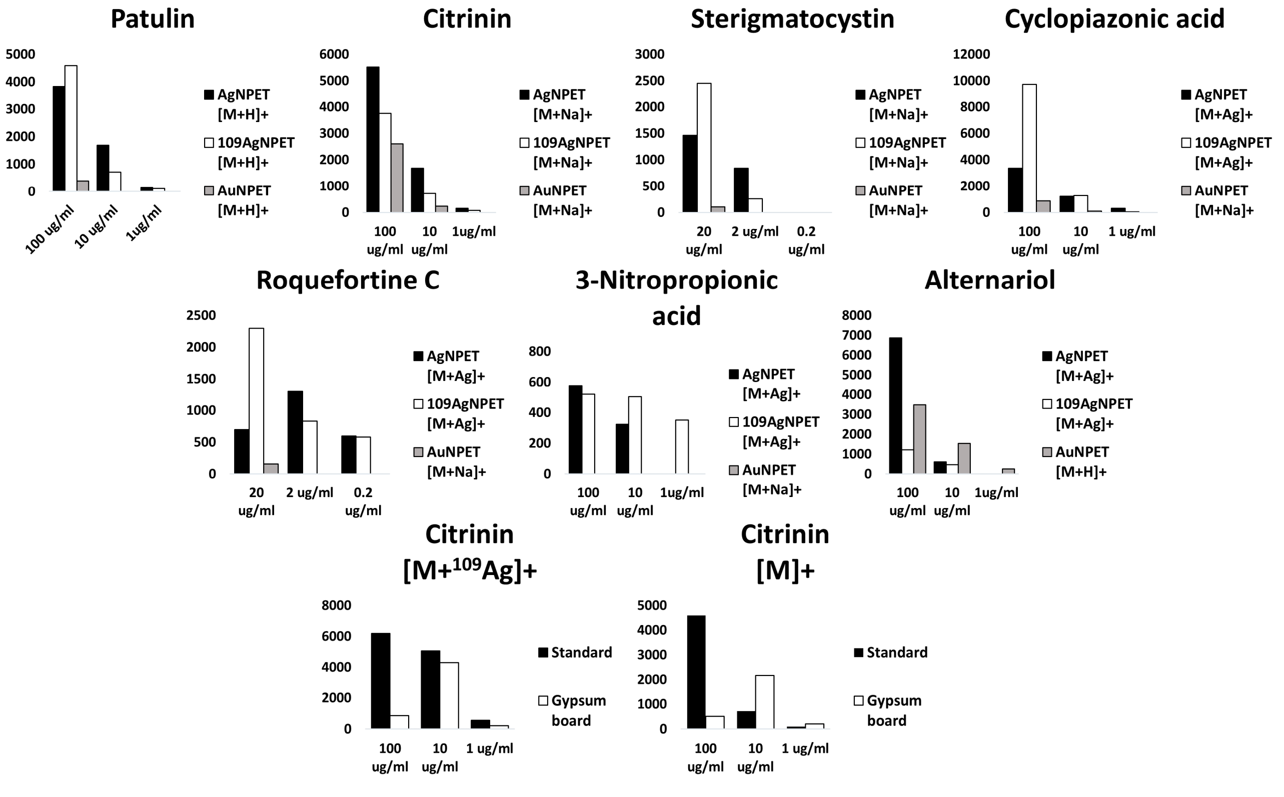

Figure 5. Column charts presenting intensity values for the most intense ions of the studied compounds for given concentrations. The colour of the bar represents the target type (black—AgNPET, grey—AuNPET, white—^{109}AgNPET). Two charts (bottom) present intensity values comparison for citrinin standard measured with the use of ^{109}AgNPET measured directly (black) and after extraction from plasterboard.

The results obtained for 3-nitropropionic acid and alternariol are very interesting. Intensive signals (300–500) were obtained for the first compound only in the ^{109}AgNPET method. The AuNPET method provided far better results in the alternariol analysis for all tested concentrations.

The intensity values for three concentrations of mycotoxin standards (100 µg/mL, 10 µg/mL and 1 µg/mL), tested with three methods—^{109}AgNPs, AgNPs and AuNPs—are shown in Figure 5. The intensity was demonstrated to depend on the concentration of the identified compound and the target type. The highest intensity for the majority of the tested compounds was achieved for identification with the ^{109}AgNPs method, including but not limited to 100 µg/mL concentration. Such a situation was observed for patulin, sterigmatocistin, cyclopiazonic acid and roquefortine C. The AgNPs method rendered the best intensity for each concentration of citrinin. This method turned out to be most effective also for 100 µg/mL 3-nitropropionic acid and alternariol. The lowest concentrations of the two compounds were identified with the highest intensity owing to ^{109}NPs and AuNPs, respectively. The lowest intensities for all tested mycotoxins were obtained in the AuNPs method, except for alternariol, which rendered the lowest signals for ^{109}NPs.

Figure 5 shows the change in the intensity of mycotoxins tested as diluted standards, and after extraction from plasterboards. Among the seven mycotoxins tested, only citrinin (cation radical adduct) was successfully determined from plasterboard.

The mycotoxin tested directly and not extracted from the building material revealed the highest intensity in each tested concentration for ^{109}Ag adduct of citrinin. The higher the concentration of the identified compound, the greater the difference in the signal intensity was. A slightly different situation was demonstrated for the cation radical adduct of citrinin. In this case, the standard solution revealed greater intensity for 100 µg/mL concentration, whereas a higher intensity for two lower concentrations was discovered for the extracts obtained from plasterboards.

Due to the unlimited number of types and composition of building materials and the common presence of additional contamination (dust), from an analytical point of view, building materials are a challenging "matrix". Moreover, the variety of fungal metabolites makes mycotoxin analysis on building materials a difficult task. The SALDI methods, including but not limited to ^{109}AgNPs, presented in this paper, may be a good alternative for MALDI MS and the LC-MS/MS method currently most popular for mycotoxin identification. They are less time-consuming (measurement time of ca. 15 s/sample; alternative LC-MS/MS—from 15 to 45 min/sample) and the whole measurement procedure is automated. However, the routine use of ^{109}AgNPs SALDI MS in mycotoxin analysis on building materials requires further research aimed at verification and validation of this method.

Neither the LC/MS/MS nor any other method used currently for mycotoxin analysis offers the opportunity to determine the spatial distribution/depth of mycotoxin penetration into the building material. Laser Desorption/Ionisation mass spectrometry allows the imaging of metabolites and an analysis of their distribution in the tested samples.

Szulc et al. (2017) used the high-resolution surface assisted laser desorption/ionisation time-of-flight mass spectrometry-based on a gold nanoparticle-enhanced target (AuNPET SALDI-ToF-MS) imaging method in order to assess the metabolite profile of the selected mould species under model conditions on microbial medium and plasterboard [7]. The authors detected compounds in the range of 80–1950 m/z and identified 89 metabolites from 48 metabolomic pathways in wated extracts from building materials. Moreover, they presented the changes in the amount and types of identified compounds as a result of various growth conditions (type of growth media, single culture or mixed population) [7].

Therefore, future studies should aim at the utilisation of such laser spectrometry methods as ^{109}AgNPET/Ag/AuNPET SALDI MSI to detect mycotoxins and determine the degree of the building material contamination with the mycotoxins, through an in-situ assessment of the spatial distribution (environmental sample with an increase in the toxigenic mould). The effectiveness of the methods should be verified by analysing the extracts obtained from other building materials susceptible to contamination with mycotoxins, e.g., wood, wallpaper, and paint coats.

3. Conclusions

Among the Laser Desorption/Ionisation mass spectrometry methods tested in the present study, the highest overall applicability and universality, as well as the lowest detection limits of the tested mycotoxins were found for ^{109}AgNPET. Other methods such as AgNPET and AuNPET SALDI MS had higher LOD and LLOQ limits. Nanoparticle-based methods were compared with commonly used MALDI MS which gave very small positive detections due to inferior calibration. The ^{109}AgNPs method, following by verification and validation, may provide an alternative to the currently most frequently used LC-MS/MS method for mycotoxin determination. Future studies should attempt to use these methods for MSI imaging to evaluate spatial distribution and depth of mycotoxin penetration into building materials.

4. Materials and Methods

4.1. Preparation of ^{109}AgNPET Target

An amount of 10 mg of silver-109 trifluoroacetate was dissolved in anhydrous, tetrahydrofurane (volume of 50 mL) and the solution was poured into a beaker with laser target plate (stainless steel target of 35 × 45 × 0.8 mm size). Solid 2,5-dihydroxybenzoic acid (35 mg) was added and the solution was left for 24 h. The target plate was then washed with tetrahydrofurane, acetone and deionised water (three times), gently cleaned with a cotton wool ball, again washed 3 times with tetrahydrofurane, and then with water and acetonitrile. The ^{109}AgNPET target was characterized by Nizioł and Ruman (2013) [43].

4.2. Preparation of AgNPET

Silver trifluoroacetate (AgTFA, 40 mg) was dissolved in anhydrous tetrahydrofurane (volume of 50 mL) and the solution was poured into a beaker containing a laser target plate (stainless steel target of 35 × 45 × 0.8 mm size). Solid 2,5-dihydroxybenzoic acid (80 mg) was added and solution was left for 24 h. The rest of the procedure—cleaning of target—is the same as for ^{109}AgNPET preparation. The AgNPET target was characterized by Nizioł et al. (2013) [44].

4.3. Preparation of AuNPET

Chloro(trimethylophosphite)gold(I) complex (amount of 8 mg) was dissolved in 15 mL of acetonitrile, and then the solution was poured into a beaker containing a target plate (stainless steel target of 35 × 45 × 0.8 mm size). The pyridine–borane complex (volume of 52 µL) was added with the use of a gas-tight syringe and, following stirring, the solution was left for 24 h. The target plate was then washed with acetonitrile and deionised water (three times), then it very gentle cleaned with a cotton wool ball and again 3-times with acetonitrile and water. AuNPET target was characterized by Sekuła et al. (2015) [35].

4.4. Moulds Mycotoxins Standards Analysis

Standards of seven moulds mycotoxin (patulin, citrinin, 3-nitropropionic acid, alternariol sterigmatocystin, cyclopiazonic acid, roquefortine C) were purchase from Sigma-Aldrich (Poznań, Poland). Standards were weighed and dissolved in acetonitrile to give a final concentration of 100 µg/mL for patulin, citrinin, 3-nitropropionic acid, alternariol and 20 µg/mL for sterigmatocystin, cyclopiazonic acid, roquefortine C in the mixture. Lower concentration solutions were prepared by diluting ten times higher concentration ones. A volume of 0.5 µL of mycotoxins solution was placed directly on 109AgNPET, AgNPET and AuNPET plate, air-dried, and the targets were inserted into MS apparatus for measurement.

MALDI experiments were performed using DHB matrix solution (saturated matrix in acetonitrile with 0.5% of trifluoroacetic acid) were made by the drying droplet method (1:1 vol/vol matrix:sample solution).

4.5. Analysis of Mycotoxin Standards on Plasterboards

Unimpregnated plasterboard with a 9.5 mm thickness and A2 class of fire resistance (Siniat, Warszawa, Poland) was purchase from retail sales. Sample sizes of 0.5 × 1 cm were cut from the plasterboard. Volumes of 100 µL of the mycotoxin solutions (contains all tested mycotoxins, see Section 4.4) were applied to the samples. After 30 min, the plasterboard fragments were transferred to test tubes, and 2 mL of acetonitrile were added to each sample. Samples were homogenised manually, and a volume of 1.5 mL solution was collected from each sample and transferred into new Eppendorf tubes. The collected solutions were centrifuged (6000 rpm, 1 min) and the supernatants (1.4 mL) were left to dry under a high vacuum. After drying, acetonitrile was added to each sample to obtain the same concentration of mycotoxins in the sample as in the standard solutions. A volume of 0.5 µL of the mixture was placed directly on 109AgNPET and AuNPET plate, air-dried and targets were inserted into the MS apparatus for measurements. MALDI MS measurements were performed as stated in the previous Section 4.4.

4.6. LDI Mass Spectrometry

LDI-ToF mass spectrometry experiments were performed in the reflectron mode on Bruker Autoflex Speed ToF mass spectrometer (Bruker Autoflex Speed, Bruker Daltonics, Bremen, Germeny) equipped with a SmartBeam II laser (355 nm). The laser impulse energy was in range of 100–150 µJ, laser repetition rate 1 kHz. The total number of laser shots was 4000 for each sample spot. The mentioned amount of laser shots was divided into four points symmetrically placed around the spot centre. At each point, 1000 laser shots were performed with a default random walk (random points with 50 laser shots). The measurement range was m/z 80–2000. Suppression was on for ions of m/z lower than 80. The first accelerating voltage was held at 19 kV, and the second ion source voltage at 16.7 kV. The reflector voltages were 21 kV (the first) and 9.55 kV (the second). The data were calibrated and analysed with FlexAnalysis (version 3.3, Bruker Daltonics Leipzig, Germany) using centroid calibration model. The mass calibration for ^{109}AgNPET used was enhanced cubic calibration typically based on at least five calibration points and it was made using internal standards which were silver-109 ions and cluster from $^{109}Ag^+$ to $^{109}Ag_9{}^+$; for AgNPET calibration was made using all isotopic peaks from Ag^+ to $Ag_5{}^+$; for AuNPET was made using gold ions and cluster from Au^+ to $Au_5{}^+$. MALDI spectra were calibrated on DHB ions: $[M + H]^+$ (m/z 155.03444) and $[2M + H]^+$ (m/z 309.06105). All quantification data were made based on triplicate experiments. Data in Table 1 present average intensities from triplicate experiments. All spectra were baseline corrected and recalibrated in FlexAnalysis 3.3. For estimation of LOD and LLOQ, linear regression for S/N ratios of 3 and 5, respectively, was used. Regression was based on spectral data of the lowest concentration sample with detectable analyte signal.

Author Contributions: Conceptualization, J.S.; methodology, A.K. and T.R.; software, A.K. and T.R.; validation, J.S. and T.R.; formal analysis, J.S. and T.R.; investigation, J.S., A.K. and T.R.; resources, J.S. and T.R.; data curation, J.S., A.K. and T.R.; writing—original draft preparation, J.S. and T.R.; writing—review and editing, J.S.; visualization, T.R.; supervision, J.S.; project administration, J.S. and T.R.; funding acquisition, J.S. and T.R. All authors have read and agreed to the published version of the manuscript.

Funding: The publication is based on the results of MINIATURA 3 project No. 2019/03/X/NZ9/00874 entitled "Assessment of mycotoxin content on building materials with laser methods mass spectrometry" financed by National Science Centre, Poland. The nanoparticle-based research part was supported by the National Science Centre (Poland), research project OPUS Number 2016/23/B/ST4/00062.

Institutional Review Board Statement: Not applicable.

Informed Consent Statement: Not applicable.

Data Availability Statement: Data sharing not applicable.

Conflicts of Interest: The authors declare no conflict of interest.

References

1. Sulyok, M.; Berthiller, F.; Krska, R.; Schuhmacher, R. Development and validation of a liquid chromatography/tandem mass spectrometric method for the determination of 39 mycotoxins in wheat and maize. *Rapid Commun. Mass Spectrom.* **2006**, *20*, 2649–2659. [CrossRef] [PubMed]
2. Capriotti, A.L.; Caruso, G.; Cavaliere, C.; Foglia, P.; Samperi, R.; Laganà, A. Multiclass mycotoxin analysis in food, environmental and biological matrices with chromatography/mass spectrometry. *Mass Spectrom. Rev.* **2012**, *31*, 466–503. [CrossRef] [PubMed]
3. Zöllner, P.; Mayer-Helm, B. Trace mycotoxin analysis in complex biological and food matrices by liquid chromatography–atmospheric pressure ionisation mass spectrometry. *J. Chromatogr. A* **2006**, *1136*, 123–169. [CrossRef] [PubMed]
4. Anfossi, L.; Giovannoli, C.; Baggiani, C. Mycotoxin detection. *Curr. Opin. Biotechnol.* **2016**, *201637*, 120–126. [CrossRef]
5. Brewer, J.H.; Thrasher, J.D.; Straus, D.C.; Madison, R.A.; Hooper, D. Detection of mycotoxins in patients with chronic fatigue syndrome. *Toxins* **2013**, *5*, 605–617. [CrossRef]
6. Andersen, B.; Frisvad, J.C.; Søndergaard, I.; Rasmussen, I.S.; Larsen, L.S. Associations between fungal species and water-damaged building materials. *Appl. Environ. Microbiol.* **2011**, *77*, 4180–4188. [CrossRef]
7. Szulc, J.; Ruman, T.; Gutarowska, B. Metabolome profiles of moulds on carton-gypsum board and malt extract agar medium obtained using an AuNPET SALDI-ToF-MS method. *Int. Biodeterior. Biodegr.* **2017**, *125*, 13–23. [CrossRef]
8. Hyvärinen, A.; Meklin, T.; Vepsäläinen, A.; Nevalainen, A. Fungi and actinobacteria in moisture-damaged building materials—Concentrations and diversity. *Int. Biodeterior. Biodegr.* **2002**, *49*, 27–37. [CrossRef]
9. Gutarowska, B.; Piotrowska, M. Methods of mycological analysis in buildings. *Build. Environ.* **2007**, *42*, 1843–1850. [CrossRef]
10. Gutarowska, B. Metabolic activity of moulds as a factor of building materials biodegradation. *Pol. J. Microbiol.* **2010**, *59*, 119–124. [CrossRef]
11. Nielsen, K.F. Mycotoxin production by indoor molds. *Fungal Genet. Biol.* **2003**, *39*, 103–117. [CrossRef]
12. Straus, D.C. Molds, mycotoxins, and sick building syndrome. *Toxicol. Ind. Health* **2009**, *25*, 617–635. [CrossRef] [PubMed]
13. Tuuminen, T.; Lohi, J. Dampness and mold hypersensitivity syndrome is a Biotoxicosis that should be diagnosed promptly. *Adv. Clin. Toxicol.* **2019**, *4*, 000144. [CrossRef]
14. Hyvönen, S.; Lohi, J.; Tuuminen, T. Moist and mold exposure is associated with high prevalence of neurological symptoms and MCS in a finnish hospital workers cohort. *Saf. Health Work.* **2020**, *11*, 173–177. [CrossRef]
15. Soroka, P.M.; Cyprowski, M.; Szadkowska-Stańczyk, I. Occupational exposure to mycotoxins in various branches of industry. *Med. Pr.* **2008**, *59*, 333–345. (In Polish)
16. Nieminen, S.M.; Karki, R.; Auriola, S.; Toivola, M.; Laatsch, H.; Laatikainen, R.; Hyvarinen, A.; Von Wright, A. Isolation and identification of *Aspergillus fumigatus* mycotoxins on growth medium and some building materials. *Appl. Environ. Microbiol.* **2002**, *68*, 4871–4875. [CrossRef]
17. Engelhart, S.; Loock, A.; Skutlarek, D.; Sagunski, H.; Lommel, A.; Färber, H.; Exner, M. Occurrence of toxigenic *Aspergillus versicolor* isolates and sterigmatocystin in carpet dust from damp indoor environments. *Appl. Environ. Microbiol.* **2002**, *68*, 3886–3890. [CrossRef]
18. Johanning, E.; Gareis, M.; Nielsen, K.F.; Dietrich, R.; Märtlbauer, E. Airborne Mycotoxin Sampling and Screening Analysis. In *Indoor Air 2002 Proceedings of the 9th International Conference on Indoor Air Quality and Climate, 30 June–5 July 2002, Monterey, CA, USA*; Levin, H., Bendy, G., Cordell, J., Eds.; The International Academy of Indoor Air Sciences: Santa Cruz, CA, USA, 2002; Volume 5, pp. 1–6.
19. Jarvis, B.B.; Miller, J.D. Mycotoxins as harmful indoor air contaminants. *Appl. Microbiol. Biotechnol.* **2005**, *66*, 367–372. [CrossRef]
20. Frisvad, J.C.; Thrane, U.; Filtenborg, O. Role and use of secondary metabolites in fungal taxonomy. In *Chemical Fungal Taxonomy*; Frisvad, J.C., Bridge, P.D., Arora, D.K., Eds.; Marcel Dekker: New York, NY, USA, 1998; pp. 289–319.
21. Adan, O.C.G.; Samson, R.A. *Fundamentals of Mold Growth in Indoor Environments and Strategies for Healthy Living*; Wageningen Academic Publishers: Wageningen, The Netherlands,, 2011. [CrossRef]
22. Frisvad, J.C.; Nielsen, K.F.; Samson, R.A. Recommendations concerning the chronic problem of misidentification of mycotoxinogenic fungi associated with foods and feeds. *Adv. Exp. Med. Biol.* **2006**, *571*, 33–46.
23. Stoev, S.D.; Daskalov, H.; Radic, B.; Domijan, A.M.; Peraica, M. Spontaneous mycotoxic nephropathy in Bulgarian chickens with unclarified mycotoxin aetiology. *Vet. Res.* **2002**, *33*, 83–93. [CrossRef]
24. Shanakhat, H.; Sorrentino, A.; Raiola, A.; Romano, A.; Masi, P.; Cavella, S. Current methods for mycotoxins analysis and innovative strategies for their reduction in cereals: An overview. *J. Sci Food Agric.* **2018**, *98*, 4003–4013. [CrossRef] [PubMed]
25. Sulyok, M.; Krska, R.; Schuhmacher, R. A liquid chromatography/tandem mass spectrometric multi-mycotoxin method for the quantification of 87 analytes and its application to semi-quantitative screening of moldy food samples. *Anal. Bioanal. Chem.* **2007**, *389*, 1505–1523. [CrossRef] [PubMed]
26. Malachová, A.; Sulyok, M.; Beltrán, E.; Berthiller, F.; Krska, R. Optimization and validation of a quantitative liquid chromatography-tandem mass spectrometric method covering 295 bacterial and fungal metabolites including all regulated mycotoxins in four model food matrices. *J. Chromatogr. A* **2014**, *1362*, 145–156. [CrossRef] [PubMed]
27. Lacina, O.; Zachariasova, M.; Urbanova, J.; Vaclavikova, M.; Cajka, T.; Hajslova, J. Critical assessment of extraction methods for the simultaneous determination of pesticide residues and mycotoxins in fruits, cereals, spices and oil seeds employing ultra-high performance liquid chromatography-tandem mass spectrometry. *J. Chromatogr. A* **2012**, *1262*, 8–18. [CrossRef] [PubMed]

28. Beltrán, E.; Ibáñez, M.; Portolés, T.; Ripollés, C.; Sancho, V.; Marín, S.; Yusà, V.; Hernández, F. Development of sensitive and rapid analytical methodology for food analysis of 18 mycotoxins included in a total diet study. *Anal. Chim. Acta* **2013**, *783*, 39–48. [CrossRef]
29. Nielsen, K.F. Mould Growth on Building Materials. Secondary Metabolites, Mycotoxins and Biomarkers. Ph.D. Thesis, Technical University of Denmark, Kgs. Lyngby, Denmark, 2002.
30. Cassagne, C.; Ranque, S.; Normand, A.C.; Fourquet, P.; Thiebault, S.; Planard, C.; Hendrickx, M.; Piarroux, R. Mould routine identification in the clinical laboratory by matrix-assisted laser desorption ionization time-of-flight mass spectrometry. *PLoS ONE* **2011**, *6*, e28425. [CrossRef]
31. Ulrich, S.; Biermaier, B.; Bader, O.; Wolf, G.; Straubinger, R.K.; Didier, A.; Sperner, B.; Schwaiger, K.; Gareis, M.; Gottschalk, C. Identification of *Stachybotrys* spp. by MALDI-TOF mass spectrometry. *Anal. Bioanal. Chem.* **2016**, *408*, 7565–7581. [CrossRef]
32. Nizioł, J.; Rode, W.; Laskowska, B.; Ruman, T. Novel monoisotopic 109AgNPET for laser desorption/ionization mass spectrometry. *Anal. Chem.* **2013**, *85*, 1926–1931. [CrossRef]
33. Nizioł, J.; Ossoliński, K.; Ossolińnski, T.; Ossolińska, A.; Bonifay, V.; Sekuła, J.; Dobrowolski, Z.; Sunner, J.; Beech, I.; Ruman, T. Surface-transfer mass spectrometry imaging of renal tissue on gold nanoparticle enhanced target. *Anal. Chem.* **2016**, *88*, 7365–7371. [CrossRef]
34. Kuo, T.; Chen, Y.; Wang, C.; Shen, T.; Wang, H.; Pan, X.; Wang, D.; Liou, C.C.; Chang, Y.; Chen, Y.; et al. Highly oriented Langmuir–Blodgett film of silver cuboctahedra as an effective matrix-free sample plate for surface-assisted laser desorption/ionization mass spectrometry. *Nanoscale* **2017**, *9*, 11119–11125. [CrossRef]
35. Sekuła, J.; Nizioł, J.; Misiorek, M.; Dec, P.; Wrona, A.; Arendowski, A.; Ruman, T. Gold nanoparticle-enhanced target for MS analysis and imaging of harmful compounds in plant, animal tissue and on fingerprint. *Anal. Chim. Acta* **2015**, *895*, 45–53. [CrossRef] [PubMed]
36. Sekuła, J.; Nizioł, J.; Rode, W.; Ruman, T. Gold nanoparticle-enhanced target (AuNPET) as universal solution for laser desorption/mass spectrometry analysis and imaging of low molecular weight compounds. *Anal. Chim. Acta* **2015**, *875*, 61–72. [CrossRef] [PubMed]
37. Liu, Y.-C.; Chang, Y.-H.; Lin, Y.-H.; Liou, C.-C.; Kuo, T.-R. High-Performance Sample Substrate of Gold Nanoparticle Multilayers for Surface-Assisted Laser Desorption/Ionization Mass Spectrometry. *Nanomaterials* **2019**, *9*, 1078. [CrossRef] [PubMed]
38. Pan, X.Y.; Chen, C.H.; Chang, Y.H.; Wang, D.Y.; Lee, Y.C.; Liou, C.C.; Wang, Y.X.; Hu, C.C.; Kuo, T.R. Osteoporosis risk assessment using multilayered gold-nanoparticle thin film via SALDI-MS measurement. *Anal. Bioanal. Chem.* **2019**, *411*, 2793–2802. [CrossRef]
39. Szulc, J.; Otlewska, A.; Ruman, T.; Kubiak, K.; Karbowska-Berent, J.; Kozielec, T.; Gutarowska, B. Analysis of paper foxing by newly available omics techniques. *Int. Biodeter. Biodegr.* **2018**, *132*, 157–165. [CrossRef]
40. Szulc, J.; Ruman, T.; Karbowska-Berent, J.; Kozielec, T.; Gutarowska, B. Analyses of microorganisms and metabolites diversity on historic photographs using innovative methods. Analyses of microorganisms and metabolites diversity on historic photographs using innovative methods. *J. Cult. Herit.* **2020**, *45*, 101–113. [CrossRef]
41. Szulc, J.; Jabłonskaja, I.; Jabłońska, E.M.; Ruman, T.; Karbowska-Berent, J.; Gutarowska, B. Metabolomics and metagenomics characteristic of historic beeswax seals. *Int. Biodeter. Biodegr.* **2020**, *152*, 105012. [CrossRef]
42. Tuomi, T.; Reijula, K.; Johnsson, T.; Hemminki, K.; Hintikka, E.L.; Lindroos, O.; Kalso, S.; Koukila-Kähkölä, P.; Mussalo-Rauhamaa, H.; Haahtela, T. Mycotoxins in crude building materials from water-damaged buildings. *Appl. Environ. Microbiol.* **2000**, *66*, 1899–1904. [CrossRef]
43. Nizioł, J.; Rode, W.; Zieliński, Z.; Ruman, T. Matrix-free laser desorption–ionization with silver nanoparticle-enhanced steel targets. Matrix-free laser desorption-ionization with silver nanoparticle enhanced steel targets. *Int. J. Mass Spectrom.* **2013**, *335*, 22–32. [CrossRef]
44. Nizioł, J.; Ruman, T. Surface-transfer mass spectrometry imaging on monoisotopic silver nanoparticle enhanced target. *Anal. Chem.* **2013**, *85*, 12070–12076. [CrossRef]

ACS
MEASUREMENT SCIENCE Au
AN OPEN ACCESS JOURNAL OF THE AMERICAN CHEMICAL SOCIETY

Laser Ablation Synthesis in Solution and Nebulization of Silver-109 Nanoparticles for Mass Spectrometry and Mass Spectrometry Imaging

Aneta Płaza, Artur Kołodziej, Joanna Nizioł, and Tomasz Ruman*

Cite This: https://doi.org/10.1021/acsmeasuresciau.1c00020 **Read Online**

ACCESS | Metrics & More | Article Recommendations | Supporting Information

ABSTRACT: Preparation of monoisotopic silver-109 nanoparticles (^{109}AgNPs) by pulsed fiber laser (PFL) ablation synthesis in solution (LASiS) with the use of a 2D galvoscanner (2D GS) is described. The procedure of covering of custom-made stainless-steel MALDI targets containing studied objects via nebulization is also presented. Examples of application of the new method (PFL-2D GS LASiS and nebulization) in mass spectrometry (MS) analyses and MS imaging (MSI) are shown. These include tests with a nonionic nucleoside and saccharide, ionic amino acids, and also a low-molecular-weight polymer. Fingerprint MS imaging is shown as an example of a fast and simple MSI procedure.

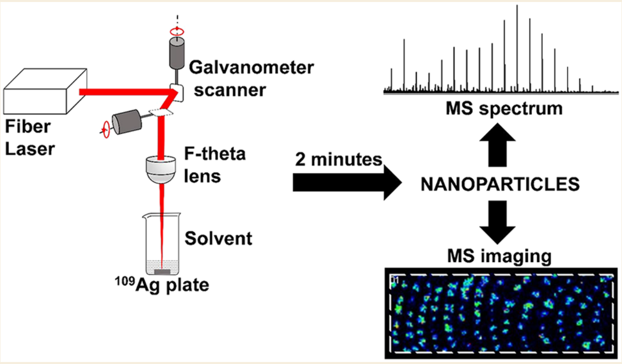

KEYWORDS: *silver-109 monoisotopic nanoparticles, laser ablation synthesis in solution, low molecular weight compounds, mass spectrometry, matrix-free laser desorption/ionization, surface-assisted desorption/ionization*

INTRODUCTION

One of the most utilized laser mass spectrometry methods is matrix-assisted laser desorption/ionization mass spectrometry (MALDI MS), which was developed by Tanaka et al. in 1988.[1] It offers soft ionization potential, being therefore a powerful analytical tool for the analysis of ionic high-molecular-weight molecules, such as peptides, proteins, and DNA/RNA,[2−4] but also, it is useful for detection of some nonionic classes of chemical compounds such as lipids, etc.[5−7] However, MALDI has not been too often applied to detect low-molecular-weight (LMW) compounds (MW < 1000 Da), because MALDI matrices are low-molecular-weight organic acids and produce a variety of matrix-related ions during the desorption/ionization process, which complicates the spectrum and causes suppression of analyte peaks.[8−10]

Discussed problems have been partly solved by the development of surface-assisted desorption/ionization (SALDI) mass spectrometry techniques, where target plates are coated with various nanostructures.[7,11−17] Applications of nanoparticles not only allow reduction of spectral interference but also simplify the mass spectrum. The sample preparation step is also much simpler; usually only application of sample is required.[16,17] What is more, methods based on nanostructures produce very good spot-to-spot reproducibility and greatly reduce the "sweet-spot" problem.[13]

The literature describes two main approaches for the synthesis of nanostructures: the top-down approach, where a larger structure is broken down into NPs, and the bottom-up approach, in which material is synthesized from the molecular or atomic level.[18,19] Chemical reduction is classified as a bottom-up approach and is one of the most common strategies in use for the synthesis of nanoparticles for experiment MS.[17,20,21] However, chemical purity problems arise due to the use of substances for chemical reactions such as metal precursors, reducing agents, stabilizers, and oxidized products, which are the source of reagent-related ions and yield numerous interfering signals.[22−25]

The above-mentioned problem was solved with the application of laser ablation synthesis in solution (LASiS) for the production of nanoparticles.[26] LASiS employs pulsed laser irradiation to ablate a solid material target submerged in liquid, ejecting NPs from the plasma plume into the surrounding solution.[27] This method allows for stabilizer- and reducing-agent-free NP production.[26−29] LASiS produces nanoparticle suspensions of a relatively high chemical purity compared to chemical methods.[30]

Received: July 3, 2021

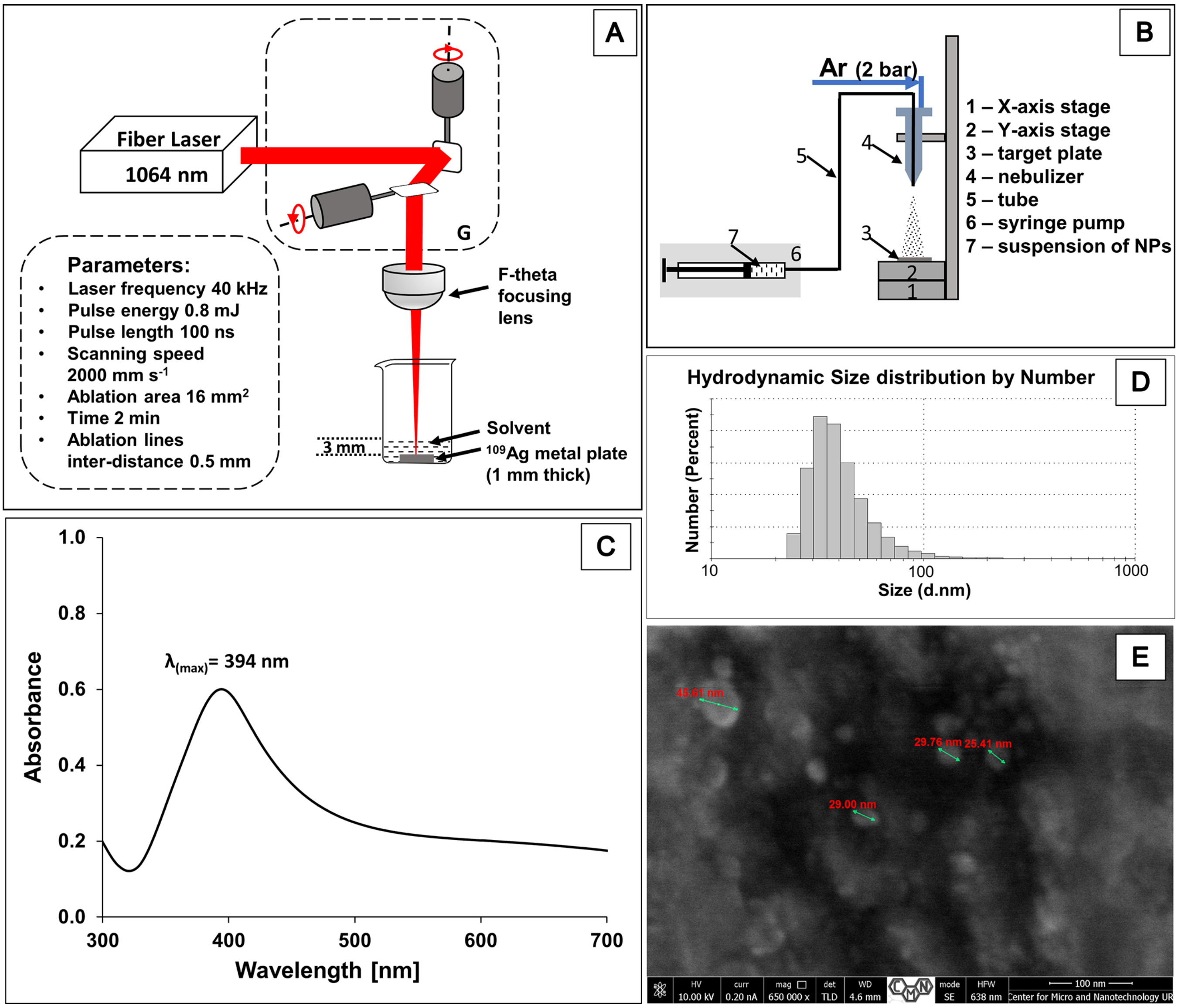

Figure 1. (A) Laser ablation setup for the preparation of ^{109}AgNPs; G − 2D galvanometer laser scanner. Right panel (B) presents setup for nebulization of nanoparticles. Panel (C) presents UV−vis spectrum of ^{109}AgNP suspension in acetonitrile. Panel (D) shows results of DLS measurement of ^{109}Ag nanoparticles' hydrodynamic size distribution by number. (E) High-resolution SEM image of target modified with ^{109}AgNPs generated by PFL 2D GS (three sizes in the center are 29.00, 29.76, and 25.41 nm).

This study describes a new method of production of chemically pure silver-109 nanoparticles in suspension with an application method for covering of studied objects or surfaces. For the first time, 1064 nm pulsed fiber laser (PFL) with 2D galvanometer scanner (2D GS) is shown as a very good source of nanoparticles. The GS module allows very precise and fast scanning of a focused laser beam on the sample surface, virtually removing any heat buildup or local melting of the ablation target. It allows very efficient and fast production of relatively big amounts of nanoparticles compared to systems without it. Moreover, the GS module allowed us to use a 20 W pulsed fiber laser directly on the ablation target with a full laser frequency of 80 kHz. Generated silver-109 nanoparticles are shown to be highly useful for LDI mass spectrometry and also mass spectrometry imaging (MSI). This work presents LDI MS results for test compounds belonging to groups such as amino acids, saccharides, nucleosides, and polymers as well as MSI results for the fingerprint.

EXPERIMENTAL SECTION

Materials

A silver-109 isotope of 99.7% isotopic purity was bought from Trace Sciences International (USA). L-Histidine and D-ribose were purchased from Sigma-Aldrich (99% purity). Thymidine was purchased from Alfa Aesar (99% purity). Poly(propylene glycol) (PPG, average Mn 1000 Da) was purchased from Sigma-Aldrich. All solvents were of HPLC quality, except for water (18 MΩ cm water produced locally). Steel targets were machined from H17 stainless steel. Before the LDI MS and MS imaging experiments, steel targets were cleaned through soaking in boiling solvents: toluene (3 × 100 mL, each plate for 30 s), chloroform (3 × 100 mL, each plate for 30 s), acetonitrile (3 × 100 mL, each plate for 30 s), and deionized water (3 × 100 mL, each plate for 30 s). Every plate was dried in high vacuum (ca. 0.01 mbar, 24 h). Optical photographs were made with the use of an Olympus SZ10 microscope equipped with an 8 MPix Olympus digital camera and also a Canon 6D camera with a macro-type 90 mm focal length lens.

PFL 2D GS Laser Ablation Synthesis in Solution (LASiS) of Silver-109 Nanoparticles

The experimental arrangement for the ^{109}AgNP preparation by laser ablation is shown in Figure 1A. The silver-109 foil (∼1 mm thick) was placed at the bottom of a glass vessel containing solvent (acetonitrile or isopropanol). The ^{109}Ag foil was covered by an approximately 3 mm thick layer of solvent (total solvent volume was 3 mL). The laser ablation was carried out with a 1064 nm pulsed fiber laser (Raycus RFL-P20QE/A3). A suspension was obtained after 2 min of irradiation with a pulse energy of 0.8 mJ (100 ns pulse length) at a 40 kHz repetition rate. Laser ablation was accomplished at a scanning speed of 2000 mm/s; the ablation area was 4 × 4 mm. The suspension was immediately transferred into a syringe and used in the nebulization step.

Nebulization of ^{109}AgNP Suspension

The experimental setup for the nebulization of ^{109}AgNP suspension is shown in Figure 1B. The entire nanoparticle nebulization process was controlled by a computer. The H17 steel plate (laser mass spectrometry target plate) was placed on the table of a translation system consisting of a motorized XY table (EzM-42XL-A powered by closed-loop Ezi-SERVO motors). A glass syringe (1 mL) was filled with a previously prepared suspension of silver-109 nanoparticles and placed in a syringe pump (pumping speed 250 μL/min). The custom-made software directed the 2D system table with 10 mm/s speed using a sequence of movement designed to uniformly cover a target plate. The nebulizer was obtained from a Bruker Amazon ETD ESI ion source. Argon at a pressure of 2 bar was used as the nebulizing gas. Generally, all studied objects—for MS and MSI—were placed on the target plate before nebulization.

^{109}AgNP Characterization

The ^{109}AgNP suspension was characterized by UV−vis spectroscopy (Jasco V-670 spectrophotometer). The spectrum was registered in quartz cuvettes within a 200−800 nm spectral range. The blank sample contained acetonitrile. The suspension of ^{109}AgNPs was also characterized by dynamic light scattering (DLS) using a Zetasizer-Nano ZS from Malvern Instruments. DLS measurements were performed by backscattering at a fixed detector angle of 173°. Isopropanol was used as a dispersant.

LDI MS Experiments

LDI-ToF mass spectrometry experiments were performed using a Bruker Autoflex Speed ToF mass spectrometer equipped with a SmartBeam II laser (355 nm). The laser pulse energy was approximately 90−140 μJ, and the laser repetition rate was 1 kHz. Compounds were measured within 80−1500 or 80−2000 m/z windows, and ion deflection was turned on for ions lighter than m/z 79. The first accelerating voltage was held at 19 kV, and the second ion source voltage was held at 16.7 kV. The reflector voltages used were 21 and 9.55 kV. The spectra for histidine, thymidine, and ribose were acquired by integrating approximately 4000 shots, for which the PPG 5000 shots package was used. Spectra were internally calibrated and analyzed with FlexAnalysis (version 3.3). Mass calibration (typically enhanced cubic calibration based on 5−10 points) was performed using internal standards (silver ions and clusters from $^{109}Ag^+$ to $^{109}Ag_{10}^+$).

LDI MS Imaging Experiments

Measurements were performed using a Bruker Autoflex Speed time-of-flight mass spectrometer in reflectron mode. The apparatus was equipped with a SmartBeam II 1000 Hz, 355 nm laser. The laser impulse energy was approximately 90−140 μJ, the laser repetition rate was 1 kHz, and deflection was used for m/z lower than 80 Da. The m/z range was 80−1500 for the fingerprint experiment (40 × 40 μm spatial resolution). The first accelerating voltage was held at 19 kV, and the second ion source voltage was held at 16.7 kV. Reflector voltages used were 21 kV (the first) and 9.55 kV (the second). The experiments were made with 1000 laser shots per individual spot with random walk applied (FlexImaging 4.0). A random spot measurement pattern was used for all MSI experiments. All spectra were calibrated with the use of silver ions ($^{109}Ag^+$ to $^{109}Ag_{10}^+$). All of the generated ion images were within the ±0.05% m/z range. TIC normalization was used for all results shown.

LDI Sample Preparation

Stock solution (0.1 mg/mL) of each analyte was prepared by dissolving it in water (histidine, ribose, thymidine). In order to prepare analyte solutions of lower concentrations, the stock solution was diluted with ultrapure water. A solution of poly(propylene glycol) in isopropanol of a 10 μg/mL concentration was prepared. A 0.5 μL volume of each of the final solutions was applied to the steel target and air-dried followed by nebulization with the ^{109}AgNP suspension.

MALDI Sample Preparation

MALDI experiments were performed using a DHB matrix solution (saturated matrix in acetonitrile with 0.5% of trifluoroacetic acid) by the drying droplet method (1:1 v/v matrix:sample solution). A volume of 1 μL of sample mixed with matrix solution was placed directly on steel plate and air-dried, and the target was inserted into an MS apparatus for measurement. Calibration was performed on matrix signals.

Imaging Sample

Preparation of the ungroomed fingerprint for mass spectrometry imaging was obtained by touching the clean steel target for approximately 1 s. Then, the object was covered with a layer of nanoparticles by nebulization, as described in paragraph 2.3.

High-Resolution Scanning Electron Microscopy (HR SEM)

A target modified with ^{109}AgNPs generated by a PFL 2D GS method was inserted into the Helios Nanolab 650 electron microscope. The voltage was set at 10 and 30 kV, and the current was set as 0.2 nA. Images were made in nonimmersive mode.

■ RESULTS AND DISCUSSION

PFL 2D GS LASiS of ^{109}AgNPs

The laser mass spectrometry usually is realized via MALDI methodology. It employs organic low-molecular-weight matrices, such as α-cyano-4-hydroxycinnamic acid (CHCA) and 2,5-dihydroxybenzoic acid (DHB). This methodology is preferred only for ionic substances, such as peptides and proteins of molecular weights higher than 1000 Da due to (i) numerous matrix signals in the region of m/z < 1000, (ii) unreliable calibration, (iii) low mass accuracy, (iv) low ionization potential for neutral organic compounds, and (v) the sweet-spot effect. Moreover, due to the acidity of the standard matrix solutions, the analysis of various substances may be problematic.[31]

Most of above-mentioned MALDI problems may be solved by using metal nanoparticles, for example, silver ones, as desorption/ionization agents.[16,21,32] Silver nanoparticles were produced by different means including chemical, physical, and biological methods. Chemical synthesis is most commonly used to obtain AgNPs. The reaction involves the reduction of Ag^+ to elemental silver by electron transfer under various conditions. The chemical reduction method requires two substances: a metal salt precursor and a reducing agent. However, almost all procedures contain also a stabilizer. Among the many silver precursors, we can distinguish silver nitrate, silver ammonia complexes, and silver sulfate. In turn, the role of the reducing agent is often assumed by sodium borohydride or sodium citrate. Both the type of precursor and reductant used can influence the properties of the AgNPs obtained.[21] Preparation of silver nanoparticles by a chemical reduction method for laser mass spectrometry was presented by Hua and co-workers. Authors used silver nitrate as the metal precursor and sodium cyanoborohydride as the reducing agent.

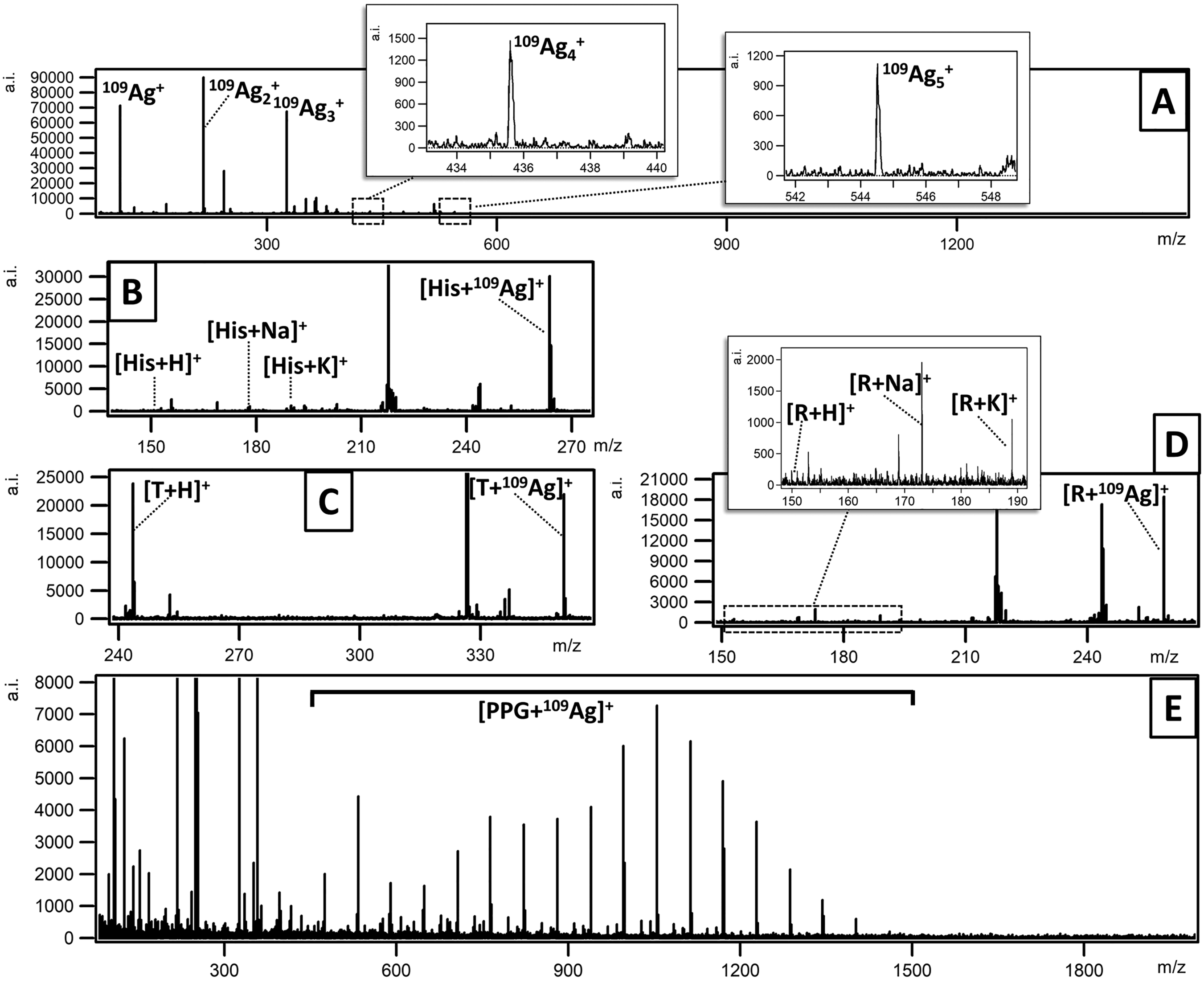

Figure 2. LDI MS positive reflectron mode spectrum of target plate covered with ^{109}AgNPs generated by PFL 2D GS (A). Others panels present LDI MS spectra fragments for histidine (B), thymidine (C), and ribose (D) of 0.1 mg/mL concentrations deposited on the target plate and covered with silver-109 nanoparticles obtained with PFL 2D GS LASiS. The last panel (E) presents an LDI MS spectrum of poly(propylene glycol) of a 10.0 μg/mL concentration spot at the same target as the above-mentioned compounds.

AgNPs were used as matrices for studying the MALDI MS of peptides such as bradykinin and angiotensin I. The obtained results present only proton adducts of the mentioned compounds along with a relatively high noise level.[33] In contrast, Sherrod et al. used commercially available 20 and 60 nm silver nanoparticles to ionize peptides and observed no signals on the MS spectrum.[34] Ding and co-workers used a chemical reduction method to obtain silver nanoparticles of different sizes. Silver nitrate or silver perchlorate was used as the metal precursor, while sodium citrate and/or sodium borohydride was used as the reducing agent. The AgNPs obtained were used as a matrix for amyloid-beta peptide MALDI-ToF-MS measurements. However, the processes of purifying the suspension from reaction byproducts or unreacted substrates make this method of producing silver nanoparticles very time-consuming and complicated.[35]

The above-mentioned problems were partly solved by Yonezawa and co-workers, who were the first to demonstrate a method for producing nanoparticles by laser ablation in an aqueous medium and their applicability as a matrix for laser MS.[24] Compared to chemical synthesis, laser ablation synthesis in solution has some very unique properties including: (i) cost-effectiveness, (ii) simplicity, (iii) time-efficiency, (iv) spectrum simplicity and low chemical background, (v) the ability to prepare NPs from a variety of metals or alloys, and (vi) in situ dispersion of the nanoparticles in a variety of liquids. In general, LASiS produces suspensions of a relatively high chemical purity as compared to chemical methods.

In this work, LASiS has been used to obtain chemically pure monoisotopic silver-109 nanoparticles. Natural silver contains two isotopes: ^{107}Ag (ca., 51.8%) and ^{109}Ag (ca., 48.2%). It is logical to state that the use of monoisotopic silver-based MS methods provide analyte peaks that are roughly 2-fold higher in intensity compared to normal silver. Signals based on a single silver-109 isotope have also a higher signal-to-noise (S/N) ratio. What is more, internal calibration with the use of silver-109 signals is greatly improved due to many times higher intensity and S/N of complex Ag_x^+ (x = 2−30) ions compared to normal silver.

Nanoparticles were generated by a pulsed 1064 nm fiber laser with galvoscanner head scanning of an ablated surface. The experimental setup for the ^{109}AgNP preparation is shown in Figure 1A. For fast synthesis of nanoparticles, a high-frequency (60−80 kHz), high-pulse-energy (up to 1 mJ/pulse) laser was used. However, in order to avoid unwanted thermal effects such as melting, solvent boiling, and oxidation of solvent and also of nanoparticles, a two-dimensional (2D) galvoscanner (GS) was used. A galvoscanner head with an f-theta lens attached to a fiber laser allowed for precise and very fast shifting of a focused laser beam on the surface of an ablated metal foil.

Prepared nanoparticles were first studied by UV−vis spectroscopy. Particular wavelengths of light can induce the metallic electrons to oscillate, which causes an effect known as surface plasmon resonance (SPR). It is associated with a specific size and shape of the silver nanoparticles as well as chemical surroundings. Therefore, the UV−vis spectroscopy method can be of some aid in determining the size and shape of nanoparticles. The literature describes that as the diameter of AgNPs increases, the absorbance band shifts toward longer wavelengths and also broadens.[36,37] The UV−vis spectrum obtained for PFL 2D GS LASiS of ^{109}AgNPs is shown in Figure 1C. The ^{109}AgNP postreaction suspension UV−vis spectrum recorded after 3 min of synthesis contains a local maximum at 394 nm, which suggests that the size of most of nanoparticles is approximately 10 nm. However, one can observe an asymmetric broadening of the SPR toward longer wavelengths, which is characteristic for a fraction of spheroidal particles. The occurrence of spheroids may indicate particle aggregation processes taking place in the suspension.[29] Similar results were reported by several authors.[21,29,36]

Figure 1D presents the results of dynamic light scattering (DLS) measurement of ^{109}AgNP size distribution by number after a few minutes after preparation of a suspension. The DLS chart of the size distribution by number indicates the highest content of nanoparticles being around 30 nm in diameter, with a distribution ranging from 20 to 100 nm. A high-resolution scanning electron microscope image of a modified target (Figure 1E) also confirms that individual nanoparticles are in roughly round/spherical shape and are of 25−35 nm size. A number of HRTEM and DLS results on size measurements of silver nanoparticles obtained with LASiS in different organic solvents indicate that NPs with a size of ∼10 nm are the most common group.[21,29] DLS results suggest bigger nanoparticles as judged from a UV−vis spectrum. Most probably, this is due the fact that the nanoparticle suspension used for the DLS measurement was prepared in a different solvent than the one optimized for LASiS. Many studies show the effect of solvent on the size of nanoparticles obtained.[29]

Application of nanoparticles in laser mass spectrometry requires a suitable method of application on the surface containing a studied object, which may be, for example, a sample spot or tissue slice. One approach of using AgNPs as a matrix is dry metal sputtering, which allows for preparation of a homogeneous layer with minimal or no lateral migration of the analyte on the laser beam size scale.[38] Silver deposition by sputtering has been applied to various types of samples, including fingerprints,[39] but also to a human carotid[40] or samples of colorectal cancer metastases to the liver.[41] However, the prevalence of this method is low, probably due to the need for a specialized sputtering system. Moreover, sputtering requires that a sample is treated in very high vacuum, which can be problematic for some of tissues due to warping and cracking. Yang, Fournelle, and Chaurand presented silver-assisted laser desorption ionization (AgLDI) MSI, where a silver salt solution was sprayed to obtain a homogeneous layer on thin tissue sections. However, the method did not achieve the same high spatial resolution as Dufresne et al. or other researchers.[38,42]

For our LDI MS measurements, 0.5 μL of each of solution of histidine, ribose, thymidine, and PPG polymer was applied to a stainless-steel plate and air-dried. The plate with all test objects was placed on the table of the translation system as shown in Figure 2B. Aliquots of colloidal silver-109 (1 mL) were sprayed three times onto the sample. Each portion was injected into the nebulizer at a constant rate of 250 μL/min. The entire nanoparticle nebulization process was controlled by a computer using a sequence of movements aimed at evenly covering the target plate.

The LDI MS spectrum of ^{109}AgNPs produced by PFL 2D GS LASiS and deposited on the surface of stainless steel of target plate by nebulization is shown in Figure 2A. The mass spectrum made in the 80−1500 m/z range contains virtually only silver-109 ion peaks of $^{109}\mathrm{Ag}^+$ to $^{109}\mathrm{Ag}_{10}{}^+$ composition. Various low-molecular-weight compounds such as ionic amino acid histidine and nonionic ribose and thymidine were tested to verify the potential of ionization of organic compounds with the silver-109 nanoparticles obtained with PFL 2D GS LASiS.

The first analyzed compound histidine (Figure 2B) was found mainly as a ^{109}Ag adduct but sodium, potassium, and protonated adducts signals were also found. Histidine was recently analyzed on diamond nanowires acting as an LDI active surface, presenting a spectrum with a number of unknown signals in the m/z 50−250 region.[43] Our previous attempt to analyze histidine was made using a ^{109}AgNPET target. The S/N ratio of the histidine−^{109}Ag adduct for ^{109}AgNPET was 214,[44] while for PFL 2D GS LASiS, ^{109}AgNPs is higher at 280. What is more, the target covered by PFL 2D GS LASiS ^{109}AgNPs that is ready for mass spectrometry can be made within 10 min of time, which is in contrast to our previous method ^{109}AgNPET, where target preparation took 48 h.

Thymidine was also tested as a very good example of a biologically important, medium-polarity nonionic compound. The LDI MS spectrum of thymidine (T; 0.1 mg/mL) with PFL 2D GS LASiS ^{109}AgNPs in reflectron positive mode is shown in Figure 2C. The thymidine MS spectrum obtained with the use of PFL 2D GS LASiS ^{109}AgNPs shows two highest peaks, assigned to a thymidine−silver adduct with an S/N ratio of 138 and protonated with an S/N ratio of 175. Measuring nucleosides using modified graphene as a matrix was shown by Wang et al.; however, the results presented a low S/N ratio.[45]

Another compound tested was ribose, a nonionic medium-polarity saccharide. The LDI MS spectrum within m/z 80−1500 in reflectron positive mode of ribose on a target covered by PFL 2D GS LASiS ^{109}AgNPs is shown in Figure 2D. The highest peak visible in the spectrum belongs to the ribose−$^{109}\mathrm{Ag}^+$ adduct. Protonated, potassium, and sodium adducts were also visible, and the S/N ratios for protonated, sodium, potassium, and ribose−^{109}Ag adducts were 3, 23, 12, and 150, respectively. Bibi and Ju utilized quantum dots (QDs) with some modifications as a matrix for LDI-TOF MS to small monosaccharides including ribose.[46] In contrast, Zhang and colleagues showed that the use of traditional MALDI matrices such as DHB or CHCA is not suitable for the analysis of small

https://doi.org/10.1021/acsmeasuresciau.1c00020
ACS Meas. Sci. Au XXXX, XXX, XXX−XXX

oligosaccharides such as ribose. The matrix-derived peaks were dominant on the spectrum and were the cause of ribose signal suppression.[47]

Poly(propylene glycol) is a compound belonging to the polymer group, consisting of propylene oxide-mers. The repeating monomer unit mass of approximately 57.9 is of the $CH_2CH(CH_3)O$ chemical formula. The LDI mass spectrum of PPG is shown in Figure 3E. As can be seen, the spectrum contains a typical polymer structure with a dominating mass of approximately m/z 1000, which positively corroborates with the polymer used. For example, the highest polymer signal at m/z 1055 revealed is the $^{109}Ag^+$ ion adduct of a PPG with 16-mer units. Comparison of polypropylene glycol spectra between MALDI and SALDI were made by Okuno et al. The authors identified a problem with the reproducibility of MALDI mass spectra for PPG, which showed a strong dependence on the analyte/matrix ratio and on the type of solvent and/or chemical matrix.[48]

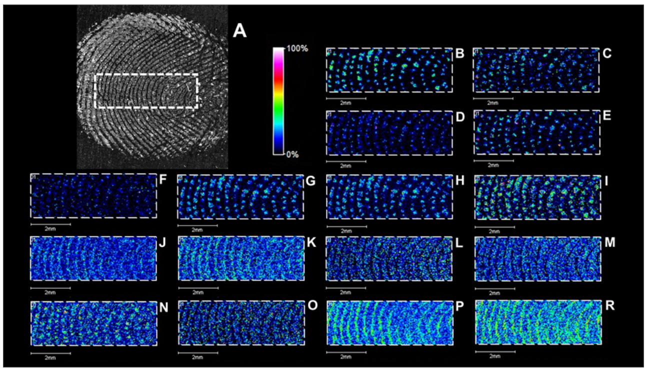

Figure 3. Results of LDI MS imaging of a fingerprint with PFL 2D GS LASiS ^{109}AgNPs. Optical microscope images of a fingerprint (A). Images (B−R) (TIC-normalized) represent spatial distribution of ions of m/z 96.922 (B), 98.996 (C), 106.050 (D), 148.061 (E), 178.0592 (F), 183.078 (G), 183.175 (H), 185.069 (I), 240.947 (J), 241.942 (K), 283.264 (L), 311.295 (M), 333.119 (N), 334.283 (O), 363.324 (P), and 391.355 (R). Spatial resolution 40 × 40 μm.

Comparison of the new method with previously published ones is shown in Table 1. The upper part of table presents comparison of m/z matching errors (calculated and experimental) of a few test low-molecular-weight compounds shown as ppm values. Very big, unacceptable m/z errors of MALDI are surely an effect of calibration performance. The silver-method-based spectrum was calibrated with the use of nine signals, while the MALDI one was calibrated with only two matrix signals. It should be noted that the ribose signal is marked as "not found" as a big m/z difference and low intensity did not allow it to be assigned. The lower part of Table 1 contains comparison of previously published method ^{109}AgNPET that is based on the chemical synthesis of nanoparticles with the one based on PFL 2D GS LASiS. It is clearly seen that PFL 2D GS LASiS ^{109}AgNPs produce much higher signals under laser irradiation, which in turn allows better calibration, especially in the higher m/z region.

Table 1. Comparison of Mass Spectrometry Data of PFL GS LASiS Nanoparticles with Chemically Synthesized Ones (AgNPET) and Also with MALDI

	calculated−experimental m/z errors in ppms	
		Δ m/z [ppm]
compound	MALDI	PFL 2D GS LASiS
histidine	184	8
thymidyne	314	12
ribose	not found	7
3-methylhippuric acid	1207	21
alternariol	77	8
	comparison of signal intensity	
	^{109}AgNPET [16]	PFL 2D GS LASiS ^{109}AgNPs
$^{109}Ag^+$	14 453	59 969
$^{109}Ag_2^+$	21 351	89 591
$^{109}Ag_3^+$	19 818	77 933
$^{109}Ag_4^+$	386	1810
$^{109}Ag_5^+$	785	10 579

MS Imaging with PFL 2D GS LASiS ^{109}AgNPs

The fingerprint was chosen as a test subject to determine the applicability of PFL 2D GS LASiS ^{109}AgNPs for imaging exogenous and endogenous compounds on a human finger. Francese and co-workers[49] were the first to demonstrate the applicability of MALDI MSI for fingerprint trace analysis. The fingerprint is one of the most important means of biometric identification, as it is a source of both physical and chemical information. The physical information provided by a fingerprint is the geometry, distribution, and size of sweat pores and also local shapes such as terminations, bifurcations, islands, spurs, etc. Chemical information found on fingerprints includes exogenous and endogenous substances, including drugs, explosives, toxins, poisons, cosmetics, toiletries, etc. Endogenous compounds found on the skin include lipids, peptides, amino acids, proteins, urea, simple inorganic compounds, as well as organic salts.

The LDI MS imaging experiment involved a fingerprint left on the stainless-steel surface. Preparation of the fingerprint is extremely simple, and only requires a finger to touch the target surface. A suspension of monoisotopic silver-109 nanoparticles was sprayed onto the obtained fingerprint. Table 2 contains names and ion data for some of the compounds found in the imaging experiment. Ion images for some of the ions from Table 2 are shown in Figure 3 and the Supporting Information (S1).

The compounds that were identified in the studied fingerprint belong to different groups such as inorganic salts (e.g., NaCl, KCl), simple organic compounds (e.g., urea, amino acids, short carboxylic acids), fatty acids, lipids, and others. Most of these compounds are considered endogenous, secreted through the skin or sweat pores.

Ion images for ions presented in Table 2 are shown in Figure 3. In the fingerprint, six amino acids such as serine, cysteine, glutamic acid, asparagine, histidine, and lysine were detected. Figure 3 contains four images showing the spatial distribution of amino acids with the following m/z values of 106.050 (D), 148.061 (E), 178. 0592 (F), and 185.0692 (I), which were assigned to protonated serine, protonated glutamic acid, a histidine−sodium adduct, and a lysine−potassium adduct, respectively. As judged from the ion image, these amino acid ions are found in close proximity to sweat pores, which produce round structures rich in the mentioned ions. Numerous studies show that amino acids/proteins are one of the most numerous groups of compounds present in a fingerprint.[50] Figure 3 also contains images showing ions with relatively low m/z, such as 96.922 (B) and 98.996 (C) assigned to adduct $[KClNa]^+$ and a urea−potassium adduct.

Table 2. Compounds and Their Ions Found in MSI Experiment

	compound[a]	ion formula	$m/z_{\text{calc.}}$[b]	
1.	KCl	$[KCl + Na]^+$	96.9223	Figure 3B
2.	urea	$[CH_4N_2O + K]^+$	98.9961	Figure 3C
3.	1-hexanoic acid	$[C_6H_{12}O_2{-}H_2O + H]^+$	99.0810	S1.A
4.	serine	$[C_3H_7NO_3 + H]^+$	106.0504	Figure 3D
5.	1-hexanoic acid	$[C_6H_{12}O_2 + H]^+$	117.0916	S1.B
6.	L-cysteine	$[C_3H_7NO_2S + H]^+$	122.0276	S1.C
7.	L-glutamic acid	$[C_5H_9NO_4 + H]^+$	148.0610	Figure 3E
8.	2-aminoadipic acid	$[C_6H_{10}O_4 + Na]^+$	169.0477	S1.D
9.	asparagine	$[C_4H_8N_2O_3 + K]^+$	171.0172	S1.E
10.	histidine	$[C_6H_9N_3O_2 + Na]^+$	178.0592	Figure 3F
11.	octanoic acid	$[C_8H_{16}O_2 + K]^+$	183.0787	Figure 3G
12.	dodecanoic acid	$[C_{12}H_{24}O_2{-}H_2O + H]^+$	183.1749	Figure 3H
13.	2-aminoadipic acid	$[C_6H_{10}O_4 + K]^+$	185.0216	S1.F
14.	L-lysine	$[C_6H_{14}N_2O_2 + K]^+$	185.0692	Figure 3I
15.	pyruvic acid	$[C_3H_4O_3 + {}^{109}Ag]^+$	196.9208	S1.G
16.	glyceric acid	$[C_3H_6O_4 + {}^{109}Ag]^+$	214.9313	S1.H
17.	pentyl 2-hydroxybenzoate	$[C_{12}H_{16}O_2 + Na]^+$	215.1048	S1.I
18.	glutaric acid	$[C_5H_8O_4 + {}^{109}Ag]^+$	240.9470	Figure 3J
19.	asparagine	$[C_4H_8N_2O_3 + {}^{109}Ag]^+$	240.9582	S1.J
20	aspartic acid	$[C_4H_7NO_4 + {}^{109}Ag]^+$	241.9422	Figure 3K
21.	phenylacetic acid	$[C_8H_8O_2 + {}^{109}Ag]^+$	244.9572	S1.K
22.	3-oxoglutaric acid	$[C_5H_6O_5 + {}^{109}Ag]^+$	254.9262	S1.L
23.	mevalonic acid	$[C_6H_{12}O_4 + {}^{109}Ag]^+$	256.9783	S1.M
24.	ribose	$[C_5H_{10}O_5 + {}^{109}Ag]^+$	258.9575	S1.N
25.	9-octadecenoic acid	$[C_{18}H_{34}O_2 + H]^+$	283.2637	Figure 3L
26.	*cis*-13-eicosenoic acid	$[C_{20}H_{38}O_2 + H]^+$	311.2950	Figure 3M
27.	pentadecenoic acid	$[C_{15}H_{28}O + {}^{109}Ag]^+$	333.1187	Figure 3N
28.	methyl linoleate	$[C_{19}H_{34}O_2 + K]^+$	333.2196	S1.O
29.	*cis*-13-eicosenoic acid	$[C_{20}H_{38}O_2 + Na]^+$	333.2770	S1.P
30.	*N*-dodecyl-4-methyl-1-piperazine carboxamide	$[C_{18}H_{37}N_3O + Na]^+$	334.2834	Figure 3O
31.	tricosanoic acid	$[C_{23}H_{46}O_2{-}H_2O + H]^+$	337.3470	S1.R
32.	butyl octadecanoate	$[C_{22}H_{44}O_2 + Na]^+$	363.3239	Figure 3P
33.	tetracosanoic acid	$[C_{24}H_{48}O_2 + Na]^+$	391.3552	Figure 3R

[a] Putative identification. [b] $m/z_{\text{calc.}}$ − calculated monoisotopic m/z value.

These ions correspond to compounds secreted directly by sweat pores (KCl/NaCl and urea) that can be used to localize sweat pores as well as dorsal patterns.

Another group of compounds that were detected in the fingerprint were free fatty acids such as octanoic, dodecanoic, octadecenoic acid, eicosenoic, pentadecenoic, and tetracosanoic acids. Figure 3 presents ion images showing the spatial distribution of mentioned fatty acids with the following m/z values of 183.0787 (G), 183.1749 (H), 283.2637 (L), 311.2950 (M), 333.1187 (N), and 391.3552 (R), which are attributed to an octanoic acid−potassium adduct, protonated dodecanoic acid with water molecule loss, protonated 9-octadecenoic acid and protonated *cis*-13-eicosanoic acid, a pentadecenoic acid−silver-109 adduct, and a tetracosanoic acid−sodium adduct, respectively. The mentioned ions are presenting very clearly representations of fingerprint ridges. Free fatty acids were previously identified in a fingerprint using different analytical techniques such as MALDI or SALDI MS.[50]

■ CONCLUSIONS

A novel method for synthesis and application of monoisotopic silver-109 nanoparticles onto a studied surface for LDI MS and MSI is presented. The methodology was proven to be very useful for analysis and MS imaging of low-molecular-weight (LMW) compounds and polymers as well as for mass spectrometry imaging. LASiS with the use of 1064 nm pulsed nanosecond fiber laser on galvomotors allowed highly efficient synthesis of nanoparticles of extremely high chemical purity. LASiS of ^{109}AgNPs coupled with nebulization was used for surface-transfer mass spectrometry imaging of a fingerprint, allowing investigation of ridge patterns and sweat pores as well as determination of spatial distribution of compounds.

■ ASSOCIATED CONTENT

Supporting Information

The Supporting Information is available free of charge at https://pubs.acs.org/doi/10.1021/acsmeasuresciau.1c00020.

Ion images of fingerprint (PDF)

■ AUTHOR INFORMATION

Corresponding Author

Tomasz Ruman − *Rzeszów University of Technology, Faculty of Chemistry, Inorganic and Analytical Chemistry Department, 35-959 Rzeszów, Poland;* orcid.org/0000-0002-9899-8627; Phone: (+48 17) 865-1896; Email: tomruman@prz.edu.pl

Authors

Aneta Płaza − *Doctoral School of Engineering and Technical Sciences at the Rzeszów University of Technology, Rzeszów 35-959, Poland;* orcid.org/0000-0003-1719-8730

Artur Kołodziej − *Doctoral School of Engineering and Technical Sciences at the Rzeszów University of Technology,* *Rzeszów 35-959, Poland*; orcid.org/0000-0002-9222-0937

Joanna Nizioł – *Rzeszów University of Technology, Faculty of Chemistry, Inorganic and Analytical Chemistry Department, 35-959 Rzeszów, Poland*

Complete contact information is available at:
https://pubs.acs.org/10.1021/acsmeasuresciau.1c00020

Author Contributions

The manuscript was written through equal contributions of all authors. All authors have given approval to the final version of the manuscript.

Notes

The authors declare no competing financial interest.

■ ACKNOWLEDGMENTS

Mrs. Małgorzata Walczak is acknowledged for DLS measurements. Zuzanna Krupa is acknowledged for providing a fingerprint. This work was supported by the National Science Centre (NCN), SONATA grant no. UMO-2018/31/D/ST4/00109.

■ REFERENCES

(1) Tanaka, K.; Waki, H.; Ido, Y.; Akita, S.; Yoshida, Y.; Yoshida, T.; Matsuo, T. Protein and polymer analyses up to m/z 100,000 by laser ionization time-of-flight mass spectrometry. *Rapid Commun. Mass Spectrom.* **1988**, *2*, 151–153.

(2) Karas, M.; Hillenkamp, F. Laser Desorption Ionization of Proteins with Molecular Masses Exceeding 10 000 Da. *Anal. Chem.* **1988**, *60*, 2299–2301.

(3) Albrethsen, J. Reproducibility in protein profiling by MALDI-TOF mass spectrometry. *Clin. Chem.* **2007**, *53*, 852–858.

(4) Tost, J.; Gut, I. G. DNA analysis by mass spectrometry—past, present and future. *J. Mass Spectrom.* **2006**, *41*, 981–995.

(5) Estrada, R.; Yappert, M. C. Alternative approaches for the detection of various phospholipid classes by matrix-assisted laser desorption/ionization time-of-flight mass spectrometry. *J. Mass Spectrom.* **2004**, *39*, 412–422.

(6) Leopold, J.; Popkova, Y.; Engel, K. M.; Schiller, J. Recent developments of useful MALDI matrices for the mass spectrometric characterization of lipids. *Biomolecules* **2018**, *8* (4), 173.

(7) Kołodziej, A.; Ruman, T.; Nizioł, J. Gold and silver nanoparticles-based laser desorption/ionization mass spectrometry method for detection and quantification of carboxylic acids. *J. Mass Spectrom.* **2020**, *55*, e4604.

(8) Domon, B.; Aebersold, R. Mass spectrometry and protein analysis. *Science* **2006**, *312* (5771), 212–217.

(9) Berkenkamp, S.; Kirpekar, F.; Hillenkamp, F. Infrared MALDI mass spectrometry of large nucleic acids. *Science* **1998**, *281* (5374), 260–262.

(10) Shrivas, K.; Wu, H. F. Single drop microextraction as a concentrating probe for rapid screening of low molecular weight drugs from human urine in atmospheric-pressure matrix-assisted laser desorption/ionization mass spectrometry. *Rapid Commun. Mass Spectrom.* **2007**, *21*, 3103–3108.

(11) Ha, M. S.; Seo, H.; Bae, D. H.; Yeo, W. S. Detection of enrofloxacin and its metabolite ciprofloxacin using gold nanoparticles and laser desorption/ionization time-of-flight mass spectrometry. *Anal. Sci.* **2014**, *30* (4), 451–455.

(12) López de Laorden, C.; Beloqui, A.; Yate, L.; Calvo, J.; Puigivila, M.; Llop, J.; Reichardt, N. C. Nanostructured indium tin oxide slides for small-molecule profiling and imaging mass spectrometry of metabolites by surface-assisted laser desorption ionization MS. *Anal. Chem.* **2015**, *87* (1), 431–440.

(13) Chiang, C. K.; Chen, W. T.; Chang, H. T. Nanoparticle-based mass spectrometry for the analysis of biomolecules. *Chem. Soc. Rev.* **2011**, *40* (3), 1269–1281.

(14) Abdelhamid, H. N. Nanoparticle assisted laser desorption/ionization mass spectrometry for small molecule analytes. *Microchim. Acta* **2018**, *185*, 200.

(15) Chu, H. W.; Unnikrishnan, B.; Anand, A.; Mao, J. Y.; Huang, C. C. Nanoparticle-based laser desorption/ionization mass spectrometric analysis of drugs and metabolites. *J. Food Drug Anal.* **2018**, *26*, 1215–1228.

(16) Nizioł, J.; Rode, W.; Laskowska, B.; Ruman, T. Novel monoisotopic ^{109}AgNPET for laser desorption/ionization mass spectrometry. *Anal. Chem.* **2013**, *85*, 1926–1931.

(17) Sekuła, J.; Nizioł, J.; Rode, W.; Ruman, T. Gold nanoparticle-enhanced target (AuNPET) as universal solution for laser desorption/ionization mass spectrometry analysis and imaging of low molecular weight compounds. *Anal. Chim. Acta* **2015**, *875*, 61–72.

(18) Das, R. K.; Pachapur, V. L.; Lonappan, L.; Naghdi, M.; Pulicharla, R.; Maiti, S.; Cledon, M.; Dalila, L. M. A.; Sarma, S. J.; Brar, S. K. Biological synthesis of metallic nanoparticles: plants, animals and microbial aspects. *Nanotechnol. Environ. Eng.* **2017**, *2*, 18.

(19) Bayda, S.; Adeel, M.; Tuccinardi, T.; Cordani, M.; Rizzolio, F. The History of Nanoscience and Nanotechnology: From Chemical–Physical Applications to Nanomedicine. *Molecules* **2020**, *25*, 112.

(20) Magro, M.; Zaccarin, M.; Miotto, G.; Da Dalt, L.; Baratella, D.; Fariselli, P.; Gabai, G.; Vianello, F. Analysis of hard protein corona composition on selective iron oxide nanoparticles by MALDI-TOF mass spectrometry: identification and amplification of a hidden mastitis biomarker in milk proteome. *Anal. Bioanal. Chem.* **2018**, *410*, 2949–2959.

(21) Xu, L.; Wang, Y.-Y.; Huang, J.; Chen, C.-Y.; Wang, Z.-X.; Xie, H. Silver nanoparticles: Synthesis, medical applications and biosafety. *Theranostics* **2020**, *10*, 8996–9031.

(22) McLean, J. A.; Stumpo, K. A.; Russell, D. H. Size-selected (2–10 nm) gold nanoparticles for matrix assisted laser desorption/ionization of peptides. *J. Am. Chem. Soc.* **2005**, *127*, 5304–5305.

(23) Pilolli, R.; Palmisano, F.; Cioffi, N. Gold nanomaterials as a new tool for bioanalytical applications of laser desorption ionization mass spectrometry. *Anal. Bioanal. Chem.* **2012**, *402*, 601–623.

(24) Yonezawa, T.; Kawasaki, H.; Tarui, A.; Watanabe, T.; Arakawa, R.; Shimada, T.; Mafune, F. Detailed investigation on the possibility of nanoparticles of various metal elements for surface assisted laser desorption/ionization mass spectrometry. *Anal. Sci.* **2009**, *25*, 339–346.

(25) Amendola, V.; Litti, L.; Meneghetti, M. LDI-MS assisted by chemical-free gold nanoparticles: enhanced sensitivity and reduced background in the low-mass region. *Anal. Chem.* **2013**, *85*, 11747–11754.

(26) Rafique, M.; Rafique, M. S.; Kalsoom, U.; Afzal, A.; Butt, S. H.; Usman, A. Laser ablation synthesis of silver nanoparticles in water and dependence on laser nature. *Opt. Quantum Electron.* **2019**, *51*, 179.

(27) Sadrolhosseini, A. R.; Mahdi, M. A.; Alizadeh, F.; Rashid, S. A. Laser Ablation Technique for Synthesis of Metal Nanoparticle in Liquid. In *Laser Technology and its Applications*; Ma, Y., Ed.; IntechOpen, 2018; pp 63–81.

(28) Freeland, B.; McCann, R.; Alkan, G.; Friedrich, B.; Foley, G.; Brabazon, D. Stable nano-silver colloid production via Laser Ablation Synthesis in Solution (LASiS) under laminar recirculatory flow. *Advances in Materials and Processing Technologies* **2020**, *6*, 677–685.

(29) Amendola, V.; Polizzi, S.; Meneghetti, M. Free silver nanoparticles synthesized by laser ablation in organic solvents and their easy functionalization. *Langmuir* **2007**, *23*, 6766–6770.

(30) Sportelli, M. C.; Izzi, M.; Volpe, A.; Clemente, M.; Picca, R. A.; Ancona, A.; Lugarà, P. M.; Palazzo, G.; Cioffi, N. The Pros and Cons of the Use of Laser Ablation Synthesis for the Production of Silver Nano-Antimicrobials. *Antibiotics* **2018**, *7*, 67.

(31) Ruman, T.; Długopolska, K.; Jurkiewicz, A.; Rut, D.; Frączyk, T.; Ciesla, J.; Leś, A.; Szewczuk, Z.; Rode, W. Thiophosphorylation of

free amino acids and enzyme protein by thiophosphoramidate ions. *Bioorg. Chem.* **2010**, *38*, 74−80.

(32) Nizioł, J.; Ruman, T. Surface-transfer mass spectrometry imaging on monoisotopic silver nanoparticle enhanced target. *Anal. Chem.* **2013**, *85*, 12070−12076.

(33) Hua, L.; Chen, J.; Ge, L.; Tan, S. N. Silver nanoparticles as matrix for laser desorption/ionization mass spectrometry of peptides. *J. Nanopart. Res.* **2007**, *9*, 1133−1138.

(34) Sherrod, S. D.; Diaz, A. J.; Russell, W. K.; Cremer, P. S.; Russell, D. H. Silver Nanoparticles as Selective Ionization Probes for Analysis of Olefins by Mass Spectrometry. *Anal. Chem.* **2008**, *80*, 6796−6799.

(35) Jamkhande, P. G.; Ghule, N. W.; Bamer, A. H.; Kalaskar, M. G. Metal nanoparticles synthesis: An overview on methods of preparation, advantages and disadvantages, and applications. *J. Drug Delivery Sci. Technol.* **2019**, *53*, 101174.

(36) De Leersnyder, I.; Rijckaert, H.; De Gelder, L.; Van Driessche, I.; Vermeir, P. High Variability in Silver Particle Characteristics, Silver Concentrations, and Production Batches of Commercially Available Products Indicates the Need for a More Rigorous Approach. *Nanomaterials* **2020**, *10*, 1394.

(37) Desai, R.; Mankad, V.; Gupta, S.; Jha, P. Size Distribution of Silver Nanoparticles: UV-Visible Spectroscopic Assessment. *Nanosci. Nanotechnol. Lett.* **2012**, *4* (1), 30−34.

(38) Dufresne, M.; Thomas, A.; Breault-Turcot, J.; Masson, J.-F.; Chaurand, P. Silver-Assisted Laser Desorption Ionization for High Spatial Resolution Imaging Mass Spectrometry of Olefins from Thin Tissue Sections. *Anal. Chem.* **2013**, *85* (6), 3318−3324.

(39) Gustafsson, O. J. R.; Guinan, T. M.; Rudd, D.; Kobus, H.; Benkendorff, K.; Voelcker, N. H. Metabolite mapping by consecutive nanostructure and silver-assisted mass spectrometry imaging on tissue sections. *Rapid Commun. Mass Spectrom.* **2017**, *31* (12), 991−1000.

(40) Patterson, N. H.; Doonan, R. J.; Daskalopoulou, S. S.; Dufresne, M.; Lenglet, S.; Montecucco, F.; Thomas, A.; Chaurand, P. Three-dimensional imaging MS of lipids in atherosclerotic plaques: Open-source methods for reconstruction and analysis. *Proteomics* **2016**, *16*, 1642−1651.

(41) Patterson, N. H.; Yang, E.; Kranjec, E. A.; Chaurand, P. Co-registration and analysis of multiple imaging mass spectrometry datasets targeting different analytes. *Bioinformatics* **2019**, *35* (7), 1261−1262.

(42) Perdian, D. C.; Cha, S.; Oh, J.; Sakaguchi, D. S.; Yeung, E. S.; Lee, Y. J. In situ probing of cholesterol in astrocytes at the single-cell level using laser desorption ionization mass spectrometric imaging with colloidal silver. *Rapid Commun. Mass Spectrom.* **2010**, *24* (8), 1147−1154.

(43) Coffinier, Y.; Szunerits, S.; Drobecq, H.; Melnyk, O.; Boukherroub, R. Diamond nanowires for highly sensitive matrix-free mass spectrometry analysis of small molecules. *Nanoscale* **2012**, *4*, 231−238.

(44) Arendowski, A.; Nizioł, J.; Ruman, T. Silver-109-based laser desorption/ionization mass spectrometry method for detection and quantification of amino acids. *J. Mass Spectrom.* **2018**, *53*, 369−378.

(45) Dong, X.; Cheng, J.; Li, J.; Wang, Y. Graphene as a Novel Matrix for the Analysis of Small Molecules by MALDI-TOF MS. *Anal. Chem.* **2010**, *82*, 6208−6214.

(46) Bibi, A.; Ju, H. Quantum dots assisted laser desorption/ionization mass spectrometric detection of carbohydrates: qualitative and quantitative analysis. *J. Mass Spectrom.* **2016**, *51*, 291−297.

(47) Zhang, H.; Cha, S.; Yeung, E. S. Colloidal graphite-assisted laser desorption/ionization MS and MS(n) of small molecules. 2. Direct profiling and MS imaging of small metabolites from fruits. *Anal. Chem.* **2007**, *79* (17), 6575−84.

(48) Okuno, S.; Wada, Y.; Arakawa, R. Quantitative analysis of polypropyleneglycol mixtures by desorption/ionization on porous silicon mass spectrometry. *Int. J. Mass Spectrom.* **2005**, *241* (1), 43−48.

(49) Francese, S.; Bradshaw, R.; Ferguson, L. S.; Wolstenholme, R.; Clench, M. R.; Bleay, S. Beyond the ridge pattern: multi-informative analysis of latent fingermarks by MALDI mass spectrometry. *Analyst* **2013**, *138*, 4215−4228.

(50) Girod, A.; Ramotowski, R.; Weyermann, C. Composition of fingermark residue: A qualitative and quantitative review. *Forensic Sci. Int.* **2012**, *223* (1), 10−24.

Chemical Technology & Biotechnology, 2022, 61-69

LASER GENERATED GOLD NANOPARTICLES FOR MASS SPECTROMETRY OF LOW MOLECULAR WEIGHT COMPOUNDS

Aneta PŁAZA-ALTAMER[1*], Artur KOŁODZIEJ[1], Joanna NIZIOŁ[2] and Tomasz RUMAN[2]

[1] Doctoral School of Engineering and Technical Sciences at the Rzeszów University of Technology,
8 Powstańców Warszawy Ave., 35-959 Rzeszów, Poland

[2] Rzeszów University of Technology, Faculty of Chemistry, 6 Powstańców Warszawy Ave., 35-959 Rzeszów, Poland

[*]Corresponding author: a.plaza@prz.edu.pl, 178651310

Abstract: Preparation of gold nanoparticles (AuNPs) by pulsed fiber laser (PFL) laser generated nanomaterial (LGN) with the use of 2D galvo-scanner (2D GS) is described. The procedure of covering of custom-made stainless steel MALDI targets containing studied objects via nebulization is also presented. Examples of application of new method (PFL-2D GS LGN and nebulization) in laser desorption/ionization mass spectrometry (LDI MS) analyses are shown. These include tests with amino acids and also low molecular weight polymer.

Keywords: gold nanoparticles; laser generated nanomaterial; low molecular weight compounds; mass spectrometry; matrix-free laser desorption/ionization; surface-assisted desorption/ionization.

1. Introduction

The development of matrix assisted laser desorption/ionization in mass spectrometry (MALDI-MS) is attributed to Tanaka et. al [1]. Due to its soft ionization potential, MALDI is one of the most selective, sensitive and efficient mass spectrometry methods. This allows it to be widely used for the analysis of ionic high-molecular weight compounds such as peptides, proteins [2], synthetic polymers [3] or polysaccharides [4], but it is also possible to detect low molecular weight (LMW) compounds such as lipids [5,6]. However, a disadvantage of MALDI which prevents it from being used too frequently for the detection of LMW compounds (MW <1000 Da) is the need to use MALDI matrices, which are low molecular weight organic acids that generate a variety of matrix-bound ions during the desorption/ionization process. The suppression of the analyte peaks then occurs, which complicates the spectra and significantly hinders the analysis of the tested compounds [7–9].

In part, the problems outlined have been resolved by developing the surface ionization assisted mass spectrometry (SALDI) technique. SALDI uses target plates coated with various nanostructures [6,10,11]. The nanoparticles used simplify the mass spectrum by reducing spectral interferences. Sample preparation is also the much simpler step demanding only applying the sample to the target plate [12]. What is more, advantage of using nanoparticles (NPs) is the reduction of the "sweet-spot" effect and very good point-to-point reproducibility [11].

Nanoparticles can be made by chemical, physical or biological methods [13,14]. The most commonly used methods for obtaining nanoparticles for MS is chemical reduction [12,15,16]. However, this approach raises a number of problems. One of them is the chemical purity of the obtained suspension. The necessity to use substances for chemical reactions, such as metal precursors, reducing agents, stabilizers, and oxidized products, make them a source of reagent-related ions and generate numerous interfering signals [17–19]. Another way NPs can also be obtained by breaking up a larger structure, for example with a laser, which is classified as physical method [13,14]. The method of generating nanoparticles by means of a laser (LGN) has many advantages, owing to which the obtained NPs are successfully used in mass spectrometry [20–22]. LGN uses pulsed laser irradiation to ablate a target from a solid material immersed in a liquid, ejecting NPs from the plasma cloud into the surrounding solution. This method allows for the production of a nanoparticle suspension of relatively high chemical purity, due to the lack of necessity to use stabilizers and reducing agents required in the chemical reduction method [20,23–25].

The most popular method of laser mass spectrometry is MALDI, which uses low molecular weight organic matrices such as 2,5-dihydroxybenzoic acid (DHB), sinapic acid (SA) or α-cyano-4-hydroxycinnamic acid (CHCA). Unfortunately, the acidic nature of the matrix solutions can make the analysis of various compounds difficult. Moreover, MALDI is the most useful for ionic compounds, and due to numerous matrix signals in the *m/z* <1000 range, low mass accuracy, unreliable calibration and the "sweet spot" effect, it is rarely used for testing low-molecular compounds [26].

Most of above-mentioned MALDI problems may be solved by using metal nanoparticles, for example gold ones, as a desorption/ionization agents [6,12,27,28]. Since the publication of Russell's work on a method for obtaining controlled-size gold nanostructures, they have become increasingly used [29], which is confirmed by an extensive review of Abdelhamid and Wu [30]. So far, various techniques have been introduced to synthesize AuNP, including chemical, physical and biological. However, the most commonly used method is the chemical reduction, which requires two substances: a metal salt precursor and a reducing agent. In addition, almost all treatments also contain a stabilizer such as capping agent preventing NPs aggregation. The reaction involves the reduction of Au_3^+ to elemental gold by electron transfer under various conditions. Among the many gold precursors, we can distinguish chloroauric acid [31] or chloro(trimethylphosphite)gold(I) [12]. In turn, the role of the reducing agent is often assumed by sodium borohydride ($NaBH_4$), sodium citrate, hydrogen peroxide or ascorbic acid [13,32]. The type of the used precursor and reducer affects the properties and size of the AuNPs obtained [31].

Preparation and application of gold nanoparticles by chemical reduction method for laser mass spectrometry was presented by Tseng and Su [33]. Authors used $HAuCl_4$ as the metal precursor and sodium borohydride as the reducing agent. The obtained nanoparticles were used as templates in LDI MS for the detection of low molecular weight neutral carbohydrates such as glucose, ribose, maltose, and cellobiose. The mass spectra present mainly sodium and potassium adducts of the mentioned compounds. However, mass spectrum of mixture glucose, maltose and ribose shows a lot of interfering signals.

The above-mentioned problems were partly solved by Amendola and co-workers, who were the first to demonstrate a method for producing nanoparticles by laser ablation synthesis in solution (LASiS) and their applicability as a matrix for LDI MS [19]. Due to the simplicity of the method, the synthesis of nanoparticles with the use of laser ablation in a solution allows to save time while providing suspensions of relatively high chemical purity compared to chemical methods. The mass spectra with nanoparticles generated by the LASiS method have a low chemical background, which simplifies the analysis of the tested compounds. In addition, LASiS enables the production of NPs from a wide variety of metal alloys.

In last year publication, for the first time, 1064 nm pulsed fiber laser (PFL) with 2D galvanometer scanner (2D GS) is shown as a very good source of silver-109 nanoparticles [20]. This study describes a new method of production of chemically pure gold nanoparticles in suspension with an application method for covering of studied objects or surfaces. Laser generated gold nanoparticles are shown to be highly useful for LDI mass spectrometry. This work presents LDI MS results for test compounds such as amino acids and polymers.

2. Results and discussion

2.1. PFL 2D GS LGN of AuNPs

In this work, LGN has been used to obtain chemically pure gold nanoparticles. Nanoparticles were generated by pulsed 1064 nm fiber laser with galvoscanner head scanning of ablated surface. The experimental setup for the AuNPs preparation is shown in Fig. 1A. For fast synthesis of nanoparticles, high-frequency (60 kHz), high pulse energy (up to 1 mJ/pulse) laser was used. However, in order to avoid unwanted thermal effects such as melting, solvent boiling and oxidation of solvent and also of nanoparticles, two-dimensional (2D) galvo-scanner (GS) was used. Galvo-scanner head with f-theta lens attached to fiber laser allowed for precise and very fast shifting of focused laser beam on the surface of ablated gold plate.

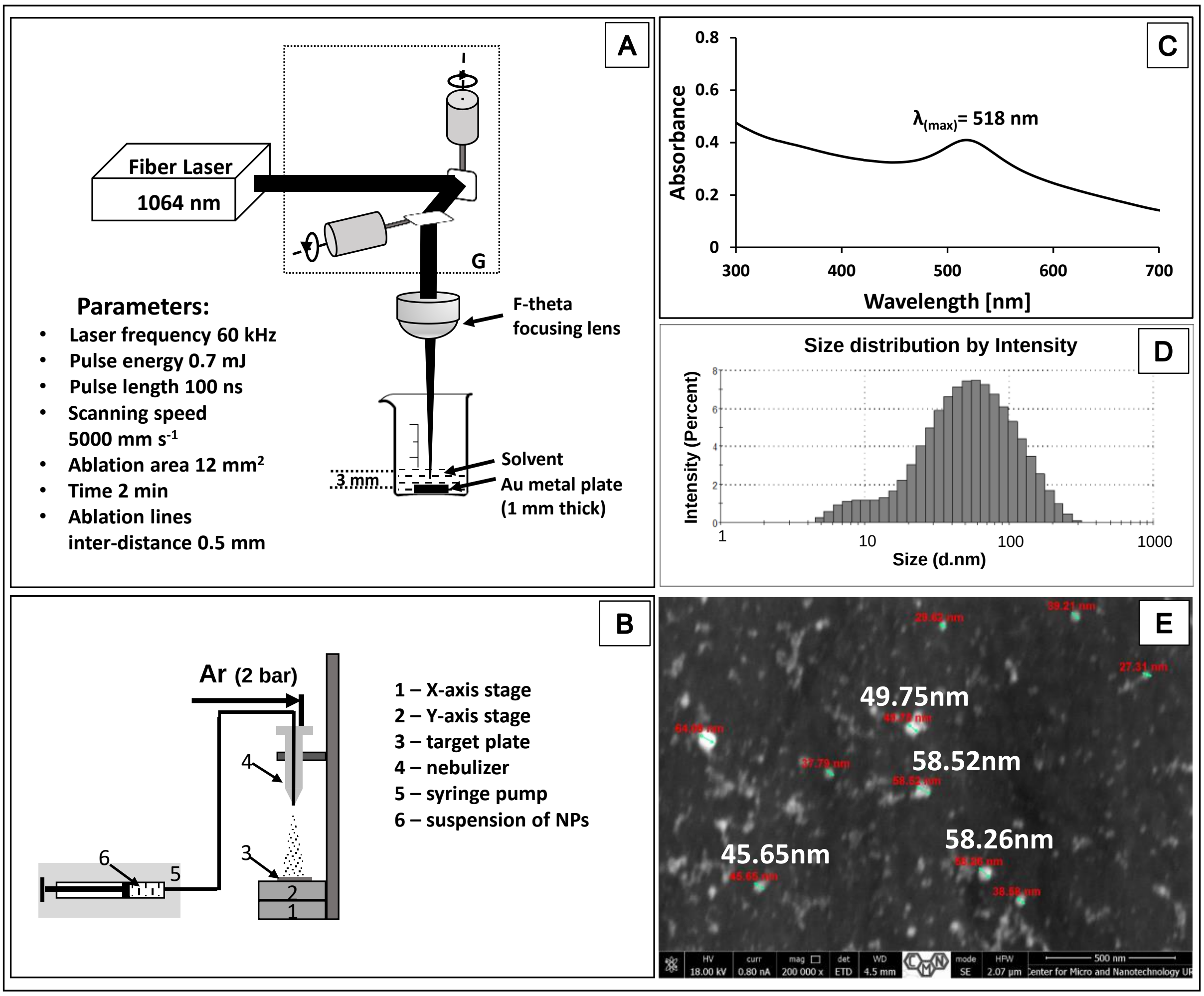

Fig 1. Laser ablation setup for the preparation of AuNPs (A); G – 2D galvanometer laser scanner. Down panel (B) presents setup for nebulization of nanoparticles. Panel C presents UV-VIS spectrum of AuNPs suspension in mixture solvents isopropanol and water (1:1 v/v). Panel D shows results of DLS measurement of Au nanoparticles hydrodynamic size distribution by intensity. E – High resolution SEM image of target modified with AuNPs generated by PFL 2D GS LGN.

First, the prepared nanoparticles were examined using UV-VIS spectroscopy, which allows determination of the size and shape of NPs. The vibrations of metallic electrons caused by particular wavelengths of light produce an effect known as surface plasmon resonance (SPR). It is related to the given size and shape of gold nanoparticles, as well as to their chemical environment. The literature describes that as the AuNPs diameter increases, the absorbance band shifts towards longer wavelengths and also widens [34]. The UV-VIS spectrum obtained for PFL 2D GS LGN AuNPs is presented in Fig. 1C. The UV-VIS spectrum of the post-reaction AuNP suspension recorded after 3 minutes of synthesis shows a local maximum at 518 nm, which suggests that the size of most nanoparticles is approx. 12 nm. However, an asymmetrical broadening of the SPR towards longer wavelengths, characteristic of the spheroidal particle fraction, can be observed. The presence of spheroids may indicate particle aggregation processes taking place in the suspension [34,35].

Figure 1D presents results of dynamic light scattering (DLS) measurement result of AuNPs size distribution by intensity after few minutes after preparation of suspension. DLS chart of the size distribution by intensity indicates the highest content of nanoparticles around 60 nm in diameter, with a distribution ranging from 5 to 120 nm. High resolution scanning electron microscope image of modified target (Fig. 1E) also confirms that individual nanoparticles are in roughly round/spherical shape and are of 37-64 nm size. A number of HRTEM and DLS results on size measurements of gold nanoparticles obtained with LGN present similarly size. DLS results suggest bigger nanoparticles as judged from UV-vis spectrum. Most probably, this is due the fact that the nanoparticle suspension used for the DLS measurement was prepared in a different solvent than the one optimized for LGN. Many studies show the effect of solvent on the size of nanoparticles obtained [34,35].

The use of nanoparticles in LDI MS requires an appropriate method of application to the surface containing the tested object. One of the approaches using AuNPs as a matrix is dry metal sputtering to obtain a homogeneous layer with minimal or no lateral migration of the analyte. However, this method requires an appropriate spraying system and is therefore rarely used [36]. For our LDI MS measurements, 0.5 μl of each of solution of alanine, arginine, histidine, lysine, methionine, phenylalanine, serine and tyrosine and PPG polymer was applied to a stainless-steel plate and air-dried. The plate with all test objects was placed on the table of the translation system as shown in Figure 1B. Aliquots of colloidal gold (1 mL) were sprayed three times onto the sample. Each portion was injected into the nebulizer at a constant rate of 250 μl/min. The entire nanoparticle nebulization process was controlled by a computer using a sequence of movements aimed at evenly covering the target plate. The LDI MS spectrum of AuNPs produced by PFL 2D GS LGN and deposited on the surface of stainless steel of target plate by nebulization is shown in Figure 2A. Mass spectrum made in 80-1500 *m/z* range contains virtually only gold ion peaks of Au^+ to Au_5^+ composition. Various amino acids as low molecular weight compounds were tested to verify the potential of ionization of organic compounds with the gold nanoparticles obtained with PFL 2D GS LGN.

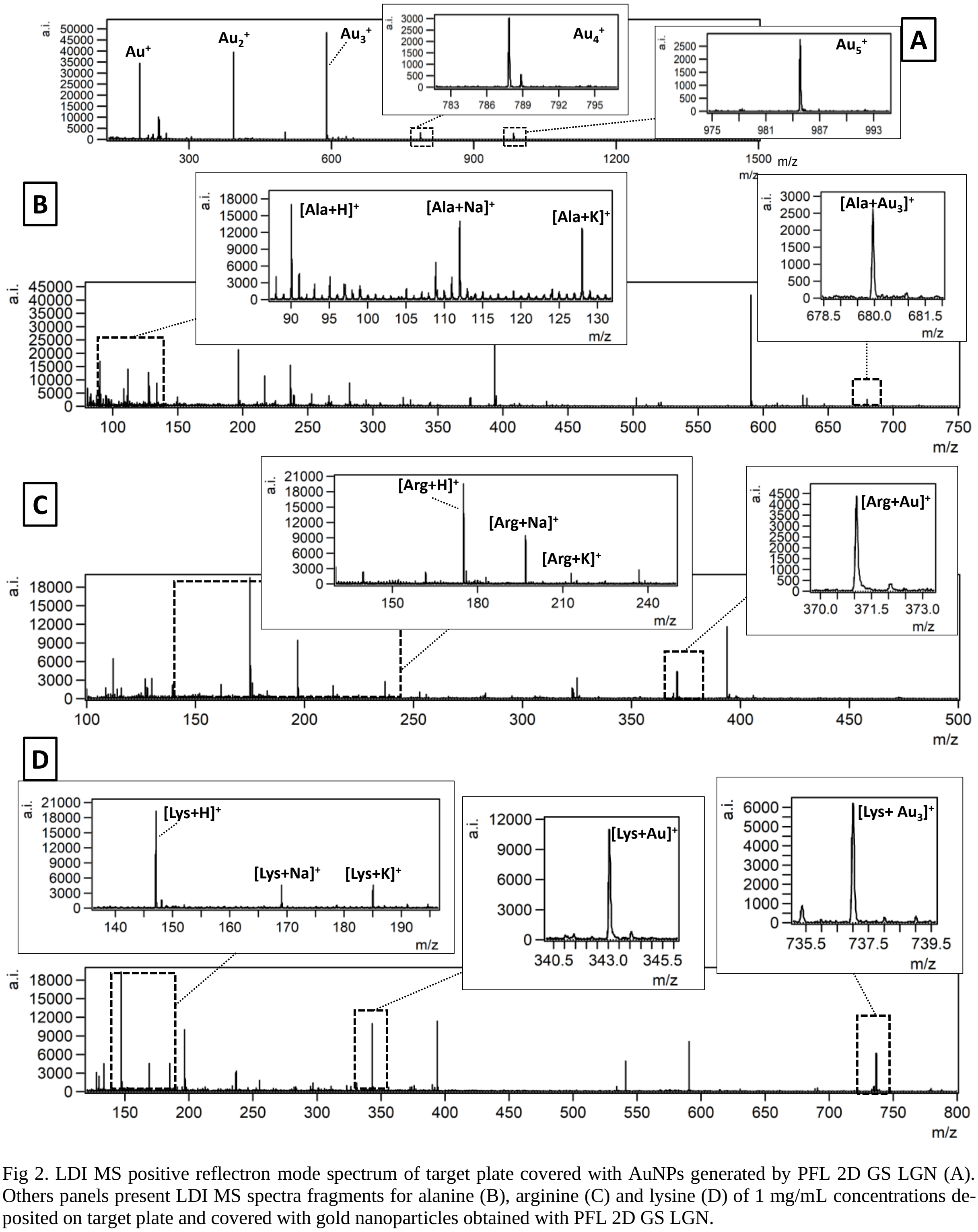

Fig 2. LDI MS positive reflectron mode spectrum of target plate covered with AuNPs generated by PFL 2D GS LGN (A). Others panels present LDI MS spectra fragments for alanine (B), arginine (C) and lysine (D) of 1 mg/mL concentrations deposited on target plate and covered with gold nanoparticles obtained with PFL 2D GS LGN.

The first analyzed compounds were alanine, arginine and lysine (Fig. 2). All listed compounds were found mainly as protonated adduct. Other adducts such as sodium, potassium as well as with Au^+ or Au_3^+ ions were also observed, but their intensities were significantly lower. For alanine (Fig. 2B), the highest S/N ratio equals 124 was observed for $[C_3H_7NO_2+H]^+$ adduct with *m/z* 90.0847. Ion of formula $[C_3H_7NO_2+Au_3]^+$ was also observed with signal intensity $2.5 \cdot 10^3$. Arginine (Fig. 2C), had the highest S/N ratio (294) for $[C_6H_{14}N_4O_2+H]^+$ adduct with *m/z* 175.1179. Lysine (Fig. 2D) was found on the mass spectrum in the form of five types of adducts: protonated, sodium and potassium as well as with Au^+ and Au_3^+ of which the protonated adduct had the highest signal intensity of $1.7 \cdot 10^5$. On the other hand, lysine-gold adduct with chemical formula $[C_6H_{14}N_2O_2 + Au]^+$ with *m/z* 343.0651 had signal intensity of $1.1 \cdot 10^4$ and also trigold adduct $[C_6H_{14}N_2O_2 + Au_3]^+$ with *m/z* 737.0090 was found with signal intensity $6.1 \cdot 10^3$.

Alanine was analyzed on ^{109}AgNPET target for LDI MS, presenting a spectrum with the higher intensity $1.2 \cdot 10^5$ for alanine-silver 109 adduct for concentration 50 ng per spot [37]. Nitta and coworkers detected arginine with the use of laser-based mass spectrometer at amount of 100 pmol with the use of PtNPs [38]. Lysine was analyzed on AuNPET target for LDI MS, presenting a spectrum with the intensity of $7.6 \cdot 10^4$ for protonated adduct for concentration 0.1 mg/mL. The mass spectrum also showed a gold adduct $[C_6H_{14}N_2O_2 + Au]^+$ with signal intensity of $3.0 \cdot 10^4$ [39].

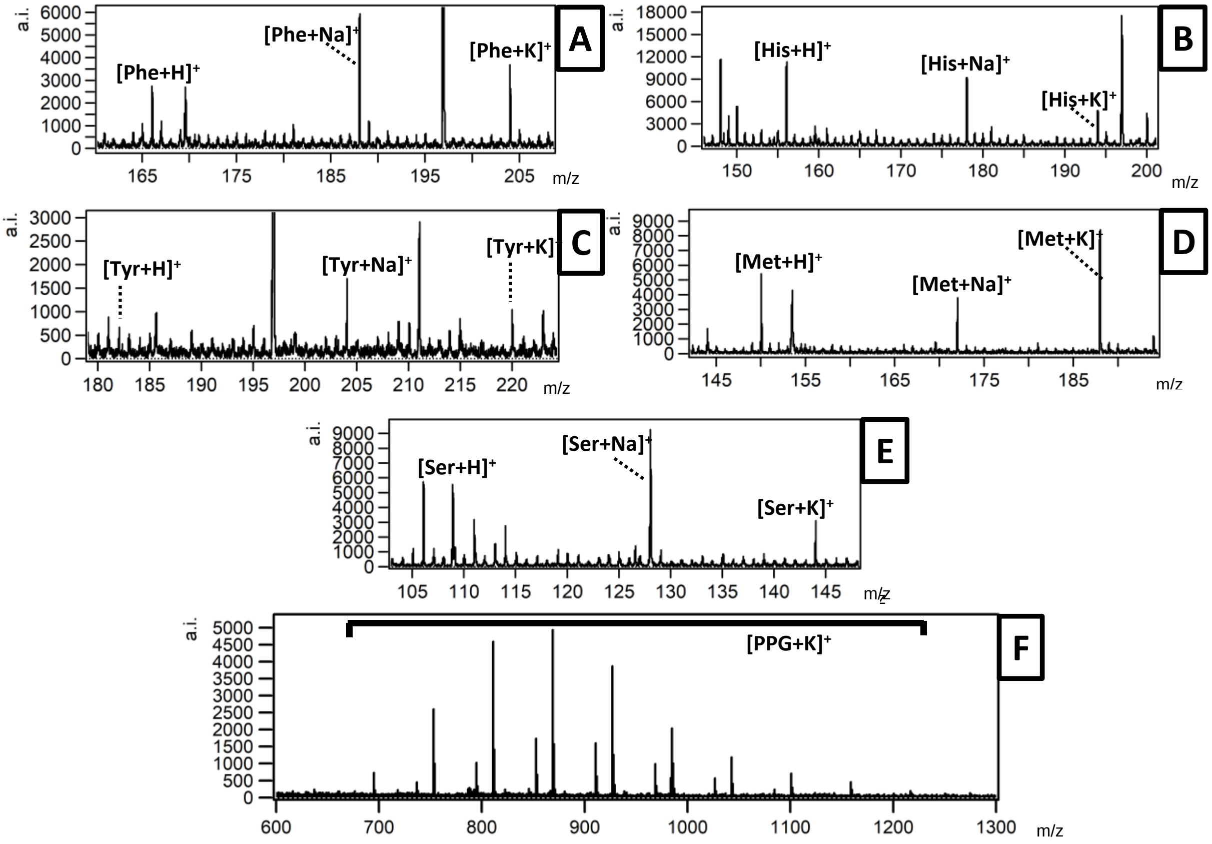

Fig 3. LDI MS positive reflectron mode mass spectra. Individual panels show fragment mass spectrum for A-phenylalanine, B-histidine, C-tyrosine, D-methionine, E-serine, respectively. The last panel (F) presents LDI MS spectrum of poly(propylene glycol) at 10.0 μg/mL concentration.

Figure 3 shows the fragments of the mass spectra obtained for phenylalanine, histidine, tyrosine, methionine, serine and poly(propylene glycol) using AuNPs LDI MS. No adducts of the tested compounds with gold ions were observed in any of the spectra in Fig. 3. For phenylalanine (Fig. 3A), tyrosine (Fig.3C) and serine (Fig. 3E) the highest signals were observed for $[C_9H_{11}NO_2{+}Na]^+$ adduct at *m/z* 188.0793 with signal intensity $4.5 \cdot 10^3$, $[C_9H_{11}NO_3{+}Na]^+$ adduct at *m/z* 204.0693 with signal intensity $1.0 \cdot 10^3$ and $[C_3H_7NO_3{+}Na]^+$ adduct at *m/z* 128.0789 with signal intensity $8.1 \cdot 10^3$. Sodium and potassium adducts were also present but with lower intensities. Histidine MS spectrum obtained with the use of PFL 2D GS LGN AuNPs is shown in Figure 3B. This compound was found mainly as protonated adduct $[C_6H_9N_3O_2 + H]^+$ with signal intensity of $8.9 \cdot 10^3$. On the other hand, on methionine (Fig. 3E) mass spectrum was dominated by potassium adduct $[C_5H_{11}NO_2S + K]^+$ at *m/z* 188.0242 with signal intensity $6.5 \cdot 10^3$.

Poly(propylene glycol) has repeating monomer unit of chemical formula $CH_2CH(CH_3)O$ with mass of approx. 57.9 Da. The LDI mass spectrum of PPG is shown in Fig. 3F. The spectrum show a typical polymer structure where the dominant mass is approximately at *m/z* 1000. For example, the highest polymer signal at *m/z* 869 revealed is the K^+ ion adduct of a PPG with 14 mer units. Shoji Okuno et al. compared the PPG spectra obtained with MALDI and SALDI. The authors identified a problem with the reproducibility of the MALDI mass spectra for PPG, which showed a strong dependence on the type of solvent and/or chemical matrix and the analyte/matrix ratio [40].

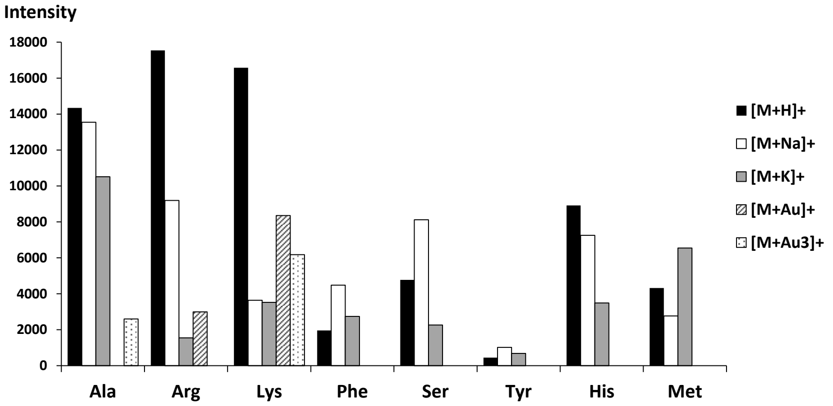

Fig 4. Signal intensity diagram for protonated, sodium, potassium, Au^+ and Au_3^+ adducts for individual amino acids.

Figure 4 contains bar chart of signal intensities for H^+, Na^+, K^+, Au^+ and Au_3^+ adducts for individual amino acids. Adducts with gold ions have been identified for only three amino acids: alanine, arginine and lysine. Proton, sodium and potassium adducts were detected on all mass spectra. For alanine, arginine, lysine and histidine, the proton adduct was the dominant adduct on the spectrum. On the other hand, the Na^+ adduct dominated in the LDI MS spectra of phenylalanine, serine and threonine.

2.2. Conclusions

Methods of synthesis and application of chemically pure monoisotopic gold nanoparticles onto studied surface for LDI MS was presented. Methodology was proven to be very useful for analysis of amino acids and also for characterization of low-mass polymers. Procedures shown are cost-effective, fast, efficient and instrument-limited.

3. Experimental

3.1. Materials

The gold foil (~ 1 mm thick) of 99.9% purity was bought from Polish Mint (Poland). Alanine, arginine, histidine, methionine, phenylalanine and serine were purchased from Sigma-Aldrich (99% purity). Lysine and tyrosine were purchased from Fluka Analytical Standards (98% purity). Poly(propylene glycol) (PPG, average Mn 1000 Da) was purchased from Sigma-Aldrich. All solvents were of HPLC grade, except for water (18 MΩ·cm water produced locally). Steel targets were machined from H17 (1.4016) stainless steel. Before the LDI MS experiments steel targets were cleaned through soaking in boiling solvents: toluene (3x100 mL, each plate for 30 s), chloroform (3x100 mL, each plate for 30 s), acetonitrile (3x100 mL, each plate for 30 s) and deionized water (3x100 mL, each plate for 30 s). Every plate was dried in high vacuum (ca. 0.01 mbar, 24h).

3.2. Methods

3.2.1 PFL 2D GS Laser Generated Nanomaterial (LGN) of gold nanoparticles

The experimental arrangement for the AuNPs preparation by laser ablation is shown in Fig.1A. The gold foil was placed at the bottom of a glass vessel containing mixture solvents isopropanol and water (1:1 v/v). The Au foil was covered by an approximately 3 mm thick layer of mixture solvents (total solvent volume was 4 mL). The laser ablation was carried out with a 1064 nm pulsed fiber laser (Raycus RFL-P20QE/A3). Suspension was obtained after 2 min. irradiation with pulse energy of 0.7 mJ (100 ns pulse length) at a 60 kHz repetition rate. Laser ablation was accomplished at a scanning speed of 5000 mm/s, the ablation area was 4x4 mm. Suspension was immediately transferred into a syringe and used in the nebulization step.

3.2.2 Nebulization of AuNPs suspension

The experimental setup for the nebulization of AuNPs suspension is shown in Fig.1B. The entire nanoparticle nebulization process was controlled by a computer. The H17 steel plate (laser mass spectrometry target plate) was placed on the table of a translation system consisting of a motorized XY table (EzM-42XL-A powered by closed-loop Ezi-SERVO motors). Glass syringe (1 mL) was filled with a previously prepared suspension of gold nanoparticles and placed in a syringe pump (pumping speed 250 μL/min). The custom-made software directed the 2D system table with 10 mm/s speed using a sequence of movement designed to uniformly cover a target plate. Nebulizer was obtained from Bruker Amazon ETD ESI ion source. Argon at a pressure of 2 bar was used as the nebulizing gas. Generally, all studied samples for MS were placed on the target plate before nebulization.

3.2.3 AuNPs characterization

AuNPs suspension was characterized by UV–VIS spectroscopy (Jasco V-670 spectrophotometer). Spectrum was registered in quartz cuvettes within 200–800 nm spectral range. The blank sample contained mixture solvents isopropanol and water (1:1 v/v). The suspension of AuNPs was also characterized by dynamic light scattering (DLS) using a Zetasizer-Nano ZS from Malvern Instruments. DLS measurements were performed by backscattering at a fixed detector angle of 173°. Isopropanol was used as dispersant.

3.2.4 LDI MS Experiments

Laser desorption/ionization – Time-of-Flight (LDI-ToF) mass spectrometry experiments were performed in reflectron mode using Bruker Autoflex Speed time-of-flight mass spectrometer equipped with a SmartBeam II laser (352 nm). Laser impulse energy was approx. 90-140 μJ, laser repetition rate 1000 Hz. The total number of laser shots was 4000 for each spot. This amount of laser shots was divided into four, symmetrically positioned points laying in distance of ca. 1/3 of spot radius from its center. At each point, 1000 laser shots were made with default random walk applied (random points with 50 laser shots). Measurement range was *m/z* 80-1500. Suppression was turned on typically for ions of *m/z* lower than 80. Reflector voltages used were 21 kV (the first) and 9.55 kV (the second). The data was calibrated and analyzed with FlexAnalysis (version 3.3) using centroid calibration model. Mass calibration (enhanced cubic calibration based on 7-8 calibration points) was performed using internal standards (gold ions Au^+ to Au_5^+).

3.2.5 LDI Sample Preparation

Solution (1 mg/mL) of each analyte was prepared by dissolving it in water (alanine, arginine, histidine, lysine, methionine, phenylalanine, serine and tyrosine). A solution of poly(propylene glycol) in isopropanol of 10 μg/mL concentration was prepared. A 0.5 μL volume of each of the final solution was applied to the steel target and air-dried followed by nebulization with AuNPs suspension.

3.2.6 High resolution scanning electron microscopy (HR SEM)

Target modified with AuNPs generated by PFL 2D GS method was inserted into the Helios Nanolab 650 electron microscope. Voltage was set at 10 and 30 kV, current was 0.2 nA. Images were made in nonimmersive mode.

Acknowledgements
Mrs. Małgorzata Walczak is acknowledged for DLS measurements. This work was supported by the National Science Centre (NCN), SONATA grant no. UMO-2018/31/D/ST4/00109.

References

[1] Tanaka, K., Waki, H., Ido, Y., Akita, S., Yoshida,Y., Yoshida, T., Matsuo, T., *Rapid Commun. Mass Spectrom.* 1988, 2, 151–153.
[2] Egelhofer, V., Gobom, J., Seitz, H., Giavalisco, P., Lehrach, H., Nordhoff, E., *Anal. Chem.* 2002, 74, 1760–1771.
[3] Montaudo, G., Samperi, F., Montaudo, M.S., *Prog. Polym. Sci.* 2006, 31, 277-357.
[4] Wang, J., Zhao, J., Nie, S., Xie, M., Li, S., *Food Hydrocolloids* 2022, 124, 107237.
[5] Leopold, J., Popkova, Y., Engel, K., Schiller, J., *Biomolecules* 2018, 8, 173.
[6] Kołodziej, A., Płaza-Altamer, A., Nizioł, J., Ruman, T., *Int. J. Mass Spectrom.* 2022, 474, 116816.
[7] Domon, B., *Science* 2006, 312, 212–217.
[8] Berkenkamp, S., *Science* 1998, 281, 260–262.
[9] Shrivas, K., Wu, H-F., *Rapid Commun. Mass Spectrom*. 2007, 21, 3103–3108.
[10] Kołodziej A, Ruman, T., Nizioł, J., *J Mass Spectrom.* 2020, 55, e4604.
[11] Abdelhamid, HN., *Microchim Acta* 2019, 186, 682.
[12] Chiang, C-K., Chen, W-T., Chang, H-T., *Chem. Soc. Rev.* 2011, 40, 1269–1281.
[13] Sekuła, J., Nizioł, J., Rode, W., Ruman, T., *Anal. Chim. Acta* 2015, 875, 61–72.
[14] Herizchi, R., Abbasi, E., Milani, M., Akbarzadeh, A., *Artif Cells Nanomed Biotechnol* 2016, 44, 596–602.
[15] Khan, A., Rashid, R., Murtaza, G., Zahra, A., *Trop. J. Pharm Res* 2014, 13, 1169.
[16] Magro, M., Zaccarin, M., Miotto, G., Da Dalt, L., Baratella, D., Fariselli, P., Gabai, G., Vianello, F., *Anal Bioanal Chem* 2018, 410, 2949–2959.
[17] Xu, L., Wang, Y-Y., Huang, J., Chen, C-Y., Wang, Z-X., Xie, H., *Theranostics* 2020, 10, 8996–9031.
[18] McLean, JA., Stumpo, KA., Russell, DH., *J. Am. Chem. Soc.* 2005, 127, 5304–5305.
[19] Pilolli, R., Palmisano, F., Cioffi, N., *Anal Bioanal Chem* 2012, 402, 601–623.
[20] Amendola, V., Litti, L., Meneghetti, M., *Anal. Chem.* 2013, 85, 11747–11754.
[21] Płaza, A., Kołodziej, A., Nizioł, J., Ruman, T., *ACS Meas. Au* 2022, 2, 1, 14-22.
[22] Płaza-Altamer, A., Kołodziej, A., Nizioł, J., Ruman, T., *J Mass Spectrom* 2022;57 (3): .
[23] Rafique, M., Rafique, MS., Kalsoom, U., Afzal, A., Butt, SH., Usman, A., *Opt Quant Electron* 2019, 51, 179.
[24] Zulfajri, M., Huang, W-J., Huang, G-G., Chen, H-F., *Materials* 2021, 14, 11, 2937.
[25] Amendola, V., Meneghetti, M., *Phys. Chem. Chem. Phys.* 2009, 11, 3805.
[26] Ruman, T., Długopolska, K., Jurkiewicz, A., Rut, D., Frączyk, T., Cieśla, J., Leś, A., Szewczuk, Z., Rode, W., *Bioorg. Chem.* 2010, 38, 74–80.
[27] Arendowski, A., Ossoliński, K., Ossolińska, A., Ossoliński, T., Nizioł, J., Ruman, T., *Adv Med Sci* 2021, 66, 326–335.
[28] Arendowski, A., Ossoliński, K., Nizioł, J., Ruman, T., *Int. J. Mass Spectrom* 2020, 456, 116396.
[29] McLean, JA., Stumpo, KA., Russell, DH., *J. Am. Chem. Soc.* 2005, 127, 5304–5305.
[30] Abdelhamid, HN., Wu, H-F., *Anal Bioanal Chem* 2016, 408, 17, 4485–4502.
[31] Daruich De Souza, C., Ribeiro Nogueira, B., Rostelato, MECM., *J. Alloys Compd* 2019, 798, 714–740.
[32] Slepička, P., Slepičková Kasálková, N., Siegel, J., Kolská, Z., Švorčík, V., *Materials* 2019, 13, 1.
[33] Su, C-L., Tseng, W-L., *Anal. Chem.* 2007, 79, 4, 1626–1633.
[34] Haiss, W., Thanh, NTK., Aveyard, J., Fernig, DG., *Anal. Chem.* 2007, 79, 4215–4221.
[35] Amendola, V., Meneghetti, M., *J. Phys. Chem. C* 2009, 113, 11, 4277–4285.
[36] Dufresne, M., Thomas, A., Breault-Turcot, J., Masson, J-F., Chaurand, P., *Anal. Chem*. 2013, 85, 3318–3324.
[37] Arendowski, A., Nizioł, J., Ruman, T., *J. Mass Spectrom.* 2018, 53, 369–378.
[38] Nitta, S., Kawasaki, H., Suganuma, T., Shigeri, Y., Arakawa, R., *J. Phys. Chem. C* 2013, 117, 238–245.
[39] Arendowski, A., Ruman, T., *Anal. Methods* 2018, 10, 45, 5398–5405.
[40] Okuno, S., Wada, Y., Arakawa, R., *Int. J. Mass Spectrom* 2005, 241, 43–48.

Article received: September 2022
Article accepted: October 2022

International Journal of Mass Spectrometry 474 (2022) 116816

Contents lists available at ScienceDirect

International Journal of Mass Spectrometry

journal homepage: www.elsevier.com/locate/ijms

Infrared pulsed fiber laser-produced silver-109-nanoparticles for laser desorption/ionization mass spectrometry of carboxylic acids

Artur Kołodziej [a], [*], Aneta Płaza-Altamer [a], Joanna Nizioł [b], Tomasz Ruman [b]

[a] Doctoral School of Engineering and Technical Sciences at the Rzeszów University of Technology, 8 Powstańców Warszawy Ave., 35-959, Rzeszów, Poland
[b] Rzeszów University of Technology, Faculty of Chemistry, 6 Powstańców Warszawy Ave., 35-959, Rzeszów, Poland

ARTICLE INFO

Article history:
Received 15 October 2021
Received in revised form
31 January 2022
Accepted 8 February 2022
Available online xxx

Keywords:
Carboxylic acids
Fatty acids
Silver
Nanoparticles
Mass spectrometry imaging
Quantification

ABSTRACT

Application of monoisotopic cationic ^{109}Ag nanoparticles (^{109}AgNPs) obtained by PFL (pulsed fiber laser) 2D GS (galvo-scanner) LASiS (laser ablation synthesis in solution) for high resolution laser desorption/ionization mass spectrometry and mass spectrometry imaging of carboxylic acids is presented. Six acids, azelaic, 3-methylhippuric, linoleic, oleic, arachidic and erucic acid were used as test compounds for quantification with a MALDI-type mass spectrometer. Comparison of commonly made manual measurements with semi-automatic MSI was performed providing very interesting findings. Carboxylic acids were directly tested in 1 000 000-fold concentration change conditions ranging from 1 mg/mL to 1 ng/mL, which equates to 300 ng to 300 fg of carboxylic acid per measurement spot. Methods were also tested on samples of spiked human blood serum for quantification of carboxylic acids and verification of the influence of biological matrix on the measurement.

1. Introduction

One of the most utilized soft ionization methods was developed by Tanaka et al., in 1988: matrix assisted laser desorption ionization mass spectrometry (MALDI-MS) [1]. This method is widely used in proteomics for protein analysis [2], in microbiology [3] for the identification of microorganisms and in pharmacy for the analysis of anticancer drugs [4]. Although it has many advantages such as high sensitivity and efficiency, the MALDI method is rarely used for the detection and quantification of low molecular weight compounds. The main problem is the necessity to use organic matrices, which include acids of low molecular weight, and during the analysis they produce various types of ions that interfere with the signals of the analyzed sample in the range of low masses [5]. This problem can be avoided by using nanoparticles instead of traditional matrices. Many published articles showing the use of nanoparticles in LMW analysis confirm their usefulness [6–9].

Monoisotopic nanoparticles of silver-109 were used to analyze various types of compounds, including amino acids, fatty acids, sugars or mycotoxins [10–13], where they have proved to be very effective in cationization. In this publication we present quantification result of carboxylic acids (including fatty acids) with chemically pure silver-109 nanoparticles produced by a 1064 nm pulsed fiber laser with 2D galvanometer scanner.

Significant advantage of nanoparticles-based method compared to MALDI is the replacement of organic matrix. This allows easy sample preparation, low chemical background, easier data analysis and fast data collection [6]. Silver nanoparticles provides unique advantages such as providing the possibility of internal calibration due to silver-related ion peaks and producing highly reproducible signals. Additionally, antibacterial and antifungal properties of silver nanoparticles help with the preservation of analyzed sample [14]. What is more, silver-109 nanoparticles (^{109}AgNPs) have a number of additional advantages: (i) simple isotopic pattern; (ii) higher intensity of analyte signal, (iii) higher detection sensitivity, (iv) much better compatibility with the analysis of complex mixtures, such as biological samples [13]. Chemically pure ^{109}AgNPs are of critical importance for mass spectrometry. They can be produced by pulsed fiber laser (PFL) 2D GS (galvo-scanner) laser ablation synthesis in solution (LASiS) that generates nanoparticle suspensions of a relatively high chemical purity compared to chemical methods as stabilizer- and reducing-agent-free NPs are obtained [15].

In this work we compare manual nanoparticle-based laser desorption/ionization mass spectrometry (LDI MS) and semi-

---

[*] Corresponding author.
E-mail address: a.kolodziej@prz.edu.pl (A. Kołodziej).

https://doi.org/10.1016/j.ijms.2022.116816
1387-3806/

automatically-performed mass spectrometry imaging (MSI) in quantification of carboxylic acids along with discussion of results and comparison with various matrix-assisted laser desorption/ionization (MALDI) and high-performance liquid chromatography coupled with mass spectrometry (HPLC-MS) methods previously used in carboxylic acids analysis.

2. Materials and methods

2.1. Materials

All carboxylic acid standards were purchased from Sigma-Aldrich. Steel targets were machined from H17 stainless steel (1.4016 steel). Before the LDI MS and MS imaging experiments steel targets were cleaned through soaking in boiling solvents: toluene (3 × 100 ml, each plate for 30 s), chloroform (3 × 100 ml, each plate for 30 s), acetonitrile (3 × 100 ml, each plate for 30 s) and deionized water (3 × 100 ml, each plate for 30 s). Every plate was dried in high vacuum (ca. 0.01 mbar, 24 h). All solvents were of HPLC quality, except for water (18 MΩ cm water produced locally).

2.2. Pulsed fiber laser 2-axis galvanometer scanner (PFL 2D GS) LASiS of silver-109 nanoparticles

The silver-109 foil (~1 mm thick, 99.7%+ isotopic purity) was bought from Trace Sciences International (USA) was placed at the bottom of a glass vessel containing solvent (acetonitrile). The ^{109}Ag foil was covered by an approximately 3 mm thick layer of acetonitrile (total solvent volume was 3 mL). The laser ablation was carried out with a 1064 nm pulsed fiber laser (Raycus RFL-P20QE/A3). Suspension was obtained after 2 min Irradiation with pulse energy of 0.8 mJ (100 ns pulse length) at a 40 kHz repetition rate. Laser ablation was accomplished at a scanning speed of 2000 mm/s, the ablation area was 4 × 4 mm [15]. Suspension was immediately transferred into a syringe and used in the nebulization step.

2.3. Sample preparation and handling

All carboxylic acids standards (azelaic, 3-methylhippuric, linoleic, oleic, arachidic and erucic acids) were dissolved in water to give a final concentration of 1 mg/mL. Lower concentrations were prepared by diluting of ten-times higher concentration ones. Volume of 1 μL of blood plasma was dissolved in 249 μL of ultrapure water, then 250 μL of 100 μg/mL acid solution were added. Volumes of 0.3 μL of carboxylic acid and blood plasma spiked with carboxylic acid solutions were placed directly on the target plate, air dried, and then the target was nebulized with ^{109}AgNPs suspension, as stated in section 2.4.

2.4. Nebulization of ^{109}AgNPs suspension

The entire nanoparticle nebulization process was controlled by a computer. The H17 steel plate (laser mass spectrometry target plate) was placed on the table of a translation system consisting of a motorized XY table (powered by closed-loop servomotors). Glass syringe (1 mL) was filled with a previously prepared suspension of silver-109 nanoparticles and placed in a syringe pump (pumping speed 250 μL/min). The custom-made software directed the 2D system table with 10 mm/s translation speed using a sequence of movements prepared to uniformly cover a target plate. Nebulizer was a standard flow Bruker ion source ‘needle’ or nebulizer. Argon at a pressure of 2 bar was used as the nebulizing gas.

2.5. LDI mass spectrometry

LDI-ToF mass spectrometry experiments were performed in reflectron mode using a Bruker Autoflex Speed time-of-flight mass spectrometer equipped with a SmartBeam II laser (355 nm). Laser impulse energy was approx. 90–140 μJ, laser repetition rate was 1000 Hz. The total number of laser shots was 4000 for each spot. These laser shots were divided into four, symmetrically positioned points laying in distance of *ca.* 1/3 of spot radius from its center. At each point, 1000 laser shots were made with default random walk applied (random points with 50 laser shots). The measurement range of interest was *m/z* 80–1500. Suppression was turned on typically for ions of *m/z* lower than 80. Reflector voltages used were 21 kV (first) and 9.55 kV (second). The data was calibrated and analyzed with FlexAnalysis (version 3.3) using centroid calibration model. Mass calibration (enhanced cubic calibration based on 8–9 calibration points) was performed using internal standards (silver-109 ions and clusters from $^{109}\mathrm{Ag}^{+}$ to $^{109}\mathrm{Ag}_9^{+}$).

2.6. LDI mass spectrometry imaging

Measurements were performed using a Bruker Autoflex Speed time-of-flight mass spectrometer in reflectron positive mode. The apparatus was equipped with a SmartBeam II 1000 Hz 355 nm laser. Laser impulse energy was approximately 100–120 μJ, laser repetition rate was 1000 Hz, and deflection was set on *m/z* lower than 80 Da. The *m/z* range was 80–1500 and spatial resolution 500 × 500 μm. The imaging experiments were made with 2000 laser shots per individual spot with a default random walk applied (FlexImaging 4.0). All spectra were pre-calibrated (cubic calibration function) with the use of silver-109 ions ($^{109}\mathrm{Ag}^{+}$ to $^{109}\mathrm{Ag}_9^{+}$) as internal standard. The first accelerating voltage was held at 19 kV, and the second ion source voltage was held at 16.7 kV. Reflector voltages used were 21 kV (first) and 9.55 kV (second). All of the shown imaging pictures are for ±0.05% *m/z* window. MSI experiments were performed on all spots of carboxylic acid standards and blood plasma solution.

3. Results and discussion

Synthesis, properties and application of silver-109 nanoparticles obtained in PFL 2D GS LASiS method were shown in our recent publication [15]. In that article, advantages of laser-assisted generation of nanoparticles over chemical synthesis were presented. There are many literature positions proving that silver nanoparticles are very efficient in ionization of compounds allowing detection of various low molecular weight compounds also in complex biological mixtures e.g. blood plasma or urine samples [8,13,16–18].

We selected various carboxylic acids important for human metabolism or that may contribute to various diseases. Azelaic acid has anti-inflammatory, antibacterial and anti-keratizing actions. Due to these properties, azelaic acid is used in acne treatment [19]. 3-Methylhippuric acid is one of main metabolite of toluene and xylene, and can be used as indicator of exposure to these neurotoxic compounds [20,21]. Linoleic and oleic acids may induce apoptosis of human lymphocytes, on the other hand both of these acids are angiogenesis initiators [22,23]. Arachidic acid was used in preparation of anticancer drug delivery nanoparticles, erucic acid can be accumulated in human organism which can lead to some heart disorder e.g. myocardial lipidosis that cause decrease in the contractile performance of heart muscles [24,25].

3.1. Quantification results

Standards of all listed acids were directly measured in concentrations ranging from 1 mg/mL to 1 ng/mL which equates to 1 000 000-fold concentration change. Limit of detection (LOD) values were calculated with the use of signal/noise (S/N) value of 3 for lowest concentration samples. Every sample was placed on target plate in 0.3 μL volume equating to 0.3 μg to 0.3 pg of acid per measurement spot which is approx. 159 pmol to 1.59 fmol respectively calculated for example for azelaic acid molar mass. Shot-to-shot and spot-to-spot analyses were conducted for three exemplary carboxylic acids. Result of this analysis is presented in Supporting file (S1). This analysis proves high reproducibility of the results, for the shot-to-shot analysis, the spread of the results around the mean value was 11, 10 and 10% for 3-methylhippuric, oleic and arachidic acids respectively. For spot-to-spot analysis, spread of the results was 17, 27 and 10% for 3-methylhippuric, oleic and arachidic acids respectively. LOD and lower limits of quantification (LLOQ) values were calculated for manual LDI MS experiment and semi-automatic MSI and they are presented in Table 1.

For 3-methylhippuric acid, mass spectrometry imaging allowed to obtain lower limit of detection value than manual LDI MS. For the remaining analyzed carboxylic acids, due to the very high values of the standard deviation, it is difficult to clearly show which method allows to obtain better results. It is worth noting that application of LASiS silver-109 nanoparticles allowed to obtain 3 to 5 times lower LOD and LLOQ values for studied acids compared to previously described ^{109}AgNPET method that employs chemically produced nanoparticles [12].

Fig. 1 presents results LDI MS and MSI analyses for azelaic acid with ^{109}AgNPs PFL 2D GS laser generated nanomaterial. Manual measurements were performed at four random locations inside sample spot for each analyzed acid, the measurement scheme is presented in Fig. 1A. Azelaic acid was found in spectra mainly as silver-109 adduct of $[M+^{109}Ag]^+$ formula in amounts of 300 ng to 300 fg per sample spot. Intensities of azelaic acid-silver-109 adduct peaks were of $1.53{\cdot}10^5$ for the highest concentration, $5.18{\cdot}10^4$ for 100 μg/mL, $1.5{\cdot}10^4$ for 10 μg/mL, $5.32{\cdot}10^3$ for 1 μg/mL, $1.64{\cdot}10^3$ for 100 ng/mL, $1.2{\cdot}10^3$ for 10 ng/mL and 850 for 1 ng/mL. All of data is presented in as logInt (intensity) *vs* logc (concentration) plot (Fig. 1B). Regression analysis results of collected data is presented in Fig. 2B chart. Within this work, a preliminary calculations were conducted by fitting different trendline functions (polynomial, power, linear) to experimental data. Polynomial trendline was selected as best fitting and therefore applied to all studied compounds. For azelaic acid, results were obtained in the widest concentration range with a very good fit of trendline, the R^2 value is 0.993 for trendline.

After manual LDI MS measurement of sample the same spots with carboxylic acids were analyzed by semi-automatic MSI method. Fig. 1C presents scheme of semi-automatic MSI method which was used in the measurement of all carboxylic acids. Fig. 1D shows results of this analysis. During this measurement whole sample spot is covered by a grid of measurement points with specified resolution. Similarly, to LDI MS polynomial trendline gives very good fit (R^2 0.982). In Fig. 1D ion images of sample distribution proves that the sample is distributed non-homogeneously on the plate.

Limit of detection based on S/N ratio of 3 was found to be 434 pg (3.23 pmol) of azelaic acid per measured spot for LDI MS. In contrast, LOD for MSI was found to be 754 pg (5.62 pmol) per measured spot.

Literature provides information on LOD value for LDI MS method for this carboxylic acid that was provided by our team in previous publication. The LOD value was 31.4 μM [12], which is approx. 3-Times higher than LOD value obtained by using LASiS method. However, Garelnabi et al. presented results of GC analysis of azelaic acid with LOD value of 1 nM and LLOQ value 50 nM [26].

The next analyzed acid was 3-methylhippuric acid (3-MHA). Fig. 2A and C presents results of LDI MS and MSI analyses for this carboxylic acid with PFL 2D GS LASiS-produced ^{109}AgNPs. Similarly, as azelaic acid, measurements of 3-MHA were taken at four random locations, which is presented in Fig. 1A. 3-MHA was found in spectra mainly as silver-109 adduct of $[M+^{109}Ag]^+$ ion formula in 1 mg/mL to 1 μg/mL concentration samples. Intensities for 3-MHA were $1.9{\cdot}10^5$ for 1 mg/mL, $1.32{\cdot}10^5$ for 100 μg/mL, $2.57{\cdot}10^4$ for 10 μg/mL and $8.76{\cdot}10^3$ for 1 μg/mL. Similarly to azelaic acid analysis, charts with trendline are shown in Fig. 2A and C. The best fit for both analyses is polynomial trendline with R^2 value 0.977 and 0.967 for LDI MS and MSI respectively.

LOD value for 3-methylhippuric acid was found to be 215 pg (1.14 pmol) per spot for LDI MS and 190 pg (1.01 pmol) per measurement spot for MSI. In our publication LOD value was found 7.4 μM [12] which is over 2-times higher than LOD during this analysis. Hollow-fiber liquid-phase microextraction method provided LOD value of 2 μg/mL [27]. However, Behbahani et al. used high performance liquid chromatography with ultraviolet detector (HPLC-UV) method that provided better results (LOD = 0.2 ng/mL), but do not allows compound identification by *m/z* ratio [20].

Fig. 2B and D presents results of quantification by LDI MS and MSI for linoleic acid with ^{109}AgNPs produced by PFL 2D GS LASiS. This acid was found in spectra mainly as a silver-109 adduct of $[M+^{109}Ag]^+$ ion formula at *m/z* 389.1444. Plots of log intensity vs. log concentration (Fig. 2B) for polynomial trendline gave R-square value of 0.997. On the other hand, application of MSI allowed to obtain fit of R^2 being equal to 0.993. Limit of detection was found to be 237 pg (1.23 pmol) of linoleic acid per measured spot. MALDI-

Table 1
Limits of detection and lower limit of quantification for studied carboxylic acids.

Carboxylic acid	Manual LDI MS		Semi-automatic MSI	
	LOD[a] (ng/ml) μM	LLOQ[b] (ng/ml)	LOD[a] (ng/ml) μM	LLOQ[b](ng/ml)
Azelaic acid	1445 ± 1682 11	3211 ± 2803	2513 ± 2907 19	5585 ± 4846
3-Methylhippuric acid	716 ± 474 3.8	1590 ± 790	633 ± 194 3.3	1407 ± 324
Linoleic acid	791 ± 1122 4.1	1757 ± 1869	1075 ± 1647 5.5	2390 ± 2745
Oleic acid	201 ± 283 0.78	448 ± 472	317 ± 440 1.2	705 ± 734
Arachidic acid	1110 ± 415 3.9	2468 ± 692	2835 ± 1613 10	6299 ± 2689
Erucic acid	269 ± 386 0.94	598 ± 643	547 ± 775 1.9	1216 ± 1292

[a] Based-on S/N ratio of 3.
[b] Based on S/N ratio of 5; LLOQ – lower limit of quantification.

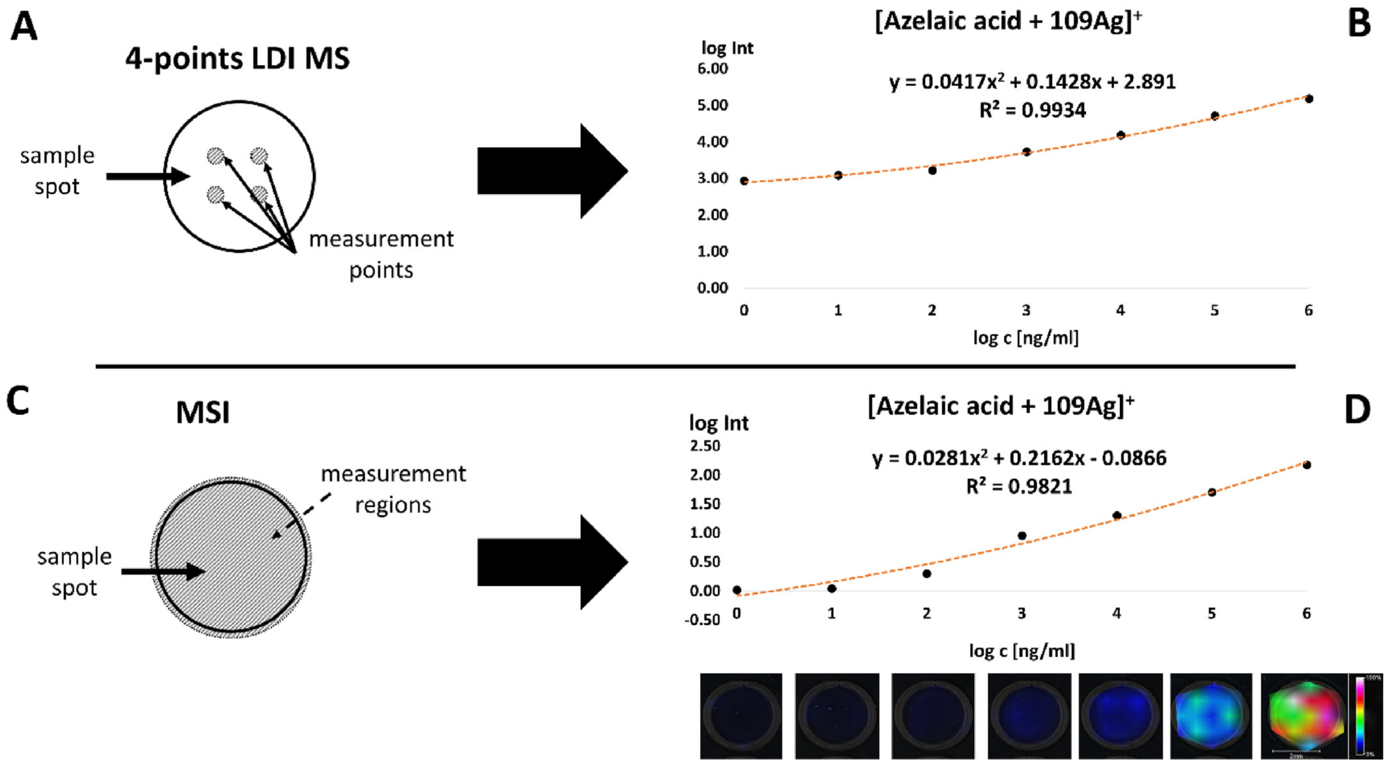

Fig. 1. Panel A shows the scheme of manual LDI MS measurement with 4 random measurement points. Panel C presents scheme of semi-automatic MSI measurements. Graphs B and D present results of quantification based on silver-109 adduct of azelaic acid signal for different concentrations obtained in LDI MS and MSI experiments. Both panels (B, D) contain the equation and the R^2 value for polynomial trendline. Panel D also contain $[\text{azelaic acid}+^{109}\text{Ag}]^+$ ion images for each concentration.

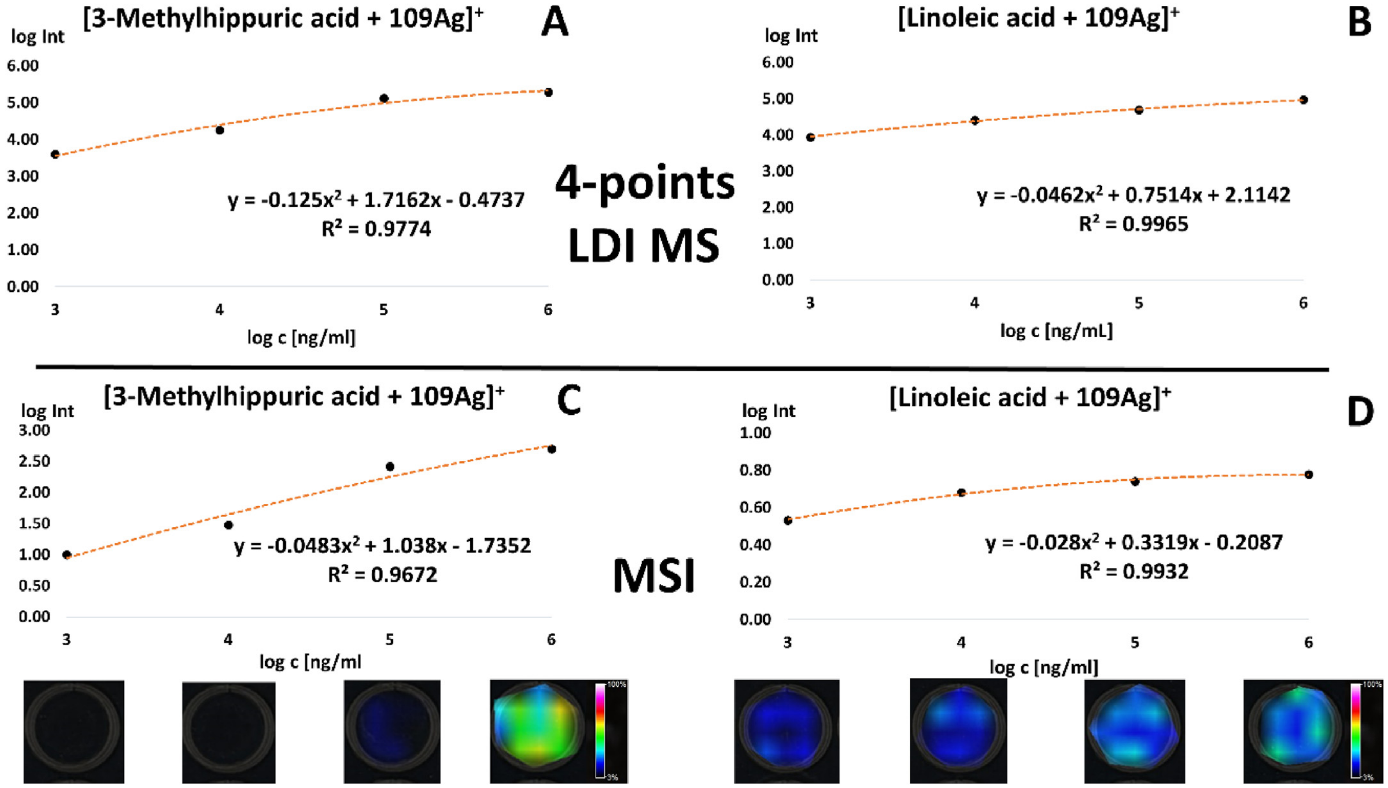

Fig. 2. Column charts A and C present results of quantification based on silver-109 adduct of 3-methylhippuric acid signal for different concentrations obtained in LDI MS and MSI experiments. Charts B and D present the same results for linoleic acid. All charts show decimal logarithm of intensity value *vs* decimal logarithm of concentration of acids. All panels contain the equation and the R^2 value for polynomial trendline. Panels C and D also contain $[\text{3-methylhippuric acid}+^{109}\text{Ag}]^+$ and $[\text{linoleic acid}+^{109}\text{Ag}]^+$ ions images for each concentration.

FTICR MS (matrix-assisted laser/desorption ionization-Fourier transform ion cyclotron resonance mass spectrometry) method provides LOD value of 1.9 μM and high-performance liquid chromatography coupled with charged aerosol detector (HPLC-CAD) and ion trap/time of flight mass spectrometry (MS-IT-TOF) provided limit of detection value 1.1 ng/mL [28,29]. Again, ion images proved nonuniform compound localization that is the reason of much better MSI results compared to manual measurements.

Fig. 3A and C shows the results of oleic acid analysis. As with previously tested acids, it was analyzed in two measurement modes: manual LDI MS and semi-automatic MSI. The measurement method is shown in Fig. 1A and C. Oleic acid was found in spectra mainly as silver-109 adduct of $[M+^{109}Ag]^+$ at *m/z* value of 391.1601. The results of manual measurements for this acid are shown in the graph in Fig. 3A. Signals were found for five concentrations with intensities $1.88\cdot 10^5$ for 1 mg/mL, $1.68\cdot 10^5$ for 100 μg/mL, $9.33\cdot 10^4$ for 10 μg/mL, $4.12\cdot 10^4$ for 1 μg/mL and $1.63\cdot 10^4$ for 100 ng/mL. Plot in Fig. 3C present results of semi-automatic MSI method. Polynomial trendline is the best fit for both LDI MS (R^2 value 0.997) and MSI (R^2 value 0.981) for this carboxylic acid. LOD was found to be 60 pg (0.24 pmol) of oleic acid per measured spot. Methods such as HPLC-CAD/MS-IT-TOF provided LOD as low as 0.014 μg/mL [29]. On the other hand, high performance liquid chromatography-evaporative light scattering detection method provide LOD value of 13.7 ng [31].

Next analyzed acid was arachidic acid, results is presented in Fig. 3B and D. Arachidic acid was found in spectra mainly as silver-109 adduct of $[M+^{109}Ag]^+$ at *m/z* value of 421.2070. The results of manual measurements for are shown in Fig. 4B. Signals were found for four concentrations with intensities of $1.36\cdot 10^5$ for 1 mg/mL, $6.05\cdot 10^4$ for 100 μg/mL, $7.38\cdot 10^3$ for 10 μg/mL and $9.32\cdot 10^2$ for 1 μg/mL. As in the previous analyses, polynomial trendline is best fitted for LDI MS (R^2 0.994). For MSI R^2 value of polynomial trendline

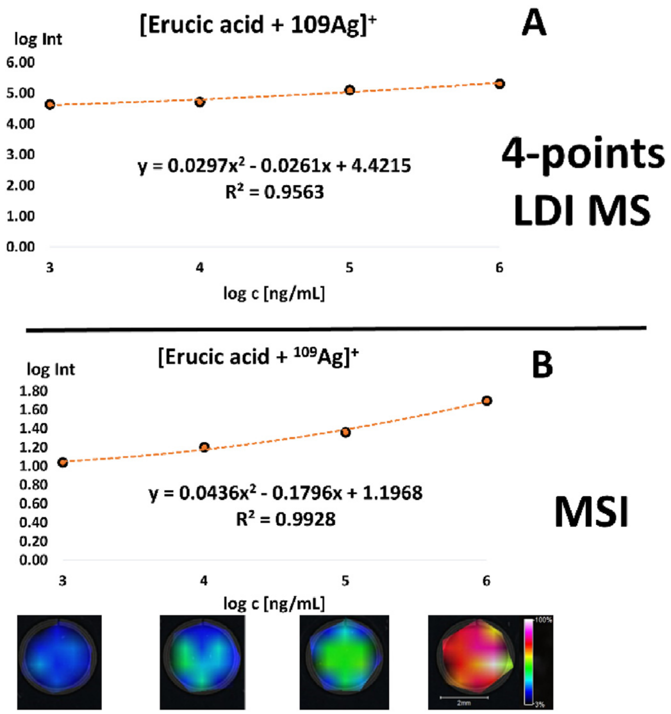

Fig. 4. Charts A and B present results of quantification based on silver-109 adduct signal of erucic acid for different concentrations obtained in LDI MS and MSI experiments. Both panels (A, B) contain the equation and the R^2 value for polynomial trendline. Panel B also contain ion $[\text{erucic acid}+^{109}Ag]^+$ images for each concentration.

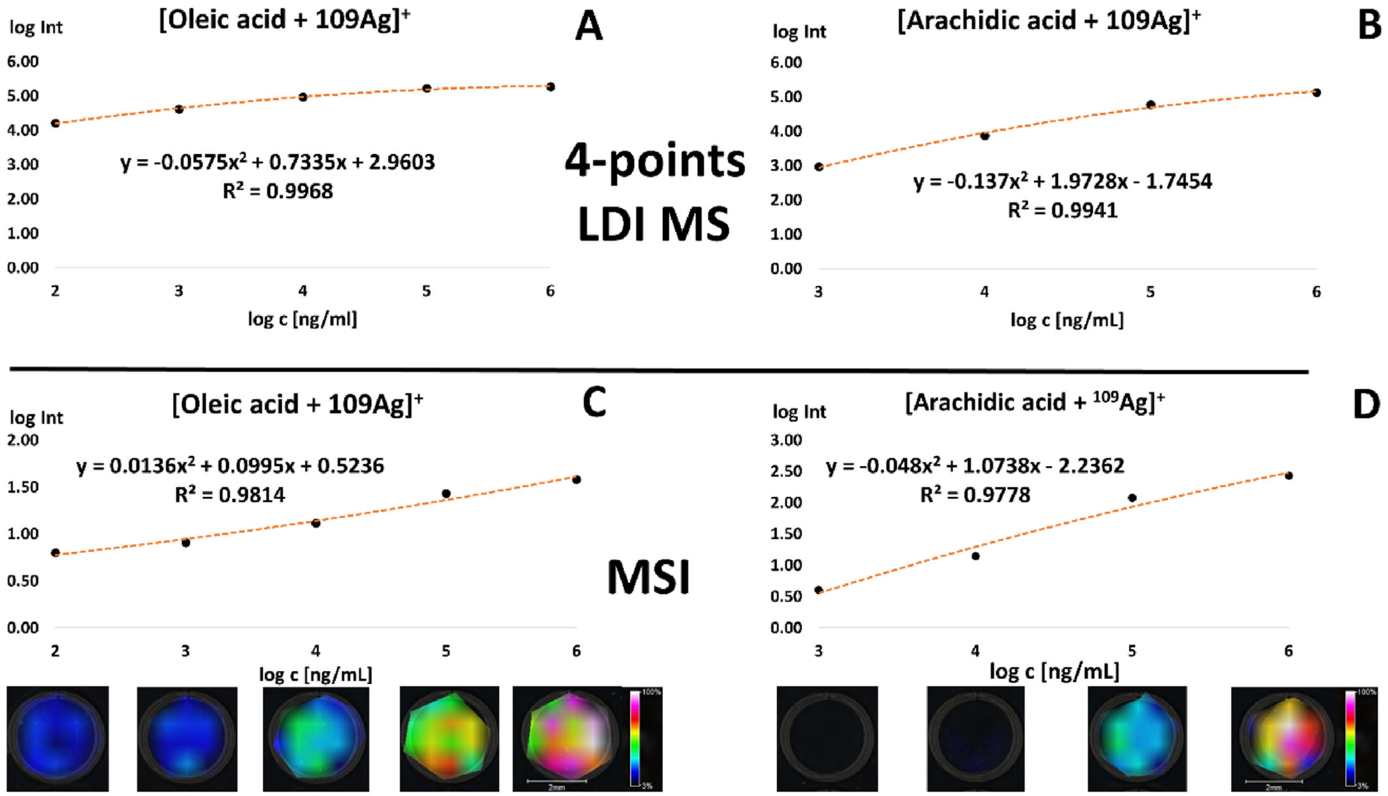

Fig. 3. Charts A and C present results of quantification based on silver-109 adduct of oleic acid signal for different concentrations obtained in LDI MS and MSI experiments. Charts B and D present the same results for arachidic acid. All charts show decimal logarithm of intensity value *vs* decimal logarithm of concentration of acids. All panels contain the equation and the R^2 value of polynomial trendline. Panels C and D also contain ions $[\text{oleic acid}+^{109}Ag]^+$ and $[\text{arachidic acid}+^{109}Ag]^+$ images for each concentration.

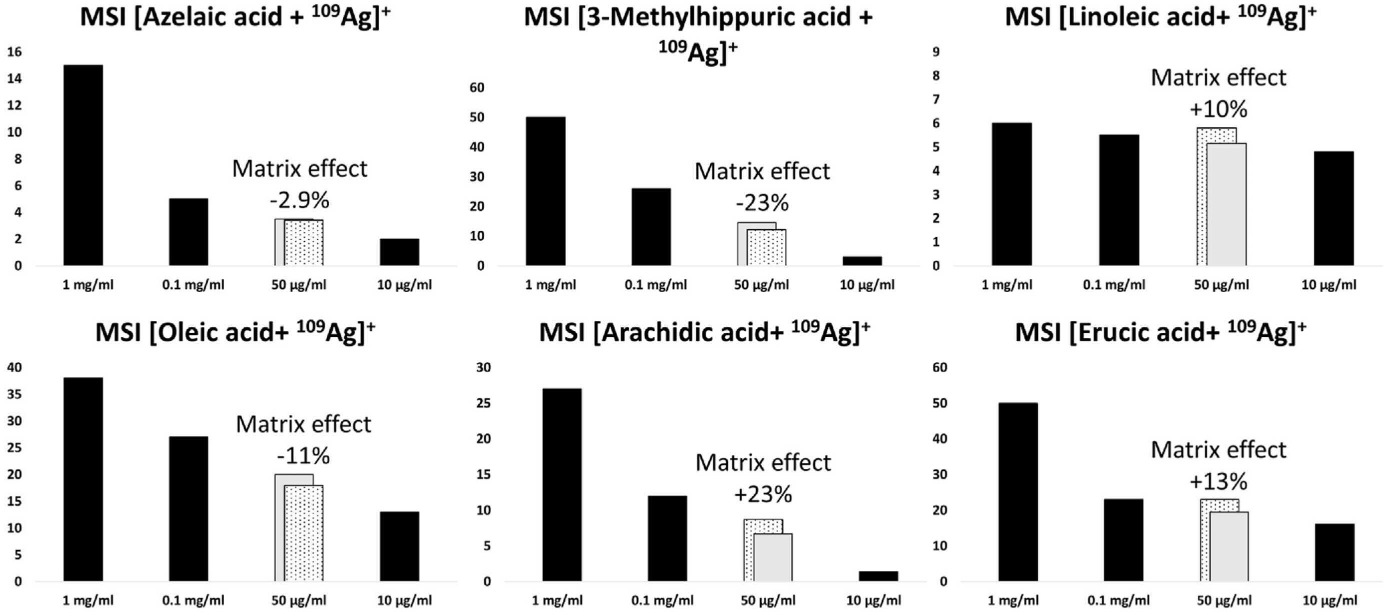

Fig. 5. Results of quantitative analysis of selected carboxylic acids in human blood serum by MSI with silver-109 nanoparticles produced by LASiS. For concentration 50 μg/mL theoretical intensity of signal was calculated (grey bar) and compared with experimental intensity of signal of analyzed acid in human blood serum spiked with carboxylic acid (white bar with dots). Intensities of signals for water solutions of carboxylic acid standards are also presented (black bars).

exceed 0.978. LOD value was found to be 333 pg (1.19 pmol) per measurement spot. In HPLC-CAD/MS-IT-TOF limit of detection value was 0.006 μg/mL and in HPLC-evaporative light scattering detection was 21.7 ng [29,30].

The last analyzed carboxylic acid was erucic acid, results of this analysis is presented in Fig. 4. Arachidic acid was found in spectra mainly as silver-109 adduct of $[M+^{109}Ag]^+$ at *m/z* value of 447.2227. The results of manual measurements for are shown in Fig. 4A. Signals were found for four concentrations with intensities $2.03{\cdot}10^5$ for 1 mg/mL, $1.29{\cdot}10^5$ for 100 μg/mL, $5.17{\cdot}10^4$ for 10 μg/mL and $4.33{\cdot}10^4$ for 1 μg/mL. As in the case of the previous analyzes, Fig. 4 shows the quantification results along with the equation and R^2 for the polynomial trendline. The trendline has very good fit with an R^2 of 0.956 for LDI MS and 0.993 for MSI. LOD value for LDI MS was 81 pg (0.29 pmol) per spot and in MSI LDI MS method 164 pg (0.58 pmol) per measurement spot. For erucic acid LOD value obtained by LC-MS method was 0.0025 μM and LLOQ value was 0.05 μM [31].

A regression analysis of the data obtained during semi-automatic MSI experiments was performed for all carboxylic acids. The use of mass spectrometry imaging for the quantification of carboxylic acids allowed to obtain good results for the polynomial function in all cases with R^2 ranging from 0.96 to 0.99. It should be noted that the regressions were performed over a very wide concentration range, from 1000-fold for 3-methylhippuric, linoleic, arachidic and erucic acids to 1 000 000-fold concentration change for azelaic acid.

These analyses indicate the usefulness of MSI for quantitative analysis of carboxylic acids and most probably other compounds. The measurement region allows coverage of the whole sample spot by using a grid or raster of measurement points with specified resolution. Application of MSI for analysis of all samples allows detecting signals of carboxylic acid-silver-109 adducts in various concentrations. As can be seen on Figs. 1D, 2C and 2D, 3C, 3D and 4B ion images prove that studied sample is deposited non-uniformly throughout of all studied sample spots. Limit of detection values obtained in both methods are worse than the values obtained during HPLC-MS analysis, however, the advantages of methods presented here are: (i) much shorter analysis time, (ii) the possibility of obtaining ion images and (iii) very fast and easy sample preparation.

3.2. *Detection of carboxylic acids in human blood serum*

Results obtained for 2-propanol solutions of carboxylic acids were compared to the ones based on human blood plasma in order to estimate suppression effect of biological matrix. The serum sample had been 500-fold diluted in deionized water, then the same volume of 100 μg/mL of carboxylic acid solution was added. The final concentration of analyzed acids in serum was approx. 50 μg/mL. The highest intensity signals for the tested carboxylic acids in serum were cationic adducts with silver-109.

Fig. 5 summarizes results of this analysis, theoretical intensities for 50 μg/mL of carboxylic acid solutions were calculated based on intensity value of 0.1 mg/mL sample. These values were compared with experimental data obtained for human blood serum spiked with carboxylic acids. For azelaic, 3-methylhippuric, linoleic and oleic acids, the calculated intensity is higher than experimental, for arachidic and erucic intensities of signals in blood serum were higher. The matrix effect was the lowest for azelaic acid −2.9% and the highest value was for 3-methylhippuric and arachidic acids (−23% and +23%). For rest of the result matrix effect was approx. In range of ±10%. The presented results clearly show that the biological matrix (in this example, blood serum) has moderate impact on the intensity value of the carboxylic acid during the MSI experiment, especially for azelaic acid where estimated value was nearly identical to data acquired during MALDI-ToF MSI experiment.

4. Conclusion

The application of ^{109}AgNPs generated by new method PFL 2D GS LASiS for manual LDI MS and semi-automatic MSI allowed detection and quantification of carboxylic acids in wide concentration range. Results of obtained data for both types of experiments indicate that mass spectrometry imaging method allows better quantification than for commonly used MALDI manual measurements. Ion images obtained in MSI experiments proved highly non-uniform analyte deposition that makes semi-automatic, multi-pixel MSI a modern requirement rather than improvement. The biological matrix has little effect on the intensity value of the analyzed carboxylic acids in MSI. It is shown that polynomial function allows for very good fit of experimental quantification results for wide concentration range. The potential application of this methodology is forensic or metabolomic analysis of human body fluids, also for quantification of synthetic and biological samples.

Notes

The authors declare no competing and financial interest.

Author statement

A. Kołodziej: Formal analysis, Investigation, Writing - Original Draft, Writing - Review & Editing, Visualization.

A. Płaza: Investigation, Writing - Original Draft, Writing - Review & Editing.

J. Nizioł: Data Curation, Funding acquisition.

T. Ruman: Conceptualization, Methodology, Resources, Writing - Original Draft, Writing - Review & Editing, Supervision.

Declaration of competing interest

The authors declare that they have no known competing financial interests or personal relationships that could have appeared to influence the work reported in this paper.

Acknowledgments

This work was supported by the National Science Centre (NCN, Poland), SONATA grant no. UMO-2018/31/D/ST4/00109.

References

[1] K. Tanaka, H. Waki, Y. Ido, S. Akita, Y. Yoshida, T. Yoshida, T. Matsuo, Protein and polymer analyses up to m/z 100 000 by laser ionization time-of-flight mass spectrometry, Rapid Commun. Mass Spectrom. 2 (1988) 151–153, https://doi.org/10.1002/rcm.1290020802.

[2] N. Fasih Ramandi, M. Faranoush, A. Ghassempour, H.Y. Aboul-Enein, Mass spectrometry: a powerful method for monitoring various type of leukemia, especially MALDI-TOF in leukemia's proteomics studies Review, Crit. Rev. Anal. Chem. (2021) 1–28, https://doi.org/10.1080/10408347.2021.1871844.

[3] E. Torres-Sangiao, C. Leal Rodriguez, C. García-Riestra, Application and perspectives of MALDI–TOF mass spectrometry in clinical microbiology laboratories, Microorganisms 9 (2021) 1539, https://doi.org/10.3390/microorganisms9071539.

[4] Q. He, C. Sun, J. Liu, Y. Pan, MALDI-MSI analysis of cancer drugs: significance, advances, and applications, Trac. Trends Anal. Chem. 136 (2021) 116183, https://doi.org/10.1016/j.trac.2021.116183.

[5] C.D. Calvano, A. Monopoli, T.R.I. Cataldi, F. Palmisano, MALDI matrices for low molecular weight compounds: an endless story? Anal. Bioanal. Chem. 410 (2018) 4015–4038, https://doi.org/10.1007/s00216-018-1014-x.

[6] J. Sekuła, J. Nizioł, W. Rode, T. Ruman, Gold nanoparticle-enhanced target (AuNPET) as universal solution for laser desorption/ionization mass spectrometry analysis and imaging of low molecular weight compounds, Anal. Chim. Acta 875 (2015) 61–72, https://doi.org/10.1016/j.aca.2015.01.046.

[7] R.C. Gamez, E.T. Castellana, D.H. Russell, Sol–gel-derived silver-nanoparticle-embedded thin film for mass spectrometry-based biosensing, Langmuir 29 (2013) 6502–6507, https://doi.org/10.1021/la4008526.

[8] S.N. Jackson, K. Baldwin, L. Muller, V.M. Womack, J.A. Schultz, C. Balaban, A.S. Woods, Imaging of lipids in rat heart by MALDI-MS with silver nanoparticles, Anal. Bioanal. Chem. 406 (2014) 1377–1386, https://doi.org/10.1007/s00216-013-7525-6.

[9] Y.-Z. Zhao, Y. Xu, C. Gong, Y.-R. Ju, Z.-X. Liu, X. Xu, Analysis of small molecule compounds by matrix-assisted laser desorption ionization mass spectrometry with Fe3O4 nanoparticles as matrix, Chin. J. Anal. Chem. 49 (2021) 103–112, https://doi.org/10.1016/S1872-2040(20)60074-3.

[10] A. Arendowski, J. Nizioł, T. Ruman, Silver-109-based laser desorption/ionization mass spectrometry method for detection and quantification of amino acids, J. Mass Spectrom. 53 (2018) 369–378, https://doi.org/10.1002/jms.4068.

[11] J. Szulc, A. Kołodziej, T. Ruman, Silver-109/Silver/Gold nanoparticle-enhanced target surface-assisted laser desorption/ionisation mass spectrometry—the new methods for an assessment of mycotoxin concentration on building materials, Toxins 13 (2021) 45, https://doi.org/10.3390/toxins13010045.

[12] A. Kołodziej, T. Ruman, J. Nizioł, Gold and silver nanoparticles-based laser desorption/ionization mass spectrometry method for detection and quantification of carboxylic acids, J. Mass Spectrom. 55 (2020), e4604, https://doi.org/10.1002/jms.4604.

[13] J. Nizioł, W. Rode, B. Laskowska, T. Ruman, Novel monoisotopic ^{109} AgNPET for laser desorption/ionization mass spectrometry, Anal. Chem. 85 (2013) 1926–1931, https://doi.org/10.1021/ac303770y.

[14] J. Sekuła, J. Nizioł, W. Rode, T. Ruman, Silver nanostructures in laser desorption/ionization mass spectrometry and mass spectrometry imaging, Analyst 140 (2015) 6195–6209, https://doi.org/10.1039/C5AN00943J.

[15] A. Płaza, A. Kołodziej, J. Nizioł, T. Ruman, Laser ablation synthesis in solution and nebulization of silver-109 nanoparticles for mass spectrometry and mass spectrometry imaging, ACS Meas. Sci. Au (2021), https://doi.org/10.1021/acsmeasuresciau.1c00020.

[16] J. Nizioł, T. Ruman, Silver 109 Ag nanoparticles for matrix-less mass spectrometry of nucleosides and nucleic bases, IJCEA (2013) 46–49, https://doi.org/10.7763/IJCEA.2013.V4.259.

[17] J. Nizioł, W. Rode, Z. Zieliński, T. Ruman, Matrix-free laser desorption–ionization with silver nanoparticle-enhanced steel targets, Int. J. Mass Spectrom. 335 (2013) 22–32, https://doi.org/10.1016/j.ijms.2012.10.009.

[18] M. Yang, T. Fujino, Silver nanoparticles on zeolite surface for laser desorption/ionization mass spectrometry of low molecular weight compounds, Chem. Phys. Lett. 576 (2013) 61–64, https://doi.org/10.1016/j.cplett.2013.05.030.

[19] M.A. Sieber, J.K.E. Hegel, Azelaic acid: properties and mode of action, SPP 27 (2014) 9–17, https://doi.org/10.1159/000354888.

[20] M. Behbahani, S. Bagheri, F. Omidi, M.M. Amini, An amino-functionalized mesoporous silica (KIT-6) as a sorbent for dispersive and ultrasonication-assisted micro solid phase extraction of hippuric acid and methylhippuric acid, two biomarkers for toluene and xylene exposure, Microchim. Acta 185 (2018) 505, https://doi.org/10.1007/s00604-018-3038-5.

[21] C.-H. Chiu, C.-T. Chen, M.-H. Cheng, L.-H. Pao, C. Wang, G.-H. Wan, Use of urinary hippuric acid and o-/p-/m-methyl hippuric acid to evaluate surgical smoke exposure in operating room healthcare personnel, Ecotoxicol. Environ. Saf. 217 (2021) 112231, https://doi.org/10.1016/j.ecoenv.2021.112231.

[22] M.F. Cury-Boaventura, R. Gorjão, T.M. de Lima, P. Newsholme, R. Curi, Comparative toxicity of oleic and linoleic acid on human lymphocytes, Life Sci. 78 (2006) 1448–1456, https://doi.org/10.1016/j.lfs.2005.07.038.

[23] F.P. Samson, A.T. Patrick, T.E. Fabunmi, M.F. Yahaya, J. Madu, W. He, S.R. Sripathi, J. Tyndall, H. Raji, D. Jee, D.R. Gutsaeva, W.J. Jahng, Oleic acid, cholesterol, and linoleic acid as angiogenesis initiators, ACS Omega 5 (2020) 20575–20585, https://doi.org/10.1021/acsomega.0c02850.

[24] U. Termsarasab, H.-J. Cho, D.H. Kim, S. Chong, S.-J. Chung, C.-K. Shim, H.T. Moon, D.-D. Kim, Chitosan oligosaccharide–arachidic acid-based nanoparticles for anti-cancer drug delivery, Int. J. Pharm. 441 (2013) 373–380, https://doi.org/10.1016/j.ijpharm.2012.11.018.

[25] G. Rabbani, M.H. Baig, A.T. Jan, E. Ju Lee, M.V. Khan, M. Zaman, A.-E. Farouk, R.H. Khan, I. Choi, Binding of erucic acid with human serum albumin using a spectroscopic and molecular docking study, Int. J. Biol. Macromol. 105 (2017) 1572–1580, https://doi.org/10.1016/j.ijbiomac.2017.04.051.

[26] M. Garelnabi, D. Litvinov, S. Parthasarathy, Evaluation of a gas chromatography method for azelaic acid determination in selected biological samples, N. Am. J. Med. Sci. 2 (2010) 397–402, https://doi.org/10.4297/najms.2010.2397.

[27] F. Ghamari, A. Bahrami, Y. Yamini, F.G. Shahna, A. Moghimbeigi, Hollow-fiber liquid-phase microextraction based on carrier-mediated transport for determination of urinary methyl hippuric acids, Null 99 (2017) 760–771, https://doi.org/10.1080/02772248.2017.1280038.

[28] J. Ren, D. Zhang, Y. Liu, R. Zhang, H. Fang, S. Guo, D. Zhou, M. Zhang, Y. Xu, L. Qiu, Z. Li, Simultaneous quantification of serum nonesterified and esterified fatty acids as potential biomarkers to differentiate benign lung diseases from lung cancer, Sci. Rep. 6 (2016) 34201, https://doi.org/10.1038/srep34201.

[29] X. Zhao, Y. He, J. Chen, J. Zhang, L. Chen, B. Wang, C. Wu, Y. Yuan, Identification and direct determination of fatty acids profile in oleic acid by HPLC-CAD and MS-IT-TOF, J. Pharmaceut. Biomed. Anal. 204 (2021) 114238, https://doi.org/10.1016/j.jpba.2021.114238.

[30] J. Zhao, S.P. Li, F.Q. Yang, P. Li, Y.T. Wang, Simultaneous determination of saponins and fatty acids in Ziziphus jujuba (Suanzaoren) by high performance liquid chromatography-evaporative light scattering detection and pressurized liquid extraction, J. Chromatogr. A 1108 (2006) 188–194, https://doi.org/10.1016/j.chroma.2005.12.104.

[31] E. Koch, M. Wiebel, C. Hopmann, N. Kampschulte, N.H. Schebb, Rapid quantification of fatty acids in plant oils and biological samples by LC-MS, Anal. Bioanal. Chem. 413 (2021) 5439–5451, https://doi.org/10.1007/s00216-021-03525-y.

Received: 29 June 2022 | Revised: 26 July 2022 | Accepted: 5 August 2022
DOI: 10.1002/rcm.9375

RESEARCH ARTICLE

Rapid Communications in Mass Spectrometry WILEY

Infrared pulsed fiber laser-produced silver-109 nanoparticles for laser desorption/ionization mass spectrometry of 3-hydroxycarboxylic acids

Artur Kołodziej[1,2] | Aneta Płaza-Altamer[1,2] | Joanna Nizioł[2] | Tomasz Ruman[2]

[1]Doctoral School of Engineering and Technical Sciences at the Rzeszów University of Technology, Rzeszów, Poland

[2]Faculty of Chemistry, Rzeszów University of Technology, Rzeszów, Poland

Correspondence
A. Kołodziej, Doctoral School of Engineering and Technical Sciences at the Rzeszów University of Technology, 8 Powstańców Warszawy Ave., 35-959 Rzeszów, Poland.
Email: a.kolodziej@prz.edu.pl

Funding information
Narodowe Centrum Nauki, Grant/Award Number: UMO-2018/31/D/ST4/00109

Rationale: 3-Hydroxycarboxylic acids are one of the major components of bacterial lipopolysaccharides (LPS), also known as endotoxins. Endotoxins pose a serious health risk and can seriously damage the internal organs of humans and animals. 3-Hydroxycarboxylic acids can be used as environmental markers to determine endotoxin levels. At the time of preparation of this manuscript no studies on laser mass spectrometry (MS) and analysis with silver nanoparticles (NP) for 3-hydroxycarboxylic acids have been published in literature.

Methods: Six acids, 3-hydroxyoctanoic (3-OH-C8:0), 3-hydroxydecanoic (3-OH-C10:0), 3-hydroxydodecanoic (3-OH-C12:0), 3-hydroxytetradecanoic (3-OH-C14:0), 3-hydroxyhexadecanoic (3-OH-C16:0), and 3-hydroxyoctadecanoic (3-OH-C18:0) acids, were used as test compounds on the target containing silver-109 NPs for quantification using matrix-assisted laser desorption/ionization (MALDI)–type mass spectrometer. Methods were also tested on spiked human blood serum samples to quantify 3-hydroxycarboxylic acids and verify the influence of the biological matrix on the measurement.

Results: Analyzed acids were directly tested in 1 000 000-fold concentration change conditions ranging from 1 mg/mL to 1 ng/mL. The semi-automatic MSI (MS imaging) method allowed us to obtain two to five times lower limit of detection (LOD) and lower limit of quantitation (LLOQ) values than common LDI (Bruker Daltonics, Bremen, Germany) method for analyzed acids. For almost all results of 3-hydroxycarboxylic acids, the trendline fit was better for the semi-automatic MSI method than the manual LDI method.

Conclusion: For the first time, the use of laser MS for the quantification of 3-hydroxycarboxylic acids has been demonstrated, and it has been proven that it can be used in the quantitative analysis of such compounds over a wide range of concentrations. In addition, a comparison of two methods—manual LDI-MS and semi-automatic MSI—is presented.

1 | INTRODUCTION

Matrix-assisted laser desorption/ionization-mass spectrometry (MALDI-MS) is one of the most popular soft ionization methods in modern MS. Since 1988 when this method was presented by Tanaka et al for the first time,[1] many various modifications were developed. The MALDI method is still very popular despite the development of liquid and gas chromatography coupled with MS. This method is widely used for protein analysis in proteomics, for the identification of microorganisms in microbiology, and for the analysis of drugs distribution in pharmacy.[2–4] Although it has many advantages such as high sensitivity and efficiency, the MALDI method is rarely used for the detection and quantification of low-molecular-weight (LMW) compounds. Analysis of these compounds is difficult because of the need for organic matrices, which are usually LMW organic acids, and during analysis the matrix produces various types of ions that interfere with the signals of the analyzed sample in the low mass range. This problem can be avoided by modifying the MALDI method with nanostructures (SALDI method). In the SALDI method, traditional acid matrix is replaced by metallic nanoparticles (NPs), which allow one to obtain mass spectra without the interfering signals of the organic acid matrix. The NPs have additional advantages: allows easy sample preparation, low chemical background, easier data analysis, and fast data collection.[5] Moreover, monoisotopic silver NPs have some additional properties like the simplest possible peak pattern, a much higher intensity of analyte peaks, and simplified calculations of isotopic distribution.[6] Laser ablation methods have an advantage over chemical synthesis because they allow for very quick synthesis of NPs (several seconds vs. hours in chemical synthesis), and the synthesized NPs are stabilizer- and reducing-agent-free.[7] The literature provides many examples of the use of NPs in LMW analysis.

3-Hydroxycarboxylic acids are one of the major components of lipid A, which is the lipid part of the endotoxins that are responsible for the toxicity of gram-negative bacteria. It has also been reported in the literature that lipid A is important in the immune system response during infection with gram-negative bacteria.[8] Bacterial lipopolysaccharide is an inflammatory stimulator that may trigger septic shock, which is a severe pathophysiological syndrome in response to an infection that in many cases is fatal as it can lead to organ failure.[9] Considering this fact, detection and quantification of 3-hydroxycarboxylic acids can be used to determine the endotoxins level in various samples.[10]

As high risk is involved, the concentration of endotoxins should be strictly controlled. For this purpose, various methods, including gas chromatography (GC) and liquid chromatography (LC) or biosensors, are used for their quantification. GC is a popular method in the quantification of endotoxins, but its limitation is the need for chemical derivatization such as transesterification or acetylation of the compounds in tested samples to obtain volatile derivatives or analogues.[11,12] LC, especially when coupled with MS, allows the measurement of very low levels of endotoxins without the need to modify the samples; however, the analysis itself takes quite a long time and requires the consumption of large amounts of reagents.[9] Using biosensors is a novel approach for quantification and detection of endotoxin. These devices are even more sensitive in detecting endotoxins; in the case of aptasensor by Zamani et al the detection limit is approximately 0.2 fg/mL.[13] A common element of all biosensors is the use of metal NPs, which enables the extremely sensitive detection of endotoxins.[13–15]

This work describes a new method for the detection of 3-hydroxyacids that are markers of bacterial lipopolysaccharides (endotoxin). In this publication we also present the quantification result of 3-hydroxycarboxylic acids with a chemically pure silver-109 NPs produced by 1064 nm pulsed fiber laser with 2D galvanometer scanner. In addition, we compare manual LDI-MS with semi-automatic MS imaging (MSI) in the quantification of 3-hydroxycarboxylic acids along with discussion of results and comparison with various SALDI and MALDI methods previously used in acid analysis. It is worth noting that this is the first study that reports the possibility of using laser MS and NP-coated targets for the detection of 3-hydroxycarboxylic acids.

2 | MATERIALS AND METHODS

2.1 | Materials

All 3-hydroxyacids standards were purchased from Sigma-Aldrich. Steel targets were machined from H17 stainless steel polished to the mirror finish. Before the LDI-MS and MS imaging experiments, steel targets were cleaned by dipping them in boiling solvents: toluene, chloroform, acetonitrile, and deionized water. After washing, plates were dried in high vacuum overnight. All solvents were of HPLC grade, except for water (18 MΩ·cm water produced locally).

2.2 | Sample preparation and handling

All 3-hydroxyacids standards (3-hydroxyoctanoic, 3-hydroxydecanoic, 3-hydroxydodecanoic, 3-hydroxytetradecanoic, 3-hydroxyhexadecanoic, and 3-hydroxyoctadecanoic acids) were dissolved in water to obtain a final concentration of 1 mg/mL. Lower concentrations of the standards were prepared by diluting higher concentration ones 10 times. An amount of 1 μL of plasma was dissolved in 249 μL of ultrapure water, then 250 μL of 100 μg/mL acid solution was added. About 0.3 μL of 3-hydroxyacid standards and blood plasma spiked with acid solutions were placed directly on the target plate and air-dried, and then the target was coated with ^{109}AgNPs suspension.

2.3 | Silver-109 NP synthesis and nebulization on target

Silver-109 foil was put into the beaker, and then acetonitrile was added. Laser ablation was then performed using a pulsed fiber laser (Raycus, Wuhan, China) with a wavelength of 1064 nm. The obtained suspension of monoisotopic silver NPs was sprayed on the surface of a steel plate with acid samples applied. Argon was used as an inert gas. A detailed protocol for the synthesis using laser ablation and nebulization of NPs is available in our previous publication on the preparation of silver-109 NPs using the pulsed fiber laser.[7] After the NPs were sputtered, the target was moved to the LDI-ToF-MS apparatus.

2.4 | Laser desorption/ionization-mass spectrometry

LDI-ToF-MS experiments were performed in reflectron mode using a Bruker Autoflex Speed time-of-flight mass spectrometer equipped with a SmartBeam II laser (355 nm). Laser impulse energy was approximately 90–140 μJ, and laser repetition rate was 1000 Hz. The total number of laser shots was 4000 for each spot divided in packs of 1000 shots per one measurement point. At each point, 1000 laser shots were made with default random walk applied (random points with 50 laser shots). The measurement range was *m/z* 80–1500. Suppression was turned on typically for ions of *m/z* lower than 80. Reflector voltages used were 21 kV (the first) and 9.55 kV (the second). The data were calibrated and analyzed with FlexAnalysis (version 3.3) using centroid calibration model. Mass calibration (enhanced cubic calibration based on 8–10 calibration points) was performed using internal standards (IS, silver-109 ions and clusters from $^{109}Ag^+$ to $^{109}Ag_9{}^+$).

2.5 | LDI-MS imaging

Measurements were performed using a Bruker Autoflex Speed time-of-flight mass spectrometer in reflectron positive mode. The apparatus was equipped with a SmartBeam II 1000 Hz 355 nm laser. Laser impulse energy was approximately 100–120 μJ, the laser repetition rate was 1000 Hz, and deflection was set on *m/z* lower than 80 Da. The *m/z* range was 80–1500, and the spatial resolution was 600 × 600 μm. The imaging experiments were made with 2000 laser shots per individual spot with a default random walk applied (FlexImaging 4.0). All spectra were pre-calibrated (cubic calibration function) with the use of silver-109 ions ($^{109}Ag^+$ to $^{109}Ag_9{}^+$) as an IS. The first accelerating voltage was held at 19 kV, and the second ion source voltage was held at 16.7 kV. Reflector voltages used were 21 kV (the first) and 9.55 kV (the second). All of the shown imaging pictures are for ± 0.05% *m/z* window. MSI experiments were performed on all spots of 3-hydroxyacid standards and blood plasma solution.

3 | RESULTS AND DISCUSSION

The method of synthesis of laser-generated nanomaterial (LGN) with PFL 2D GS laser, properties of silver-109 NPs, and their application are available in our recent publication.[7] This work presents the use of laser-generated ^{109}AgNPs for qualitative and quantitative analysis of 3-hydroxycarboxylic acids. A large number of results have been reported in the literature indicating that silver NPs are effective for ionization and rapid detection of various pure low-molecular-weight compounds (especially olefin-containing compounds) or complex biological mixtures such as urine, blood serum, or plant extracts.[16–21]

3.1 | Quantification results

Standards of all listed acids were directly measured in concentrations ranging from 1 mg/mL to 1 ng/mL, which equates to 1 000 000-fold concentration change. Limit of detection (LOD) values were calculated with the use of signal/noise (S/N) ratio value of 3 for lowest concentration samples. Each sample was placed on target plate in 0.3 μL volume equating to 0.3 μg to 0.3 pg of acid per measurement spot, which is approximately 1.87 nmol to 1.87 fmol, respectively, calculated, for example, for 3-hydroxyoctanoic acid molar mass. Examples of obtained mass spectra are presented in supporting information. LOD and lower limits of quantification (LLOQ) values were calculated based on S/N ratio value for manual LDI experiment and semi-automatic MSI (Table 1).

For analyzed hydroxycarboxylic acids, MSI method allowed to obtain lower LLOD value than manual LDI-MS except 3-hydroxyoctadecanoic acid. For this acid, due to the high values of the standard deviation, it is difficult to clearly show which method produces better results. It is worth noting that the application of semi-automatic MSI method allowed us to obtain two to five times lower LOD and LLOQ values for these acids.

Figure 1 presents results of LDI-MS and MSI analyses for 3-hydroxyoctanoic acid with ^{109}AgNPs PFL 2D GS laser-generated nanomaterial. Manual measurements were performed at four random

TABLE 1 Limits of detection and lower limit of quantification for studied 3-hydroxyacids

	Manual LDI-MS		Semi-automatic MSI	
	LOD±SD[a] (ng/mL)	LLOQ±SD[b] (ng/mL)	LOD±SD[a] (ng/mL)	LLOQ±SD[b] (ng/mL)
3-Hydroxyoctanoic acid	2563 ± 1770	4272 ± 2449	1549 ± 1173	2582 ± 1956
3-Hydroxydecanoic acid	1120 ± 896	1866 ± 1494	253 ± 195	422 ± 326
3-Hydroxydodecanoic acid	1915 ± 1292	3191 ± 2153	420 ± 410	700 ± 683
3-Hydroxytetradecanoic acid	1573 ± 782	2622 ± 1304	562 ± 385	937 ± 641
3-Hydroxyhexadecanoic acid	1482 ± 782	2470 ± 1303	366 ± 80	610 ± 150
3-Hydroxyoctadecanoic acid	1351 ± 268	2252 ± 447	1721 ± 233	2868 ± 389

Note: LLOQ, lower limit of quantitation; LOD, limit of detection; LDI-MS, laser desorption/ionization-mass spectrometry; MSI, mass spectrometry imaging; SD, standard deviation.
[a] Based on S/N ratio of 3.
[b] Based on S/N ratio of 5.

locations inside the sample spot for each analyzed acid; the measurement scheme is presented in Figure 1A. The acid was found in spectra mainly as silver-109 adduct of $[M + {}^{109}Ag]^+$ formula in amounts of ca. 300 ng to 3 pg per sample spot. All these data were presented in the form of intensity vs. concentration bar chart, and both axes are presented on a logarithmic scale (Figure 1B). Regression analysis of these data provided trendline with R^2 value 0.846. After manual LDI-MS measurement of the sample the same spots with carboxylic acids were analyzed using the semi-automatic MSI method. Figure 1C presents the scheme of semi-automatic MSI method, which was used in the measurement of all 3-hydroxycarboxylic acids. Figure 1D shows results of this analysis. During this measurement the whole sample spot was covered with a grid of measurement points with a defined resolution. The regression analysis of the MSI results clearly shows a much better fit of the trendline with an R^2 value of 0.969. Figure 4D also shows ion images of $[C_8H_{16}O_3 + {}^{109}Ag]^+$ adduct for all concentrations, proving that the sample is distributed non-homogeneously on the plate.

LOD based on S/N ratio of 3 was found to be 769 pg (4.80 pmol) of 3-hydroxyoctanoic acid per measured spot for LDI-MS. In contrast, LOD for MSI and LDI-MS was found to be 456 pg (2.90 pmol) per measured spot.

Quantitative analysis of 3-hydroxycarboxylic acids is presented only for LC- and GC–MS results in the literature, but no information is available for LDI-MS methods.[9,22] The publication by Uhlig et al shows that the LOD value for 3-hydroxyoctanoic acid was 0.7 ng/mL and the LLOQ value was 1.7 ng/mL.[9]

The next analyzed acid was 3-hydroxydecanoic acid. Figures 2A and 2C present results of LDI-MS and MSI analyses for this acid with PFL 2D GS LGN ^{109}AgNPs. The acid was found in spectra mainly as silver-109 adduct of $[M + {}^{109}Ag]^+$ ion formula in 0.1 mg/mL to 0.1 μg/mL concentration samples. Similar to 3-hydroxyoctanoic analysis, bar chart with trendlines is shown in Figure 2A. R^2 value for linear trendline for manual LDI-MS was 0.974, but for the MSI experiment a higher value was obtained for linear trendline of 0.978 (Figures 2A and 2C).

The LOD value for 3-hydroxydecanoic acid was found to be 336 pg (1.79 pmol) per spot for LDI-MS and 76 pg (0.40 pmol) per measurement spot for MSI. In the LC–MS method, the LOD value for this acid was 0.9 ng/mL.[9]

The next acid was 3-hydroxydodecanoic acid. Figures 2B and 2D present results of LDI-MS and MSI analyses. This acid was measured as it was presented in Figures 1A and 1C. The acid was found in spectra mainly as silver-109 adduct of $[M + {}^{109}Ag]^+$ ion formula in 1 mg/mL to 1 ng/mL concentration samples. Adduct *m/z* value was of 325.0768. Bar chart of intensity vs. concentration (Figure 2B) presents the trendline fit with R^2 value 0.987 for a very wide concentration range. However, the application of MSI allowed slightly better fit of R^2 value being equal to 0.988 for 10^6-fold concentration range. The LOD was found to be 575 pg (2.66 pmol) for LDI-MS and 126 pg (0.58 pmol) for MSI of 3-hydroxydodecanoic acid per measured spot. In the LC–MS method the LOD value for this acid was 2.2 ng/mL.[9]

Figures 3A and 3C show the results of analysis of 3-hydroxytetradecanoic acid. Similar to previous analysis, acid was

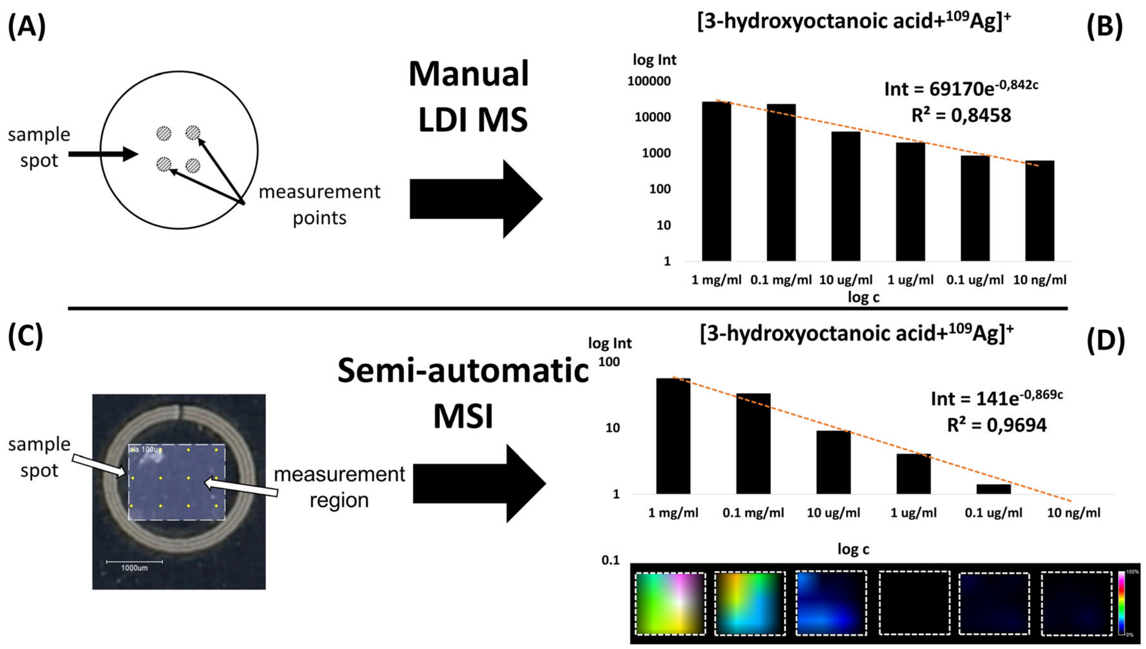

FIGURE 1 Panel A shows the scheme of manual laser desorption/ionization-mass spectrometry (LDI-MS) measurement with four random measure points. Panel C presents the scheme of semi-automatic mass spectrometry imaging (MSI) measurement. Column charts B and D present results of quantification based on silver-109 adduct of 3-hydroxyoctanoic acid signal for different concentrations obtained in LDI-MS and MSI experiments. Both panels (B, D) contain exponential trendline with its equation and R^2 value. Panel D also contains ion images for adduct [C8H16O3 + 109Ag] + images for each concentration [Color figure can be viewed at wileyonlinelibrary.com]

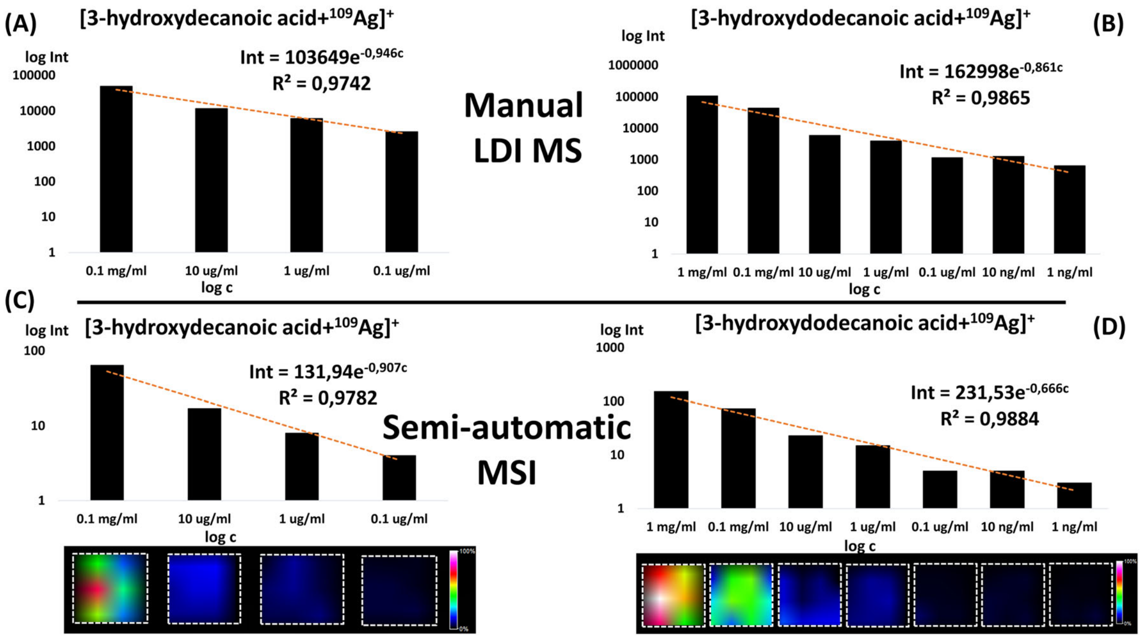

FIGURE 2 Column charts A and C present results of quantification based on silver-109 adduct of 3-hydroxydecanoic acid signal for different concentrations obtained in laser desorption/ionization-mass spectrometry (LDI-MS) and mass spectrometry imaging (MSI) experiments. Column charts B and D present the same results for 3-hydroxydodecanoic acid. All panels contain the equations and the R^2 values of exponential trendline. Panels C and D also contain ions [C10H20O3 + 109Ag] + and [C12H24O3 + 109Ag] + images for each concentration [Color figure can be viewed at wileyonlinelibrary.com]

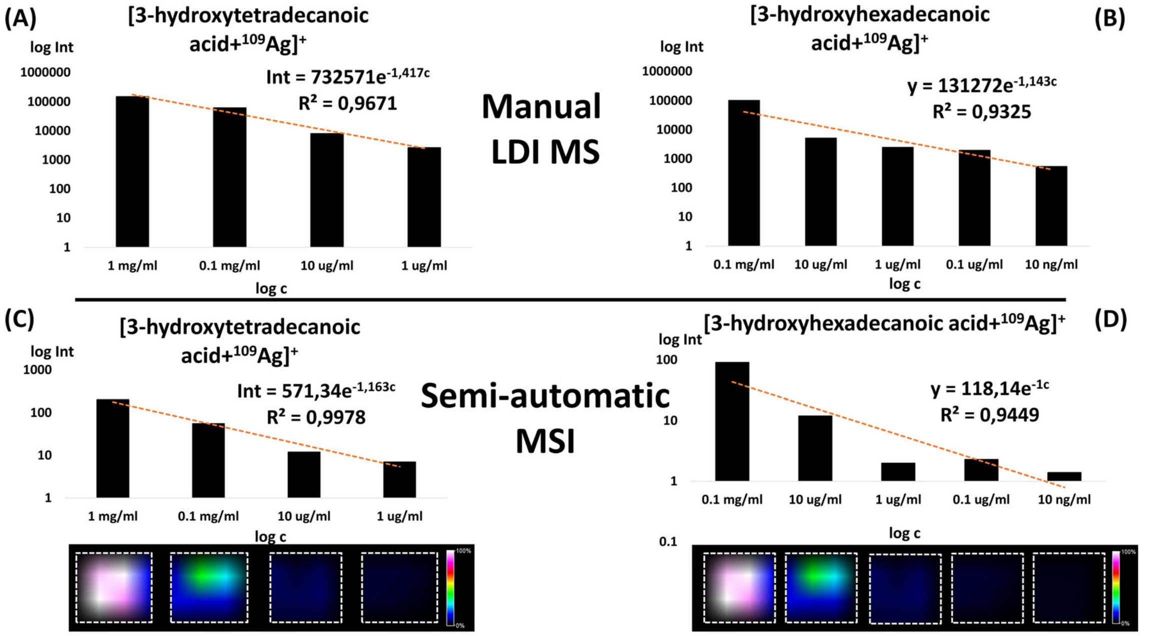

FIGURE 3 Column charts A and C present results of quantification based on silver-109 adduct of 3-hydroxytetradecanoic acid signal for different concentrations obtained in laser desorption/ionization-mass spectrometry (LDI-MS) and mass spectrometry imaging (MSI) experiments. Column charts B and D present the same results for 3-hydroxyhexadecanoic acid. All panels contain the equations and the R^2 values of exponential trendline. Panels C and D also contain ions [C14H28O3 + 109Ag] + and [C16H32O3 + 109Ag] + images for each concentration [Color figure can be viewed at wileyonlinelibrary.com]

analyzed in two measurement modes: manual LDI-MS and semi-automatic MSI. 3-Hydroxytetradecanoic acid was found in spectra mainly as silver-109 adduct of $[M + {}^{109}Ag]^+$ at the *m/z* value of 353.1081. The results of manual measurements for this acid are shown in Figure 3A for 1 mg/mL to 1 μg/mL concentration of sample. Figure 3C presents results of semi-automatic MSI method. On both charts trendline fitted to obtained during experiment result are presented. The R^2 value of exponential trendline for the manual LDI method was 0.967. For the MSI method trendline fit was better with R^2 value 0.998. The LOD was found to be 472 (1.93 pmol) for LDI-MS and 169 pg (0.69 pmol) for MSI of 3-hydroxytetradecanoic acid per measured spot. In Uhlig et al's work the LOD value 1.7 ng/mL.[9]

3-Hydroxyhexadecanoic acid was analyzed next, and the results are presented in Figures 3B and 3D. The acid was found in spectra mainly as silver-109 adduct of $[M + {}^{109}Ag]^+$ at the *m/z* value of 381.1394. The results of manual measurements are shown in Figure 4B as a bar chart of intensity vs. concentration. This acid was found in 0.1 mg/mL to 10 ng/mL concentration sample. R^2 value of trendline fit for the manual LDI method was 0.933 and that for MSI was 0.945. In all presented cases quantification results of MSI experiment resulted in better fit than manual LDI-MS. The LOD value was found to be 445 pg (1.63 pmol) for LDI-MS and 110 pg (0.40 pmol) of 3-hydroxyhexadecanoic acid per measurement spot. In the LC–MS method, the LOD value was 0.6 ng/mL.[9]

Figure 4 presents results of analysis of 3-hydroxyoctadecanoic acid. This acid was found in spectra mainly as silver-109 adduct of $[M + {}^{109}Ag]^+$ at the *m/z* value of 409.1707. The results of the manual measurements for 3-hydroxyoctadecanoic acid are shown in Figure 4A. Figure 4B present results of the semi-automatic MSI method. R^2 value of exponential trendline for manual LDI method was 0.993, and that for automated MSI was 0.988. This is the only case where the trendline fit was better for the LDI-MS method. On the contrary, the R^2 value for the MSI was almost 0.99 at a 1000-fold dilution of the sample. The LOD was found to be 405 pg (1.35 pmol) for LDI-MS and 516 pg (1.72 pmol) of 3-hydroxyoctadecanoic acid per measured spot. During the LC–MS analysis, the LOD value was 0.7 ng/mL for this acid.[9]

The use of MSI for the quantification of 3-hydroxycarboxylic acids enabled us to obtain a better fit of the experiment results than manual LDI-MS method with R^2 ca. 0.98 for five analyzed acids, and only for 3-hydroxyoctadecanoic acid the trendline fit was lower for MSI than for LDI-MS and still was above 0.98. These analyses clearly indicate the usefulness of MSI for quantitative analysis of these acids. It should be noted that the regressions were performed over a very wide concentration range, from 1000 for 3-hydroxydecanoic, 3-hydroxytetradecanoic and 3-hydroxyoctadecanoic acids to 1 000 000 fold concentration change for 3-hydroxydodecanoic acid.

The analyses presented in this publication lead to the conclusion that MSI allows for quantitative analyses. During the measurement, the entire sample spot was covered with a grid or raster of measurement points with a defined resolution. The MSI analysis can be applied to mainly detect signals of 3-hydroxycarboxylic acid-silver-109 adducts at various concentrations. The mass spectra also presented sodium and potassium adducts of the tested acids, but the sum of the intensities of these signals did not exceed 10% of the signal intensity of the silver-109 adduct. In most cases the results obtained using MSI had a better trendline fit compared to manual measurements and yielded an R^2 value 0.98 for most of the analyzed acids. As can be seen on Figures 1D, 2C, 2D, 3C, 3D, and 4B ion images prove that studied sample was deposited nonuniformly in all studied sample spots. By covering the entire surface of the spot with the sample, it is possible to better match the trendline to the obtained results. In the case of manual measurements, there is a high probability of selecting a point where the concentration of the sample

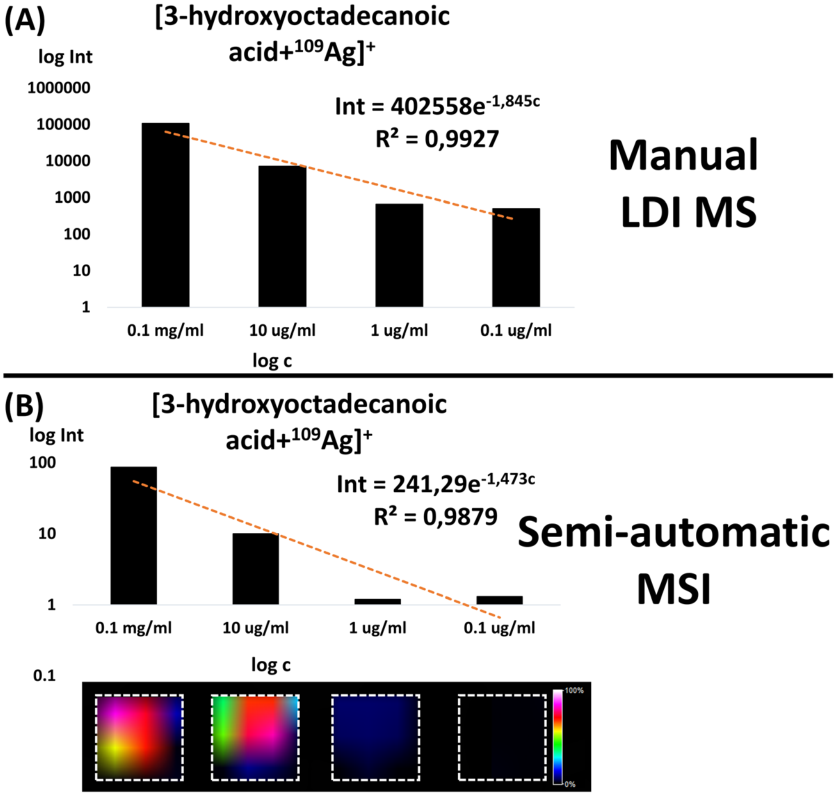

FIGURE 4 Column charts A and B present results of quantification based on silver-109 adduct signal of 3-hydroxyoctadecanoic acid for different concentrations obtained in laser desorption/ionization-mass spectrometry (LDI-MS) and mass spectrometry imaging (MSI) experiments. Both panels (A, B) contain the equations and the R^2 values for exponential trendline. Panel B also contains ion $[C18H36O3 + 109Ag]+$ images for each concentration [Color figure can be viewed at wileyonlinelibrary.com]

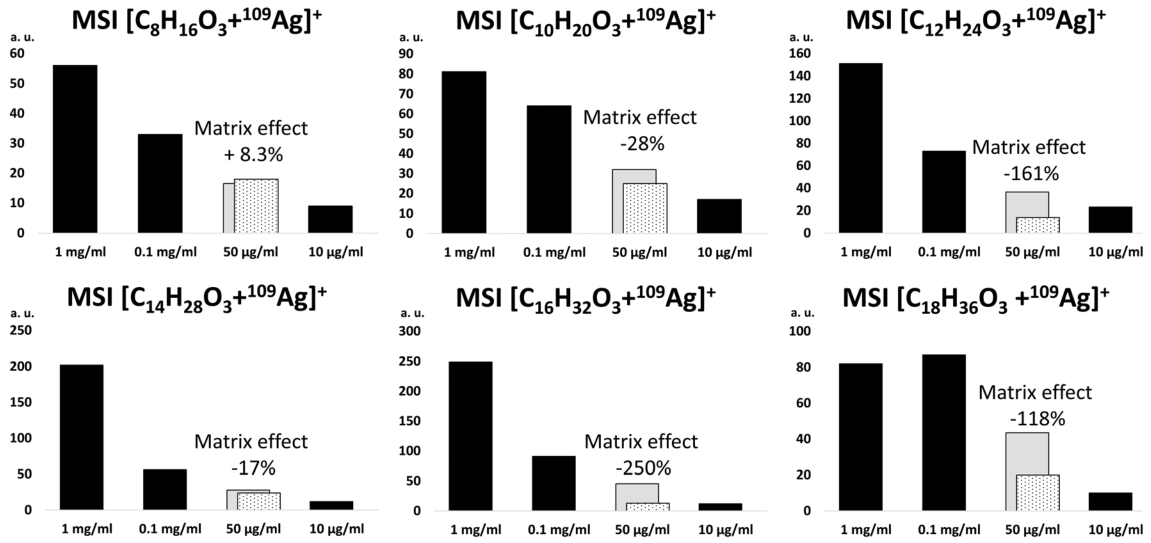

FIGURE 5 Results of quantitative analysis of selected 3-hydroxycarboxylic acids in human blood serum by semi-automatic mass spectrometry imaging (MSI) with monoisotopic silver-109 NPs PFL 2D GS LGN. For concentration 50 µg/mL theoretical intensity of signal was calculated (gray bar) and compared with the experimental intensity of signal of analyzed acid in human blood serum spiked with carboxylic acid (white bar with dots). Intensity of signals for water solutions of carboxylic acid standards 1 mg/mL, 0.1 mg/mL, and 10 µg/mL was also presented (black bars)

is higher or lower than the average concentration of the sample over the entire surface, and this is a common problem in MALDI-MS method. LOD values obtained in manual LDI-MS and semi-automatic MSI methods were worse than the values obtained during LC–MS analysis; however, the advantages of these methods are (a) the possibility of obtaining ion images (which is impossible with normal HPLC-MS analysis), (b) very easy sample preparation (usually it involves only diluting the sample in a suitable solvent and applying the solution to the steel plate), and (c) short analysis time (for manual measurement it is about seconds, and for semi-automatic MSI one sample measurement takes from a few seconds to several minutes). All the advantages presented above also apply to the GC–MS method, and additionally there is no need to perform derivatization, which allows unmodified samples to be tested.

3.2 | Detection of 3-hydroxycarboxylic acids in human blood serum

The results presented in the previous section were used to analyze the effects of suppression of the biological matrix. For this purpose, a spiked human blood serum sample was prepared. A 500-fold dilution of blood serum in distilled water was prepared, then the same volume of 100 µg/mL of carboxylic acid solution was added. The final concentration of the analyzed acids in spiked blood serum suspension was ca. 50 µg/mL. The highest intensity signals found in the spectra belonged to the 3-hydroxycarboxylic acid silver-109 adducts.

Figure 5 summarizes the results of this analysis. Theoretical intensity for 50 µg/mL of carboxylic acid solution was calculated based on intensity value of 0.1 mg/mL sample. Theoretical intensity values were compared with experimental data obtained for diluted human blood serum spiked with carboxylic acids. For 3-hydroxyoctanoic, 3-hydroxydecanoic, and 3-hydroxytetradecanoic acids matrix effect was +8.3%, −28%, and −17%, respectively. In the case of these three acids, no significant matrix effect on the measurement result was noticed. However, for 3-hydroxydodecanoic, 3-hydroxyhexadecanoic and 3-hydroxyoctadecanoic acids the matrix effect was −161%, −250%, and −118%, respectively. The results presented in this study show that the biological matrix (in this example, human blood serum) for these three acids causes a significant reduction in signal intensity compared to the predicted value, clearly indicating the presence of a matrix suppression effect. Due to the high content of lipid compounds in the blood serum, the matrix suppression effect may arise, which in turn causes a significant reduction in the intensity of the signals of the tested 3-hydroxycarboxylic acids.

4 | CONCLUSION

The application of stainless steel plates coated with silver-109 NPs synthesized by the new PFL 2D GS LGN method for the analysis of 3-hydroxycarboxylic acids was presented. ^{109}AgNPs ionize and allow for analysis using laser MS of 3-hydroxycarboxylic acids in a very wide range of concentrations, even up to 10 ng/mL (for 3-hydroxydodecanoic acid). Two measurement methods were compared: manual LDI-MS and semi-automatic MSI; the presented results of regression analyses prove the possibility of using MSI for quantitative analyses. The use of laser MS for the quantification of 3-hydroxycarboxylic acids was demonstrated for the first time. The results obtained during the experiments show that laser MS can be used to determine the concentration of endotoxins in the samples. Ion images obtained in MSI experiments proved highly nonuniform analyte deposition that makes semi-automatic, multi-pixel MSI a modern requirement rather than improvement. The biological matrix has a significant effect on the intensity value of some of the analyzed 3-hydroxycarboxylic acids in MSI.

ACKNOWLEDGMENTS

This work was supported by the Narodowe Centrum Nauki (NCN), SONATA grant no. UMO-2018/31/D/ST4/00109.

PEER REVIEW

The peer review history for this article is available at https://publons.com/publon/10.1002/rcm.9375.

DATA AVAILABILITY STATEMENT

The data that support the findings of this study are available from the corresponding author upon reasonable request.

ORCID

Artur Kołodziej https://orcid.org/0000-0002-9222-0937

REFERENCES

1. Tanaka K, Waki H, Ido Y, et al. Protein and polymer analyses up to m/z 100 000 by laser ionization time-of-flight mass spectrometry. *Rapid Commun Mass Spectrom*. 1988;2(8):151-153. doi:10.1002/rcm.1290020802
2. Greco V, Piras C, Pieroni L, et al. Applications of MALDI-TOF mass spectrometry in clinical proteomics. *Expert Rev Proteomics*. 2018;15(8):683-696. doi:10.1080/14789450.2018.1505510
3. Topić Popović N, Kazazić SP, Bojanić K, Strunjak-Perović I, Čož-Rakovac R. Sample preparation and culture condition effects on MALDI-TOF MS identification of bacteria: A review. *Mass Spectrom Rev*. Published online October 13. 2021;mas.21739. doi:10.1002/mas.21739
4. Guo S, Li K, Chen Y, Li B. Unraveling the drug distribution in brain enabled by MALDI MS imaging with laser-assisted chemical transfer. *Acta Pharm Sin B* Published Online November 16. 2021. doi:10.1016/j.apsb.2021.11.007
5. Sekuła J, Nizioł J, Rode W, Ruman T. Gold nanoparticle-enhanced target (AuNPET) as universal solution for laser desorption/ionization mass spectrometry analysis and imaging of low molecular weight compounds. *Anal Chim Acta*. 2015;875:61-72. doi:10.1016/j.aca.2015.01.046
6. Nizioł J, Rode W, Laskowska B, Ruman T. Novel monoisotopic ^{109}AgNPET for laser desorption/ionization mass spectrometry. *Anal Chem*. 2013;85(3):1926-1931. doi:10.1021/ac303770y
7. Płaza A, Kołodziej A, Nizioł J, Ruman T. Laser ablation synthesis in solution and nebulization of Silver-109 nanoparticles for mass spectrometry and mass spectrometry imaging. *ACS Meas Au* Published Online August 25. 2021. doi:10.1021/acsmeasuresciau.1c00020
8. Steimle A, Autenrieth IB, Frick JS. Structure and function: Lipid a modifications in commensals and pathogens. *Int J Med Microbiol*. 2016;306(5):290-301. doi:10.1016/j.ijmm.2016.03.001
9. Uhlig S, Negård M, Heldal KK, et al. Profiling of 3-hydroxy fatty acids as environmental markers of endotoxin using liquid chromatography coupled to tandem mass spectrometry. *J Chromatogr A*. 2016;1434:119-126. doi:10.1016/j.chroma.2016.01.038
10. Reynolds SJ, Milton DK, Heederik D, et al. Interlaboratory evaluation of endotoxin analyses in agricultural dusts—Comparison of LAL assay and mass spectrometry. *J Environ Monit*. 2005;7(12):1371-1377. doi:10.1039/B509256F
11. Mielniczuk Z, Mielniczuk E, Larsson L. Gas chromatography-mass spectrometry methods for analysis of 2- and 3-hydroxylated fatty acids: Application for endotoxin measurement. *J Microbiol Methods*. 1993;17(2):91-102. doi:10.1016/0167-7012(93)90002-Y
12. Shende N, Karale A, Marne K, et al. Quantitation of endotoxin by gas chromatography-mass spectrometry in Neisseria meningitidis serogroups a, C, W, Y and X during polysaccharide purification used in conjugate vaccine. *J Pharm Biomed Anal*. 2022;209:114536. doi:10.1016/j.jpba.2021.114536
13. Zamani M, Pourmadadi M, Seyyed Ebrahimi SA, Yazdian F, Shabani SJ. A novel labeled and label-free dual electrochemical detection of endotoxin based on aptamer-conjugated magnetic reduced graphene oxide-gold nanocomposite. *J Electroanal Chem*. 2022;908:116116. doi:10.1016/j.jelechem.2022.116116
14. Mu Z, Tian J, Wang J, Zhou J, Bai L. A new electrochemical aptasensor for ultrasensitive detection of endotoxin using Fe-MOF and AgNPs decorated P-N-CNTs as signal enhanced indicator. *Appl Surf Sci*. 2022;573:151601. doi:10.1016/j.apsusc.2021.151601
15. Zandieh M, Hosseini SN, Vossoughi M, Khatami M, Abbasian S, Moshaii A. Label-free and simple detection of endotoxins using a sensitive LSPR biosensor based on silver nanocolumns. *Anal Biochem*. 2018;548:96-101. doi:10.1016/j.ab.2018.02.023
16. Kołodziej A, Ruman T, Nizioł J. Gold and silver nanoparticles-based laser desorption/ionization mass spectrometry method for detection and quantification of carboxylic acids. *J Mass Spectrom*. 2020;55(10):e4604. doi:10.1002/jms.4604
17. Arendowski A, Nizioł J, Ruman T. Silver-109-based laser desorption/ionization mass spectrometry method for detection and quantification of amino acids. *J Mass Spectrom*. 2018;53(4):369-378. doi:10.1002/jms.4068
18. Szulc J, Kołodziej A, Ruman T. Silver-109/silver/gold nanoparticle-enhanced target surface-assisted laser desorption/ionisation mass spectrometry—The new methods for an assessment of mycotoxin concentration on building materials. *Toxins*. 2021;13(1):45. doi:10.3390/toxins13010045
19. Nizioł J, Rode W, Zieliński Z, Ruman T. Matrix-free laser desorption–ionization with silver nanoparticle-enhanced steel targets. *Int J Mass Spectrom*. 2013;335:22-32. doi:10.1016/j.ijms.2012.10.009
20. Arendowski A, Nizioł J, Ossoliński K, et al. Laser desorption/ionization MS imaging of cancer kidney tissue on silver nanoparticle-enhanced target. *Bioanalysis*. 2018;10(2):83-94. doi:10.4155/bio-2017-0195
21. Sherrod SD, Diaz AJ, Russell WK, Cremer PS, Russell DH. Silver nanoparticles as selective ionization probes for analysis of olefins by mass spectrometry. *Anal Chem*. 2008;80(17):6796-6799. doi:10.1021/ac800904g
22. Jones PM, Quinn R, Fennessey PV, et al. Improved stable isotope dilution-gas chromatography-mass spectrometry method for serum or plasma free 3-Hydroxy-fatty acids and its utility for the study of disorders of mitochondrial fatty acid β-oxidation. *Clin Chem*. 2000;46(2):149-155. doi:10.1093/clinchem/46.2.149

SUPPORTING INFORMATION

Additional supporting information can be found online in the Supporting Information section at the end of this article.

How to cite this article: Kołodziej A, Płaza-Altamer A, Nizioł J, Ruman T. Infrared pulsed fiber laser-produced silver-109 nanoparticles for laser desorption/ionization mass spectrometry of 3-hydroxycarboxylic acids. *Rapid Commun Mass Spectrom*. 2022;36(21):e9375. doi:10.1002/rcm.9375

Received: 9 August 2021 | Revised: 28 December 2021 | Accepted: 2 February 2022
DOI: 10.1002/jms.4815

RESEARCH ARTICLE

Journal of MASS SPECTROMETRY WILEY

Infrared pulsed fiber laser-produced silver-109-nanoparticles for laser desorption/ionization mass spectrometry of amino acids

Aneta Płaza-Altamer[1] | **Artur Kołodziej**[1] | **Joanna Nizioł**[2] | **Tomasz Ruman**[2]

[1]Doctoral School of Engineering and Technical Sciences, Rzeszów University of Technology, Rzeszów, Poland

[2]Faculty of Chemistry, Rzeszów University of Technology, Rzeszów, Poland

Correspondence
Aneta Płaza-Altamer, Doctoral School of Engineering and Technical Sciences at the Rzeszów University of Technology,
8 Powstańców Warszawy Ave., 35-959 Rzeszów, Poland.
Email: a.plaza@prz.edu.pl

Funding information
National Science Centre (NCN), Grant/Award Number: UMO-2018/31/D/ST4/00109

Abstract

Application of monoisotopic cationic ^{109}Ag nanoparticles (^{109}AgNPs) obtained by pulsed fiber laser (PFL) 2D galvo-scanner (GS) laser generated nanomaterial (LGN) for both high resolution laser desorption/ionization mass spectrometry and mass spectrometry imaging of amino acids is presented. Four amino acids, alanine, isoleucine, lysine, and phenylalanine were used as test compounds for quantification with matrix-assisted laser desorption/ionization mas (MALDI)-type mass spectrometer. Comparison of commonly made manual measurements with semiautomatic mass spectrometry imaging (MSI) was performed providing very interesting findings. Amino acids were directly tested in 1 000 000-fold concentration change conditions ranging from 1 mg/ml to 1 ng/ml, which equates to 500 ng to 500 fg of amino acid per measurement spot. Methods were also tested on samples of human blood plasma for quantification of endogenous amino acids.

KEYWORDS
amino acids, low molecular weight compounds, monoisotopic silver-109 nanoparticles, MSI, quantification

1 | INTRODUCTION

Amino acids are organic compounds that play an important role in the functioning of the body. They are necessary for the proper course of life processes, such as the structure of proteins, enzymes, cells, and the synthesis of hormones and neurotransmitters. The concentration of amino acids in the human body varies depending on the food consumed or the health state. Both high and low values of amino acid concentrations in the body can be indicators of metabolic disorders or developing disease. Amino acids can be found in quite wide concentration range in different biological objects, for example, different amino acids are in approximately 4- to 1500-μM concentration range in human urine.[1] In blood plasma, amino acids are typically found in 7- to 721-μM concentration range.[2] However, amino acids measured in tissue such as liver can be in wide concentration range from 0.01 to 7.5 mmol per kilogram of tissue.[3] Taking into the consideration that measured samples are often extracted and concentrated, the final concentration range in measurement-ready samples can be much wider. Hence, methods of quantification of amino acids working in wide concentration range are needed.

Matrix-assisted laser desorption ionization mass spectrometry (MALDI-MS) is one of the most common soft ionization methods used in modern mass spectrometry (MS) instruments. This method has been applied in various type of analyses e.g. proteomics, microorganism identification or cancer drug analysis.[4,5] Despite all its advantages (high sensitivity, rapidness and efficiency), the MALDI method is rarely used for detection and quantification of low molecular weight (LMW) compounds. The main problem is the need for application of matrices, which are usually low molecular weight acids and during analysis produce variety of ions which may interfere with signals of analyzed sample in low mass range.[6] This problem can be solved with application of nanoparticles instead of traditional organic matrices; many articles have been published showing the use of nanoparticles in LMW analysis.[7–10]

https://doi.org/10.1002/jms.4815

Monoisotopic silver-109 nanoparticles (^{109}AgNPs) were found to be very efficient for cationization of various type of compounds, for example, amino acids, fatty acids, saccharides, or mould toxins.[11–14] In this article, we present quantification result of amino acids on steel plate covered with chemically pure silver-109 nanoparticles produced by a new method with the use of 1064-nm pulsed fiber laser with 2D galvanometer scanner. We also compare manual laser desorption/ionization mass spectrometry (LDI MS) and semiautomatic laser desorption/ionization mass spectrometry imaging (LDI MSI) in quantification of amino acids along with discussion of results and comparison with various surface-assisted laser desorption ionization (SALDI) and MALDI methods previously used in amino acids analysis.

2 | EXPERIMENTAL SECTION

2.1 | Materials

All amino acid standards were purchased from Sigma-Aldrich. Steel targets were machined from H17 stainless steel. Before the LDI MS and MS imaging experiments steel targets were cleaned through soaking in boiling solvents: toluene (3 × 100 ml, each plate for 30 s), chloroform (3 × 100 ml, each plate for 30 s), acetonitrile (3 × 100 ml, each plate for 30 s) and deionized water (3 × 100 ml, each plate for 30 s). Every plate was dried in high vacuum (ca. 0.01 mbar, 24 h). All solvents were of HPLC quality, except for water (18 MΩ · cm water produced locally).

2.2 | Pulsed fiber laser (PFL) 2D galvo-scanner (2D GS) laser generated nanomaterial (LGN) of silver-109 nanoparticles

The silver-109 foil (~1 mm thick, 99.7% isotopic purity) was bought from Trace Sciences International (USA) was placed at the bottom of a glass vessel containing solvent (acetonitrile). The ^{109}Ag foil was covered by an approximately 3-mm thick layer of acetonitrile (total solvent volume was 3 ml). The laser ablation was carried out with a 1064-nm pulsed fiber laser (Raycus RFL-P20QE/A3). Suspension was obtained after 2 min. Irradiation with pulse energy of 0.8 mJ (100-ns pulse length) at a 40-kHz repetition rate. Laser ablation was accomplished at a scanning speed of 2000 mm/s; the ablation area was 4 × 4 mm. Suspension was immediately transferred into a syringe and used in the nebulization step.

2.3 | Nebulization of ^{109}AgNPs suspension

The entire nanoparticle nebulization process was controlled by a computer. The H17 steel plate (laser mass spectrometry target plate) was placed on the table of a translation system consisting of a motorized XY table (powered by closed-loop servomotors). Glass syringe (1 ml) was filled with a previously prepared suspension of silver-109 nanoparticles and placed in a syringe pump (pumping speed 250 μl/min). The custom-made software directed the 2D system table with 10 mm/s translation speed using a sequence of movements prepared to uniformly cover a target plate. Nebulizer was typical, standard flow Bruker ion source 'needle' or nebulizer. Argon at a pressure of 2 bar was used as the nebulizing gas. Studied objects—for MS and MSI—were placed on the target plate before nebulization.

2.4 | Sample preparation and handling

All amino acids standards (alanine, isoleucine, lysine, and phenylalanine) were dissolved in water to give a final concentration of 1 mg/ml. Lower concentrations were prepared by diluting of ten-times higher concentration ones. Volume of 0.5 μl of plasma was dissolved in 249.5 μl of ultrapure water. Volumes of 0.5 μl of amino acid and plasma solutions were placed directly on target plate, air dried, and then target was nebulized with ^{109}AgNPs suspension as stated in previous subchapter.

2.5 | LDI mass spectrometry

Laser desorption/ionization–time-of-flight (LDI-ToF) mass spectrometry experiments were performed in reflectron mode using Bruker Autoflex Speed time-of-flight mass spectrometer equipped with a SmartBeam II laser (355 nm). Laser impulse energy was approximately 90–140 μJ, laser repetition rate 1000 Hz. The total number of laser shots was 4000 for each spot. This amount of laser shots was divided into four, symmetrically positioned points laying in distance of approximately 1/3 of spot radius from its center. At each point, 1000 laser shots were made with default random walk applied (random points with 50 laser shots). Measurement range was *m/z* 80–1500. Suppression was turned on typically for ions of *m/z* lower than 80. Reflector voltages used were 21 kV (the first) and 9.55 kV (the second). The data were calibrated and analyzed with FlexAnalysis (version 3.3) using centroid calibration model. Mass calibration (enhanced cubic calibration based on 8–9 calibration points) was performed using internal standards (silver-109 ions and clusters from $^{109}\mathrm{Ag}^{+}$ to $^{109}\mathrm{Ag}_9{}^{+}$).

2.6 | LDI mass spectrometry imaging

Measurements were performed using a Bruker Autoflex Speed time-of-flight mass spectrometer in reflectron positive mode. The apparatus was equipped with a SmartBeam II 1000 Hz 352 nm laser. Laser impulse energy was approximately 100–120 μJ, laser repetition rate was 1000 Hz, and deflection was set on *m/z* lower than 80 Da. The *m/z* range was 80–1500 and spatial resolution 500 × 500 μm. The imaging experiments were made with 2000 laser shots per individual spot with a default random walk applied (FlexImaging 4.0). All spectra were precalibrated (cubic calibration function) with the use of silver-109 ions ($^{109}\mathrm{Ag}^{+}$ to $^{109}\mathrm{Ag}_9{}^{+}$) as internal standard. The first accelerating voltage was held at 19 kV, and the second ion source voltage was held at 16.7 kV. Reflector voltages used were 21 kV (the first) and 9.55 kV (the second). All of the shown imaging pictures are for ±0.05% *m/z* window. MSI experiments were performed on all spots of amino acid standards and blood plasma solution.

3 | RESULTS AND DISCUSSION

Monoisotopic silver-109 nanoparticles (^{109}AgNPs) were prepared by PFL laser generated nanomaterial with the use of 2D galvo-scanner and nebulization. This method, compared to the preparation of ^{109}AgNPs by chemical synthesis, is much faster reducing the target preparation time from 24 h to few minutes. It is also cost-effective, as no other chemicals are required and the silver-109 metal foil can be reused.[15]

3.1 | Quantification results

The LDI MS and MSI LDI MS measurements using monoisotopic silver-109 PFL 2D GS LGN were performed for four amino acids such as: alanine, isoleucine, phenylalanine and lysine. Amino acids were directly measured in concentrations ranging from 1 mg/ml to 1 ng/ml which equates to 1 000 000-fold concentration change. Limit of detection (LOD) values were calculated with the use of signal/noise (S/N) ratio values obtained from spectrum of lowest concentration samples that contained signal of interest. Every sample was placed on target plate in 0.5-μl volume equating to 500 ng to 500 fg of amino acid per measurement spot which is approximately 3.03 nmol to 3 fmol, respectively, calculated for example for phenylalanine (Phe) molar mass. A regression analysis of the obtained intensity data against the concentration was also performed. The use of mass spectrometry imaging for the quantification of amino acids allowed to obtain a very good result of the correlation with the R^2 above 0.99, which indicates the usefulness of MSI for quantitative analysis. It should be noted that the regressions were performed over a very wide concentration range for all seven tested concentrations.

Alanine (Ala) is one of α-amino acids used for the ribosome-mediated biosynthesis of proteins.[16] In mammals, alanine plays a key role in the glucose-alanine cycle. This cycle allows pyruvate and glutamate to be removed from muscle and transported to the liver. There pyruvate is used to regenerate glucose, which is returned to the muscles where it is metabolized for energy. In this way, the energy burden of gluconeogenesis is transferred to the liver instead of to the muscles, and all available ATP in the muscles can be allocated to muscle contraction. Alterations in the alanine cycle that increase the levels of serum alanine aminotransferase (ALT) are linked to the development of type II diabetes.[17]

Figure 1 presents results LDI MS and MSI analysis for alanine with ^{109}AgNPs PFL 2D GS laser generated nanomaterial. Manually made measurements were taken at four random locations, which is presented in Figure 1A. Alanine was found in spectra mainly as silver-109 adduct of $[\mathrm{Ala} + {}^{109}\mathrm{Ag}]^+$ ion formula in amounts of 500 ng to 50 pg per sample spot. Intensities of alanine-silver-109 adduct peaks were of $3.8{\cdot}10^4$ for the highest concentration, $1.5{\cdot}10^5$ for 100 μg/ml, $1.1{\cdot}10^5$ for 10 μg/ml, $1.5{\cdot}10^4$ for 1 μg/ml and $4.5{\cdot}10^3$ for 100 ng/ml. What is interesting, in manual measurement mode, the intensity for the alanine signal for the first concentration is lower than the intensity for 10- and 100-times lower concentrations (Figure 1B). This is an effect of manual placement of measurement regions, an effect existing in commonly made manual measurements of MALDI method. Comparison of results of matching the regression function to experimental results for manual MS and semiautomatic MSI measurements is presented in Table 1. Regression analysis of this data provided trendline with R^2 value 0.937 (disregarding the highest concentration). However, the best fit obtained using polynomial trendline with R^2 equals 0.962.

Mass spectrometry imaging uses a grid or raster of measurement points with specified resolution, as shown in Figure 1C. Application of MSI for analysis the same samples allowed detection of signals alanine-silver-109 adduct in all concentrations (Figure 1D). Linear regression function for LDI MS and MSI LDI MS gives similar values R^2, which was equal 0.937 and 0.936 respectively. Significantly lower R^2 values were obtained by using the power and exponential trendlines. The best results were obtained again using polynomial trendline ($R^2 = 0.975$), which is superior to manual measurements.

As can be seen on Figure 1D, ion images prove that studied amino acid is deposited nonuniformly throughout of all studied sample spots. The best fit for analysis of alanine by MSI was obtained for data set for 1 mg/ml to 10 μg/ml concentrations (Figure S1). Limit of detection based on S/N ratio of 3 was found to be 178 pg (1.99 pmol) of alanine per measured spot for LDI MS. In contrast, LOD for MSI LDI MS was found to be 1094 pg (12.28 pmol) per measured spot.

Amino acids were detected by Alterman et al. with using of MALDI. Limit of quantitation for alanine of 0.14 μM which is approximately 12 ng/ml.[18] Also, another researcher—Soga et al.—used capillary electrophoresis-electrospray ionization-tandem mass spectrometry (CE-ESI-MS/MS) for quantification amino acids i.a. alanine, obtaining limit of detection of 8.8 μM.[19]

The next analyzed amino acid was isoleucine (Ile). It is one of the branched-chain amino acids (BCAAs) for protein synthesis in human body for example hemoglobin, regulation of blood sugar and energy levels. It has also been observed that an increase in isoleucine, like other BCAAs, occurs in people with diabetes, indicating a relationship between isoleucine and insulin resistance.[20] Results of LDI MS and MSI analysis for isoleucine with PFL 2D GS LGN-produced ^{109}AgNPs were presented in Figure 1. Similarly as alanine, measurements of Ile were taken at four random locations, which is presented in Figure 1A. Isoleucine was found in spectra mainly as silver-109 adduct of $[\mathrm{Ile} + {}^{109}\mathrm{Ag}]^+$ ion formula in 1 mg/ml to 1 μg/ml samples. Isoleucine reported similar problem as in case alanine for random measurement points chose in LDI MS. Chart of logarithm of intensity vs. logarithm of concentration (Figure 1B) presents relatively high intensity for 10 μg/ml ($8.3{\cdot}10^4$) concentration and much lower for the other ones. LODs were 5890 ng/ml (2945 pg/spot). Data analysis with the use of

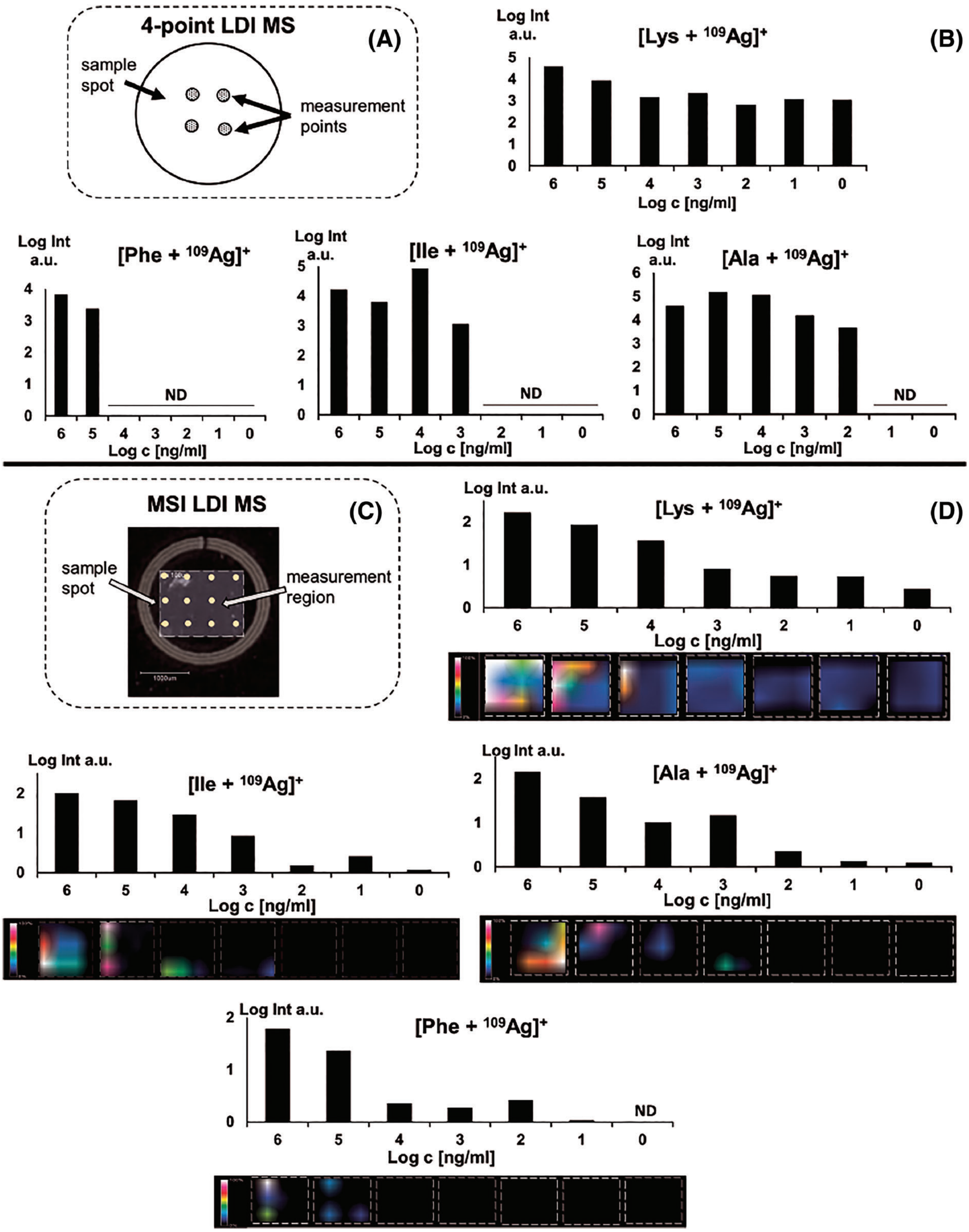

FIGURE 1 Panel A shows scheme of manual LDI MS measurement with 4 random measure points. Column charts (B and D for MS and MSI, respectively) present quantitative results for [amino acid + ^{109}Ag]$^+$ ion as logarithm of the intensity versus logarithm of the concentration for four different amino acids. Panel C presents photograph of sample spot on target plate and measurement region for MSI LDI MS with grid of measurement points. ND—not detected

different types of regression functions for LDI MS allowed to obtain the highest value for a polynomial trend line with an R^2 value of 0.434. This problem was again solved by using mass spectrometry imaging with a raster of measurement points with specified resolution, as shown in Figure 1C. The value of the regression coefficient for the linear trendline is 0.153 for the LDI MS, and for MSI is 0.926.

TABLE 1 Comparison of regression function and R^2 values for manual MS and semiautomatic MSI measurements

Amino acid	Regression function	LDI MS		LDI MSI	
		Regression equation	R^2	Regression equation	R^2
Ala	Exponential	$\text{Log Int} = -6.0819e^{-0.12 \log c}$	0.918	$\text{Log Int} = 5.6953e^{-0.687 \log c}$	0.891
	Linear	$\text{Log Int} = -0.5444 \log c + 5.8709$	0.937	$\text{Log Int} = -0.4406 \log c + 2.4565$	0.936
	Power	$\text{Log Int} = 5.439 \log c^{-0.248}$	0.795	$\text{Log Int} = 3.7367 \log c^{-1.809}$	0.722
	Polynomial	$\text{Log Int} = -0.0975 \log c^2 - 0.0568 \log c + 5.3833$	0.962	**$\text{Log Int} = 0.0613 \log c^2 - 0.8699 \log c + 3.0289$**	**0.975**
Ile	Exponential	$\log \text{Int} = 4.7044e^{-0.071 \log c}$	0.140	$\log \text{Int} = 4.958e^{-0.525 \log c}$	0.818
	Linear	$\text{Log Int} = -0.2374 \log c + 4.5907$	0.153	$\log \text{Int} = -0.3517 \log c + 2.3914$	0.926
	Power	$\log \text{Int} = 4.345 \log c^{-0.124}$	0.089	$\log \text{Int} = 3.7771 \log c^{-1.501}$	0.596
	Polynomial	$\log \text{Int} = -0.3601 \log c^2 + 1.563 \log c + 2.7903$	0.434	**$\log \text{Int} = 0.0207 \log c^2 - 0.5169 \log c + 2.6393$**	**0.936**
Lys	Exponential	$\log \text{Int} = 4.3923e^{-0.066 \log c}$	0.737	$\log \text{Int} = 3.1124e^{-0.271 \log c}$	0.961
	Linear	$\log \text{Int} = -0.2385 \log c + 4.3752$	0.693	$\log \text{Int} = -0.3074 \log c + 2.4488$	0.935
	Power	$\log \text{Int} = 4.4655 \log c^{-0.229}$	0.890	$\log \text{Int} = 2.8418 \log c^{-0.815}$	0.826
	Polynomial	$\log \text{Int} = 0.0795 \log c^2 - 0.8743 \log c + 5.3289$	0.924	**$\log \text{Int} = 0.0332 \log c^2 - 0.5729 \log c + 2.8471$**	**0.968**
Phe	Exponential	NA	NA	$\log \text{Int} = 3.9933e^{-0.661 \log c}$	0.906
	Linear	NA	NA	$\log \text{Int} = -0.3329 \log c + 1.8712$	0.800
	Power	NA	NA	$\log \text{Int} = 2.7232 \log c^{-1.761}$	0.787
	Polynomial	NA	NA	**$\log \text{Int} = 0.0853 \log c^2 - 0.93 \log c + 2.6674$**	**0.912**

Note: The best results are marked in bold.
Abbreviation: NA, not applicable.

Moreover, the best fit was obtained for the polynomial trendline with R^2 equals 0.936 in MSI measurement mode. The best linear fit for analysis isoleucine by MSI was obtained for set of concentrations from 1 mg/ml to 1 μg/ml with R^2 value of 0.955 (Figure S2). This amino acid was previously studied by Soga et al. that used capillary electrophoresis-electrospray ionization-tandem mass spectrometry (CE-ESI-MS/MS) for isoleucine with limit of detection was 1.0 μM.[19]

Another studied amino acid was lysine (Lys) which is classified as basic and aliphatic amino acid. It has been implicated to play a key role in biosynthesis of proteins, for example, structural proteins of connective tissues. The importance of lysine in many biological processes means that both underexpression and overexpression of lysine can have an adverse effect on the human body, resulting in disease.[21] Figure 1 presents results analysis LDI MS and MSI for lysine with ^{109}AgNPs produced PFL 2D GS LGN. The method of measurement of Lys with results is presented in Figure 1A. Lysine was found in spectra mainly as silver-109 adduct of $[\text{Lys} + {}^{109}\text{Ag}]^+$ with adduct monoisotopic *m/z* value of 255.0095. Bar chart of logarithm of intensity vs. logarithm of concentration (Figure 1B) presents the highest intensities for the two first concentrations and much lower for the others. Limit of detection was found to be 3.06 ng (20.89 pmol) of lysine per measured spot. Signals of lysine were found in spectra of all concentrations. For both the LDI MS and the MSI LDI MS, the best fit was obtained using a polynomial trendline, with R^2 0.924. However, application of MSI allowed much better fit of R^2 being 0.968. Moreover, the best linear fit for analysis of lysine by MSI was for 1 mg/ml to 1 μg/ml sample set with R^2 value of 0.972 (Figure S3). Again, MSI ion images (Figure 1D) proved nonuniform compound localization that is the reason of much better MSI results compared to manual measurements.

The last studied amino acid was phenylalanine which contains neutral and nonpolar benzyl side chain. Phe is precursor of tyrosine and some neurotransmitters as dopamine, epinephrine and norepinephrine. The concentration of phenylalanine in the blood is of great importance for people with a genetic condition called phenylketonuria. Patients must regulate their intake of phenylalanine due to their body's inability to metabolize it.[21] Figure 1 presents results of manual measurements (LDI MS) and semiautomatic MSI for phenylalanine with ^{109}AgNPs PFL 2D GS LGN (Figure 1A). Phenylalanine was found in spectra mainly as silver-109 adduct of $[\text{Phe} + {}^{109}\text{Ag}]^+$ at *m/z* value of 273.9830. The results of manual measurements for phenylalanine are shown in the bar graph in Figure 1B. Signals were found for only two highest concentrations. LOD was found to be 37 437 pg (226.3 pmol) of phenylalanine per measured spot. The bar chart of logarithm of signal intensity correlated with logarithm of compound concentration obtained by MSI with a series of ion images for the adduct $[\text{Phe} + {}^{109}\text{Ag}]^+$ adduct is shown in Figure 1D. Application of MSI allowed finding signals Phe-silver-109 in all concentrations. Data analysis with the use of different types of regression functions for MSI LDI MS allowed to obtain the highest value for a polynomial

TABLE 2 Comparison of LOD and LLOQ values for manual and LDI MSI measurements

	LDI MS		LDI MSI	
Amino acid	**LOD (ng/ml) µM**	**LLOQ (ng/ml)**	**LOD (ng/ml) µM**	**LLOQ (ng/ml)**
Alanine	360 ± 360 4	590 ± 600	2190 ± 2190 30	3650 ± 3640
Isoleucine	5890 ± 7820 50	9820 ± 13 040	3250 ± 2380 30	5420 ± 3970
Lysine	6110 ± 4800 40	10 180 ± 8000	1250 ± 1330 10	2080 ± 2220
Phenylalanine	74 870 ± 68 120 450	124 790 ± 113 530	5390 ± 3090 30	8980 ± 5150

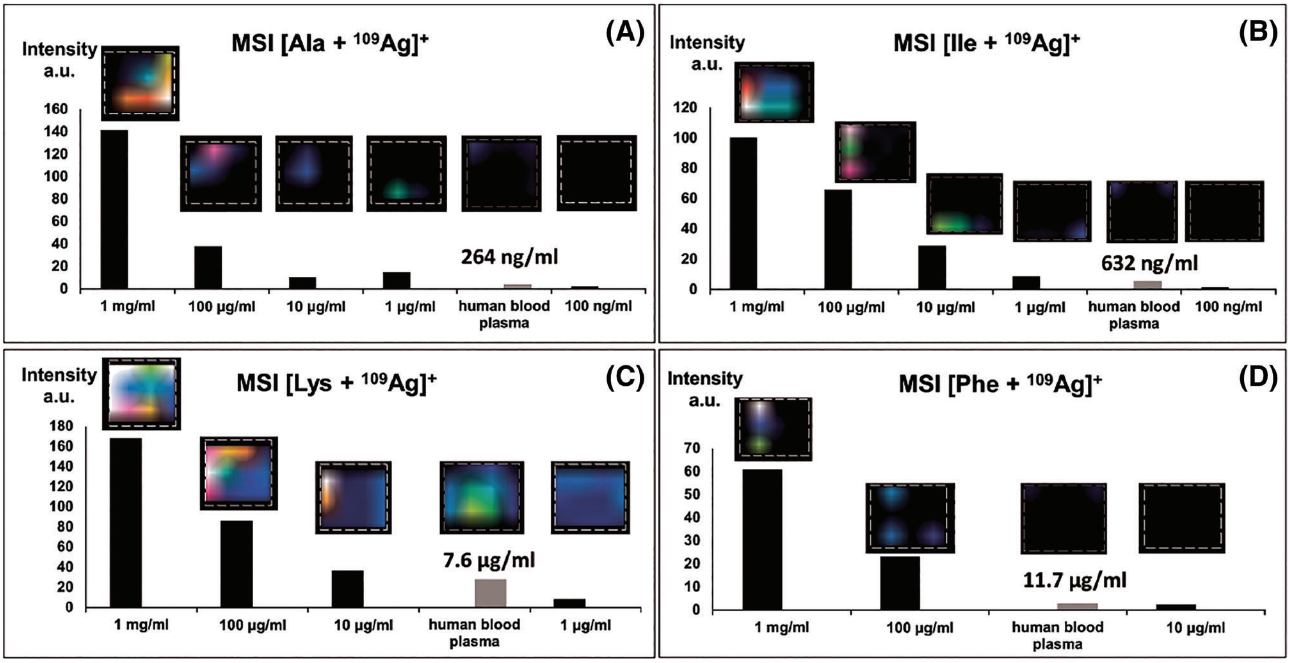

FIGURE 2 Results of quantitative analysis of selected amino acids in human blood plasma by LDI MSI with monoisotopic silver-109 nanoparticles PFL 2D GS LGN. For each identified amino acid, its labelled concentration in 0.5-µl 500-fold diluted blood plasma is given

trend line with an R^2 value of 0.912. The best linear fit for analysis phenylalanine by MSI was for 1 mg/ml to 10 µg/ml samples with R^2 value is 0.948 (Figure S4).

Table 2 shows the LOD and LLOQ values obtained for the amino acids tested by manual measurements and LDI MSI methods, respectively. Using the mass spectrometry imaging, a lower limit of detection value was achieved. In the case of lysine obtained LOD value was about 4.5 times lower. The results obtained with LDI MSI lower the randomness of the measurements, thereby providing a much more reliable quantitative analysis.

Considering the use of ^{109}AgNPs PFL 2D GS LGN in MSI to determine plasma free amino acid concentrations, the obtained LOD values of amino acids were compared with literature data. Duran[2] presented reference plasma amino acid concentration values for different age groups. For subjects over 18 years of age, the concentrations for Ala, Ile, Lys, and Phe were 182–552, 34–84, 111–248, and 39–74 µM, respectively. The reported values are much higher than the obtained LOD values in MSI experiments, so it can be concluded that the amino acids shown should be detectable in plasma.

A spot-to-spot and shot-to-shot reproducibility analysis was also performed. The obtained results are presented in bar charts in Figure S5. The results of the shot-to-shot analysis for all tested amino acids show 15% differences of intensity of the signal from the analyte. The results of the spot-to-spot analysis of isoleucine show 4% differences in signal intensities. In turn, for lysine and phenylalanine, the differences in intensities are equal 15% and 10%.

3.2 | Detection of amino acids in human blood plasma

Results obtained for water solutions of amino acids were compared to the ones based on human blood plasma in order to estimate suppression effect of biological matrix. Plasma sample had been 500-fold diluted in deionized water. The highest intensity signals for the tested amino acids in plasma were found on the MS spectrum as adducts with monoisotopic silver-109.

Figure 2 summarizes the ion images obtained from the LDI MSI experiment for single amino acid solutions and a diluted blood sample, including a plot of the amino acid-silver-109 adduct signal intensity versus concentration. The determined concentrations of alanine, isoleucine, lysine and phenylalanine identified in 0.5 μl of sample were 3.8 μg/ml, 632 ng/ml, 7.6 μg/ml, and 11.7 μg/ml respectively. Considering a 500-fold dilution of the sample, the calculated plasma amino acid concentrations are 168 μM for Ala, 41 μM for Ile, 558 μM for Lys, and 969 μM for Phe, respectively. Of the values obtained, only the concentration of Ile falls within the range given by Duran.[2] Alanine is just below normal, while lysine and phenylalanine are significantly above the ranges presented. The reason for such discrepancies in amino acid concentrations may be due to the diet, as shown by Schmidt et al.[22]They presented analysis showed that plasma concentrations of i.a. lysine and alanine differed by habitual diet group. Moreover, many studies indicate that changes in amino acid concentrations are associated with disease occurrence or progression.[17,20,21] Additionally, it is important to remember that higher concentration of Ile also originates from Leu which is of the same molecular formula. Moreover, in case of laser methods usually biological mixture separation by chromatography is omitted due to low technical compatibility, and that may introduce interferences from other compounds of complex sample.

4 | CONCLUSION

Application of monoisotopic silver-109 nanoparticles generated by new method PFL 2D GS LGN for manual LDI MS and semiautomatic LDI MSI allowed detection and quantification of amino acids in a wide range of concentration. LOD and R^2 values obtained for both types of experiments indicate that mass spectrometry imaging method allows much better quantification than for commonly used MALDI manual measurements. Ion images obtained in MSI experiments proved highly nonuniform analyte deposition that makes semiautomatic, multipixel MSI a modern requirement rather than improvement.

ACKNOWLEDGMENT

This work was supported by the National Science Centre (NCN), SONATA grant no. UMO-2018/31/D/ST4/00109.

CONFLICT OF INTEREST

The authors declare no competing and financial interest.

DATA AVAILABILITY STATEMENT

The data that support the findings of this study are available from the corresponding author upon reasonable request.

ORCID

Aneta Płaza-Altamer https://orcid.org/0000-0003-1719-8730
Artur Kołodziej https://orcid.org/0000-0002-9222-0937
Joanna Nizioł https://orcid.org/0000-0002-4783-8615
Tomasz Ruman https://orcid.org/0000-0002-9899-8627

REFERENCES

1. Harada M, Karakawa S, Miyano H, Shimbo K. Simultaneous analysis of d,l-amino acids in human urine using a chirality-switchable biaryl axial tag and liquid chromatography electrospray ionization tandem mass spectrometry. *Symmetry*. 2020;12(6):913. doi:10.3390/sym12060913
2. Duran M. Amino acids. In: Blau N, Duran M, Gibson KM, eds, *Laboratory Guide to the Methods in Biochemical Genetics*. Springer; 2008:53-89. doi:10.1007/978-3-540-76698-8_5
3. Barle H, Ahlman B, Nyberg B, Andersson K, Essén P, Wernerman J. The concentrations of free amino acids in human liver tissue obtained during laparoscopic surgery. *Clin Physiol*. 1996;16(3):217-227. doi:10.1111/j.1475-097X.1996.tb00570.x
4. Oviaño M, Rodríguez-Sánchez B. MALDI-TOF mass spectrometry in the 21st century clinical microbiology laboratory. *Enfermedades Infecc Microbiol Clin Engl Ed*. 2021;39(4):192-200. doi:10.1016/j.eimc.2020.02.027
5. He Q, Sun C, Liu J, Pan Y. MALDI-MSI analysis of cancer drugs: Significance, advances, and applications. *TrAC Trends Analyt Chem*. 2021;136:116183. doi:10.1016/j.trac.2021.116183
6. Qiao Z, Lissel F. MALDI matrices for the analysis of low molecular weight compounds: rational design, challenges and perspectives. *Chem Asian J*. 2021;16(8):868-878. doi:10.1002/asia.202100044
7. Sekuła J, Nizioł J, Rode W, Ruman T. Gold nanoparticle-enhanced target (AuNPET) as universal solution for laser desorption/ionization mass spectrometry analysis and imaging of low molecular weight compounds. *Anal Chim Acta*. 2015;875:61-72. doi:10.1016/j.aca.2015.01.046
8. Gamez RC, Castellana ET, Russell DH. Sol–gel-derived silver-nanoparticle-embedded thin film for mass spectrometry-based biosensing. *Langmuir*. 2013;29(21):6502-6507. doi:10.1021/la4008526
9. Jackson SN, Baldwin K, Muller L, et al. Imaging of lipids in rat heart by MALDI-MS with silver nanoparticles. *Anal Bioanal Chem*. 2014;406(5):1377-1386. doi:10.1007/s00216-013-7525-6
10. Zhao Y-Z, Xu Y, Gong C, Ju Y-R, Liu Z-X, Xu X. Analysis of small molecule compounds by matrix-assisted laser desorption ionization mass spectrometry with Fe_3O_4 nanoparticles as matrix. *Chinese J Anal Chem*. 2021;49(1):103-112. doi:10.1016/s1872-2040(20)60074-3
11. Arendowski A, Nizioł J, Ruman T. Silver-109-based laser desorption/ionization mass spectrometry method for detection and quantification of amino acids. *J Mass Spectrom*. 2018;53(4):369-378. doi:10.1002/jms.4068
12. Szulc J, Kołodziej A, Ruman T. Silver-109/silver/gold nanoparticle-enhanced target surface-assisted laser desorption/ionisation mass spectrometry—the new methods for an assessment of mycotoxin concentration on building materials. *Toxins*. 2021;13(1):45. doi:10.3390/toxins13010045
13. Kołodziej A, Ruman T, Nizioł J. Gold and silver nanoparticles-based laser desorption/ionization mass spectrometry method for detection and quantification of carboxylic acids. *J Mass Spectrom*. 2020;55(10):e4604. doi:10.1002/jms.4604
14. Nizioł J, Rode W, Laskowska B, Ruman T. Novel monoisotopic 109AgNPET for laser desorption/ionization mass spectrometry. *Anal Chem*. 2013;85(3):1926-1931. doi:10.1021/ac303770y
15. Płaza A, Kołodziej A, Nizioł J, Ruman T. Laser ablation synthesis in solution and nebulization of silver-109 nanoparticles for mass spectrometry and mass spectrometry imaging. *ACS Meas Sci Au*. 2021. doi:10.1021/acsmeasuresciau.1c00020
16. Nelson DL, Cox MM, Lehninger AL. *Principles of Biochemistry*. 4th ed. New York: W. H. Freeman; 2005.
17. Popović I, Nešić M, Vranješ M, Šaponjić Z, Petković M. TiO_2 nanocrystals – assisted laser desorption and ionization time-of-flight mass spectrometric analysis of steroid hormones, amino acids and

saccharides. Validation and comparison of methods. *RSC Adv*. 2016; 6(2):1027-1036. doi:10.1039/c5ra20042c

18. Alterman MA, Gogichayeva NV, Kornilayev BA. Matrix-assisted laser desorption/ionization time-of-flight mass spectrometry-based amino acid analysis. *Anal Biochem*. 2004;335(2):184-191. doi:10.1016/j.ab.2004.06.031
19. Soga T, Kakazu Y, Robert M, Tomita M, Nishioka T. Qualitative and quantitative analysis of amino acids by capillary electrophoresis-electrospray ionization-tandem mass spectrometry. *Electrophoresis*. 2004;25(13):1964-1972. doi:10.1002/elps.200305791
20. Cole JT. Metabolism of BCAAs. In: Rajendram R, Preedy VR, Patel VB, eds. *Branched Chain Amino Acids in Clinical Nutrition*. *Nutrition and Health*. Humana Press; 2015;1(1):13-24. doi:10.1007/978-1-4939-1923-9_2
21. Sprenger AG. Aromatic amino acids. In: Wendisch VF, ed. *Amino Acid Biosynthesis: Pathways, Regulation and Metabolic Engineering*. 1st ed. Springer; 2007. doi:10.1007/7171_2006_067
22. Schmidt JA, Rinaldi S, Scalbert A, et al. Plasma concentrations and intakes of amino acids in male meat-eaters, fish-eaters, vegetarians and vegans: a cross-sectional analysis in the EPIC-Oxford cohort. *Eur J Clin Nutr*. 2016;70(3):306-312. doi:10.1038/ejcn.2015.144

SUPPORTING INFORMATION

Additional supporting information may be found in the online version of the article at the publisher's website.

How to cite this article: Płaza-Altamer A, Kołodziej A, Nizioł J, Ruman T. Infrared pulsed fiber laser-produced silver-109-nanoparticles for laser desorption/ionization mass spectrometry of amino acids. *J Mass Spectrom*. 2022;57(3): e4815. doi:10.1002/jms.4815

Advances in Medical Sciences 68 (2023) 38–45

Contents lists available at ScienceDirect

Advances in Medical Sciences

journal homepage: www.elsevier.com/locate/advms

Monoisotopic silver nanoparticles-based mass spectrometry imaging of human bladder cancer tissue: Biomarker discovery

Krzysztof Ossoliński [a], Tomasz Ruman [b], Tadeusz Ossoliński [a], Anna Ossolińska [a], Adrian Arendowski [b], Artur Kołodziej [b,c], Aneta Płaza-Altamer [b,c], Joanna Nizioł [b,*]

[a] *Department of Urology, John Paul II Hospital, Kolbuszowa, Poland*
[b] *Rzeszów University of Technology, Faculty of Chemistry, Rzeszów, Poland*
[c] *Doctoral School of Engineering and Technical Sciences at the Rzeszów University of Technology, Rzeszów, Poland*

ARTICLE INFO

Keywords:
Silver nanoparticles
LDI-MS
Biomarkers
Bladder cancer
Human tumor tissue

ABSTRACT

Purpose: Bladder cancer (BC) is the 10th most common form of cancer worldwide and the 2nd most common cancer of the urinary tract after prostate cancer, taking into account both incidence and prevalence.
Materials/methods: Tissues from patients with BC and also tissue extracts were analyzed by laser desorption/ionization mass spectrometry imaging (LDI-MSI) with monoisotopic silver-109 nanoparticles-enhanced target (^{109}AgNPET).
Results: Univariate and multivariate statistical analyses revealed 10 metabolites that differentiated between tumor and normal tissues from six patients with diagnosed BC. Selected metabolites are discussed in detail in relation to their mass spectrometry (MS) imaging results. The pathway analysis enabled us to link these compounds with 17 metabolic pathways.
Conclusions: According to receiver operating characteristic (ROC) analysis of biomarkers, 10 known metabolites were identified as the new potential biomarkers with areas under the curve (AUC) higher than >0.99. In both univariate and multivariate analysis, it was predicted that these compounds could serve as useful discriminators of cancerous versus normal tissue in patients diagnosed with BC.

1. Introduction

Bladder cancer (BC) is the 12th most common form of cancer worldwide and the 2nd most common cancer of the urinary tract after prostate cancer, taking into account both incidence and prevalence [1]. Globally, 573,278 new cases of BC were diagnosed in 2020. In terms of incidence, it is the 6th most common cancer in men, the 17th in women and the 10th most frequent cancer in both sexes [1]. Cystoscopic examination of bladder remains the gold standard for BC diagnosis, but it is invasive, associated with discomfort, sometimes painful and costly. It is estimated that 4–27% of tumors are omitted during the examination. This value increases to 32–77% in the case of carcinoma *in situ* (CIS) [2].

In recent years, numerous urine-based BC biomarkers have been evaluated but currently there is no reliable diagnostic and prognostic BC biomarker that has been accepted for diagnosis and follow-up in routine practice or clinical guidelines and which could be an alternative to cystoscopy. Over the past decade, due to the molecular specificity and sensitivity mass spectrometry (MS) has been used as a main technique in biomarker discovery field [3]. Two-dimensional variety of MS – mass spectrometry imaging (MSI) plays an increasingly important role in the field of molecular imaging because it allows direct mapping of the distribution of a variety of endogenous and exogenous compounds within biological tissues with high specificity and without the need for radioactive or fluorescent radioactive labelling normally used in histochemical protocols [4]. BC tissues were studied previously with MSI techniques such as matrix-assisted laser desorption ionization (MALDI) [5] and desorption electrospray ionization (DESI) [6]. It should be noted that there are no BC MS and MSI results made with the use of nanoparticle-based methods published to date. It is important to state that nanoparticle-based methods have many advantages with regard to other methods including very efficient cationization of low molecular weight compounds, relatively high sensitivity of analyte detection, very low chemical background and high mass accuracy due to internal calibration, unlike commonly used one - MALDI. They allow for higher lateral resolutions and higher sensitivity when compared to DESI. In our recent publications we presented new methods such as gold nanoparticle-enhanced target (AuNPET) [7], silver

---

* Corresponding author. University of Technology, Faculty of Chemistry, 6 Powstańców Warszawy Ave., 35-959, Rzeszów, Poland.
E-mail address: jniziol@prz.edu.pl (J. Nizioł).

https://doi.org/10.1016/j.advms.2022.12.002
Received 21 May 2022; Received in revised form 5 September 2022; Accepted 8 December 2022

nanoparticle-enhanced target (AgNPET) [8] and monoisotopic silver-109 nanoparticles-enhanced target (^{109}AgNPET) [9] with results of their application for imaging of plant, animal and human tissues [10–12].

2. Materials and methods

2.1. Participants

Cancer and normal tissue samples were collected from 6 patients (Caucasian race, average age 65 years, 2 females and 4 males) with diagnosed BC at John Paul II Hospital in Kolbuszowa (Poland). All patients underwent transurethral resection of bladder tumor (TURBT) following a detailed clinical history and laboratory examination. Each of these patients had at least an abdominal ultrasound to exclude other tumors (patients with urolithiasis usually also had a CT scan) and a basic package of laboratory tests required for urological surgery to exclude inflammation. Whole tumor and a small fragment of adjacent healthy uroephitelium were resected (cancer and control tissue). The histopathological analysis of resected tumors from all patients, confirmed non-invasive (pTa) low-grade (LG) urothelial papillary carcinoma, according to 2004 WHO grading system [13,14]. Control tissues were free of cancer cells. The clinical characteristics of the patients are presented in Supplementary Table S1.

2.2. Materials and equipment

Silver-109 (min. 99.75% of ^{109}Ag) isotope was purchased from BuyIsotope (Neonest AB, Stockholm, Sweden) and transformed to trifluoroacetate salt by commonly known methods (involving dissolving in HNO_3, precipitation of ^{109}AgOH and reaction with trifluoroacetic acid) and recrystallized from tetrahydrofurane/hexane system. 2,5-Dihydroxybenzoic acid (DHB) was purchased from Sigma-Aldrich (St. Louis, USA). Steel targets were locally machined from H17 stainless steel. All solvents were of high-performance liquid chromatography (HPLC) quality, except for water (18 MΩ water was produced locally) and methanol (liquid chromatography-mass spectrometry - LC MS - grade, Fluka™, (Seelze, Germany). The silver-109 nanoparticles were synthesized on the surface of steel targets as described in our recent publication [9]. Optical photographs of tissue samples were made with the use of an Olympus SZ10 microscope equipped with an 8 MPix Olympus digital camera (Hamburg, Germany).

2.3. Preparation of monoisotopic silver suspension

Four miligrams of silver-109 trifluoroacetate (^{109}AgTFA) and 14 mg of DHB were quantitatively transferred to a glass tube by dissolving in 2 ml of isopropanol and 2 ml of acetonitrile. The prepared solution was placed in an ultrasonic bath set at 50 °C for about 30 min. After this time, the suspension was ready to use.

2.4. Imaging sample preparation

Tissues from 6 patients with the same tumor stage and grade were selected for LDI-MSI analysis. Three independent imaging experiments were performed to exclude possible random results, one for tissues from patient no. 1, another for patients no. 2–4 and the last for patients no. 5 and 6. The material examined was six pairs of BC and normal tissue fragments of average 3 × 3 mm size. MS imaging for patient no. 1 was carried out within about an hour after the material was collected after surgery. Until then, the tissue samples were stored at a temperature of approx. 2–4 °C. Tissues from patients no. 2–6 were stored at −60 °C and thawed to 4 °C before the MSI measurements. To remove excess liquid material, samples were touched to cellulose filter paper (3 times). Next, with the use of sterile needles and tweezers, a few imprints of the examined tissues were made on the previously prepared ^{109}AgNPET plate. The material was transferred from the BC patients to the ^{109}AgNPET substrate by briefly touching (3 s) the tissue samples to steel surface with light pressure. Steel target with imprints was placed on a computer-controlled 3D positioning table and sprayed with nanoparticles using an electrospray ionization mass spectrometry (ESI-MS) nebulizer with nitrogen as nebulizing gas (2 bar). Target was placed in a MALDI time-of-flight MS (MALDI-ToF/ToF MS) (Autoflex Speed ToF/ToF, Bruker, Bremen, Germany) and selected imprints were then directly analyzed.

2.5. LDI-MS imaging experiments

LDI-MSI experiments were performed using a Bruker Autoflex Speed ToF/ToF mass spectrometer (MALDI ToF/ToF, Bruker, Bremen, Germany) in positive-ion reflectron mode. FlexImaging 4.0 software was used for data processing and analysis. The apparatus was equipped with a SmartBeam II 1000 Hz 355 nm laser. Laser impulse energy was approximately 100–190 μJ, laser repetition rate was 1000 Hz, and deflection was set on m/z lower than 80 Da. The m/z range was 80−2000 Da, spatial resolution 250 × 250 μm. The experiments were made with 20,000 laser shots per individual spot with a default random walk applied (random points with 50 laser shots). All spectra were calibrated with the use of silver ions (^{109}Ag$^+$ to ^{109}Ag$_{10}^+$). The first accelerating voltage was held at 19 kV, and the second ion source voltage was held at 16.7 kV. Reflector voltages used were 21 kV (the first) and 9.55 kV (the second). All of the ion images were within ±0.05% of m/z. Total ion current (TIC) normalization was used for all results shown.

2.6. Preparation of tissue extracts

Small portions of frozen neoplastic bladder tissue (n = 6) and normal control tissues (n = 6) of approximately 2 mg each were transferred to Eppendorf tubes and then homogenized by three cycles of freezing and thawing. Next to the homogenates 500 μl of 2:1 (v/v) chloroform/methanol were added and then extracted for 30 min in ultrasonic bath (at 2–4 °C.) The tubes were centrifuged for 5 min at an acceleration of 6000×g and the phases were allowed to separate. The water-methanol and methanol-chloroform phases were transferred to separate tubes and then methanol-chloroform phases were diluted 100x whereas the water-methanol phases were measured without dilution. Volume of 0.3 μl of each sample was placed on ^{109}AgNPET and allowed to dry at room temperature and target placed in a MALDI ToF/ToF MS. Tissue extracts were made to confirm the structure of the identified compounds by MS/MS measurements.

2.7. LDI-MS and MS/MS of tissue extracts

LDI-MSI experiments were performed using a Bruker Autoflex Speed MALDI ToF/ToF MS (Autoflex Speed ToF/ToF, Bruker, Bremen, Germany) in positive-ion reflectron mode. The apparatus was equipped with a SmartBeam II 1000 Hz 355 nm laser. Laser impulse energy was approximately 100–190 μJ, laser repetition rate was 1000 Hz, and deflection was set on m/z lower than 80 Da. The m/z range was 80−2000 Da. Spectrum for each extract contained data from 20k laser shots with a default random walk applied (random points with 50 laser shots). All spectra were calibrated with the use of silver ions (^{109}Ag$^+$ to ^{109}Ag$_{10}^+$). The first accelerating voltage was held at 19 kV, and the second ion source voltage was held at 16.7 kV. Reflector voltages used were 21 kV (the first) and 9.55 kV (the second). MS/MS measurements were performed using the LIFT (low mass) method [15]. The mass window for precursor ion selection used was ±0 Da. FlexAnalysis (version 4.0, Bruker, Bremen, Germany) was used for data analysis.

2.8. Data processing

The average spectra of the imprint area of cancerous and normal tissue from patient no. 1 were generated and then compared in the using the SCiLS Lab software version 2016b (SCiLS, Bremen, Germany) and FlexAnalysis (version 4.0, Bruker, Bremen, Germany). Statistical analysis was performed using the Cardinal MSI (R package) [16] with hotspot suppression and Gaussian smoothing applied and MetaboAnalyst 5.0 platform [17]. Database search of chemical compounds were carried out using a custom-made program. Theoretical *m/z* values were calculated using ChemCalc program available online [18].

Data of peak mean abundance from the entire area of the examined cancer (n = 6) and control (n = 6) tissue were formatted as comma separated values (.csv) files and uploaded to the MetaboAnalyst 5.0 server [17]. Metabolite data was checked for data integrity and normalized using MetaboAnalyst's normalization protocols (normalization by sum, log transformation and auto-scaling), both for biomarker and pathway analyses. Univariate analysis (*t*-test), fold-change analysis and orthogonal partial least squares discriminant analysis (OPLS-DA) were applied to calculate the statistical significance of the metabolites between the two groups (cancer over control). To identify the potential biomarkers associated with BC, the Receiver Operating Characteristic (ROC) curve was applied using biomarker analysis module of MetaboAnalyst v 5.0. The ROC curves were generated using an algorithm based on Monte-Carlo cross validation (MCCV) through balanced subsampling coupled with linear support vector machine (SVM) for the classification method and SVM built-in for the feature ranking method. To identify the most relevant metabolic pathways involved in BC, metabolic pathway analysis was performed using MetaboAnalyst with *Homo sapiens* pathway libraries.

3. Ethical issues

The study protocol was approved by local Bioethics Committee at the University of Rzeszow, Poland (permission no. 2018/04/10) and performed in accordance with relevant guidelines and regulations, including the 1964 Helsinki declaration and its later amendments. Specimens and clinical data from patients involved in the study were collected with written consent.

4. Results and discussion

^{109}AgNPET method was used previously for LDI-MS analysis of low molecular weight (LMW) compounds and biological material and was shown to be a promising alternative to traditional MALDI method [9,19]. LDI-MSI experiments were performed by measuring series of high-resolution MS spectra with 250 × 250 μm resolution of bladder tissue imprints of *ca.* 3 × 3 mm size made on ^{109}AgNPET target plate. In order to estimate whether there is a sample-related differentiation between cancer and normal tissue imprints, a statistical analysis was performed for patient no. 1 tissue pair. Data derived from MSI experiment were analyzed by comparison of average spectra of cancer and normal areas by spatial shrunken centroids with adaptive weights (SSCA). The mentioned method allows estimation of the probability that a location of interest belongs to a particular segment and was previously used among others for segmentation of data for whole-body MALDI MSI experiment [20]. Images of the major regions of the BC tissue from patient no. 1 were outlined by SSCA segmentation as shown in Supplementary Fig. S1. What is interesting, images generated with the aid of Cardinal MSI with SSCA method are very similar to the ion images obtained in MSI experiment and suggest that: (i) areas of imprints are clearly different from target area with no fuzzy boundaries and (ii) cancerous area is clearly different from the normal one.

4.1. Identification of metabolite biomarkers

The analysis of MSI data revealed a list of 28 compounds for which the highest abundance differences between the normal and cancerous areas. Only those ion images were selected for which the trend for a given *m/z* value was similar in all 6 experiments. As judged from generated ion images 2 adducts have higher average intensities in cancer tissue, and the next 26 ions are of higher intensity in normal tissue. The list of identified compounds is presented in Supplementary Table S2. The identity of some of compounds was confirmed with LIFT® MS/MS experiments (Supplementary Table S3). Metabolite mean abundance data from both cancer and normal tissue regions of 28 identified compounds were further subjected to supervised and unsupervised multivariate statistical analysis using the MetaboAnalyst 5.0 online software. The 2D principal components analysis (PCA) score plots of both subsets indicated good separation between the cancer and the normal tissue regions (Fig. 1A).

The best separation of groups was obtained along principal components 1 and 2 (i.e. PC1 and PC2) which accounted for 61.2% and 18.8%, respectively. The separation between the BC and normal tissue samples was further examined using the supervised multivariate statistical analysis - Orthogonal Partial Least Squares Discriminant Analysis (OPLS-DA) (Fig. 1B). We conducted 2000 permutation tests to evaluate the statistical robustness of the OPLS-DA model (Supplementary Fig. S2). Good discrimination was observed between cancer and normal groups ($Q^2 = 0.774$, $R^2Y = 0.998$, *P*-value <0.03 (0/2000)). Potential BC biomarkers were selected on the basis of the variable influence on projection (VIP) value resulting from the OPLS-DA model (Fig. 1C). By combining the VIP (>1.0) with the results from the independent *t*-test (P-value from *t*-test <0.05) and fold change analysis ($0.5 < FC > 1.2$) 10 metabolites were selected as differential for BC tissue and normal samples (Table 1). All data for identified compounds analyzed within this work are presented in Supplementary Table S2.

Next, univariate ROC curve analysis was separately performed to evaluate the diagnostic ability of the models. ROC curves analyses were used to estimate the accuracy of combined signatures model of imaging data. The areas under curves (AUC) of ROC curves were used to determine the diagnostic effectiveness of important metabolites. Applying a ROC approach to biomarker analysis allowed characterization of diagnostic accuracy, and evaluation of the predictive accuracy. The results indicated that all previously selected metabolites have AUC above 0.81 (Table 1). The best ROC analyses with the highest statistical significance were obtained for hypotaurine and 3-methylbutanal (AUC = 0.944, specificity = 1.0 and sensitivity = 0.8). The classification ROC model was based on a random forest algorithm. As shown in Fig. 1D, the combination of levels of 10 selected metabolites was a better discriminator (AUC = 0.993) than each metabolite separately. The results suggest that 10 specific metabolites: glycine, hypotaurine, 3-methylbutanal, ethylphosphate, glutamine, myosmine, PI(22:0/0:0), aminopentanal, proline betaine and methylguanidine coul, significantly increase the diagnostic potential and serve as useful discriminators of cancer tissues from normal tissues in patients diagnosed with BC. Ion images of all these compounds that differentiate the neoplastic and normal area to the greatest extent are presented in Figs. 2 and 3.

Ion images of 2 amino acids that play essential roles in human tissues were generated and the structure of one of them was confirmed with LIFT MS/MS method. One of the ion images of *m/z* 98.021 (Fig. 2 A) shows spatial distribution of the $[C_2H_5NO_2{+}Na]^+$ adduct (sodiated glycine). This ion was found to be present at a higher intensity in the normal tissue compared with the cancer tissue. The decreased levels of glycine were observed in lung cancer patients [21] and in serum of BC patients [22]. Similarly, ion assigned to potassium adduct of glutamine (*m/z* 185.032, Fig. 2 E) was found at a higher intensity in the normal tissue compared to the cancer tissue. NMR-based metabolomics studies have shown the decreased blood levels of glutamine in plasma samples from pancreatic cancer patients [23]. The decrease in the levels of the amino acids discussed above indicates an increased demand for these metabolites for tumor growth. This observation suggests that tumor's biochemistry may be associated with an increased glycolytic flux that has been found to be a major source of respiratory energy for tumor cells, and with the need for increased protein synthesis in tumor cells [24]. It has also been suggested that glycolysis is required to maintain lipogenesis and cholesterogenesis, that are essential for the growth and proliferation of tumor cells [25].

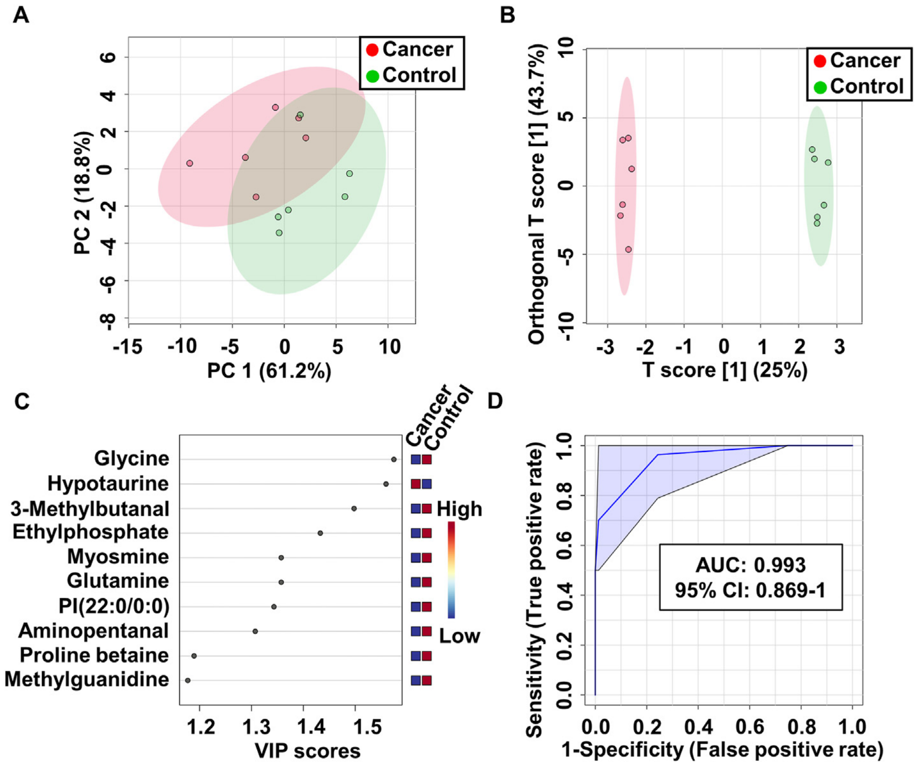

Fig. 1. Metabolomic analysis of tissue samples from bladder cancer (BC) patients. **(A)** PCA and **(B)** OPLS-DA scores plots of the cancer (red) and control (green) tissue samples. **(C)** VIP plot from OPLS-DA analysis. **(D)** The receiving operator characteristic (ROC) curves for the 10 selected metabolites.

Table 1
Mean metabolite abundance for controls vs. bladder cancer tissues. Bolded metabolites are considered statistically significantly different (P-value <0.05; VIP >1; FC $<$ 0.5 and >1.2) between controls and cancer tissues.

No.	Compound name	Adduct type	*m/z*[c]	*P*-value[d]	Fold Change[e]	VIP[f]	AUC	Power of the test	
								Sensitivity [%]	Specificity [%]
1	Glycine[a]	$[C_2H_5NO_2{+}Na]+$	98.021	0.0025	0.30	1.56	0.92	100	83
2	Hypotaurine[a]	$[C_2H_7NO_2S{+}^{109}Ag]^+$	217.924	0.0035	1.39	1.54	0.94	83	100
3	3-Methylbutanal[a]	$[C_5H_{10}O + H]^+$	87.080	0.0053	0.19	1.47	0.94	83	100
4	Ethylphosphate[a]	$[C_2H_7O_4P + K]^+$	164.971	0.0088	0.30	1.41	0.92	83	83
5	Glutamine[b]	$[C_5H_{10}N_2O_3{+}K]^+$	185.032	0.0147	0.29	1.35	0.92	83	83
6	Myosmine[b]	$[C_9H_{10}N_2{+}H]^+$	147.092	0.0147	0.29	1.35	0.92	83	83
7	PI(22:0/0:0)[a]	$[C_{31}H_{61}O_{12}P{+}^{109}Ag]^+$	765.294	0.0171	0.19	1.32	0.92	100	83
8	Aminopentanal[b]	$[C_5H_{11}NO + H]^+$	102.091	0.0214	0.39	1.29	0.83	100	67
9	Proline betaine[a]	$[C_7H_{13}NO_2{+}Na]^+$	166.084	0.0417	0.44	1.17	0.83	100	67
10	Methylguanidine[a]	$[C_2H_7N_3{+}Na]^+$	96.053	0.0451	0.45	1.16	0.81	67	83

Abbreviations: AUC - area under the curve; FC - fold change; PI - phosphatydylinositol; PS – phosphatidylserine; VIP - variable influence on projection.

[a] Putative identification.

[b] Identity confirmed with LIFT MS/MS method.

[c] Calculated *m/z* values.

[d] P-value determined from Student's t-test.

[e] Fold change between cancer and control tissue samples.

[f] VIP scores derived from OPLS-DA model.

Moreover, it was found that glycine metabolism is necessary and sufficient for cell transformation and malignancy [26].

In the present study, 11 lipids that play essential roles in the human body showed a large differentiation between neoplastic and normal tissue, and their structures were in some cases successfully confirmed with LIFT MS/MS method (Supplementary Tables S2 and S3). We found, that 5 ions of ^{109}Ag isotope adducts of phosphoglycerol PG(32:1) (*m/z* 829.398), phosphoinositol PI(22:0/0:0) (*m/z* 765.294), phosphoserines PS(*O*-30:1) (*m/z* 800.383), PS(30:1) (*m/z* 814.362), phosphoethanolamine PE(34:4) (*m/z* 820.388), 4 sodium adducts of diacylglyceride DG(44:1) (*m/z* 757.668), phosphocholine PC(40:10) (*m/z* 848.520), phosphoglycerolphosphate PGP(32:1) (*m/z* 801.471), phosphoethanolamine PE(26:1) (*m/z* 628.395), and 2 potassium adducts of phosphoserine PS(36:4) (*m/z* 822.468), sphingomyeline SM(d18:0/12:0) (*m/z* 689.499), dominated in the cancer tissue MSI region compared to normal tissue. However, only 1 lipid - PI(22:0/0:0) showed statistically significant differentiation between normal and neoplastic tissues (Fig. 3A). Lipids are the building blocks of cell membranes and play important roles in various biological processes, such as cellular signaling, chemical-energy storage, homeostasis, apoptosis, metabolism, cell adhesion and migration, neurotransmission, signal transduction, vesicular trafficking, post-translational modifications and cell–cell interactions in tissues. These cellular processes are associated with cellular transformations, cancer progression and metastasis. Lipids are linked to cancer at the metabolic level and are expected to be present in

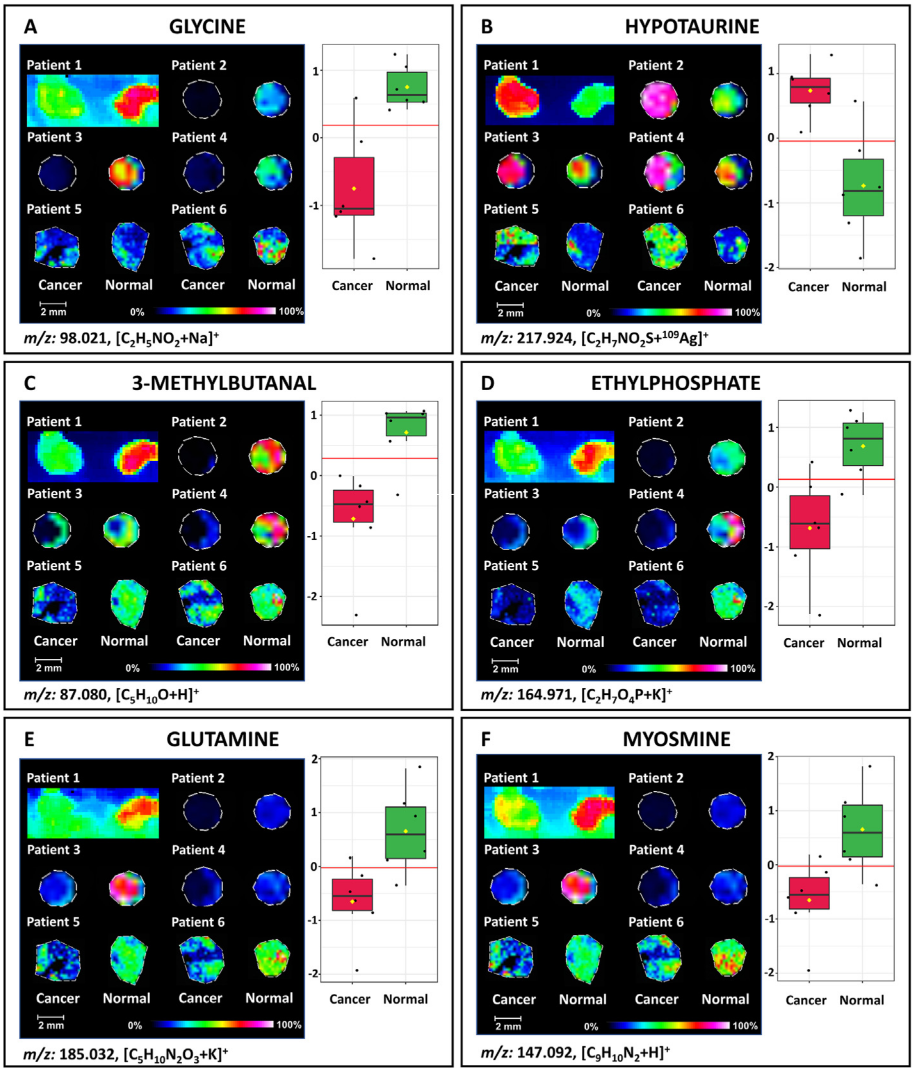

Fig. 2. Results of LDI-MSI analysis of the surface of the bladder cancer (BC) specimens on ^{109}AgNPET. The left sides of the individual metabolite panel **(A–F)** present ion images (TIC normalization) for ions of *m/z* as stated below each image. The right sides contain plots of distribution of abundance values of metabolite in control and cancer samples with optimal cut-off as a horizontal dashed line. All ion images are within ±0.05 *m/z*.

cancer cells, tissues and biofluids. Multiple studies have demonstrated altered lipid profiles in biological samples that have been screened to identify biomarkers in cancer research [27,28]. Several reports have shown the spatial distributions of many potential lipid-based biomarkers in various malignant tumors such as lung [29], breast [30], ovarian [31], colorectal [32], prostate [33], kidney [34], renal [35], bladder [36] and thyroid cancers [37]. Dill et al. [38] demonstrated distributions of the multiple lipids and free fatty acids species between cancerous and noncancerous dog bladder tissue samples with desorption electrospray ionization MS (DESI-MS). The same group of researchers in another study used human BC tissue samples to visualize of glycerophospholipid (GP) distribution in cancerous and normal tissue. They found that tumor tissue shows increased intensities for different GPs such as phosphatidylserine (PS) and phosphatidylinositol (PI) when compared to the normal tissue [36]. Wittman et al. [39], measured multiple distinct compounds in human urine samples, that differentiate BC from non-cancer controls. They selected 25 potential biomarkers related to lipid metabolism.

Ion assigned to proton adduct of 3-methylbutanal (*m/z* 87.080; Fig. 2C) was found in higher intensity in normal tissue compared to cancer tissue. 3-Methylbutanal also known as isovaleraldehyde is an aldehyde that occurs naturally in all eukaryotes. In humans, this compound has been found to be associated with several diseases. Previous research revealed significantly reduced level of 3-methylbutanal in urine samples from patients with clear cell renal cell carcinoma which may be associated with higher level of aldehyde dehydrogenase that converts aldehydes to their respective carboxylic acids and is often upregulated in cancer [40]. Furthermore, in the human lung cancer cell line, 3-methylbutanal was found at decreased concentrations [41].

One of the ion images of *m/z* 166.084 (Fig. 2C) shows spatial distribution of the sodium adduct of proline betaine. This secondary metabolite has been described previously as a highly effective osmoprotectant in many plants. In humans, proline betaine was at reduced levels in plasma samples from patients with esophageal squamous cell carcinoma compared to healthy controls which is also in line with our results [42]. Similar results were obtained in metabolomic analysis of serum samples from patients with preeclampsia [43]. Proline betaine was found to be up-regulated in urine samples from patients with uterine cervix cancer and renal cell carcinoma [44,45].

The MSI results of the bladder tissue imprint suggest, that the ion of *m/z* 96.053 (Fig. 3 D) corresponds to sodiated adduct of methylguanidine which was found in higher abundance in normal tissue. Methylguanidine is an organic compound containing a guanidine moiety in which one of the amino hydrogens is substituted by a methyl group. Endogenous methylguanidine is produced by conversion from creatinine and some

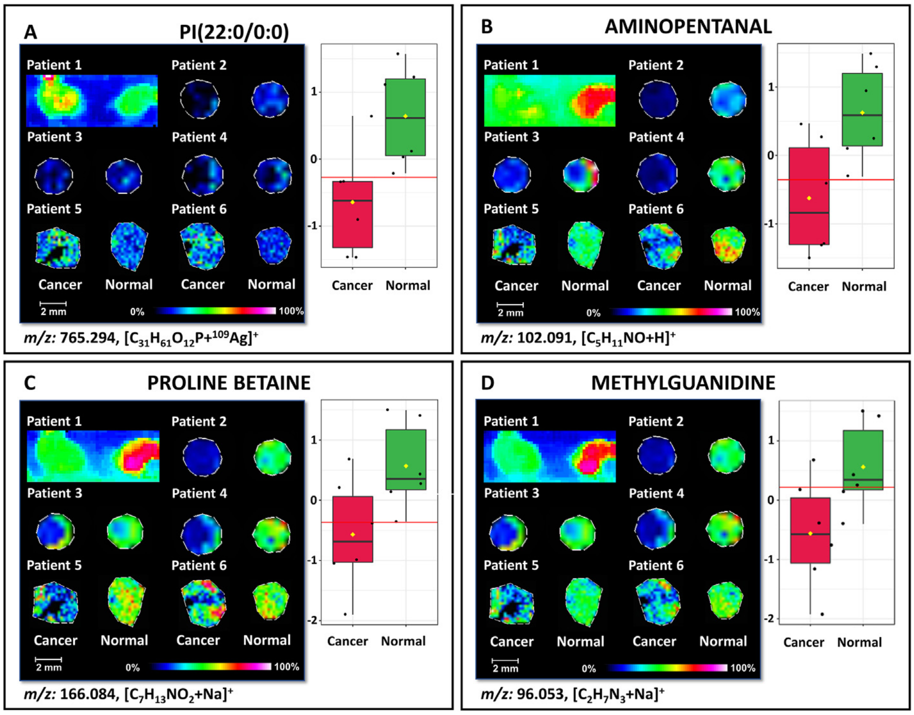

Fig. 3. Results of LDI-MSI analysis of the surface of the bladder cancer (BC) specimens on ^{109}AgNPET. **(A–D)** The left sides of the individual metabolite panel **(A–D)** present ion images (TIC normalization) for ions of *m/z* as stated below each image. The right sides contain plots of distribution of abundance values of metabolite in control and cancer samples with optimal cut-off as a horizontal dashed line. All ion images are within ±0.05 *m/z*.

amino acids [46]. Previous studies reported the potential toxicity of methylguanidine [47]. Methylguanidine was proposed as a serum potential biomarker of pancreatic cancer based on LC/GC–MS analyses which revealed a higher abundance of this compound in serum of patients with this tumor compared to controls [48]. Higher level of methylguanidine was also observed in serum of patients with cholangiocarcinoma [49]. This metabolite was identified in higher concentration in urine samples from patients with chronic pancreatitis by NMR-based metabolomics [50]. Significantly increased level of methylguanidine was identified in urine samples from dogs with BC compared to controls in an NMR-based metabolomics study [51].

Ion images presenting higher average intensity in the area of normal tissue were recorded for proton adduct of myosmine (*m/z* 147.092; Fig. 2F). Myosmine is a derivative of pyridines which can be found in tobacco and in various foods. It is suspected that this compound may be related to esophageal cancer [52]. Ion assigned to potassium adduct of ethylphosphate (*m/z* 164.971; Fig. 2 D) was found in higher intensity in normal tissue compared to cancer tissue. Ethylphosphate is an organic compound that belongs to the class of monoalkyl phosphates. This compound was identified in human saliva by LC-MS [53]. Also, the ion of *m/z* 102.091 (Fig. 3 B) was found in higher abundance in normal tissue and was assigned to $[M+H]^+$ adduct of aminopentanal.

Ion image that shows higher intensity in the area of cancer tissue has been created for the *m/z* 217.924 which corresponds to the ^{109}Ag adduct of hypotaurine (Fig. 2B). Hypotaurine is a sulfinic acid that is an intermediate in the biosynthesis of taurine from cysteine sulphinic acid. Previous research has established that hypotaurine has antioxidant properties *in vivo* [54] and also acts as a neurotransmitter [55]. Previously, using ^{1}H NMR, hypotaurine was found in increased level in serum samples of BC patients resistant to neoadjuvant chemotherapy [56]. Elevated level of hypotaurine was found in saliva of patients with medication-related osteonecrosis of the jaw [57]. In addition, hypotaurine was found to be upregulated in tissue of patients with colorectal cancer and related to the progression of this tumor [58].

4.2. *Pathway analysis*

A metabolic pathway impact analysis was performed to identify the most relevant pathways involved in the observed changes of tissue metabolite levels. Ten most significant metabolites were subjected to pathway analysis and quantitative pathway enrichment analysis. Three of them were found to be relevant to human metabolism (Table 2). Seventeen metabolic pathways i.e., glyoxylate and dicarboxylate metabolism, aminoacyl-tRNA biosynthesis, D-glutamine and D-glutamate metabolism, nitrogen metabolism, taurine and hypotaurine metabolism, arginine biosynthesis, glutathione metabolism, alanine, aspartate and glutamate metabolism, porphyrin and chlorophyll metabolism, glycine, serine and threonine metabolism, pyrimidine metabolism, primary bile acid biosynthesis, purine metabolism, mercaptopurine action pathway, thioguanine action pathway, azathioprine action pathway and mercaptopurine metabolism pathway, were found to be significantly impacted when comparing BC to normal tissue. Results from pathway impact analysis are shown in Supplementary Tables S3 and S4. Glycine,

Table 2
Selected metabolites and their involvement in different pathways.

Compound name	Pathway involved
Glycine	Glyoxylate and dicarboxylate metabolism, aminoacyl-tRNA biosynthesis, glutathione metabolism, porphyrin and chlorophyll metabolism, glycine, serine and threonine metabolism, primary bile acid biosynthesis, mercaptopurine action pathway, thioguanine action pathway, azathioprine action pathway
Glutamine	Glyoxylate and dicarboxylate metabolism, aminoacyl-tRNA biosynthesis, D-glutamine and D-glutamate metabolism, nitrogen metabolism, arginine biosynthesis, alanine, aspartate and glutamate mercaptopurine action pathway metabolism, pyrimidine metabolism, purine metabolism, thioguanine action pathway, azathioprine action pathway, mercaptopurine metabolism pathway
Hypotaurine	Taurine and hypotaurine metabolism

glutamine and hypotaurine were found to be involved in these metabolic pathways (Table 2). These pathways are well known to be related to cancer, e.g. taurine and hypotaurine metabolism have been shown to be related to BC [59,60] and renal cell carcinoma [61], sulfur metabolism has been shown to be related to breast cancer [62], and aminoacyl-tRNA biosynthesis pathway has been shown to be related to prostate cancer [63].

4.3. Diagnostic value of nanoparticles for MSI of cancer tissues

The diagnosis of most cancers is based on a molecular pathology that is currently most often performed by immunohistochemical analysis (IHC) or fluorescence *in situ* hybridization (FISH) which most often uses macromolecules such as proteins or nucleic acids of varying lengths [64, 65]. These methods are complex, time-consuming, and require specialized and expensive antibodies or labeling. Surgical excision of the bladder tumor is currently a method of choice for treating patients suffering from BC, therefore it is important to quickly and precisely define the neoplastic tissue border during surgery in order to completely remove the tumor without damaging normal tissue. Numerous previous studies have shown that metabolites enable a more precise determination of pathology and may serve as potential diagnostic biomarkers in a variety of malignancies [66]. The use of MSI allows not only to identify potential tumor biomarkers but also to determine their location on the surface of the examined tissue. Nowadays almost all of MSI is made with the use of MALDI with many of its drawbacks including (i) abundant and numerous chemical background peaks in the low-mass region ($m/z < \approx 1000$) due to the presence of the applied matrix; (ii) the frequent need for external mass calibration; (iii) low mass resolution and accuracy due to the thickness of the tissue samples; (iv) low ionization efficiency for many organic compounds present in the samples in their non-charged states; (v) inhomogeneous matrix crystallization; and (vi) commonly observed acid-catalyzed hydrolysis of various biomolecules, and thus it is not suitable for metabolites. On the other hand, some nanoparticles such as silver and gold-based lacks most of above mentioned MALDI drawbacks and are one of the most interesting choices for studying of differentiation between cancer and normal tissues.

5. Conclusion

In this study, LDI-MSI technique with the use of nanoparticle-enhanced SALDI-type ^{109}AgNPET target was used for MSI of human bladder tissue. Ion images produced for few dozens of compounds of interest presented attention-grabbing differentiation of intensities. Univariate and multivariate statistical analyses revealed 10 metabolites that differentiated cancer from normal tissues. Among these metabolites, glycine, 3-methylbutanal, ethylphosphate, glutamine, myosmine, PI(22:0/0:0), aminopentanal, proline betaine and methylguanidine were found in higher abundance in normal tissue samples and hypotaurine was found at a higher level in cancer tissue samples. These compounds may significantly increase diagnostic potential and serve as useful discriminators of cancerous versus normal tissues in patients diagnosed with BC. Published results demonstrate that nanoparticle-based LDI-MSI must be considered as a powerful tool for analysis of biological objects and especially for biomarker discovery.

Financial disclosure

This work was supported by the National Science Centre (NCN), SONATA grant no. UMO-2018/31/D/ST4/00109.

The author contributions

Study design: Krzysztof Ossoliński Tomasz Ruman, Joanna Nizioł.

Data collection: Joanna Nizioł, Adrian Arendowski, Aneta Płaza-Altamer, Krzysztof Ossoliński, Anna Ossolińska, Tadeusz Ossoliński.

Statistical Analysis: Joanna Nizioł.

Data interpretation: Joanna Nizioł, Tomasz Ruman.

Manuscript preparation: Joanna Nizioł, Krzysztof Ossoliński, Artur Kołodziej, Tomasz Ruman.

Literature Search: Joanna Nizioł, Krzysztof Ossoliński.

Funds Collection: Joanna Nizioł.

Declaration of competing interest

The authors declare no conflict of interests.

Acknowledgements

Mr Dominik Ruman is acknowledged for creating MS search engine of chemical compounds.

Appendix A. Supplementary data

Supplementary data to this article can be found online at https://doi.org/10.1016/j.advms.2022.12.002.

References

[1] Sung H, Ferlay J, Siegel RL, Laversanne M, Soerjomataram I, Jemal A, et al. Global cancer statistics 2020: GLOBOCAN estimates of incidence and mortality worldwide for 36 cancers in 185 countries. CA A Cancer J Clin 2021;71:209–49. https://doi.org/10.3322/CAAC.21660.

[2] Kamat AM, Hegarty PK, Gee JR, Clark PE, Svatek RS, Hegarty N, et al. ICUD-EAU international consultation on bladder cancer 2012: screening, diagnosis, and molecular markers. Eur Urol 2013;63:4–15. https://doi.org/10.1016/J.EURURO.2012.09.057.

[3] González de Vega R, Clases D, Fernández-Sánchez ML, Eiró N, González LO, Vizoso FJ, et al. MMP-11 as a biomarker for metastatic breast cancer by immunohistochemical-assisted imaging mass spectrometry. Anal Bioanal Chem 2019;411:639–46. https://doi.org/10.1007/s00216-018-1365-3.

[4] Paine MRL, Kooijman PC, Fisher GL, Heeren RMA, Fernández FM, Ellis SR. Visualizing molecular distributions for biomaterials applications with mass spectrometry imaging: a review. J Mater Chem B 2017;5:7444–60. https://doi.org/10.1039/C7TB01100H.

[5] Steurer S, Singer JM, Rink M, Chun F, Dahlem R, Simon R, et al. MALDI imaging–based identification of prognostically relevant signals in bladder cancer using large-scale tissue microarrays. Urol Oncol Semin Orig Investig 2014;32:1225–33. https://doi.org/10.1016/J.UROLONC.2014.06.007.

[6] Ifa DR, Wiseman JM, Song Q, Cooks RG. Development of capabilities for imaging mass spectrometry under ambient conditions with desorption electrospray ionization (DESI). Int J Mass Spectrom 2007;259:8–15. https://doi.org/10.1016/J.IJMS.2006.08.003.

[7] Sekuła J, Nizioł J, Rode W, Ruman T. Gold nanoparticle-enhanced target (AuNPET) as universal solution for laser desorption/ionization mass spectrometry analysis and imaging of low molecular weight compounds. Anal Chim Acta 2015;875:61–72. https://doi.org/10.1016/J.ACA.2015.01.046.

[8] Nizioł J, Rode W, Zieliński Z, Ruman T. Matrix-free laser desorption–ionization with silver nanoparticle-enhanced steel targets. Int J Mass Spectrom 2013;335:22–32. https://doi.org/10.1016/J.IJMS.2012.10.009.

[9] Nizioł J, Rode W, Laskowska B, Ruman T. Novel monoisotopic 109AgNPET for laser desorption/ionization mass spectrometry. Anal Chem 2013;85:1926–31. https://doi.org/10.1021/ac303770y.

[10] Nizioł J, Ruman T. Surface-transfer mass spectrometry imaging on a monoisotopic silver nanoparticle enhanced target. Anal Chem 2013;85. https://doi.org/10.1021/ac4031658.

[11] Nizioł J, Ossoliński K, Ossoliński T, Ossolińska A, Bonifay V, Sekuła J, et al. Surface-Transfer mass spectrometry imaging of renal tissue on gold nanoparticle enhanced target. Anal Chem 2016;88. https://doi.org/10.1021/acs.analchem.6b01859.

[12] Arendowski A, Nizioł J, Ossoliński K, Ossolińska A, Ossoliński T, Dobrowolski Z, et al. Laser desorption/ionization MS imaging of cancer kidney tissue on silver nanoparticle-enhanced target. Bioanalysis 2018;10:83–94. https://doi.org/10.4155/bio-2017-0195.

[13] Moch H, Cubilla AL, Humphrey PA, Reuter VE, Ulbright TM. The 2016 WHO classification of tumours of the urinary system and male genital organs—Part A: renal, penile, and testicular tumours. Eur Urol 2016;70:93–105. https://doi.org/10.1016/J.EURURO.2016.02.029.

[14] Sauter G, Algaba F, Amin MB, Busch C, Cheville J, Gasser T, et al. Tumours of the urinary system: non-invasive urothelial neoplasias. In: WHO classification of classification of tumours of the urinary system and male genital organs. IARCC Press Lyon; 2004. p. 89–157.

[15] Suckau D, Resemann A, Schuerenberg M, Hufnagel P, Franzen J, Holle A. A novel MALDI LIFT-TOF/TOF mass spectrometer for proteomics. Anal Bioanal Chem 2003;376:952–65. https://doi.org/10.1007/s00216-003-2057-0.

[16] Bemis KD, Harry A, Eberlin LS, Ferreira C, van de Ven SM, Mallick P, et al. Cardinal : an R package for statistical analysis of mass spectrometry-based imaging experiments. Bioinformatics 2015;31:2418–20. https://doi.org/10.1093/bioinformatics/btv146.

[17] Pang Z, Chong J, Zhou G, De Lima Morais DA, Chang L, Barrette M, et al. MetaboAnalyst 5.0: narrowing the gap between raw spectra and functional insights. Nucleic Acids Res 2021;49:W388–96. https://doi.org/10.1093/NAR/GKAB382.

[18] Patiny L, Borel A. ChemCalc: a building block for tomorrow's chemical infrastructure. J Chem Inf Model 2013;53:1223–8. https://doi.org/10.1021/ci300563h.

[19] Arendowski A, Nizioł J, Ruman T. Silver-109-based laser desorption/ionization mass spectrometry method for detection and quantification of amino acids. J Mass Spectrom 2018;53:369–78. https://doi.org/10.1002/jms.4068.

[20] Luehr TC, Koide EM, Wang X, Han J, Borchers CH, Helbing CC. Metabolomic insights into the effects of thyroid hormone on Rana [Lithobates] catesbeiana metamorphosis using whole-body Matrix Assisted Laser Desorption/Ionization-Mass Spectrometry Imaging (MALDI-MSI). Gen Comp Endocrinol 2018;265: 237–45. https://doi.org/10.1016/J.YGCEN.2018.02.012.

[21] Duarte IF, Rocha CM, Barros AS, Gil AM, Goodfellow BJ, Carreira IM, et al. Can nuclear magnetic resonance (NMR) spectroscopy reveal different metabolic signatures for lung tumours? Virchows Arch 2010;457:715–25. https://doi.org/10.1007/s00428-010-0993-6.

[22] Cao M, Zhao L, Chen H, Xue W, Lin D. NMR-Based metabolomic analysis of human bladder cancer. Anal Sci 2012;28:451–6. https://doi.org/10.2116/ANALSCI.28.451.

[23] Owusu-Sarfo K M. Asiago V, Deng L, Gu H, Wei S, Shanaiah N, et al. NMR-Based metabolite profiling of pancreatic cancer n.d.

[24] Moreadith RW, Lehninger AL. The pathways of glutamate and glutamine oxidation by tumor cell mitochondria. In: Role of mitochondrial NAD(P)+-dependent malic enzyme, 259; 1984. p. 6215–21.

[25] Costello LC, Franklin RB. 'Why do tumour cells glycolyse?': from glycolysis through citrate to lipogenesis. Mol Cell Biochem 2005;280:1–8. https://doi.org/10.1007/s11010-005-8841-8.

[26] Possemato R, Marks KM, Shaul YD, Pacold ME, Kim D, Birsoy K, et al. Functional genomics reveal that the serine synthesis pathway is essential in breast cancer. Nature 2011;476:346–50. https://doi.org/10.1038/nature10350.

[27] Yoshioka Y, Tsutsumi T, Adachi M, Tokumura A. Altered phospholipid profile in urine of rats with unilateral ureteral obstruction. Metabolomics 2009;5:429–33. https://doi.org/10.1007/s11306-009-0167-1.

[28] Lee GK, Lee HS, Park YS, Lee JH, Lee SC, Lee JH, et al. Lipid MALDI profile classifies non-small cell lung cancers according to the histologic type. Lung Cancer 2012;76: 197–203. https://doi.org/10.1016/J.LUNGCAN.2011.10.016.

[29] Marien E, Meister M, Muley T, Fieuws S, Bordel S, Derua R, et al. Non-small cell lung cancer is characterized by dramatic changes in phospholipid profiles. Int J Cancer 2015;137:1539–48. https://doi.org/10.1002/ijc.29517.

[30] Guo S, Wang Y, Zhou D, Li Z. Significantly increased monounsaturated lipids relative to polyunsaturated lipids in six types of cancer microenvironment are observed by mass spectrometry imaging. Sci Rep 2015;4:5959. https://doi.org/10.1038/srep05959.

[31] Kang S, Lee A, Park YS, Lee SC, Park SY, Han SY, et al. Alteration in lipid and protein profiles of ovarian cancer. Int J Gynecol Cancer 2011;21:1566–72. https://doi.org/10.1097/IGC.0b013e318226c5f5.

[32] Mirnezami R, Spagou K, Vorkas PA, Lewis MR, Kinross J, Want E, et al. Chemical mapping of the colorectal cancer microenvironment via MALDI imaging mass spectrometry (MALDI-MSI) reveals novel cancer-associated field effects. Mol Oncol 2014;8:39–49. https://doi.org/10.1016/j.molonc.2013.08.010.

[33] Goto T, Terada N, Inoue T, Kobayashi T, Nakayama K, Okada Y, et al. Decreased expression of lysophosphatidylcholine (16:0/OH) in high resolution imaging mass spectrometry independently predicts biochemical recurrence after surgical treatment for prostate cancer. Prostate 2015;75:1821–30. https://doi.org/10.1002/pros.23088.

[34] Lin L, Huang Z, Gao Y, Chen Y, Hang W, Xing J, et al. LC-MS-based serum metabolic profiling for genitourinary cancer classification and cancer type-specific biomarker discovery. Proteomics 2012;12:2238–46. https://doi.org/10.1002/pmic.201200016.

[35] Dill AL, Eberlin LS, Zheng C, Costa AB, Ifa DR, Cheng L, et al. Multivariate statistical differentiation of renal cell carcinomas based on lipidomic analysis by ambient ionization imaging mass spectrometry. Anal Bioanal Chem 2010;398:2969–78. https://doi.org/10.1007/s00216-010-4259-6.

[36] Dill AL, Eberlin LS, Costa AB, Zheng C, Ifa DR, Cheng L, et al. Multivariate statistical identification of human bladder carcinomas using ambient ionization imaging mass spectrometry. Chem Eur J 2011;17:2897–902. https://doi.org/10.1002/chem.201001692.

[37] Bandu R, Mok HJ, Kim KP. Phospholipids as cancer biomarkers: mass spectrometry-based analysis. Mass Spectrom Rev 2018;37:107–38. https://doi.org/10.1002/mas.21510.

[38] Dill AL, Ifa DR, Manicke NE, Costa AB, Ramos-Vara JA, Knapp DW, et al. Lipid profiles of canine invasive transitional cell carcinoma of the urinary bladder and adjacent normal tissue by desorption electrospray ionization imaging mass spectrometry. Anal Chem 2009;81:8758–64. https://doi.org/10.1021/ac901028b.

[39] Wittmann BM, Stirdivant SM, Mitchell MW, Wulff JE, McDunn JE, Li Z, et al. Bladder cancer biomarker discovery using global metabolomic profiling of urine. PLoS One 2014;9:e115870. https://doi.org/10.1371/journal.pone.0115870.

[40] Pinto J, Amaro F, Lima AR, Carvalho-Maia C, Jerónimo C, Henrique R, et al. Urinary volatilomics unveils a candidate biomarker panel for noninvasive detection of clear cell renal cell carcinoma. J Proteome Res 2021;20:3068–77. https://doi.org/10.1021/ACS.JPROTEOME.0C00936/ASSET/IMAGES/LARGE/PR0C00936_0004.JPEG.

[41] Hanai Y, Shimono K, Oka H, Baba Y, Yamazaki K, Beauchamp GK. Analysis of volatile organic compounds released from human lung cancer cells and from the urine of tumor-bearing mice. https://doi.org/10.1186/1475-2867-12-7; 2012.

[42] Zhu ZJ, Qi Z, Zhang J, Xue WH, Li LF, Shen ZB, et al. Untargeted metabolomics analysis of esophageal squamous cell carcinoma discovers dysregulated metabolic pathways and potential diagnostic biomarkers. J Cancer 2020;11:3944. https://doi.org/10.7150/JCA.41733.

[43] Chen T, He P, Tan Y, Xu D. Biomarker identification and pathway analysis of preeclampsia based on serum metabolomics. Biochem Biophys Res Commun 2017; 485:119–25. https://doi.org/10.1016/J.BBRC.2017.02.032.

[44] Chen Y, Xu J, Zhang R, Shen G, Song Y, Sun J, et al. Assessment of data pre-processing methods for LC-MS/MS-based metabolomics of uterine cervix cancer. Analyst 2013;138:2669–77. https://doi.org/10.1039/C3AN36818A.

[45] Oto J, Fernández-Pardo Á, Roca M, Plana E, Solmoirago MJ, Sánchez-González JV, et al. Urine metabolomic analysis in clear cell and papillary renal cell carcinoma: a pilot study. J Proteomics 2020;218:103723. https://doi.org/10.1016/J.JPROT.2020.103723.

[46] Perez G, Faluotico R. Creatinine: a precursor of methylguanidine. Export 1973 2912 1973;29:1473–4. https://doi.org/10.1007/BF01943863.

[47] Wang F, Yang B, Ling GH, Yao C, Jiang YS. Methylguanidine cytotoxicity on HK-2 cells and protective effect of antioxidants against MG-induced apoptosis in renal proximal tubular cells in vitro, vol. 32; 2010. p. 85. https://doi.org/10.3109/0886022X.2010.501935. Https://DoiOrg/103109/0886022X2010501935, 978.

[48] Xie G, Lu L, Qiu Y, Ni Q, Zhang W, Gao YT, et al. Plasma metabolite biomarkers for the detection of pancreatic cancer. J Proteome Res 2015;14:1195–202. https://doi.org/10.1021/PR501135F/SUPPL_FILE/PR501135F_SI_001.PDF.

[49] Suksawat M, Phetcharaburanin J, Klanrit P, Namwat N, Khuntikeo N, Titapun A, et al. Metabolic phenotyping predicts gemcitabine and cisplatin chemosensitivity in patients with cholangiocarcinoma. Front Public Health 2022;10:766023. https://doi.org/10.3389/FPUBH.2022.766023/FULL.

[50] Lusczek ER, Paulo JA, Saltzman JR, Kadiyala V, Banks PA, Beilman G, et al. Urinary 1H-NMR metabolomics can distinguish pancreatitis patients from healthy controls. JOP 2013;14:161.

[51] Zhang J, Wei S, Liu L, Nagana Gowda GA, Bonney P, Stewart J, et al. NMR-based metabolomics study of canine bladder cancer. Biochim Biophys Acta, Mol Basis Dis 2012;1822:1807–14. https://doi.org/10.1016/j.bbadis.2012.08.001.

[52] Wilp J, Zwickenpflug W, Richter E. Nitrosation of dietary myosmine as risk factor of human cancer. Food Chem Toxicol 2002;40:1223–8. https://doi.org/10.1016/S0278-6915(02)00039-X.

[53] Álvarez-Sánchez B, Priego-Capote F, Luque de Castro MD. Study of sample preparation for metabolomic profiling of human saliva by liquid chromatography–time of flight/mass spectrometry. J Chromatogr A 2012;1248: 178–81. https://doi.org/10.1016/J.CHROMA.2012.05.029.

[54] Aruoma OI, Halliwell B, Hoey BM, Butler J. The antioxidant action of taurine, hypotaurine and their metabolic precursors. Biochem J 1988;256:251. https://doi.org/10.1042/BJ2560251.

[55] Kalir A, Kalir HH. Biological activity of sulfinic acid derivatives. Sulphinic Acids, Esters Deriv 2010:665–76. https://doi.org/10.1002/9780470772270.CH23.

[56] Cicero DO, Zhuang J, Yang X, Zheng Q, Li K, Cai L, et al. Metabolic profiling of bladder cancer patients' serum reveals their sensitivity to neoadjuvant chemotherapy. Metabolism 2022;12:558. https://doi.org/10.3390/METABO12060558.

[57] Yatsuoka W, Ueno T, Miyano K, Uezono Y, Enomoto A, Kaneko M, et al. Metabolomic profiling reveals salivary hypotaurine as a potential early detection marker for medication-related osteonecrosis of the jaw. PLoS One 2019;14: e0220712. https://doi.org/10.1371/JOURNAL.PONE.0220712.

[58] Hou X, Hu J, Zhao X, Wei Q, Zhao R, Li M, et al. Taurine attenuates the hypotaurine-induced progression of CRC via ERK/RSK signaling. Front Cell Dev Biol 2021;9:954. https://doi.org/10.3389/FCELL.2021.631163/BIBTEX.

[59] Loras A, Suárez-Cabrera C, Martínez-Bisbal MC, Quintás G, Paramio JM, Martínez-Máñez R, et al. Integrative metabolomic and transcriptomic analysis for the study of bladder cancer. Cancers 2019;11:1–36. https://doi.org/10.3390/cancers11050686.

[60] Loras A, Martínez-Bisbal MC, Quintás G, Gil S, Martínez-Máñez R, Ruiz-Cerdá JL. Urinary metabolic signatures detect recurrences in non-muscle invasive bladder cancer. Cancers 2019;11:914. https://doi.org/10.3390/CANCERS11070914. 2019; 11:914.

[61] Yang W, Yoshigoe K, Qin X, Liu JS, Yang JY, Niemierko A, et al. Identification of genes and pathways involved in kidney renal clear cell carcinoma. BMC Bioinf 2014;15:S2. https://doi.org/10.1186/1471-2105-15-S17-S2.

[62] Ryu CS, Kwak HC, Lee KS, Kang KW, Oh SJ, Lee KH, et al. Sulfur amino acid metabolism in doxorubicin-resistant breast cancer cells. Toxicol Appl Pharmacol 2011;255:94–102. https://doi.org/10.1016/J.TAAP.2011.06.004.

[63] Vellaichamy A, Sreekumar A, Strahler JR, Rajendiran T, Yu J, Varambally S, et al. Proteomic interrogation of androgen action in prostate cancer cells reveals roles of aminoacyl tRNA synthetases. PLoS One 2009;4:e7075. https://doi.org/10.1371/journal.pone.0007075.

[64] Naumova AV, Modo M, Moore A, Murry CE, Frank JA. Clinical imaging in regenerative medicine. Nat Biotechnol 2014 328 2014;32:804–18. https://doi.org/10.1038/nbt.2993.

[65] Harris TJR, McCormick F. The molecular pathology of cancer. Nat Rev Clin Oncol 2010;7:251–65. https://doi.org/10.1038/NRCLINONC.2010.41.

[66] Baker M. Metabolomics: from small molecules to big ideas. Nat Methods 2011 82 2011;8:117–21. https://doi.org/10.1038/nmeth0211-117.

Journal of Pharmaceutical Analysis 12 (2022) 889–900

Contents lists available at ScienceDirect

Journal of Pharmaceutical Analysis

journal homepage: www.elsevier.com/locate/jpa

Original article

Metabolomic and elemental profiling of blood serum in bladder cancer

Krzysztof Ossoliński [a], Tomasz Ruman [b], Valérie Copié [c], Brian P. Tripet [c], Leonardo B. Nogueira [d], Katiane O.P.C. Nogueira [e], Artur Kołodziej [f], Aneta Płaza-Altamer [f], Anna Ossolińska [a], Tadeusz Ossoliński [a], Joanna Nizioł [b, *]

[a] Department of Urology, John Paul II Hospital, 36-100, Kolbuszowa, Poland
[b] Rzeszów University of Technology, Faculty of Chemistry, 35-959, Rzeszów, Poland
[c] The Department of Chemistry and Biochemistry, Montana State University, Bozeman, MT, 59717, USA
[d] Department of Geology, Federal University of Ouro Preto, 35400-000, Ouro Preto, Brazil
[e] Department of Biological Sciences, Federal University of Ouro Preto, 35400-000, Ouro Preto, Brazil
[f] Doctoral School of Engineering and Technical Sciences at the Rzeszów University of Technology, 35-959, Rzeszów, Poland

ARTICLE INFO

Article history:
Received 22 March 2022
Received in revised form
19 August 2022
Accepted 27 August 2022
Available online 2 September 2022

Keywords:
Bladder cancer
Biomarkers
Human serum
Metallomics
Metabolomics

ABSTRACT

Bladder cancer (BC) is one of the most frequently diagnosed types of urinary cancer. Despite advances in treatment methods, no specific biomarkers are currently in use. Targeted and untargeted profiling of metabolites and elements of human blood serum from 100 BC patients and the same number of normal controls (NCs), with external validation, was attempted using three analytical methods, i.e., nuclear magnetic resonance, gold and silver-109 nanoparticle-based laser desorption/ionization mass spectrometry (LDI-MS), and inductively coupled plasma optical emission spectrometry (ICP-OES). All results were subjected to multivariate statistical analysis. Four potential serum biomarkers of BC, namely, isobutyrate, pyroglutamate, choline, and acetate, were quantified with proton nuclear magnetic resonance, which had excellent predictive ability as judged by the area under the curve (AUC) value of 0.999. Two elements, Li and Fe, were also found to distinguish between cancer and control samples, as judged from ICP-OES data and AUC of 0.807 (in validation set). Twenty-five putatively identified compounds, mostly related to glycans and lipids, differentiated BC from NCs, as detected using LDI-MS. Five serum metabolites were found to discriminate between tumor grades and nine metabolites between tumor stages. The results from three different analytical platforms demonstrate that the identified distinct serum metabolites and metal elements have potential to be used for noninvasive detection, staging, and grading of BC.

1. Introduction

Bladder cancer (BC) is the tenth most commonly diagnosed cancer in the world with approximately 570,000 new cases diagnosed each year. The incidence rate per 100,000 person per year varies from 2.4 for women to 9.5 for men, and the mortality rate varies from 0.86 for women to 3.3 for men [1]. Globally, urothelial carcinoma (UC) identified histopathologically constitutes more than 90% of all the cases of BC. In endemic regions such as Egypt with a high prevalence of schistosomiasis infection, squamous cell carcinoma (SCC) accounts for the majority of BC. However, control over the *Schistosoma haematobium* infection has led to a shift from SCC to UC being the most prevalent type of BC [2]. The remaining 10% includes exposure to aromatic amines, hydrocarbons, dyes, some solvents, and coal tar [3]. The most common symptoms of BC include macroscopic and microscopic hematuria. The mainstay for BC diagnosis includes cystoscopy and urine cytology, and may include ultrasound and computed tomography urography. Unfortunately, cystoscopy is considered as an invasive procedure and the sensitivity of urine cytology is low. Therefore, to reduce the number of procedures, urinary markers have been proposed to track BC recurrence [4,5]. These urinary markers are associated with higher sensitivity, although at the expense of lower specificity, compared

---

Peer review under responsibility of Xi'an Jiaotong University.

* Corresponding author.
E-mail address: jniziol@prz.edu.pl (J. Nizioł).

https://doi.org/10.1016/j.jpha.2022.08.004

with the accuracy of urine cytology. However, these markers have not been incorporated into clinical guidelines regarding the diagnosis and surveillance of BC. Therefore, there is a significant need for noninvasive methods for the early detection of BC with high sensitivity, specificity, and low cost.

Instrumental analyses of small molecules in biofluids, such as blood, serum, and urine, are very powerful approaches to identify and characterize diagnostic metabolic biomarkers. Metabolite concentrations are reflective of the state of the organism and may be the indicators of disease states including cancer states [6]. In the past decade, numerous sensitive analytical methods have been developed to allow the study of the metabolic state of living system. The most frequently used analytical platforms for study of metabolites are nuclear magnetic resonance (NMR) [7] and mass spectrometry (MS), the latter usually coupled with liquid chromatography (LC) or gas chromatography (GC) [8–10].

Metabolomic methods have been used for study of BC with the aim of identifying potential biomarkers in urine, serum, and tissues [11,12]. The advantage of serum analysis is that it is much less susceptible to the dilution factor compared to urine [13]. Although from an application point of view, serum analysis is the best option, the published data are very limited. A majority of reports of BC serum metabolomics describe MS results. The first such study [14] was focused on human serum profiling of BC with LC-MS, and the authors proposed five potential biomarkers. Later, Zhou et al. [15] applied GC-MS to perform plasma metabolomics analyses of 92 patients and 48 controls. The results identified increased levels of metabolites associated with the pentose phosphate pathway, fatty acid synthesis, and nucleotide metabolism in BC samples compared with the controls. The authors focused on three metabolites that could discriminate between the BC and control groups. In the following years, several publications appeared that focused on identifying potential biomarkers of BC using LC-MS [16–20] and GC-MS [21,22]. To date, only three reports have reported metabolic differences in serum within BC with NMR. The first NMR serum metabolomics study of BC was published by Cao et al. [23] in 2012, and involved 67 BC patients and 25 healthy controls, and revealed a few metabolites for which concentrations differed significantly between these two groups. The metabolite changes were linked to impacted pathways of lipogenesis, aromatic amino acid metabolism, glycolysis, and the citrate cycle. In 2013, Bansal et al. [24] applied proton nuclear magnetic resonance (^{1}H NMR) spectroscopy to compare 36 low-grade (LG) and 31 high-grade (HG) BC samples with those of 32 healthy control patients. The study identified six metabolites that could, together, serve as differentiating biomarkers of LG versus HG BC. This same research team recently reported the use of NMR to identify variations in the concentration of previously selected potential serum BC biomarkers in 55 preoperative and 53 post-operative BC patients, and 152 controls [25].

Various studies have established the connection between levels of metals, including trace-level metals and other trace elements, with an increased risk of developing cancer in humans [26]. Toxic elements are known risk factors for genetic and epigenetic effects, which enhance the risk of developing different cancers [27]. Inductively coupled plasma optical emission spectrometry (ICP-OES) has emerged as one of the most frequently used methods for assessing the concentrations of metals in samples of biological origin [28] including BC serum [29]. Studies recruited 27 BC patients, 29 non-tumor patients with acute and chronic inflammation, and 30 healthy control patients, who were divided into validation and discovery cohorts. ICP-OES methods have also been used in the search for biomarkers of other cancers, including kidney cancer [30,31].

Herein, we report the results of the largest investigation to date, comprising the targeted and non-targeted, elemental- and metabolomics-based profiling of 200 serum samples obtained from 100 patients with BC and 100 healthy controls. This study has enabled the elucidation of the detailed metabolic and elemental changes resulting from BC, with a specific focus on the stage and grade of BC. The analytical platforms used were high-resolution ^{1}H NMR, ICP-OES, and high-resolution laser desorption/ionization MS (LDI-MS), and the associated data were subjected to robust validation by multivariate and univariate statistical analyses.

2. Materials and methods

2.1. Materials and instruments

High-resolution LDI-MSI experiments were performed on Autoflex Speed time-of-flight mass spectrometer (Bruker, Bremen, Germany) with a declared resolution of >20,000 for *m/z* values of >1,000 in positive-ion reflectron mode. The samples were placed on a stainless-steel target with automatic pipette and then covered by nebulization with a silver-109 nanoparticle (^{109}AgNP) suspension generated by pulsed fiber laser (PFL) two-dimensional (2D) galvoscanner (GS) laser synthesis in solution/suspension (LASiS) and nebulization of ^{109}AgNPs (^{109}AgNPs LDI-MS) as described in our recent publication [32]. Gold nanoparticle (AuNP)-based LDI-MS (AuNPs LDI-MS) was prepared analogically as described above with the exception for PFL-2D GS LASiS material/substrate, which was gold foil of 1 mm thickness. All solvents were of minimum LC-MS grade and were acquired from Sigma Aldrich (St. Louis, MO, USA). Deuterium oxide (D_2O) and 4,4-dimethyl-4-silapentane-1-sulfonic acid were purchased from Sigma Inc. (Boston, MA, USA). Nitric acid EMSURE ISO-grade 65% and hydrogen peroxide EMSURE ACS ISO-grade 30% were purchased from Merck KGaA (Darmstadt, Germany).

2.2. Collection of human serum samples

Serum samples were collected at John Paul II Hospital (Kolbuszowa, Poland). Control serum samples were collected from healthy volunteers after a medical examination focused on the detection of urinary cancers. Both types of serum samples from the original NMR, MS, and ICP-OES datasets were randomly divided every time into two groups, a training set, comprising 80% of all samples, and a validation set, corresponding to 20% of all samples. All the patients underwent transurethral resection of bladder tumor following detailed clinical questioning and laboratory testing. The local bioethics committee approved the study (Permission No.: 2018/04/10). Just over half of the patients ($n = 54$) had LG BC and papillary urothelial neoplasm of low malignant potential (PUNLMP) ($n = 3$), whereas the remaining patient group exhibited HG disease ($n = 41$). In two cases, both HG and LG neoplasms were detected. Most of these patients ($n = 69$) displayed noninvasive papillary carcinomas (pathologic stage Ta, pTa) stage disease, 19 had submucosal invasive tumors (pathologic stage T1 (pT1)) stage, and 12 patients had muscle invasive BC (pathologic stage T2 (pT2)). The average age of patients diagnosed with BC and in the NC group was 74 ± 10 and 64 ± 12 years, respectively. The clinical characteristics of the patients are presented in Table S1. A 2.6 mL of blood sample was drawn from each participant and centrifuged (3,000 *g*, 10 min, room temperature), then separated and kept at −60 °C.

2.3. Preparation of serum metabolite extracts for ^{1}H NMR metabolomics

Medium-to-high polarity metabolites were extracted from serum samples as stated in our recent publication [33] and detailed in Section S1 in the Supplementary data.

2.4. Preparation of serum samples for LDI-MS studies

Serum samples were thawed at room temperature and diluted 500 times with methanol. Then, 0.3 μL of serum sample was placed directly on target plates (^{109}Ag and Au PFL-2D GS LASiS [32]). After the solvent was evaporated in air, the plates with the samples were measured with Autoflex Speed apparatus.

2.5. Data processing and spectral acquisition

NMR and MS spectral acquisition and processing are shown in the Supplementary data (Sections S2–S4).

2.6. ICP-OES analysis

Determination of the concentrations of Ca, Fe, K, Na, Mg, as well as minor elements (Mn, P, and S) and trace elements (Cu and Zn) in serum, was performed for 116 samples (65 BC and 51 NC) as stated in our recent publication [31] and detailed in Section S5 in the Supplementary data and Table S2.

2.7. Multivariate statistical analysis

All metabolite datasets were analyzed using the MetaboAnalyst 5.0 [34]. The statistical analysis approach presented in this publication is similar to one we previously presented [31] and another unrelated study [35]; details are presented in the Supplementary data (Section S6).

3. Results

In this work, we studied the metabolic profiles of BC in an effort to propose serum-specific metabolic and/or elemental markers for the specific detection of BC. Two hundred (100 BC and 100 normal control (NC)) ^{1}H NMR spectra were recorded of metabolite extracts from patients and healthy control serum samples. Four hundred LDI mass spectra were recorded with the use of ^{109}Ag and Au PFL-2D GS LASiS targets. Additionally, 116 ICP-OES spectra of samples from 65 patients with BC and 51 NCs were studied.

3.1. Differences between BC and control serum by ^{1}H NMR

Two hundred extracts from sera (100 cancer and 100 control) were analyzed with ^{1}H NMR spectroscopy. Overall, 39 compounds were identified in each serum sample following standard protocols [36,37]. An overlay of control and cancer NMR spectra, presented as blue and red traces, respectively, in Figs. 1B and C, shows a relatively high degree of similarity in the raw NMR data. These spectral regions depict NMR signals observed from 3-hydroxybutyrate and acetate metabolites, respectively. The intensity-normalized spectral overlays shown in Figs. 1B and C clearly indicate that 3-hydroxybutyrate levels (Fig. 1B) are higher and acetate levels (Fig. 1C) are lower in the serum profiles of patients with BC (red) compared with healthy controls (blue). Detailed analysis of the spectra indicated significant differences in metabolite levels between serum samples from patients with BC and healthy controls.

Metabolite concentration datasets obtained by NMR metabolomics were randomly divided into two subsets: a training dataset to train the model ($n = 80$ BC and $n = 80$ NCs), and a validation dataset to assess the validity and robustness of the trained model ($n = 20$ BC and $n = 20$ NCs). Metabolite concentrations from both datasets were subjected to statistical analyses to assess differences in metabolite levels. The results of these analyses are summarized in Tables S3 and S4. The 2D principal components analysis (PCA) score plots of both subsets indicated good separation between the cancer and the controls (Fig. 2A). In the validation set, separation between cancer and control serum samples was also observed along principal components 1 and 2 (Fig. 2B). The three-dimensional (3D) PCA plots for training and validation sets are provided in Figs. S1A and B.

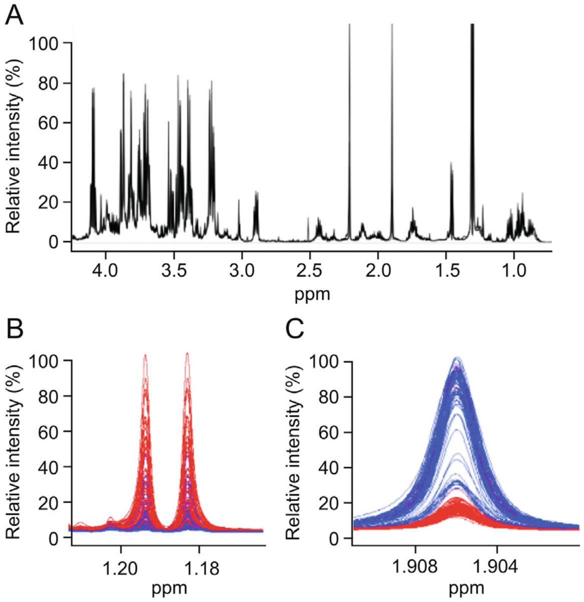

Fig. 1. (A) Characteristic proton nuclear magnetic resonance (^{1}H NMR) spectrum fragment (0.5–4.2 ppm) of a protein-free metabolite extract mixture obtained from serum sample from a patient with BC, recorded on a 600 MHz (14 T) solution NMR spectrometer. Expanded NMR spectral regions, corresponding to ^{1}H chemical shift ranges of (B) 1.16–1.21 ppm for 3-hydroxybutyrate and (C) 1.900–1.911 ppm for acetate, with a spectral overlay of 80 serum metabolic profiles obtained from healthy control patients depicted in blue (blue spectral traces) and BC patients in red (red spectral traces).

A supervised multivariate analysis of the training set with the aid of orthogonal partial least-squares discriminant analysis (OPLS-DA) indicated the strong separation of the BC and NC groups (Fig. 2C). Two thousand permutation tests were conducted to evaluate the statistical robustness of the OPLS-DA model (Figs. S2A and B). Good discrimination was observed between the two groups ($Q^2 = 0.880$, $R^2Y = 0.914$, $P < 0.0005$ (0/2000)), revealing significant differences in the metabolic profiles of cancer versus control serum samples. Group separations were observed with OPLS-DA in the validation set (Fig. 2D) and were confirmed by the good results of the permutation test ($Q^2 = 0.780$, $R^2Y = 0.932$, $P < 0.0005$ (0/2000)) (Figs. S2C and D). Potential serum BC biomarkers were selected on the basis of the S-plot resulting from the OPLS-DA model. Variables with $|P(\text{corr})| > 0.5$ were considered significant. Four variables (acetate, propionate, pyroglutamate, and choline) were positively correlated with the group separation, as determined by a $P(\text{corr})[1]$ score of >0.5, while one metabolite (isobutyrate) negatively correlated with the group separation, as assessed by $-P(\text{corr})[1] < -0.5$ (Fig. S1C). The S-plot of the OPLS-DA model in the validation set confirmed almost all of the selected metabolites (except for propionate) as the most significant for the differentiation of the BC and NC groups (Fig. S1D). Finally, four metabolites were identified as significant discriminators: acetate, pyroglutamate, and choline, which all exhibited higher concentrations in the sera of NCs, and isobutyrate, which was significantly elevated in the sera of BC patients. The P-value of each variable was calculated using independent t-tests and only variables with P-values and false discovery rate < 0.05 were considered significant. Metabolite concentration information for a set of 39 significant metabolites is presented in

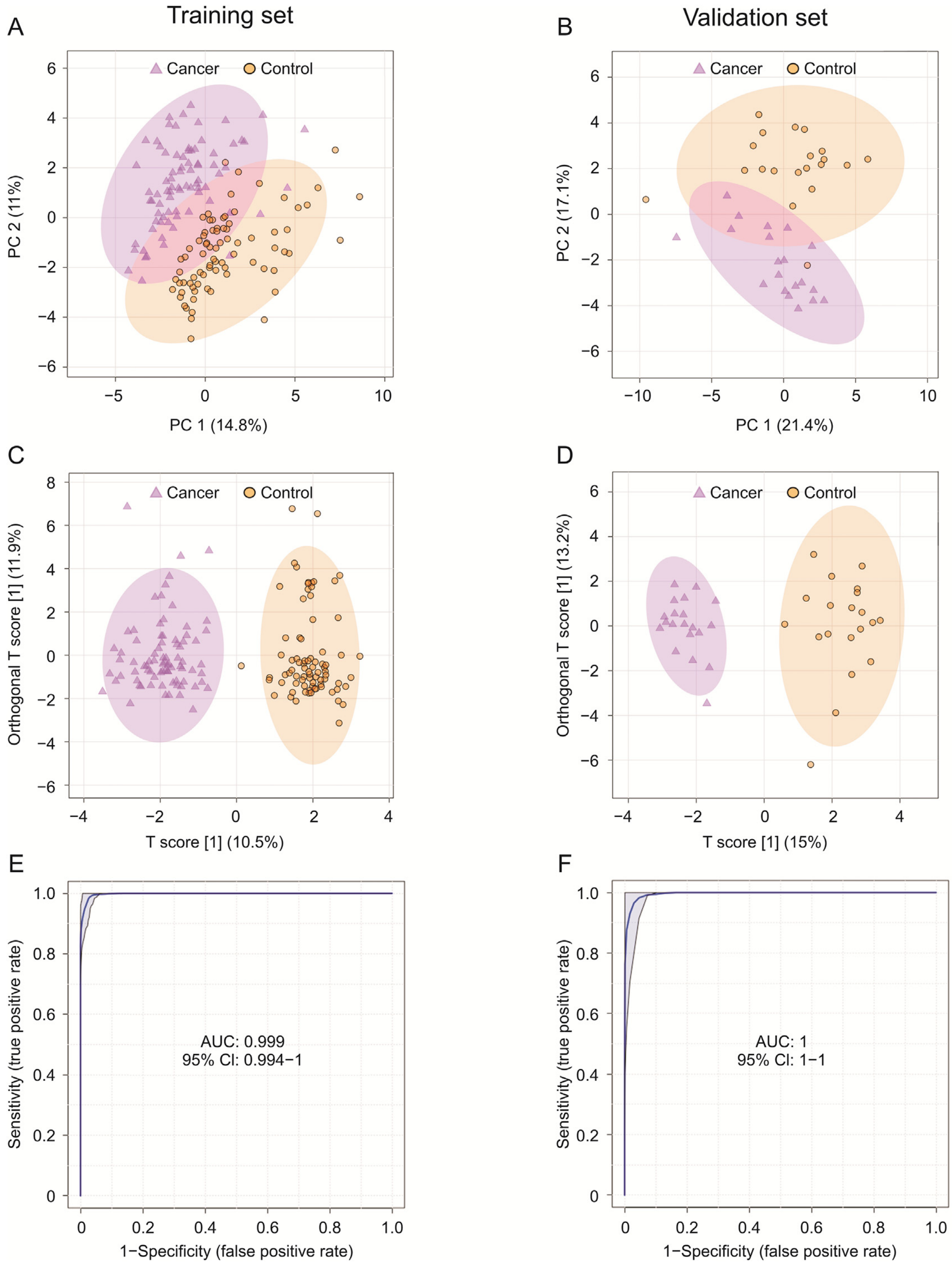

Fig. 2. Two-dimensional principal component analysis (PCA) and orthogonal partial least-squares discriminant analysis (OPLS-DA) score plots of the tumor (violet) and control (orange) serum samples in the (A and C) training set and (B and D) validation set for ^{1}H NMR data. The receiving operator characteristic (ROC) curves of the combination of four differential metabolites, namely, isobutyrate, pyroglutamate, choline, and acetate, in the (E) training set and (F) validation set. AUC: area under the ROC curve; CI: confidence interval; PC: principal component.

Tables S3 and S4. Next, univariate receiver operating characteristic (ROC) curve analysis was separately performed on both the training and validation sets to evaluate the diagnostic ability of the models. The quality of the ranking represents the area under the curve (AUC) above 0.7. The results indicated that in the serum samples, all four previously selected metabolites (acetate, choline, pyroglutamate, and isobutyrate) exhibited very high AUC (above 0.82). The best ROC analyses with the highest significance were obtained for isobutyrate (AUC = 0.953, specificity = 0.9, and sensitivity = 0.9), followed by pyroglutamate (AUC = 0.894, specificity = 0.8, and sensitivity = 0.9), propionate (AUC = 0.859, specificity = 1.0, and sensitivity = 0.7), choline (AUC = 0.828, specificity = 0.8, and sensitivity = 0.8), and acetate (AUC = 0.824, specificity = 0.8, and sensitivity = 1.0). The range of concentrations compared to all these metabolites in the serum samples of cancer patients compared to NCs is reported in Fig. S3. The most significant results from our statistical analyses of compounds identified as potential biomarkers of BC are presented in Table 1.

The classification ROC model was built with the use of MetaboAnalyst 5.0 online service and was based on a random forest algorithm. As shown in Figs. 2E and F, the combination of levels of these metabolites was a better discriminator (AUC > 0.999) than each metabolite separately in both data sets. An excellent discriminating classification was found for four metabolites, i.e., acetate, propionate, choline, and isobutyrate, with an AUC of 0.999. For this model, the confidence interval ranged from 0.994 to 1.000 (Fig. 2E). The validation of the ROC model is shown in Fig. S4 and a permutation test with 1000 permutations yielded a P-value < 0.001, supporting the validity of the ROC analysis. The average of the predicted class probabilities of each sample and the average accuracy of the ROC curve demonstrated good classification discriminatory power, with most of the samples classified accurately in their respective groups. The results suggested that four specific metabolites, namely, acetate, propionate, choline, and isobutyrate, could significantly increase diagnostic potential and serve as useful discriminators of cancerous versus healthy phenotypes in patients diagnosed with BC.

3.2. Differences between grades of BC with ^{1}H NMR

To determine whether metabolomics analysis of serum samples by ^{1}H NMR could help discriminate between different grades of BCs, PCA and OPLS-DA analyses were performed on the entire metabolite dataset. The analysis of BC included 95 serum samples from patients with a uniquely defined grade of cancer; three samples from patients with PUNLMP and two samples from patients with tumor only partially classified as HG were excluded. Finally, 41 serum extracts from patients with HG cancer and 54 samples from patients with LG cancer were used for analysis. The 2D and 3D PCA score plots, which revealed relatively low discrimination between LG and HG cases with a few outliers, are shown in Figs. S5A and B. Likewise, the OPLS-DA score plots highlighted little separation between the HG and LG cancer groups (Fig. S5C), yet yielded an acceptable P-value ($P = 0.002$). The statistical significance of the model was examined using Q^2 (0.192) and permutation tests ($n = 2000$), which yielded a P-value lower than 0.05. Detailed assessments of the quality of the OPLS-DA model are shown in Fig. S6. The S-plot analysis of the OPLS-DA model indicated that 15 metabolites were significant contributors to the small separation observed between LG vs. HG samples in the 2D and 3D OPLS-DA score plot (Fig. S7). Of these 15 metabolites, leucine, histidine, alanine, 3-methyl-2-oxovalerate, tyrosine, phenylalanine, choline, tryptophan, hypoxanthine, asparagine, valine, proline, threonine, 2-hydroxybutyrate, and glutamine were found to be positively correlated with group separation with a P(corr)[1] score > 0.5. These biomarker candidates were subjected to a t-test to assess the significance of altered levels in LG versus HG. All 15 metabolites were found to exhibit statistically significant differences in concentration ($P < 0.05$; q < 0.05 and $|P(\text{corr})| > 0.5$), suggesting that examining the different levels of these metabolites in human sera may be an effective way to identify LG and discriminate LG from HG in patients with BC. AUC values for five of the 15 metabolites were found to be greater than 0.74 (Fig. S8). Additionally, ROC curve analysis of these five metabolites (i.e., leucine, histidine, alanine, 3-methyl-2-oxovalerate, and tyrosine) only yielded a satisfactory AUC value of 0.775 (Fig. S9A), and a valid permutation test with a P-value < 0.001. The average accuracy based on 100 cross validations amounted to a value of 0.693 (Fig. S9D). These analyses support that leucine, histidine, alanine, 3-methyl-2-oxovalerate, and tyrosine may be good indicators discriminating bladder tumor grades.

3.3. Differences between stages of BC identified by ^{1}H NMR

Analysis of tumor stages was also performed for the entire ^{1}H NMR dataset of serum metabolite extracts. Metabolite profiling analysis included 88 serum samples from patients with non-muscle

Table 1
Summary of targeted quantitative analysis of potential biomarkers of BC from proton nuclear magnetic resonance (^{1}H NMR) and inductively coupled plasma optical emission spectrometry (ICP-OES) spectral analyses of serum samples (P-value < 0.05; $|P(\text{corr})[1]| > 0.5$; area under the curve (AUC) > 0.75).

Comparison mode	Data set	Metabolite/element	AUC	VIP [t]	P(corr)[1]	P-value [a]	Fold change [b]
Cancer vs. control	^{1}H NMR	Isobutyrate	0.95	2.2	−0.718	4.3×10^{-23}	1.9
		Pyroglutamate	0.89	1.9	0.626	7.8×10^{-18}	0.5
		Propionate	0.86	2.0	0.638	4.2×10^{-15}	0.8
		Choline	0.83	1.7	0.536	7.6×10^{-13}	0.7
		Acetate	0.82	2.3	0.729	1.6×10^{-12}	0.4
	ICP-OES	Li	0.71	1.4	0.512	5.8×10^{-4}	0.1
		Fe	0.85	2.0	−0.740	1.1×10^{-8}	1.9
Low-grade vs. high-grade	^{1}H NMR	Leucine	0.80	1.5	0.711	1.3×10^{-6}	0.8
		Histidine	0.79	1.7	0.830	2.2×10^{-6}	0.7
		Alanine	0.77	1.5	0.718	1.4×10^{-5}	0.8
		3-methyl-2-oxovalerate	0.77	1.4	0.690	2.2×10^{-5}	0.6
		Tyrosine	0.75	1.2	0.568	6.3×10^{-5}	0.8
pTa/pT1 vs. pT2	^{1}H NMR	Histidine	0.80	1.9	−0.832	0.0001	1.9
		Alanine	0.79	1.7	−0.732	0.0002	1.6
		Tryptophan	0.77	1.7	−0.718	0.0002	1.6
		Glutamine	0.77	1.5	−0.645	0.0017	1.4
		Glycine	0.75	1.4	−0.593	0.0069	1.4
		Methylhistidine	0.88	1.3	−0.580	0.0094	2.1
		Choline	0.88	1.3	−0.566	0.0015	1.5
		Isobutyrate	0.82	1.2	−0.537	0.0021	1.4
		Threonine	0.78	1.2	−0.531	0.0009	1.3

[a] P-value determined from Student's t-test.

[b] Fold change between cancer and control serum calculated from the concentration mean values for each group; pTa: noninvasive papillary carcinomas; pT1: submucosal invasive tumors; pT2: muscle invasive bladder cancer; VIP: variable influence on projection.

invasive BC (pTa/pT1) and 12 serum samples from patients with muscle invasive BC (pT2). Preliminary PCA analysis was performed using the entire dataset of metabolite concentrations. PCA and OPLS-DA score plots indicated relatively low separation between the pTa/pT1 and pT2 stage of BC, with a few outliers that were removed prior to the further OPLS-DA analysis. Figs. S5D–F contain the 2D, 3D-PCA, and OPLS-DA scores plots of the two groups that were classified by BC grades. The quality factors for the OPLS-DA model included Q^2 of 0.141 and R^2Y of 0.347 and permutation test *P*-value lower than 0.05 (Figs. S6C and D). The S-plot analysis of the OPLS-DA model revealed the 12 serum metabolites that appeared to be most relevant for sample differentiation between pTa/pT1 and pT2 cancer grade: histidine, alanine, tryptophan, glutamine, glycine, methylhistidine, choline, isobutyrate, threonine, phenylalanine, leucine, and 3-methyl-2-oxovalerate (Fig. S7C). All those compounds corresponded to $|P(\text{corr})| > 0.05$ and variable influence on projection (VIP) > 1.2 and were found to be at a higher concentration in the sera of patients with noninvasive pTa/pT1 BC stage (Fig. S7D). However, the ROC analysis narrowed this group down to nine metabolites with an AUC greater than 0.75: histidine, alanine, tryptophan, glutamine, glycine, methylhistidine, choline, isobutyrate, and threonine. The ROC curve analysis of nine potential biomarkers is shown in Fig. S10. For those nine selected metabolites, a ROC curve analysis was performed to assess the performance of this model in distinguishing between pTa/pT1 and pT2 BC stages, and yielded an AUC value of 0.844, which indicated the good discriminatory ability of the model (Fig. S9E). The permutation test based on the measured area under the ROC curve (AUC) for that model yielded a *P*-value < 0.01 (Fig. S9F). The average of the predicted class probabilities of each sample across 100 cross validations and the associated permutation tests are shown in Figs. S9G and H. Analysis of the changes in metabolite concentration for a given stage of BC, i.e., pTa/pT1 versus pT2, reveals higher levels of histidine, alanine, tryptophan, glutamine, glycine, methylhistidine, choline, isobutyrate, and threonine in the serum samples of BC patients with a pTa/pT1 stage of tumor compared to the sera of BC patients with a pT2 stage tumor. The comparison of the three groups of cancer stage (pT1 vs. pTa vs. pT2) did not reveal any statistically significant differences.

3.4. Elemental profile of serum in BC determined by ICP-OES

The concentrations of chemical elements obtained from ICP-OES analysis of 116 extracts of serum samples (65 BC and 51 NCs) were subjected to statistical data analysis. A total of 12 elements were identified and quantified. The mean concentration of each of these elements is summarized in Tables S5 and S6. Prior to statistical analysis, the data were randomly divided into two subsets: a training set (control, $n = 42$ and cancer, $n = 52$) and a validation set (control, $n = 10$ and cancer, $n = 13$). As shown in Fig. 3A, the PCA score plot revealed a trend for separation between the two groups in the training set. Results from the OPLS-DA analysis, shown in Fig. 3B, provided a slightly clearer separation (compared to the PCA analysis) between cancer and controls, and the validation parameters for the model were R^2X and Q^2 values of 0.334 and 0.476, respectively (Fig. S11). The analysis of the VIP scores of the OPLS-DA model in the training set is presented at Fig. 3C.

Three elements (Cu, Fe, and Li) could be used to distinguish between the two groups of study participants; however, only two of them (Cu and Fe) were confirmed to be the most significant

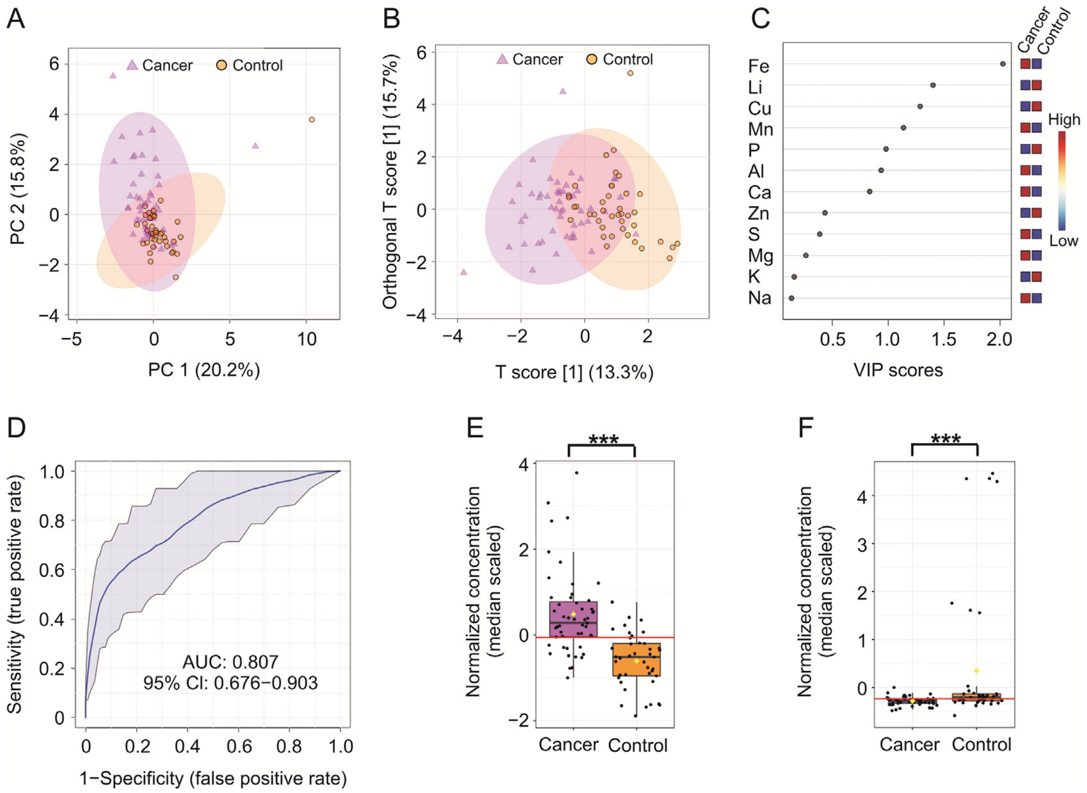

Fig. 3. Statistical analysis of serum metabolite profiles created from inductively coupled plasma optical emission spectrometry (ICP-OES) data. Two-dimensional (A) principal component analysis and (B) orthogonal partial least-squares discriminant analysis (OPLS-DA) score plots of the tumor (violet) and control (orange) serum samples for ICP-OES data in the training set. (C) The potential discriminatory elements identified from the variable importance in projection (VIP) scores derived from the OPLS-DA model in the training set. (D) The receiving operator characteristic (ROC) curves of the combination of two differential elements, Fe and Li. (E and F) The box-and-whisker plots of Fe and Li level values observed in the control and BC serum samples. *** $P < 0.001$. PC: principal component; AUC: area under the curve; CI: confidence interval.

discriminators following model validation assessments (Fig. S12). The loading S-plot of OPLS-DA of the training set revealed that Fe was negatively correlated with group separation, with $-P(\mathrm{corr})[1] < -0.5$, and indicated that a significantly higher level of this element was found in the serum of patients diagnosed with BC compared with the control group. Subsequently, Li was found to be positively correlated with the group separation, with $P(\mathrm{corr})[1] > 0.5$, indicating that it was found in higher levels in the serum samples of NCs. ROC analysis revealed that Fe was the most significant, with an associated AUC value of 0.850, sensitivity of 0.8, and specificity of 0.8, whereas for Li, the AUC value was 0.710, sensitivity was 0.8, and specificity was 0.6. In addition, ROC curve analysis assessing the performance of the ICP-OES model in distinguishing between cancer and control samples was performed using only two selected elements (Fe and Li). This analysis yielded an AUC value of 0.807 for the training set, which indicated good discriminatory power to separate the two (BC and NC) groups (Fig. 3D). The permutation test yielded a significant *P*-value of <0.001. The average accuracy amounted to a value of 0.728 (Fig. S13D).

These statistical analyses demonstrated that differential levels of Fe and Li are potentially good indicators of BC in human serum. The results from the statistical analyses of these two selected elements are summarized in Table 1.

3.5. Untargeted metabolic profiling by PFL-2D GS LASiS AuNPs and ^{109}AgNPs LDI-MS

In total, 335 and 650 features were detected in the serum samples of 200 participants analyzed with PFL-2D GS LASiS AuNPs and ^{109}AgNPs LDI-MS. Statistical analysis was performed using data randomly divided into two subsets: a training set (n = 80 BC and n = 80 NCs) and a validation dataset (n = 20 BC and n = 20 NCs).

2D-PCA and OPLS-DA score plots of mass spectral features created for PFL-2D GS LASiS ^{109}AgNPs LDI-MS data revealed clear discrimination between cancer and control serum samples in both subsets (Fig. S14). The analysis of both subsets (training and validation set) indicated 216 common features with $|p[1]|$ and $|P(\mathrm{corr})|$ above 0.5, of which 96 *m/z* values were more abundant in serum from patients with BC compared with the control group, and 119 features displayed the opposite trend. The validation of the OPLS-DA model using 2000 permutations resulted in R^2Y and Q^2 values of 0.986 ($P < 0.0005$) and 0.982 ($P < 0.0005$) (Fig. S15). All 11 previously selected *m/z* mass spectral features were found to exhibit AUC values of >0.73. Figs. S16A and D indicate the combination of *m/z* values, which is a better discriminator (AUC >99% in the training and validation set) than independent evaluation of each feature, which reinforces the improved capacity of biomarker patterns to accurately distinguish between the BC and NC groups. In the next step, putative identification of mass spectral features was performed by searching various metabolite databases, i.e., Human Metabolome Database [38], MetaCyc Metabolic Pathway Database [39], LIPID MAPS® Lipidomics Gateway [40], and Metlin [41]. Seventeen mass spectral features were putatively identified as naturally occurring metabolites in the human body. Important mass spectral features and annotated metabolite IDs resulting from the PFL-2D GS LASiS ^{109}AgNPs LDI-MS analyses are reported in Table S7. All statistical data with mean feature abundance for control versus cancer serum samples based on PFL-2D GS LASiS ^{109}AgNPs LDI-MS in the training and validation datasets are presented in Tables S8 and S9.

The acquired data from untargeted PFL-2D GS LASiS AuNPs LDI-MS analysis were also analyzed using PCA and OPLS-DA to identify novel metabolites. In both cases, score plots showed clear separation in both subsets, suggesting that the PFL-2D GS LASiS AuNPs LDI-MS-based serum metabolomics model could be used to identify BC (Fig. S17). The S-plots derived from the OPLS-DA model using the training set ($R^2Y = 0.962$, $Q^2 = 0.955$) and the validation set ($R^2Y = 0.982$, $Q^2 = 0.964$) generated a list of mass spectral features (*m/z*) of interest that were found to be important for group discrimination (Fig. S18). All relevant mass spectral features are reported in Tables S10 and S11. The analysis of both subsets (training and validation sets) identified 172 common features with $|p[1]|$ and $|P(\mathrm{corr})|$ above 0.5, of which 44 *m/z* values were more abundant in the sera of BC patients compared to the control group, and 128 features exhibited the opposite trend. This analysis was followed by a multivariate ROC analysis. As shown in Fig. S19, the combination of mass spectral features in both subsets was found to be a more powerful discriminator between control and BC serum samples (AUC > 99%), compared with that of any individual mass spectral feature.

The results presented above suggest that selected mass spectral features can significantly increase the performance of the diagnostic model and can be used to distinguish cancer serum samples from controls. Putative identifications of selected features allowed for the identification of eight compounds that are often present in the human body (Table S7).

3.6. Pathway analysis of potential cancer biomarkers

Metabolic pathway impact analysis suggested that 14 out of 25 metabolites identified in the NMR and LDI-MS analyses were relevant to human metabolism. Seven pathways (glycine, serine and threonine metabolism, glycerophospholipid metabolism, propanoate metabolism, glutathione metabolism, pyruvate metabolism, glyoxylate and dicarboxylate metabolism, and glycolysis/gluconeogenesis) were significantly impacted in BC compared with the controls. The results from this pathway impact analysis are shown in Fig. 4A and Table S12. The bubble area (Fig. 4A) reveals the degree of impact on the pathway and the color represents the significance (highest in red and lowest in white). Quantitative enrichment analysis found 10 additional pathways relevant to BC, i.e., amino sugar metabolism, aspartate metabolism, betaine metabolism, ethanol degradation, fatty acid biosynthesis, methionine metabolism, phosphatidylcholine biosynthesis, phosphatidylethanolamine biosynthesis, phospholipid biosynthesis, and vitamin K (K1 and K2) metabolism (Fig. 4B and Table S13).

4. Discussion

In this study, NMR, ICP-OES, and LDI-MS with both ^{109}AgNPs and AuNPs-based targets were employed to evaluate changes in serum metabolite and element levels between patients with BC and controls. BC is characterized by several metabolic changes that promote cancer cell proliferation and thus tumor growth [42]. These changes in metabolism provide an essential source of energy for intracellular metabolism and building blocks for rapidly dividing tumor cells. The Warburg effect, a hallmark of cancer cell metabolic activity, involves aerobic glycolysis in the presence of an aerobic environment and fully functioning mitochondria, and relies on increased glucose uptake and the conversion of glucose to lactate. This type of energy gain for cancer cells is much less energy efficient than mitochondrial respiration (2 adenosine triphosphate (ATP) vs. 36 ATP respectively) [43]. However, studies have shown that the rate of glucose-to-lactate conversion is 10–100 faster compared with that of the complete mitochondrial oxidation of glucose [44]. Moreover, the decoupling of glycolysis from oxidative phosphorylation offers a biosynthetic advantage for cancer cells by enabling the increased production of diverse biosynthetic precursors [45].

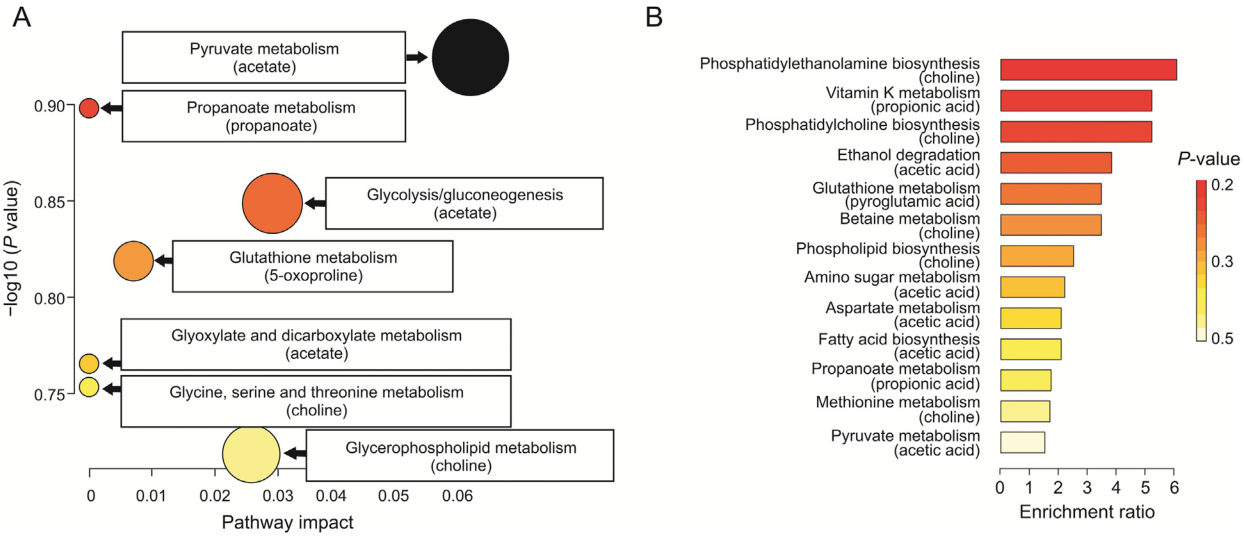

Fig. 4. Pathway topology analysis of statistically significant metabolites in bladder cancer (BC) that were found in the nuclear magnetic resonance and mass spectrometry (MS) datasets. (A) Kyoto Encyclopedia of Genes and Genomes pathway analysis. (B) Quantitative enrichment analysis based on Small Molecule Pathway Database.

In this study, we investigated the serum metabolic profiles among LG BC, HG BC, non-muscle invasive bladder cancer (pTa/pT1), muscle invasive BC (MIBC, pT2), and healthy subjects. The OPLS-DA modeling of the ^{1}H NMR metabolomics data revealed a clear separation between the BC and control serum sample groups. Metabolites with the highest AUC values (>0.82) included isobutyrate, pyroglutamate, propionate, choline, and acetate. The differences in the concentration of pyroglutamate, acetate, propionate, and choline were statistically significantly and higher in the sera of healthy individuals, whereas isobutyrate concentrations were much higher in the sera of BC patients.

Negative charges of short-chain fatty acids are considered to be crucial metabolic and immune cell regulators [46]. Acetate plays a key role in the metabolism of acetyl coenzyme A (acetyl-CoA), bioenergetics, cell proliferation, and regulation [47]. In cells, acetate is mainly used to generate acetyl-CoA through an ATP-dependent reaction by acetyl-CoA synthetase. Tumor cells use acetate in the form of acetyl-CoA, primarily for fuel or as a carbon source for lipid synthesis [48]. Acetyl-CoA synthetase 2 (ACSS2), one of the enzymes capable of using acetate as a substrate, contributes to cancer cell growth and is highly upregulated in multiple cancer types [49]. Based on these studies, we surmise that the lower levels of acetate in the serum samples of patients with BC may be due to its significant uptake and utilization by ACSS2 in cancer cells. Recently, Lee et al. [50] reported that acetate in urine, along with four urine metabolites, may contribute to the discrimination of different urological cancers. Their research showed that acetate levels in urine were slightly elevated in kidney cancer patients compared to patients with bladder and prostate cancer. Unfortunately, these results were not directly compared to those of a healthy control group [50].

Other metabolites present at lower concentration in the sera of BC cancer patients compared with healthy controls include choline and propionate. Studies have shown that the consumption of choline may protect against cancer [51]. Propionate, a metabolite produced by the intestinal microbiota, reduces the proliferation of cancer cells in the liver and the lungs [52,53]. Acetate and propionate are the end-products of the indigestible carbohydrate fermentation in the human colon, and are distributed systemically via blood circulation. These compounds have been shown to exhibit anti-inflammatory properties in immune cells, inhibit colon cancer cell growth, and induce cancer cell death by apoptosis [53,54]. The levels of serum propionate are also associated with circulating immune cells in patients with multiple sclerosis, and lower serum propionate levels were found in patients with multiple sclerosis compared with the healthy controls [55]. In our study, the increased absorption of propionate by cancer cells is reflected by the lower propionate concentration in the sera of the patients with BC. However, no study to date has focused on the role of propionate in the progression of BC.

Choline is a water-soluble quaternary amine that is often grouped with vitamin B owing to its chemical similarities, and is a key nutrient for humans. This compound has various key functions in the human body, especially with respect to neurochemical processes [56]. Choline is involved in phospholipid production and triglyceride metabolism, and is therefore necessary for the proper structure and function of cell membranes. In this study, patients with BC had lower serum levels of choline compared with the controls, which could be a consequence of increased choline absorption by cancer cells. Our results are consistent with those of other studies that have shown that cancer cells often increase the synthesis of fatty acids; in turn, these can act as substrates for phosphatidylcholine synthesis, which is increased in tumor cells [57,58]. Furthermore, the increase in serum choline levels in cancer patients is consistent with our previous study results, where choline levels were found to be decreased in the sera of patients with renal cell carcinoma compared with controls [59]. The opposite situation was observed in urine, where urine choline levels were increased in patients with BC [60,61].

Ohara et al. [62] revealed that isobutyrate exerted an anticancer effect by suppressing the growth/metabolic networks supporting colorectal cancer. Previously, Wang et al. [63] showed that the levels of isobutyrate were lower in fecal samples of patients with colorectal cancer compared to those of healthy control individuals. To date, there is no report that isobutyrate is a potential biomarker of BC. In our research, isobutyrate levels were found to be significantly altered, as shown by the cancer-to-control mean concentration (fold change) ratio of 1.9.

Pyroglutamate is a cyclized derivative of L-glutamate and is related to the gamma-glutamyl cycle, which is the main pathway for glutathione synthesis [64]. Glutathione is a major antioxidant produced in the human body, the levels of which can drop significantly as a result of oxidative stress or chemical exposure. In the case of low glutathione levels, the level of pyroglutamate from which it is reconstituted is also decreased [65]. Pyroglutamate was found to be a promising biomarker for the diagnosis of nonalcoholic liver disease [64]. Several studies have observed elevated levels of pyroglutamate in the biofluids of patients with several genetic disorders and an acetaminophen-induced metabolic disorder [66]. Most of the research devoted to urinary or serum metabolomics of BC has suggested a higher level of pyroglutamate in patients with BC compared with healthy controls [22,67]. However, both of these cited publications are based on GC-MS results with derivatization, which can be considered inferior in terms of quantitation compared to the measurement of unmodified extracts with NMR.

Fe is a crucial trace element in which the deficiency or excess is associated with numerous disease states [68]. ICP-OES analysis indicated an increase in serum Fe in patients with BC, which is surprising, given that these patients often have micro/macrohematuria, so Fe deficiency would be expected [69]. However, the higher level of Fe in serum of patients with BC may be explained by the activation of mechanisms stimulating Fe absorption from the gastrointestinal tract, which provides a possible compensation for the level of Fe in the blood. Moreover, previous studies have suggested that excess Fe in the sera of patients with cancer may be associated with malignant transformation and cancer progression [70]. In tumor tissues, rapid cell proliferation and increased DNA synthesis are often observed, which require high Fe bioavailability. In the human body, the main source of Fe in the blood is heme, which is released following the breakdown of red blood cells [70]. Further, our results are consistent with earlier studies that reported elevated serum Fe levels in various types of diseases, such as hepatocellular carcinoma, lung cancer, and colorectal cancer [71].

Li is an alkali metal used to treat psychiatric disorders, and has potential benefits for the treatment of leukemia or thyroid disorders [72]. It inhibits several enzymes, including inositol monophosphatase and glycogen synthase kinase-3 [73]. However, the ingestion of Li causes many side effects, including hypercalcemia, cardiovascular, and gastrointestinal and parathyroid disorders [74]. Recent studies demonstrated that Li uptake is associated with reduced tumor incidence, probably through inhibited cell proliferation, which may be linked to reduced DNA replication and S-phase cell cycle arrest [75]. Wach et al. [29] detected significantly increased concentration of Li in the sera of patients with BC compared with healthy controls using ICP-OES.

Lower concentration of the serum amino acids histidine, alanine, tryptophan, glutamine, glycine, and threonine in patients with muscle invasive BC (pT2) in comparison to non-muscle invasive BC (pTa/pT1) may suggest the higher uptake of these amino acids and their potential role in protein synthesis underlying muscle cancer invasion. This inference is supported by proteomic studies that reported significant differences in tissue protein expression, which were correlated with BC ability to invade into muscle tissue [76]. Another possibility as to why these amino acids are present at lower concentrations may be due to general state of cachexia and malnutrition observed in patients with MIBC, which is usually a systemic disease and often manifests at a stage when metastases are present. Interestingly, lower concentrations of serum amino acids (leucine, histidine, alanine, and tyrosine) can be also observed in LG BC when compared to HG BC. In healthy organisms, de novo lipogenesis is limited to hepatocytes and adipocytes. Cancer cells may reactivate this anabolic pathway, which relies on glucose, glutamine, and acetate to synthesize citrate. Both acetate and citrate are substrates for extramitochondrial acetyl-CoA production, which is essential for fatty acid and cholesterol biosynthesis [57].

To date, several papers have focused on metabolite analyses in urine and blood from BC patients in an effort to potentially differentiate the different grades of this cancer. However, to our knowledge, only two studies have explored the relationships between changes in metabolite levels in urine and different tumor stages (Ta/Tis, T1, and >T2) [61,77]. At present, there are no reports of serum profiling in patients with different types of BC, probably owing to the fact that this type of analysis would require quite a large group of patients and healthy controls.

A pilot urine analysis conducted by Kim et al. [67] in 2010 studied a relatively small group of patients and revealed slightly elevated levels of alanine, glutamine, leucine, tyrosine, and glycine and slightly decreased levels of threonine and tryptophan in patients with BC compared with controls. Subsequent studies also using GC-MS confirmed higher levels of alanine in the serum of the healthy controls compared to patients with BC, but the levels of alanine were not found to be potentially diagnostic of BC stages [22]. In our study, a slightly lower concentration of alanine in the serum of patients with BC was found compared to the control group; however, this trend was not found to be statistically significant in differentiating between the two groups. However, we measured significantly lower levels of alanine in the sera of patients with LG and pTa/pT1 BC, which has not been previously reported in the literature.

Troisi et al. [22] obtained comparable results to Kim et al. [67] study with respect to glutamine level changes, but also found higher levels of threonine in the sera samples from the LG group compared with the HG group, and a higher level of glycine in the HG group compared with the LG group. The results from our study indicated that differential concentrations of glycine, glutamine, and threonine in human sera may be used as diagnostic markers and may help distinguish between different stages of BC, as we have found that these metabolites were present at higher concentrations in the sera of patients with pTa/pT1 stage disease compared to those with pT2 stage. Bansal et al. [24] undertook an NMR-based study of serum metabolite profiles and identified glutamine as one of three metabolites that can differentiate between LG and HG BC, as it was reported to be slightly elevated in the sera of patients with HG BC [24]. Our results on serum glutamine levels are consistent with published studies, and suggest that elevated levels of glutamine in the pTa/pT1 stage of BC may be the result of increased glutaminolysis, which is observed in some types of tumors as an important mechanism to provide an additional source of cellular energy [78].

Bansal et al. [24] also reported histidine as one of the six metabolites that can distinguish patients with LG and HG BC from healthy controls, and was reported to be in higher concentrations in the sera of LG BC patients compared to HG BC patients and healthy controls. The authors' finding about serum histidine levels was consistent with that of our study, which found higher serum levels of histidine in LG and pTa/pT1 BC cancer [24,79]. The link between differential levels of serum histidine and BC progression, as well as concentration changes in methylhistidine, tyrosine, leucine, and tryptophan, has also been reported by Alberice et al. [80]. The authors' study reported elevated levels of these metabolites in the sera of patients with bladder tumors compared to those of patients with early stages of BC [80]. In contrast, an LC-MS-based study reported lower levels of histidine in the urine of patients with BC compared to healthy controls [56,81]. Moreover, Li et al. [60] indicated an increased level of L-methylhistidine in the urine of patients with BC. Histidine is a precursor for histamine synthesis in a reaction catalyzed by histidine decarboxylase (HDC). The overexpression of HDC has been observed in various cancers. Histidine via histamine is associated with inflammation in the urinary bladder, which is commonly associated with cancer development in this organ [82].

Our research has shown a significant difference in serum leucine levels in BC patients with LG compared to HG. In addition to the research of Kim et al. [67] and Alberice et al. [80], the level of leucine in patients with BC was also examined by Cao et al. [23], who reported, using NMR, lower levels of leucine/isoleucine as well as tyrosine and glycine in the sera of patients with HG BC compared to LG BC, which was consistent with our findings. Another study, conducted by Loras et al. [83], reported increased levels of tyrosine and tryptophan in the urine of patients with BC compared to healthy controls. Our research results are also consistent with those of Yumba Mpanga et al. [84], which indicated significantly higher levels of tryptophan in the urine of patients with HG BC compared to LG BC group.

The use of the gold and silver-109-modified targets in LDI-MS experiments allowed for direct measurement of serum samples without analyte separation and extraction. Using this technique, serum analysis allowed the identification of 13 compounds that were found in greater concentrations in control serum samples compared to those of patients with BC, and 12 compounds that displayed the opposite trend; these included three compounds found independently using both silver-109- and gold-based MS methods. Most of these compounds were lipids, 12 of which belonged to the class of sphingolipids, and the remaining contained fatty acyls, saccharolipids, polyketides, nucleosides or nucleotides, and others.

Lipid metabolism plays a key role in various processes associated with cancer cells. Fatty acids are the building blocks of complex lipids, which are used for energy storage or as building blocks of cell membranes [85]. As reported by many authors, BC initiation and progression are associated with changes in lipid metabolism [86]. Sphingolipids are a group of lipids comprising sphingoid bases (i.e., set of aliphatic amino alcohols that include sphingosine) that play an important role in regulation of diverse cellular processes including cellular apoptosis, proliferation, angiogenesis, senescence, and transformation [87]. The importance of sphingolipids in the regulation of cancer growth and pathogenesis has been well described in the literature [88]. The sphingolipid metabolism may be responsible for the invasion and mobility of cancer cells in muscle-infiltrating BC [89]. Human BC cells have also been shown to upregulate the cannabinoid receptors 2, which induces cell apoptosis by stimulating de novo ceramide synthesis [90].

Lastly, the gold- and silver-109-based LDI-MS spectral analyses shown in this work have indicated a higher concentration of serum cyanidin in healthy individuals. Cyanidin is classified as a natural antioxidant present in both fruits and vegetables, and has confirmed with anticancer properties. It has been reported to induce apoptosis and differentiation in prostate and renal cancer cells [91,92].

5. Conclusion

We demonstrate that high-resolution NMR, ICP-OES, and gold- and silver-109-based LDI-MS, together with multivariate statistics, are powerful sets of tools for the characterization of the serum metabolome and elemental differences in BC. With regard to biomarker discovery using ^{1}H NMR spectroscopy, four potentially robust metabolic biomarkers were identified for 100 tumor serum samples from patients with BC patients after comparison against 100 healthy controls owing to the excellent predictive ability of AUC > 0.999. Two elements (Fe and Li) exhibited significant concentration differences in the serum of NCs compared to that of patients with BC, suggesting that they may serve as useful biomarkers of BC. Additionally, 22 compounds (mainly lipids) were observed to differentiate between cancer and control samples, as judged from laser MS results. We also identified five metabolites that might be used as potential biomarkers to distinguish LG and HG and nine metabolites that may serve to differentiate between the pTa/pT1 and pT2 stages of BC. Our results suggest that differential serum metabolite profiles and elements can help identify patients with BC compared with NCs, with significant discriminating power between different stages and grades of BC. Moreover, our findings demonstrate that combining serum metabolite profiles and elements has a stronger predictive value than either compound/element alone to assess disease severity and progression in BC.

CRediT author statement

Krzysztof Ossoliński: Investigation, Resources, Writing - Original draft preparation; **Tomasz Ruman:** Methodology, Resources, Data curation, Writing - Reviewing and Editing, Supervision; **Valérie Copié:** Resources, Data curation, Writing - Reviewing and Editing, Funding acquisition; **Brian P. Tripet:** Resources, Data curation, Writing - Reviewing and Editing, Visualization, Funding acquisition; **Leonardo B. Nogueira:** Resources, Investigation, Data curation; Writing - Original draft preparation; **Katiane O.P.C. Nogueira:** Data curation, Writing - Original draft preparation; **Artur Kołodziej:** Investigation, Data curation; **Aneta Płaza-Altamer:** Investigation; **Anna Ossolińska:** Resources; **Tadeusz Ossoliński:** Resources; **Joanna Nizioł:** Conceptualization, Methodology, Formal analysis, Investigation, Data curation, Writing - Original draft preparation, Reviewing and Editing, Visualization, Supervision, Project administration, Funding acquisition.

Declaration of competing interest

The authors declare that there are no conflicts of interest.

Acknowledgments

Research was supported mainly by the National Science Center (Poland) (Project SONATA No.: UMO-2018/31/D/ST4/00109). ^{1}H NMR spectra were recorded at Montana State University (MSU), Bozeman, USA, on a cryoprobe-equipped 600 MHz (14 T) AVANCE III solution NMR spectrometer housed in MSU's NMR Center. Funding for MSU NMR Center's NMR instruments has been provided in part by the National Institutes of Health Shared Instrumentation Grant program (Grant Nos.: 1S10RR13878 and 1S10RR026659), the National Science Foundation (Grant Nos: NSF-MRI:DBI-1532078 and NSF-MRI CHE 2018388), the Murdock Charitable Trust Foundation (Grant No.: 2015066:MNL), and support from the office of the Vice President for Research, Economic Development, and Graduate Education at MSU.

Appendix A. Supplementary data

Supplementary data to this article can be found online at https://doi.org/10.1016/j.jpha.2022.08.004.

References

[1] H. Sung, J. Ferlay, R.L. Siegel, et al., Global cancer statistics 2020: GLOBOCAN estimates of incidence and mortality worldwide for 36 cancers in 185 countries, CA Cancer J. Clin. 71 (2021) 209–249.
[2] H.A.A. Amin, M.H. Kobaisi, R.M. Samir, Schistosomiasis and bladder cancer in Egypt: Truths and myths, open access maced, Open Access Maced. J. 7 (2019) 4023–4029.
[3] M. Burger, J.W. Catto, G. Dalbagni, et al., Epidemiology and risk factors of urothelial bladder cancer, Eur. Urol. 63 (2013) 234–241.
[4] F.A. Yafi, F. Brimo, J. Steinberg, et al., Prospective analysis of sensitivity and specificity of urinary cytology and other urinary biomarkers for bladder cancer, Urol. Oncol. 33 (2015) 66.e25–66.e31.
[5] F. Soria, M.J. Droller, Y. Lotan, et al., An up-to-date catalog of available urinary biomarkers for the surveillance of non-muscle invasive bladder cancer, World J. Urol. 36 (2018) 1981–1995.

[6] Q. Yang, A.-H. Zhang, J.-H. Miao, et al., Metabolomics biotechnology, applications, and future trends: A systematic review, RSC Adv. 9 (2019) 37245–37257.
[7] G. Raja, Y. Jung, S.H. Jung, et al., ^{1}H-NMR-based metabolomics for cancer targeting and metabolic engineering – A review, Process Biochem. 99 (2020) 112–122.
[8] X.-W. Zhang, Q.-H. Li, Z.-D. Xu, et al., Mass spectrometry-based metabolomics in health and medical science: A systematic review, RSC Adv. 10 (2020) 3092–3104.
[9] P.K. Cheung, M.H. Ma, H.F. Tse, et al., The applications of metabolomics in the molecular diagnostics of cancer, Expert Rev. Mol. Diagn. 19 (2019) 785–793.
[10] Z. Pan, D. Raftery, Comparing and combining NMR spectroscopy and mass spectrometry in metabolomics, Anal. Bioanal. Chem. 387 (2007) 525–527.
[11] K. Ng, A. Stenzl, A. Sharma, et al., Urinary biomarkers in bladder cancer: A review of the current landscape and future directions, Urol. Oncol. 39 (2021) 41–51.
[12] R. Batista, N. Vinagre, S. Meireles, et al., Biomarkers for bladder cancer diagnosis and surveillance: A comprehensive review, Diagnostics (Basel) 10 (2020), 39.
[13] M.C. Walsh, L. Brennan, J.P. Malthouse, et al., Effect of acute dietary standardization on the urinary, plasma, and salivary metabolomic profiles of healthy humans, Am. J. Clin. Nutr. 84 (2006) 531–539.
[14] L. Lin, Z. Huang, Y. Gao, et al., LC-MS-based serum metabolic profiling for genitourinary cancer classification and cancer type-specific biomarker discovery, Proteomics 12 (2012) 2238–2246.
[15] Y. Zhou, R. Song, Z. Zhang, et al., The development of plasma pseudotargeted GC-MS metabolic profiling and its application in bladder cancer, Anal. Bioanal. Chem. 408 (2016) 6741–6749.
[16] G. Tan, H. Wang, J. Yuan, et al., Three serum metabolite signatures for diagnosing low-grade and high-grade bladder cancer, Sci. Rep. 7 (2017), 46176.
[17] D. Sahu, Y. Lotan, B. Wittmann, et al., Metabolomics analysis reveals distinct profiles of nonmuscle-invasive and muscle-invasive bladder cancer, Cancer Med. 6 (2017) 2106–2120.
[18] V. Vantaku, S.R. Donepudi, D.W.B. Piyarathna, et al., Large-scale profiling of serum metabolites in African American and European American patients with bladder cancer reveals metabolic pathways associated with patient survival, Cancer 125 (2019) 921–932.
[19] C.S. Amara, C.R. Ambati, V. Vantaku, et al., Serum metabolic profiling identified a distinct metabolic signature in bladder cancer smokers: A key metabolic enzyme associated with patient survival, Cancer Epidemiol. Biomarkers Prev. 28 (2019) 770–781.
[20] X. Liu, M. Zhang, X. Cheng, et al., LC-MS-based plasma metabolomics and lipidomics analyses for differential diagnosis of bladder cancer and renal cell carcinoma, Front. Oncol. 10 (2020), 717.
[21] Z. Lepara, O. Lepara, A. Fajkić, et al., Serum malondialdehyde (MDA) level as a potential biomarker of cancer progression for patients with bladder cancer, Rom. J. Intern. Med. 58 (2020) 146–152.
[22] J. Troisi, A. Colucci, P. Cavallo, et al., A serum metabolomic signature for the detection and grading of bladder cancer, Appl. Sci. 11 (2021), 2835.
[23] M. Cao, L. Zhao, H. Chen, et al., NMR-based metabolomic analysis of human bladder cancer, Anal. Sci. 28 (2012) 451–456.
[24] N. Bansal, A. Gupta, N. Mitash, et al., Low- and high-grade bladder cancer determination via human serum-based metabolomics approach, J. Proteome Res. 12 (2013) 5839–5850.
[25] A. Gupta, K. Nath, N. Bansal, et al., Role of metabolomics-derived biomarkers to identify renal cell carcinoma: A comprehensive perspective of the past ten years and advancements, Expert Rev. Mol. Diagn. 20 (2020) 5–18.
[26] S.J. Mulware, Trace elements and carcinogenicity: A subject in review, 3 Biotech 3 (2013) 85–96.
[27] S. Mishra, S.P. Dwivedi, R.B. Singh, A review on epigenetic effect of heavy metal carcinogens on human health, Open Nutraceuticals J. 3 (2010) 188–193.
[28] R.S. Amais, G.L. Donati, M.A. Zezzi Arruda, ICP-MS and trace element analysis as tools for better understanding medical conditions, Trends Analyt. Chem. 133 (2020), 116094.
[29] S. Wach, K. Weigelt, B. Michalke, et al., Diagnostic potential of major and trace elements in the serum of bladder cancer patients, J. Trace Elem. Med. Biol. 46 (2018) 150–155.
[30] M. Abdel-Gawad, E. Elsobky, M. Abdel-Hameed, et al., Quantitative and qualitative evaluation of toxic metals and trace elements in the tissues of renal cell carcinoma compared with the adjacent non-cancerous and control kidney tissues, Environ. Sci. Pollut. Res. Int. 27 (2020) 30460–30467.
[31] J. Nizioł, V. Copié, B.P. Tripet, et al., Metabolomic and elemental profiling of human tissue in kidney cancer, Metabolomics 17 (2021), 30.
[32] A. Płaza, A. Kołodziej, J. Nizioł, et al., Laser ablation synthesis in solution and nebulization of silver-109 nanoparticles for mass spectrometry and mass spectrometry imaging, ACS Meas. Sci. Au 2 (2022) 14–22.
[33] J. Nizioł, K. Ossoliński, B.P. Tripet, et al., Nuclear magnetic resonance and surface-assisted laser desorption/ionization mass spectrometry-based metabolome profiling of urine samples from kidney cancer patients, J. Pharm. Biomed. Anal. 193 (2021), 113752.
[34] Z. Pang, J. Chong, G. Zhou, et al., MetaboAnalyst 5.0: Narrowing the gap between raw spectra and functional insights, Nucleic Acids Res. 49 (2021) W388–W396.
[35] S.Y. Ho, K. Phua, L. Wong, et al., Extensions of the external validation for checking learned model interpretability and generalizability, Patterns (N Y) 1 (2020), 100129.
[36] A.H. Emwas, E. Saccenti, X. Gao, et al., Recommended strategies for spectral processing and post-processing of 1D ^{1}H-NMR data of biofluids with a particular focus on urine, Metabolomics 14 (2018), 31.
[37] L. Yu, I.W. Liou, S.W. Biggins, et al., Copper deficiency in liver diseases: A case series and pathophysiological considerations, Hepatol. Commun. 3 (2019) 1159–1165.
[38] D.S. Wishart, D. Tzur, C. Knox, et al., HMDB: The human metabolome database, Nucleic Acids Res. 35 (2007) D521–D526.
[39] R. Caspi, R. Billington, C.A. Fulcher, et al., The MetaCyc database of metabolic pathways and enzymes, Nucleic Acids Res. 46 (2017) D633–D639.
[40] M. Sud, E. Fahy, D. Cotter, et al., LIPID MAPS-nature lipidomics Gateway: An online resource for students and educators interested in lipids, J Chem. Educ. 89 (2012) 291–292.
[41] C.A. Smith, G. O'Maille, E.J. Want, et al., METLIN A metabolite mass spectral database, Ther. Drug Monit. 27 (2005) 747–751.
[42] F. Massari, C. Ciccarese, M. Santoni, et al., Metabolic phenotype of bladder cancer, Cancer Treat. Rev. 45 (2016) 46–57.
[43] W. Jones, K. Bianchi, Aerobic glycolysis: Beyond proliferation, Front. Immunol. 6 (2015), 227.
[44] M.V. Liberti, J.W. Locasale, The Warburg effect: How does it benefit cancer cells? Trends Biochem. Sci. 41 (2016) 211–218.
[45] M.G. Vander Heiden, L.C. Cantley, C.B. Thompson, Understanding the Warburg effect: The metabolic requirements of cell proliferation, Science 324 (2009) 1029–1033.
[46] J. Frampton, K.G. Murphy, G. Frost, et al., Short-chain fatty acids as potential regulators of skeletal muscle metabolism and function, Nat. Metab. 2 (2020) 840–848.
[47] S.A. Comerford, Z. Huang, X. Du, et al., Acetate dependence of tumors, Cell 159 (2014) 1591–1602.
[48] A.M. Hosios, M.G. Vander Heiden, Acetate metabolism in cancer cells, Cancer Metabol. 2 (2014), 27.
[49] Z.T. Schug, J. Vande Voorde, E. Gottlieb, The metabolic fate of acetate in cancer, Nat. Rev. Cancer 16 (2016) 708–717.
[50] S. Lee, J.Y. Ku, B.J. Kang, et al., A unique urinary metabolic feature for the determination of bladder cancer, prostate cancer, and renal cell carcinoma, Metabolites 11 (2021), 591.
[51] S. Sun, X. Li, A. Ren, et al., Choline and betaine consumption lowers cancer risk: A meta-analysis of epidemiologic studies, Sci. Rep. 6 (2016), 35547.
[52] L.B. Bindels, P. Porporato, E.M. Dewulf, et al., Gut microbiota-derived propionate reduces cancer cell proliferation in the liver, Br. J. Cancer 107 (2012) 1337–1344.
[53] K. Kim, O. Kwon, T.Y. Ryu, et al., Propionate of a microbiota metabolite induces cell apoptosis and cell cycle arrest in lung cancer, Mol. Med. Rep. 20 (2019) 1569–1574.
[54] K.M. Maslowski, A.T. Vieira, A. Ng, et al., Regulation of inflammatory responses by gut microbiota and chemoattractant receptor GPR43, Nature 461 (2009) 1282–1286.
[55] S. Trend, J. Leffler, A.P. Jones, et al., Associations of serum short-chain fatty acids with circulating immune cells and serum biomarkers in patients with multiple sclerosis, Sci. Rep. 11 (2021), 5244.
[56] S.K. Tayebati, I. Martinelli, M. Moruzzi, et al., Choline and choline alphoscerate do not modulate inflammatory processes in the rat brain, Nutrients 9 (2017), 1084.
[57] N. Koundouros, G. Poulogiannis, Reprogramming of fatty acid metabolism in cancer, Br. J. Cancer 122 (2020) 4–22.
[58] R.F. Saito, L.N.S. Andrade, S.O. Bustos, et al., Phosphatidylcholine-derived lipid mediators: The crosstalk between cancer cells and immune cells, Front. Immunol. 13 (2022), 768606.
[59] J. Nizioł, K. Ossoliński, B.P. Tripet, et al., Nuclear magnetic resonance and surface-assisted laser desorption/ionization mass spectrometry-based serum metabolomics of kidney cancer, Anal. Bioanal. Chem. 412 (2020) 5827–5841.
[60] J. Li, B. Cheng, H. Xie, et al., Bladder cancer biomarker screening based on non-targeted urine metabolomics, Int. Urol. Nephrol. 54 (2022) 23–29.
[61] A. Loras, C. Suárez-Cabrera, M.C. Martínez-Bisbal, et al., Integrative metabolomic and transcriptomic analysis for the study of bladder cancer, Cancers 11 (2019), 686.
[62] T. Ohara, T. Mori, Antiproliferative effects of short-chain fatty acids on human colorectal cancer cells via gene expression inhibition, Anticancer Res. 39 (2019) 4659–4666.
[63] X. Wang, J. Wang, B. Rao, et al., Gut flora profiling and fecal metabolite composition of colorectal cancer patients and healthy individuals, Exp. Ther. Med. 23 (2022), 250.
[64] S. Qi, D. Xu, Q. Li, et al., Metabonomics screening of serum identifies pyroglutamate as a diagnostic biomarker for nonalcoholic steatohepatitis, Clin. Chim. Acta 473 (2017) 89–95.
[65] T.W. Sedlak, B.D. Paul, G.M. Parker, et al., The glutathione cycle shapes synaptic glutamate activity, Proc. Natl. Acad. Sci. U S A 116 (2019) 2701–2706.
[66] J.A. Eckstein, G.M. Ammerman, J.M. Reveles, et al., Analysis of glutamine, glutamate, pyroglutamate, and GABA in cerebrospinal fluid using ion pairing HPLC with positive electrospray LC/MS/MS, J. Neurosci. Methods 171 (2008) 190–196.
[67] J.W. Kim, G. Lee, S.M. Moon, et al., Metabolomic screening and star pattern recognition by urinary amino acid profile analysis from bladder cancer patients, Metabolomics 6 (2010) 202–206.

[68] A. Yiannikourides, G.O. Latunde-Dada, A short review of iron metabolism and pathophysiology of iron disorders, Medicines (Basel) 6 (2019), 85.

[69] H. Mazdak, F. Yazdekhasti, A. Movahedian, et al., The comparative study of serum iron, copper, and zinc levels between bladder cancer patients and a control group, Int. Urol. Nephrol. 42 (2010) 89–93.

[70] R.A.M. Brown, K.L. Richardson, T.D. Kabir, et al., Altered iron metabolism and impact in cancer biology, metastasis, and immunology, Front. Oncol. 10 (2020), 476.

[71] S.V. Torti, D.H. Manz, B.T. Paul, et al., Iron and cancer, Annu. Rev. Nutr. 38 (2018) 97–125.

[72] W. Young, Review of lithium effects on brain and blood, Cell Transplant. 18 (2009) 951–975.

[73] S.Y. Aghdam, S. Barger, Glycogen synthase kinase-3 in neurodegeneration and neuroprotection: Lessons from lithium, Curr. Alzheimer Res. 4 (2007) 21–31.

[74] M. Kiełczykowska, M. Polz-Dacewicz, E. Kopciał, et al., Selenium prevents lithium accumulation and does not disturb basic microelement homeostasis in liver and kidney of rats exposed to lithium, Ann. Agric. Environ. Med. 27 (2020) 129–133.

[75] A. Sun, I. Shanmugam, J. Song, et al., Lithium suppresses cell proliferation by interrupting E2F-DNA interaction and subsequently reducing S-phase gene expression in prostate cancer, Prostate 67 (2007) 976–988.

[76] A. Latosinska, M. Mokou, M. Makridakis, et al., Proteomics analysis of bladder cancer invasion: Targeting EIF3D for therapeutic intervention, Oncotarget 8 (2017) 69435–69455.

[77] J. Pinto, Â. Carapito, F. Amaro, et al., Discovery of volatile biomarkers for bladder cancer detection and staging through urine metabolomics, Metabolites 11 (2021), 199.

[78] M. Meng, S. Chen, T. Lao, et al., Nitrogen anabolism underlies the importance of glutaminolysis in proliferating cells, Cell Cycle 9 (2010) 3921–3932.

[79] A. Gupta, N. Bansal, N. Mitash, et al., NMR-derived targeted serum metabolic biomarkers appraisal of bladder cancer: A pre- and post-operative evaluation, J. Pharm. Biomed. Anal. 183 (2020), 113134.

[80] J.V. Alberice, A.F. Amaral, E.G. Armitage, et al., Searching for urine biomarkers of bladder cancer recurrence using a liquid chromatography-mass spectrometry and capillary electrophoresis-mass spectrometry metabolomics approach, J. Chromatogr. A 1318 (2013) 163–170.

[81] K. Łuczykowski, N. Warmuzińska, S. Operacz, et al., Metabolic evaluation of urine from patients diagnosed with high grade (HG) bladder cancer by SPME-LC-MS method, Molecules 26 (2021), 2194.

[82] L. Graff, M. Frungieri, R. Zanner, et al., Expression of histidine decarboxylase and synthesis of histamine by human small cell lung carcinoma, Am. J. Pathol. 160 (2002) 1561–1565.

[83] A. Loras, M. Trassierra, D. Sanjuan-Herráez, et al., Bladder cancer recurrence surveillance by urine metabolomics analysis, Sci. Rep. 8 (2018), 9172.

[84] A. Yumba Mpanga, D. Siluk, J. Jacyna, et al., Targeted metabolomics in bladder cancer: From analytical methods development and validation towards application to clinical samples, Anal. Chim. Acta 1037 (2018) 188–199.

[85] C.R. Santos, A. Schulze, Lipid metabolism in cancer, FEBS J. 279 (2012) 2610–2623.

[86] M.Y. Lee, A. Yeon, M. Shahid, et al., Reprogrammed lipid metabolism in bladder cancer with cisplatin resistance, Oncotarget 9 (2018) 13231–13243.

[87] H. Furuya, Y. Shimizu, T. Kawamori, Sphingolipids in cancer, Cancer Metastasis Rev. 30 (2011) 567–576.

[88] B. Ogretmen, Sphingolipids in cancer: Regulation of pathogenesis and therapy, FEBS Lett. 580 (2006) 5467–5476.

[89] S. Kawamura, C. Ohyama, R. Watanabe, et al., Glycolipid composition in bladder tumor: A crucial role of GM3 ganglioside in tumor invasion, Int. J. Cancer 94 (2001) 343–347.

[90] A. Bettiga, M. Aureli, G. Colciago, et al., Bladder cancer cell growth and motility implicate cannabinoid 2 receptor-mediated modifications of sphingolipids metabolism, Sci. Rep. 7 (2017), 42157.

[91] V. Sorrenti, L. Vanella, R. Acquaviva, et al., Cyanidin induces apoptosis and differentiation in prostate cancer cells, Int. J. Oncol. 47 (2015) 1303–1310.

[92] X. Liu, D. Zhang, Y. Hao, et al., Cyanidin curtails renal cell carcinoma tumorigenesis, Cell. Physiol. Biochem. 46 (2018) 2517–2531.

scientific reports

OPEN

Untargeted ultra-high-resolution mass spectrometry metabolomic profiling of blood serum in bladder cancer

Joanna Nizioł[1]✉, **Krzysztof Ossoliński**[2], **Aneta Płaza-Altamer**[3], **Artur Kołodziej**[3], **Anna Ossolińska**[2], **Tadeusz Ossoliński**[2] & **Tomasz Ruman**[1]

Bladder cancer (BC) is a common urological cancer of high mortality and recurrence rates. Currently, cystoscopy is performed as standard examination for the diagnosis and subsequent monitoring for recurrence of the patients. Frequent expensive and invasive procedures may deterrent patients from regular follow-up screening, therefore it is important to look for new non-invasive methods to aid in the detection of recurrent and/or primary BC. In this study, ultra-high-performance liquid chromatography coupled with ultra-high-resolution mass spectrometry was employed for non-targeted metabolomic profiling of 200 human serum samples to identify biochemical signatures that differentiate BC from non-cancer controls (NCs). Univariate and multivariate statistical analyses with external validation revealed twenty-seven metabolites that differentiate between BC patients from NCs. Abundances of these metabolites displayed statistically significant differences in two independent training and validation sets. Twenty-three serum metabolites were also found to be distinguishing between low- and high-grade of BC patients and controls. Thirty-seven serum metabolites were found to differentiate between different stages of BC. The results suggest that measurement of serum metabolites may provide more facile and less invasive diagnostic methodology for detection of bladder cancer and recurrent disease management.

Bladder cancer (BC) is the second most frequently diagnosed cancer of the urinary tract after prostate cancer in the world. In 2020, this disease affected over 473,000 individuals worldwide and was responsible for 212 536 deaths[1]. According to TNM Classification of Malignant Tumors system proposed by American Joint Committee on Cancer (AJCC), bladder cancer can be classified according to whether the tumor infiltrates into or out of the muscular tissue as muscle-invasive bladder cancer (MIBC) and non-muscle-invasive bladder cancer (NMIBC) respectively[2]. NMIBC is the most common type of BC and includes noninvasive papillary carcinomas (pathologic stage Ta), submucosal invasive tumors (T1) and carcinoma in situ (CIS). MIBC includes tumor which extends into the muscle (stage T2), into the perivisceral fat layer (stage T3) or nearby organs (stage T4). Statistically, in case of 80% of patients tumor do not spread outside of the bladder wall. BC can also be classified by histology as low-grade (LG) tumor that rarely spread from their primary site, and high-grade ones (HG) that are more aggressive and invasive[3].

Generally, the first treatment for early BC is a trans urethral resection of bladder tumor (TURBT) sometimes followed by intravesical instillation of mitomycin or *Bacillus* Calmette-Guerin (BCG) therapy. On the other hand, standard treatment for MIBC is a radical cystectomy with pelvic lymph-node dissection. This is combined with neoadjuvant or adjuvant cisplatin based chemotherapy[4]. Despite such aggressive type of treatment, the survival rate of bladder cancer patients is low. Thus, it is essential to combine local and systemic therapies to improve outcomes. High-grade tumors are usually detected by cytology with high specificity and selectivity, but in the case of low-grade tumors, their determination is very difficult.

Metabolomic instrumental analysis is powerful family of tools mainly often used for study of biofluids. Small molecules levels in biofluids such as serum reflects the current state of the organism allowing for identification and characterization of potential disease biomarkers. The number of metabolomics studies in the diagnosis and

[1]Faculty of Chemistry, Rzeszów University of Technology, 6 Powstańców Warszawy Ave., 35-959 Rzeszow, Poland. [2]Department of Urology, John Paul II Hospital, Grunwaldzka 4 St., 36-100 Kolbuszowa, Poland. [3]Doctoral School of Engineering and Technical Sciences at the Rzeszów University of Technology, 8 Powstańców Warszawy Ave., 35-959 Rzeszow, Poland. ✉email: jniziol@prz.edu.pl

understanding of many diseases is rapidly growing in recent years[5]. Numerous analytical methods have been used to better understand the metabolic changes occurring in living systems and especially cancer phenotypic changes. However, two analytical platforms including nuclear magnetic resonance (NMR) spectroscopy[6] and mass spectrometry (MS) often coupled with liquid chromatography (LC)[7] allow to achieve the most comprehensive screening of cancer metabolomes. MS in comparison to NMR, allows the detection of much broader range of compounds with much higher sensitivity, resolution, and precision using very small amount of sample[8]. Over the past fifteen years, metabolomic analytical methods have been used extensively to investigate BC and to identify potential biomarkers of this cancer in urine, serum, and tissues[9,10]. Compared to urine, serum metabolomics is less prone to be affected by dilution factor. Serum is also more readily available than tissue and procedure less invasive[11]. Despite the advantages of examining the metabolomes of human sera, there are only a few studies on serum metabolomics focused on BC biomarker discovery. So far, most studies related to the analysis of serum of patients with bladder cancer have been carried out using NMR[12–14] or mass spectrometry coupled with liquid[7,15–19] and gas chromatography (GC) [3,20,21]. The first such study of serum from BC patients with LC–MS is from 2012, when Lin et al.[22] analyzed serum profiles of BC with LC–MS, and revealed five potential biomarkers for diagnosis of different types of genitourinary cancer. Five years later Tan et al. (Tan 2017) analyzed serum metabolites of 120 BC patients and 52 healthy persons using ultrahigh performance liquid chromatography (UHPLC) coupled with quadrupole time-of-flight (Q-TOF) mass spectrometry in conjunction with univariate and multivariate statistical analyses. They selected and validated 3 differential metabolites including inosine, acetyl-*N*-formyl-5-methoxykynurenamine and phosphatidylserine, PS(*O*-18:0/0:0) that could discriminate HG and LG BC patients and also LG BC and healthy controls. In the same year, Sahu et al. applied GC and LC–MS to identify metabolite associated with urothelial carcinoma in 72 patients and 7 patients without urothelial neoplasia[17]. Their research indicated potential metabolic pathways altered in NMIBC and MIBC BC. In 2019, Vantaku et al. presented serum targeted metabolomic analysis based on LC–MS to investigated to investigate the molecular differences in BC patients from different parts of the world. The study included two independent cohorts of 54 European Americans and 18 African Americans patients and corresponding healthy controls[16]. In the same year, Amara et al.[15] applied LC–MS for targeted analysis of serum metabolites of 67 BC smokers and 53 post-operative BC patients and 152 healthy controls. Their research showed that serum analysis before and after tumor resection can reveal progressive and significant changes of concentration of selected metabolites. In 2021, Troisi et al. applied LC–MS to profile serum metabolites of 64 patients with BC, 74 patients with RCC, and 141 healthy controls. They used different ensemble machine learning models in order to identify metabolites that differentiate cancer patients from controls and allow to classify the tumor in terms of its stage and grade (Troisi 2021).

In this work we report the first results of untargeted analysis of human sera with ultra-high-resolution mass spectrometry coupled to ultra-high-performance liquid chromatography. This study employed the large number of patients—100 cancer patients and 100 controls. Untargeted analysis was focused on serum metabolic changes generated by bladder cancer but also stratifying the disease by stage and grade. Our study reveals potential BC biomarkers for early detection, screening and differential diagnosis.

Materials and methods

All chemicals were of analytical reagent grade. Deionized water (18 MΩ cm) was produced locally. LC–MS-grade methanol was bought from Sigma Aldrich (St. Louis, MO, USA).

Instrumentation. Instrumental configuration consisted of a Bruker Elute UHPLC system operated by Hystar 3.3 software and a ultra-high-resolution mass spectrometer Bruker Impact II (60,000+ resolution version; Bruker Daltonik GmbH) ESI QTOF-MS equipped with Data Analysis 4.2 (Bruker Daltonik GmbH), and Metaboscape (2021b). A Waters UPLC column ACQUITY BEH (C18 silica, 1.7 µm particles, 50 × 2.1 mm) with compatible column guard was used for all analyses. Two mobile phases were: A = Water with 0.1% formic acid, B = acetonitrile with 0.1% formic acid (v/v). Samples in autosampler were thermostated at 4 °C temperature. Volume of 5 µL of extract was loaded on the column at a flow rate of 200 µL min^{-1}, using 4% B. B percentage was changed with time as follows: 0 min—1%, 0.56 min—1% B, 4.72 min—99%, 5.56 min—99%, 5.6 min—1%, 9.45 min—1%. Solvent flow was 450 µL min^{-1}. Column was thermostated at 40 °C temperature. Internal calibration on 10 mM sodium formate (water: isopropanol 1:1 v/v) ions was performed automatically in Metaboscape with the use of syringe pump at an infusion flow rate of 0.12 mL h^{-1}, using a high precision calibration (HPC) mode. Analyses in positive autoMSMS mode were carried out using the following parameters: *m/z* 50–1200; capillary voltage: 4.5 kV; nebulizer: 2.7 bar; dry gas: 12 L min^{-1}; drying gas temperature: 220 °C; hexapole voltage: 50 Vpp; funnel 1: 200 Vpp; funnel 2: 200 Vpp; pre-pulse storage time: 5 µs; transfer time: 60 µs. Collision-Induced Dissociation (CID) was used with following settings: absolute threshold (per 100 sum): 200 cts; absolute threshold 88 cts; active exclusion 3 spectra; release after 0.3 min, isolation mass: for *m/z* = 100, width was 3, for 500 width was 4, for 1000 was 6 and for 1300 was 8); collision energy value was 30 eV. MS frequency was 20 Hz and MSMS from 5 to 30. The untargeted annotations were performed in Metaboscape (ver. 2021b) with a criterion of mass deviation (Δ*m/z*) under 2 ppm and mSigma value under 15 as the maximum acceptable deviation of the mass of the compound and the isotopic pattern respectively. For identification and molecular formula generation, exact mass of parent ions was matched with < 3 ppm error and mSigma value < 50 in most cases. All the molecular formulas were obtained using the Smart Formula tool and the C, H, N, O, P, S, Cl, Br, I and F elements. MSMS spectra was automatically matched against MSMS libraries: Bruker HMDB 2.0 library, MassBank of North America (MoNA)[23] library and NIST ver. 2020 MSMS library[24]. The quality control (QC) sample were prepared from 100 different serum extracts and were measured every ten samples throughout the analytical run to provide a set of data from which method stability and repeatability can be assessed. All measurements were made in technical triplicates.

Collection of human blood samples. Serum samples were collected from one hundred bladder cancer patients (average age 73, Caucasian race) at John Paul II Hospital in Kolbuszowa (Poland). Control serum samples were collected from healthy volunteers after medical examination focused on detection of urinary cancers. All the patients underwent transurethral resection of bladder tumor (TURBT) following detailed clinical questioning and laboratory testing. The study was approved by local Bioethics Committee at the University of Rzeszow (Poland, permission no. 2018/04/10) and performed in accordance with relevant guidelines and regulations. All patients involved in the study were informed about the purpose of this research and planned procedures, and signed an informed consent form. Just over half of the patients (n = 54) had low-grade bladder cancer and papillary urothelial neoplasm of low malignant potential (PUNLMP) (n = 3), while the remaining patient group exhibited high-grade disease (n = 41). In two cases, both high- and low-grade neoplasms were detected. The majority of these patients (n = 69) displayed noninvasive papillary carcinomas (pathologic stage Ta, pTa) stage disease, nineteen had submucosal invasive tumors (pathologic stage T1, pT1) stage and twelve patients had muscle invasive bladder cancer (pathologic stage T2, pT2). The average age for diagnosed patients with BC was 74 ± 10 years while in NCs group the average age was 64 ± 12. The entire NCs group consists of patients admitted to the urology department for surgical treatment of benign urological conditions (urolithiasis, benign prostate hyperplasia, testicular hydrocele, varicocele, phimosis, ureteropelvic junction stenosis, urinary incontinence, urethral stricture). Each of these patients has had performed at least an abdominal ultrasound to rule out neoplasms (patients with urolithiasis usually also had a computed tomography (CT) scan) and a basic bundle of lab tests required for urological surgery that rule out inflammation. Patients were selected according to a similar age range. After familiarizing patients with the research program, patients from the control group gave written consent to donate residual serum for study (no additional blood was drawn for the purpose of this study, except that taken before urological surgery). The clinical characteristics of the patients are presented in supplementary information 1, table S1. Approximately 2.6 ml of blood was drawn from each participant. Samples were centrifuged at 3000 rpm for 10 min at room temperature. The serum was then separated and kept at − 60 °C until further use.

Sample preparation. Polar metabolites were extracted from serum samples as described in our recent publication (Nizioł, Ossoliński, et al. 2021). In brief, deep frozen blood plasma samples (300 µL) were thawed on ice to 4 °C before use. Samples were then centrifuged at 12,000×*g* for 5 min also at 4 °C temperature. Volume of 300 µL of serum was pipetted into sterile 2.0 mL Eppendorf tubes and room-temperature acetone (900 µL) was added and vial vortexed for 1 min. Resulting suspension was incubated at room temperature for 20 min followed by 30 min at − 20 °C. Tubes was then centrifuged at 6000×*g* for 5 min at 4 °C temperature to sediment serum precipitated proteins and phospholipids and then clarified supernatant A (800 µL) was transferred to a new 2 ml microcentrifuge tube. Volume of 500 µL of a 3:1 acetone/H_2O solution was added to the pellet and vortexed vigorously until the pellet was resuspended, this tube was then centrifuged at 12,000×*g* for 10 min at 4 °C to sediment serum precipitated proteins again. Resulting supernatant B was then combined with supernatant A. Volume of 260 µL of combined supernatants were vacuum dried in speedvac-type concentrator and dissolved in 400 µL of methanol, vortexed and centrifuged (12,000×*g* for 5 min at 4 °C). Supernatant volume of 100 µL was transferred into HPLC vial insert of 130 µL capacity and inserted into Elute autosampler.

Multivariate statistical analysis. All metabolite datasets exported from Metaboscape v.2021b were analyzed using the MetaboAnalyst 5.0 online software[25]. Prior to analysis, data was log-transformed, auto-scaled and normalized by sum. Resulting metabolite profiles were then subjected to unsupervised Principal Component Analysis (PCA). The separation between the BC and control groups observed in the 2D and 3D PCA scores plot was further examined using the supervised multivariate statistical analysis such as Orthogonal Partial Least Squares Discriminant Analysis (OPLS-DA). The quality of the OPLS-DA models was assessed by the goodness of fit (R^2Y) and the predictive ability of the models (Q^2). VIP plots were generated to recognize metabolites most significantly responsible for groups separation. Metabolites with VIP value higher than 1.0 were considered potential biomarker candidates. To test the accuracy of the multivariate statistical models, and to rule out that the observed separation in the OPLS-DA is due to chance ($p < 0.05$), permutation tests were performed with 2000-fold repetition. Statistical significance of metabolite level differences was assessed with paired parametric t-test using Mann–Witney and Bonferroni correction. *P* values and false discovery rates (FDR; q-value) less than 0.05 were considered statistically significant. Receiver operating characteristic curve (ROC) analyses together with random forest modeling were commenced to evaluate the diagnostic value of all selected metabolites. The performance of the metabolites was estimated using the area under the curve (AUC), 95% confidence interval, specificity and selectivity. Only variables with an AUC value higher than 0.75 were considered to be relevant. Multivariate statistical analyses were performed independently for the training and validation datasets. Compounds differentiating between tumor and control serum samples were selected based on external validation, which uses two independent datasets (here called training and validation dataset) to validate the performance of a model[26]. The final set of potential BC biomarkers selected fulfilled all criteria in both testing and validation data sets. Chemometric tools such as 2D PCA, OPLS-DA and ROC analysis were also used to assess metabolic profile similarities and differences between different grades and stages of bladder cancer. To identify metabolic pathways impacted by bladder cancer, a metabolic pathway impact analysis was made in MetaboAnalyst 5.0 and the Kyoto Encyclopedia of Genes and Genomes (KEGG) pathway library for *Homo sapiens*[27]. Quantitative pathway enrichment analysis was conducted based on Small Molecule Pathway Database (SMPD). Each impacted pathway was classified according to statistical *p* value, Holm p (*p* value adjusted by Holm–Bonferroni method) and FDR (*p* value adjusted using False Discovery Rate), calculated from pathway topology analysis.

Ethics approval. The study protocol was approved by local Bioethics Committee at the University of Rzeszow (Poland) (permission no. 2018/04/10).

Results

In this study, we characterized the metabolic profiles of one-hundred patients suffering from bladder cancer, in an effort to develop serum-specific metabolic signatures for early and specific detection of bladder cancer. For this purpose, we recorded ultra-high-resolution LC–MS spectra of 200 total (100 BC and 100 control = NCs) metabolite extracts from patient and healthy control serum samples in an effort to identify potential discriminant biomarkers of bladder cancer. Datasets from the BC patients and NCs were divided into two groups, a training set, comprising 80% of all samples and a validation set, corresponding to 20% of all samples. Patient samples of a given stage of BC in the training set accounted for 80% of all samples of that stage. Serum metabolic profiling was performed independently on the two datasets. The training set was used to identify serum diagnostic markers for cancer and stage of its malignancy and, in turn, the validation set was used to independently validate the diagnostic performance of serum metabolite biomarkers.

Distinguishing between bladder cancer and control serum samples. In total, 5498 m/*z* features were found in each serum sample in both training and validation set with applied filtration that required that software show only features that were in at least nine samples. Unsupervised 2D PCA score plots of both subsets indicated a good separation between cancer patients and controls based on distinct and characteristic metabolite profiles. The best separation of groups in the training set was obtained along principal components 1 and 2 (i.e. PC1 and PC2) which accounted for 27.8% and 5.5% respectively. Only a few outliers were detected in the central 95% of the field of view (Fig. 1a). In turn, in the validation set, the best separation between cancer and control serum samples was also observed along PC1 (28.2%) and PC2 and (6.6%) (Fig. 1b).

A supervised multivariate analysis using OPLS-DA analysis was carried out to explore the metabolic differences between the BC and NC groups. In the training set, the score plot indicated a clear separation between those two groups (Fig. 1c). Two thousand permutation tests were conducted to validate the OPLS-DA model (Fig. S1 A). Good discrimination was observed between the two groups ($Q^2 = 0.971$, $R^2Y = 0.992$, *p* value < 5E-04 (0/2000)), revealing substantial differences in the metabolic profiles of cancer versus control serum samples. Model overview showing high R^2Y and Q^2 indicating good interpretability and predictability by this OPLS-DA model (Fig. S1 B). A similar tendency to discriminate BC patients and NCs was observed in OPLS-DA model of the validation set (Fig. 1d), which was confirmed by the very good results of the permutation test ($Q^2 = 0.929$, $R^2Y = 0.995$, *p* value < 5E-04 (0/2000)) (Fig. S1C). Potential serum bladder cancer biomarkers were selected on the basis of the VIP plot resulting from the OPLS-DA model. By combining the VIP (> 1.0) with the results from the independent t-test (*p* value and FDR from t-test < 0.05) 1012 variables were selected in training set as differential for BC patients and NCs (Table 1, Supplementary information 2). In turn, in validation set 1052 variables were considered as significant (Table 2, Supplementary information 2). Finally, 864 common *m/z* and rt values were indicated, both in the training and validation sets. Among these features, to 121 m/*z* values were assigned to a specific chemical compound (Table 1). Next, univariate ROC analysis was separately performed on both training and validation sets to evaluate the diagnostic ability of the models. The results indicated that in the serum samples all 85 out of previously selected 121 metabolites exhibit very high area under the curve (AUC) above 0.8. As shown in Fig. 1e,f, the combination of mass features in both subsets was found to be a powerful discriminator of control versus bladder cancer serum samples (AUC > 99%). Finally, set of twenty-seven potential BC biomarkers were selected with cut-off criteria of FC > 2 and < 0.5, Δ*m/z* < 2 ppm and mSigma < 50 in both testing and validation data sets. The sensitivity and specificity of the selected 27 metabolites were also determined and all metabolites disclosed sensitivity and specificity greater than 77 and 85%, respectively (Table 1 and S1, Supplementary information 2).

Distinguishing between low- and high- grade bladder cancer and control serum samples. To determine whether metabolomics analysis of serum samples could help discriminate between different grades of BC, another series of PCA and OPLS DA analyses were performed on the training (80 NCs, 32 patients with HG and 45 patients with LG,) and validation (20 NCs, 8 patients with HG and 12 patients with LG,) data sets (Tabe S1) excluding three samples from patients with PUNLMP. PCA and OPLS-DA scores plots revealed good discrimination between separately control and cancer groups of varying grades of tumors (LG vs NCs and HG vs NCs) in both training and validation set (Fig. 2, S2). Quality factors for those models amounted to $Q^2 > 0.89$ and $R^2Y > 0.982$, with p values based on permutation tests (n = 2000) smaller than 5E-4 (Fig. S3, S4) indicating a perfect discrimination of metabolites profiles between those groups. However, we did not observe a substantial difference between the LG and HG BC patients in the PCA scores plot (data not shown).

In HG BC vs NCs OPLS-DA model 1500 variables were considered as significant (VIP > 1, *p* value < 0.05) in both training and validation set. Among these features, 138 m/*z* values were assigned to a specific chemical compound. Analysis of LG BC vs NCs in OPLS-DA model in training and validation set revealed common 1600 m/*z* values as significant contributors to the separation between those two groups of which 148 were assigned to specific compound. Univariate ROC curve analyses indicated that these models have a good diagnostic performance (Fig. 2, S2). AUC values for five out of fifteen metabolites were found to be greater than 0.75. Finally, set of twenty-three potential LG and HG BC biomarkers were selected with cut-off criteria of FC > 2 and < 0.5, Δ*m/z* < 2 ppm and mSigma < 50 in both testing and validation data sets. The sensitivity and specificity of the

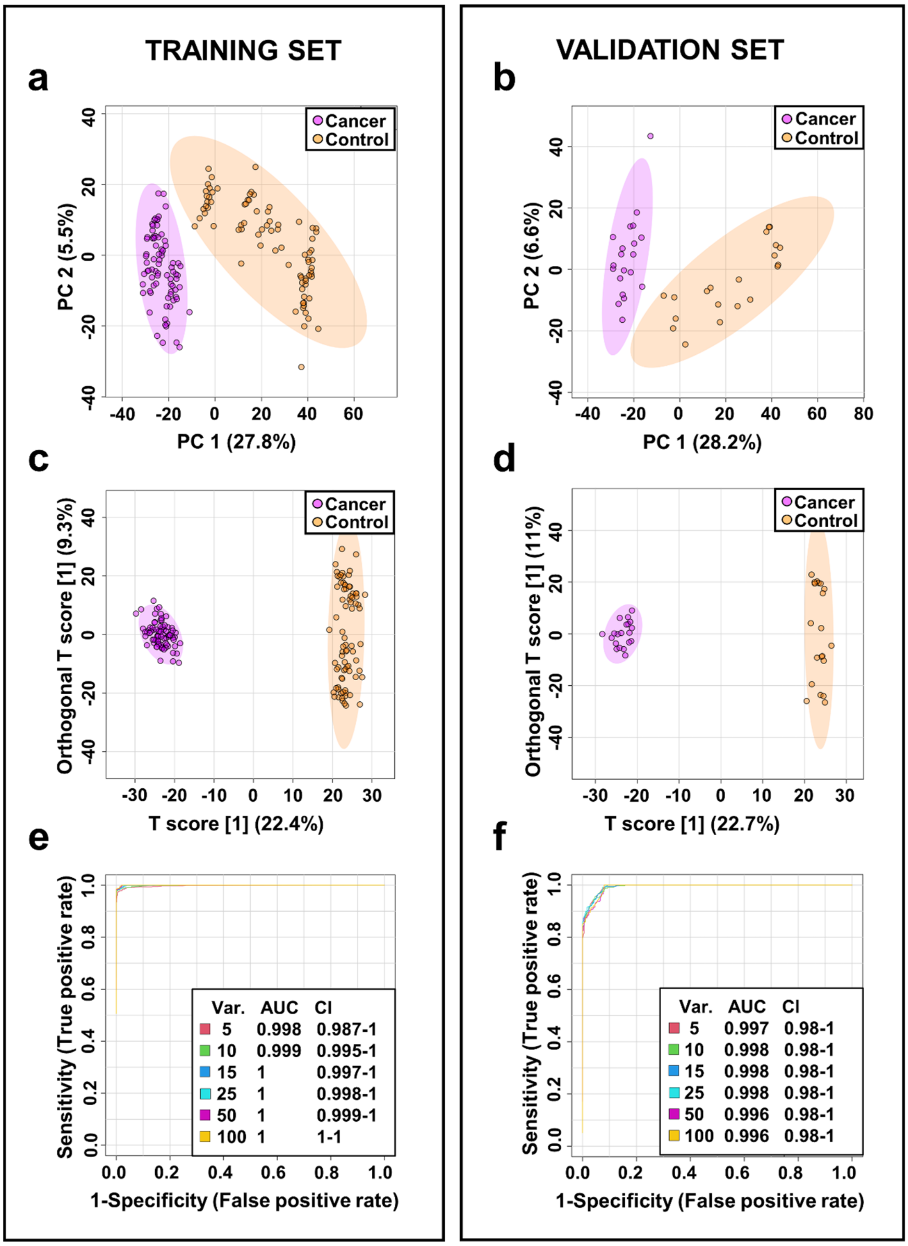

Figure 1. Metabolomic analysis of serum samples from BC and NCs. PCA and OPLS-DA scores plots of the tumor (violet) and control (orange) serum samples in the training set (**a**,**c**) and validation set (**b**,**d**). The receiving operator characteristic (ROC) curves in the training set (**e**) and validation set (**f**).

selected 23 metabolites were also determined and all metabolites disclosed sensitivity and specificity greater than 78% (Table 2 and S2, Supplementary information 2).

Distinguishing between different stages of bladder cancer and control serum samples. Analysis of tumor stages was performed for the entire LC–MS dataset of serum metabolite extracts from patients diagnosed with bladder cancer. Metabolite profiling analysis included 69 serum samples from patients with noninvasive papillary carcinomas (pTa) 19 samples from pT1 stage and 12 from patients with muscle invasive bladder cancer (pT2).

PCA and OPLS-DA scores plot indicated good separation between NCs and different stages of BC (pTa vs NCs, pT1 vs NCs and pT2 vs NCs, Fig. 3). Quality factors for those models were $Q^2 > 0.904$ and $R^2Y > 0.988$, with p values based on permutation tests ($n = 2000$) smaller than 5E-4 (Fig. S5) indicating a very good discrimination of metabolites profiles between those groups. Fold Change and VIP plot analysis of the OPLS-DA model indicated 63, 66 and 69 m/*z* values that appeared to be most relevant for sample differentiation between pTa BC vs NCs, pT1 BC vs NCs and pT2 BC vs NCs respectively out of pool of features assigned to specific chemical compounds. Next, ROC curve analysis was performed to assess the performance of three models in distinguishing

No	Name	Structure	m/z[a]	Δm/z [ppm]	RT [s]	VIP[b]	FC[c]	*p* value	FDR	AUC	Spec. [%][d]	Sens. [%][d]
1	Aureonitol[e,g,h]	$C_{13}H_{18}O_2$	207.1378	−0.7	173.2	1.82	0.20	5.00E−27	3.20E−25	0.993	96	98
2	Norcamphor[e,g,h]	$C_7H_{10}O$	111.0803	−1.0	143.2	1.79	0.29	5.80E−27	3.30E−25	0.992	96	100
3	Perillyl alcohol[e,g]	$C_{10}H_{16}O$	153.1273	−0.8	210.3	1.83	0.25	6.30E−27	3.30E−25	0.992	96	100
4	Thymol[e,f,g]	$C_{10}H_{14}O$	151.1116	−0.8	204.2	1.78	0.39	7.30E−27	3.40E−25	0.991	94	99
5	Methyl 2-octynoate[e,g,h]	$C_9H_{14}O_2$	155.1065	−1.3	177.7	1.72	0.31	8.40E−27	3.40E−25	0.991	95	98
6	3,5,5-Trimethyl-2-cyclohexen-1-one[e,g,h]	$C_9H_{14}O$	139.1116	−0.9	193.2	1.83	0.17	9.80E−27	3.50E−25	0.990	96	99
7	Alantolactone[e,g,h]	$C_{15}H_{20}O_2$	233.1535	−0.3	194.6	1.80	0.23	9.80E−27	3.50E−25	0.990	94	98
8	4-Heptanone[e,f,g]	$C_7H_{14}O$	115.1116	−0.9	206.7	1.79	0.24	1.00E−26	3.50E−25	0.990	94	96
9	7-Epi-Jasmonic acid[e,g,h]	$C_{12}H_{18}O_3$	211.1328	−0.2	160.9	1.80	0.19	1.50E−26	4.10E−25	0.988	96	96
10	Dihydrojasmone[e,g,h]	$C_{11}H_{18}O$	167.1429	−0.8	228.3	1.78	0.41	1.60E−26	4.20E−25	0.988	94	94
11	Valeric acid[e,f,g]	$C_5H_{10}O_2$	103.0753	−0.8	132.2	1.75	0.41	2.30E−26	5.10E−25	0.987	91	96
12	4,4,7a-trimethyl-3a,5,6,7-tetrahydro-3*H*-indene-1-carboxylic acid[e,g,h]	$C_{13}H_{20}O_2$	209.1534	−0.8	197.8	1.75	0.4	5.50E−26	9.20E−25	0.983	94	95
13	1-Acetylindole[e,g,h]	$C_{10}H_9NO$	160.0757	0.1	131.1	1.65	2.13	1.50E−25	2.20E−24	0.978	93	98
14	Linoleic acid[e,g]	$C_{18}H_{32}O_2$	281.2473	−0.8	258.6	1.52	2.55	3.50E−25	4.40E−24	0.975	94	94
15	1-Phenyl-1-pentanone[e,g,h]	$C_{11}H_{14}O$	163.1116	−0.8	200.5	1.73	0.34	7.50E−25	8.30E−24	0.971	94	86
16	Umbelliferone[e,g,h]	$C_9H_6O_3$	163.0389	−0.6	182.1	1.69	0.49	1.10E−24	1.10E−23	0.970	91	90
17	Elaidic acid[e,g]	$C_{18}H_{34}O_2$	283.2629	−0.9	278.4	1.67	3.33	1.20E−24	1.30E−23	0.969	95	94
18	3-Ethylphenol[e,g,h]	$C_8H_{10}O$	123.0803	−0.9	122.9	1.72	0.36	1.30E−24	1.30E−23	0.969	96	95
19	D-Limonene[e,g]	$C_{10}H_{16}$	137.1324	−0.7	143.9	1.72	0.30	2.90E−24	2.60E−23	0.965	91	90
20	6-Hydroxy-4,4,7a-trimethyl-5,6,7,7a-tetrahydrobenzofuran-2(4*H*)-one[e,h]	$C_{11}H_{16}O_3$	197.1171	−0.8	143.2	1.60	0.41	8.60E−23	6.00E−22	0.950	89	90
21	LysoPE(P-18:0/0:0) [e,g,h]	$C_{23}H_{48}NO_6P$	466.3288	−1.0	294.2	1.58	0.38	1.30E−22	8.40E−22	0.948	86	91
22	Palmitoleoyl Ethanolamide[e,g,h]	$C_{18}H_{35}NO_2$	298.2738	−0.9	236.5	1.41	2.08	1.50E−22	1.00E−21	0.947	90	91
23	PE(P-16:0e/0:0) [e,g,h]	$C_{21}H_{44}NO_6P$	438.2977	−0.6	267.5	1.48	0.48	4.70E−20	2.30E−19	0.920	85	88
24	3-Hexanone[e,g,h]	$C_6H_{12}O$	211.1328	−0.2	160.9	1.40	0.50	5.20E−18	2.10E−17	0.896	86	96
25	Epsilon-caprolactam[e,f,g,h]	$C_6H_{11}NO$	114.0914	−0.2	114.5	1.16	2.35	5.70E−18	2.30E−17	0.896	85	81
26	L-Acetylcarnitine[e,f,g]	$C_9H_{17}NO_4$	204.1230	−0.3	22.9	1.37	2.36	1.50E−16	5.40E−16	0.878	85	78
27	LysoPC(18:3)[e,g,h]	$C_{26}H_{48}NO_7P$	518.3236	−1.0	237.9	1.25	0.48	1.30E−15	4.60E−15	0.866	86	78

Table 1. Differential metabolites for discrimination between BC patients and NCs (*p* value < 0.05; FDR < 0.05; VIP > 1; FC < 0.5 and > 2). [a]Experimental monoisotopic mass; [b]VIP scores derived from OPLS-DA model; [c]fold change between cancer and control serum calculated from the abundance mean values for each group—cancer-to-normal ratio; [d]ROC curve analysis for individual biomarkers; [e]the metabolites identified by high precursor mass accuracy; [f]the metabolites identified by matching retention time; [g]the metabolites identified by matching isotopic pattern; [h]the metabolites identified by matching MS/MS fragment spectra; AUC: area under the curve; CI: confidence interval; FC: fold change; FDR: false discovery rate; *m/z*: mass-to-charge ratio; RT: retention time; Sens.: Sensitivity; Spec.: Specificity; VIP: variable influence on projection.

between pTa; pT1 and pT2 bladder cancer stages and NCs. Finally, set of thirty-seven potential pTa, pT1 and pT2 BC biomarkers were selected with cut-off criteria of FC > 2 and < 0.5, Δ*m/z* < 2 ppm and mSigma < 50 in both testing and validation data sets (Table 3). The sensitivity and specificity of the selected 37 metabolites were also determined and all metabolites disclosed sensitivity and specificity greater than 74 and 62%, respectively S3, Supplementary information 2). Comparison of the three groups of cancer stage (pT1 vs. pTa vs. pT2) did not reveal any statistically significant differences (data not shown).

Pathway analysis of potential biomarkers. A metabolic pathway impact analysis was performed using MetaboAnalyst 5.0 to identify the most relevant pathways involved in the observed changes of serum metabolite levels. Forty-five metabolites identified in the UHPLC-UHRMS analysis were subjected to pathway analysis and quantitative pathway enrichment analysis. Forty-nine compounds were found to be relevant to human metabolism. Five metabolic pathways, including linoleic acid metabolism, glycerophospholipid metabolism, alpha-linolenic acid metabolism, arachidonic acid metabolism and biosynthesis of unsaturated fatty acids were found to be significantly impacted comparing BC to controls. Results from pathway impact analysis is shown in Fig. 4a and Table S2 (supplementary information 1).

To expand the metabolomic analysis of pathways related to bladder cancer, we performed a quantitative enrichment analysis using the MetaboAnalyst 5.0 pathway enrichment module and its associated Small Molecule Pathway Database (SMPDB). Two additional pathways were found to be relevant to bladder cancer: beta oxidation of very long chain fatty acids, phospholipid biosynthesis and oxidation of branched chain fatty acids (Fig. 4b and Table S3.

No	Metabolites	Formula	*m/z*[a]	RT [s]	HG versus control				LG versus control			
					VIP[b]	FC[c]	Spec. [%][d]	Sens. [%][d]	VIP[b]	FC[c]	Spec. [%][d]	Sens. [%][d]
1	Aureonitol [e,g,h]	$C_{13}H_{18}O_2$	207.1378	173.22	1.82	0.20	98	97	1.84	0.20	100	96
2	7-Epi-Jasmonic acid [e,g,h]	$C_{12}H_{18}O_3$	211.1328	160.86	1.80	0.19	96	97	1.83	0.19	96	96
3	3,5,5-Trimethyl-2-cyclohexen-1-one [e,g,h]	$C_9H_{14}O$	139.1116	193.16	1.86	0.17	95	94	1.87	0.17	98	93
4	Alantolactone [e,g,h]	$C_{15}H_{20}O_2$	233.1535	194.63	1.80	0.25	95	94	1.84	0.22	98	93
5	Valeric acid[e,f,g]	$C_5H_{10}O_2$	103.0753	132.22	1.78	0.41	98	94	1.79	0.41	95	93
6	4-Heptanone [e,g,h]	$C_7H_{14}O$	115.1116	206.71	1.78	0.24	96	97	1.81	0.23	96	93
7	Methyl 2-octynoate [e,g,h]	$C_9H_{14}O_2$	155.1065	177.72	1.77	0.30	98	91	1.84	0.32	98	98
8	4,4,7a-trimethyl-3a,5,6,7-tetrahydro-3*H*-indene-1-carboxylic acid [e,g,h]	$C_{13}H_{20}O_2$	209.1534	197.75	1.74	0.40	98	91	1.75	0.40	96	89
9	Thymol [e,g,h]	$C_{10}H_{14}O$	151.1116	204.15	1.74	0.39	99	94	1.76	0.39	99	93
10	Umbelliferone [e,g,h]	$C_9H_6O_3$	163.0389	182.05	–	–	–		1.74	0.49	94	91
11	4,7-Dimethyl-1,3-benzothiazol-2-ylamine [e,g,h]	$C_9H_{10}N_2S$	179.0638	142.04	1.66	2.00	93	88	–	–	–	–
12	D-Limonene[e,g]	$C_{10}H_{16}$	137.1324	143.88	1.66	0.30	89	94	1.70	0.31	86	93
13	LysoPE(P-18:0/0:0) [e,g,h]	$C_{23}H_{48}NO_6P$	466.3288	294.22	1.63	0.36	91	91	1.55	0.39	86	87
14	1-Acetylindole [e,g,h]	$C_{10}H_9NO$	160.0757	131.14	1.58	2.14	93	94	1.61	2.13	98	93
15	6-Hydroxy-4,4,7a-trimethyl-5,6,7,7a-tetrahydrobenzofuran-2(4*H*)-one[e,h]	$C_{11}H_{16}O_3$	197.1171	143.16	1.57	0.43	94	81	1.64	0.40	91	89
16	PE(P-16:0e/0:0) [e,g,h]	$C_{21}H_{44}NO_6P$	438.2977	267.49	1.56	0.44	88	88	–	–	–	–
17	LysoPC(20:3) [e,g,h]	$C_{28}H_{52}NO_7P$	546.3545	259.45	1.48	0.45	84	81	–	–	–	–
18	Linoleic acid[e,g]	$C_{18}H_{32}O_2$	281.2473	258.56	1.43	2.64	94	94	1.39	2.44	93	93
19	LysoPC(18:3)[e,g,h]	$C_{26}H_{48}NO_7P$	518.3236	237.91	1.33	0.45	78	78	–	–	–	–
20	L-Acetylcarnitine[e,f,g]	$C_9H_{17}NO_4$	204.1230	22.91	1.33	2.39	79	84	1.35	2.29	86	80
21	Epsilon-caprolactam[e,f,g,h]	$C_6H_{11}NO$	114.0914	114.47	1.19	2.08	89	94	1.32	2.58	89	82
22	3-Hexanone[e,g,h]	$C_6H_{12}O$	101.0960	152.86	–	–	–	–	1.42	0.49	79	93
23	Elaidic acid[e,g]	$C_{18}H_{34}O_2$	283.2629	278.39	–	–	–	–	1.67	3.36	91	98

Table 2. Differential metabolites for discrimination between LG and HG BC patients and NCs (*p* value < 0.05; FDR < 0.05; VIP > 1; FC < 0.5 and > 2). [a]Experimental monoisotopic mass; [b]VIP scores derived from OPLS-DA model; [c]fold change between cancer and control serum calculated from the abundance mean values for each group—cancer-to-normal ratio; [d]ROC curve analysis for individual biomarkers; [e]the metabolites identified by high precursor mass accuracy; [f]the metabolites identified by matching retention time; [g]the metabolites identified by matching isotopic pattern; [h]the metabolites identified by matching MS/MS fragment spectra; AUC: area under the curve; CI: confidence interval; FC: fold change; FDR: false discovery rate; HG: high-grade; LG: low-grade; *m/z*: mass-to-charge ratio; RT: retention time; Sens.: Sensitivity; Spec.: Specificity; VIP: variable influence on projection.

Discussion

Over the past decade, metabolomics studies have provided valuable information on the metabolic profile of patients suffering from various diseases, including cancer, and identified potential markers of developing or recurring disease. Cancer cells have the ability to reprogram their metabolism in order to support the increased need for energy caused by rapid proliferation. Monitoring of changes in the levels of various metabolites in cancer cells or body fluids may be a potential source of new cancer biomarkers. To date, many studies have been published indicating the high potential of metabolomic markers in the diagnosis of various cancers and in understanding of the mechanisms of cancer initiation and development[28].

In this study UHPLC-UHRMS and -UHRMS/MS methods were employed to evaluate changes in serum metabolite levels between 100 bladder cancer patients and 100 normal controls. The largest class of compounds differentiating the NCs group from the BC patients were lipids and lipid-like molecules. Lipids are the fundamental building blocks of all cell membranes and serve as a long-term energy storage. Furthermore, lipids have many other important functions within living organisms including transmit nerve impulses, production and regulation of certain hormones, cushion vital organs, intracellular signal transmission and cell transporting systems. Lipid metabolism is involved in various processes associated with cancer cells. Over the past decade, numerous studies have demonstrated that lipids and metabolites associated with lipid metabolism may be potential markers in human cancers including bladder cancer[29]. We found that the plasma content of 10 glycerophospholipids including PE(P-16:0e/0:0), PC(16:1/16:1), PC(16:0/18:3), LPE(P-18:0/0:0), LPC(14:0/0:0), LPC(P-18:0), LPC(18:3), LPC(18:2), LPC(20:3), LPC(22:5) were significantly higher in the serum of NCs than in the BC subjects. This finding is in line with previous metabolomic studies that demonstrated an association of changes in the levels of these lipids in the blood with various cancers[30]. Thus, alterations in these lipids' metabolism may, therefore, play important roles in the development and progression of bladder cancer.

Glycerophospholipids (GPs), also called phospholipids include phosphatidylethanolamines (PE), phosphatidylcholines (PC) and phosphatidylethanolamines (PE), all of which are glycerol-based phospholipids. These compounds are a major component of the membranes of animal cells in which they are asymmetrically distributed

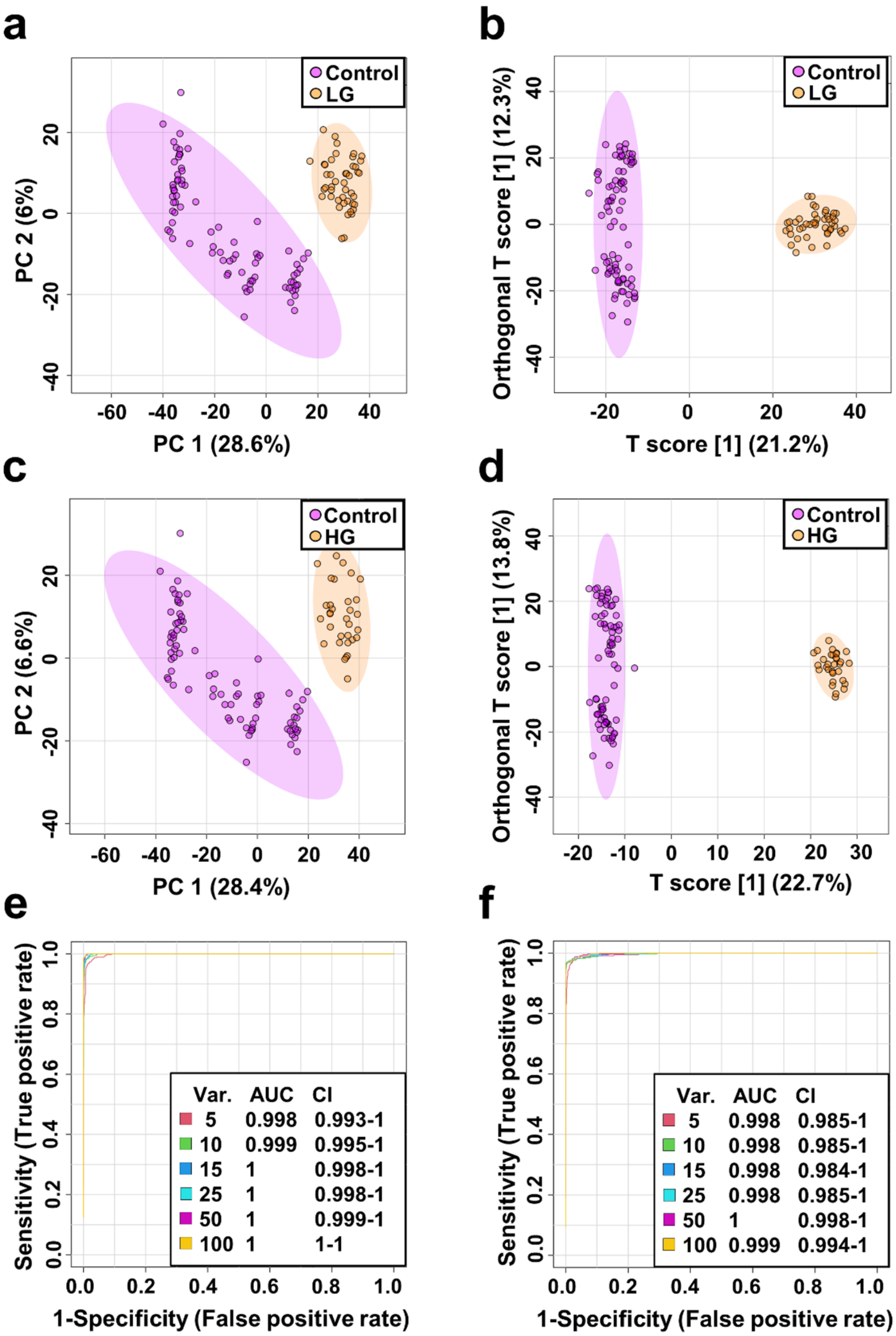

Figure 2. Metabolomic differentiation between different grades of BC and NCs in training set. PCA (**a**) and OPLS-DA (**b**) scores plots of the control (violet) and low-grade (orange). PCA (**c**) and OPLS-DA (**d**) scores plots of the control (violet) and high-grade (orange). ROC curves for LG (**e**) and HG (**f**) BC serum samples vs NCs.

acting as the matrix of different membrane proteins. Many previous studies have found low serum PE levels in various cancers including colon, prostate, lung, and breast cancers indicating these compounds as potential tumor markers[31,32]. Serum levels of PE(P-16:0e/0:0) were found by Lin et. al significantly lower in patients with kidney cancer compared to controls[22]. Some studies have provided evidence that translocation of PE from the inner to the outer leaflet of the plasma membrane indicating a loss of asymmetric distribution of aminophospholipids has been shown as the first sign of impending apoptosis. Thus, lower levels of PE(P-16:0e/0:0) in serum may be an early symptom of apoptotic cell death[33]. Moreover, human phosphatidylethanolamine-binding protein is associated with resistance to apoptosis of tumor cells[34]. It has been reported that exogenous PEs inhibits the growth and indicates an apoptosis of human hepatoma HepG2 cells[35]. Lysophosphatidylethanolamine LPC, LysoPC), LysoPE (P-18:0/0:0) also known as LPE(18:0) was found in lower level in plasma of patients with liver, gastric colorectal, ovarian and lung cancer compared to the control group[32,36,37]. Lysophosphatidylcholines (LPC, lysoPC)

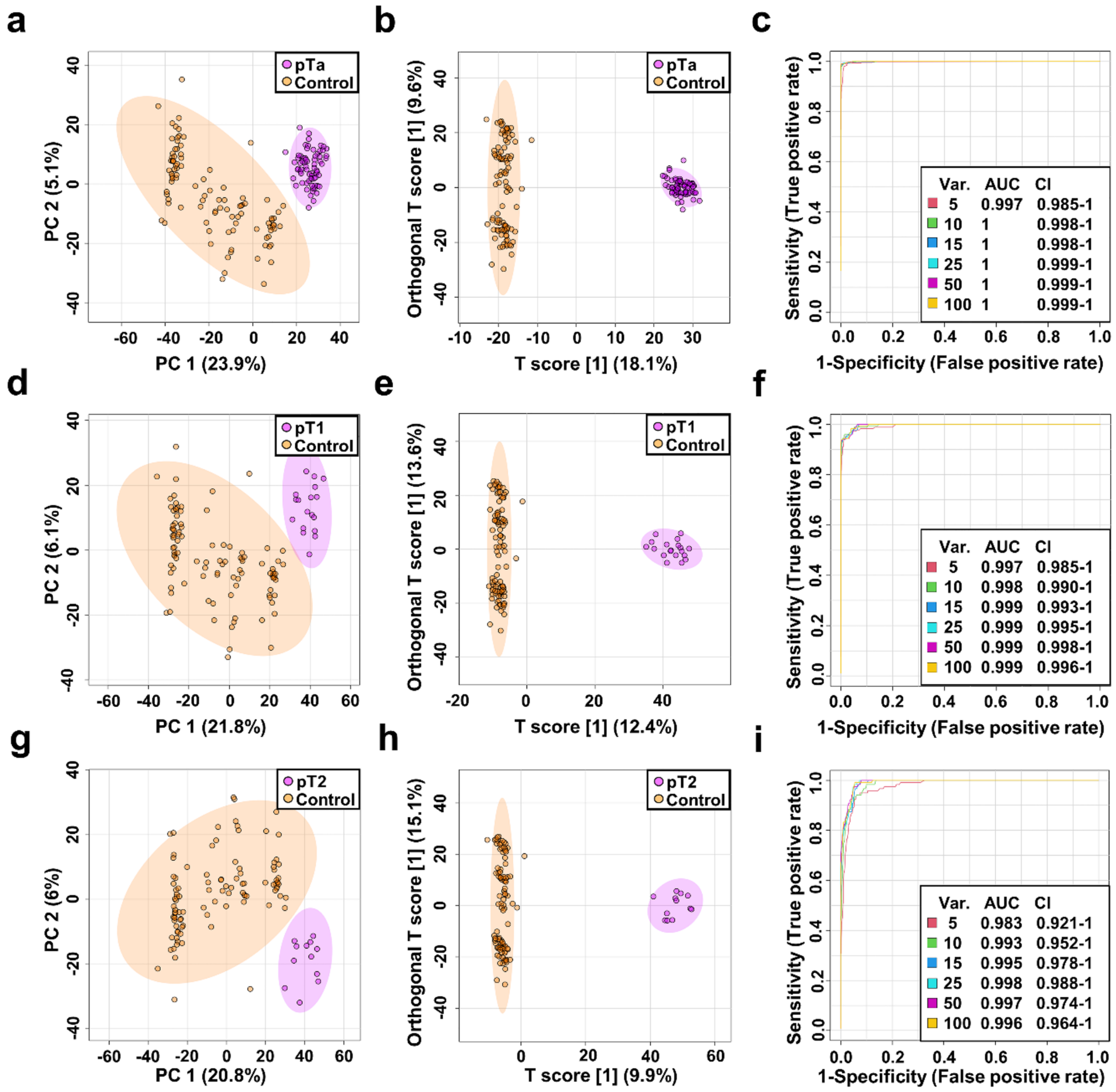

Figure 3. Metabolomic differentiation between different stages of BC and NCs. PCA (**a**), OPLS-DA (**b**) scores plots and ROC curve (**c**) of the pTa (violet) and control (orange). PCA (**d**), OPLS-DA (**e**) scores plots and ROC curve (**f**) of the pT1 (violet) and control (orange). PCA (**g**), OPLS-DA (**h**) scores plots and ROC curve (**i**) of the pT2 (violet) and control (orange).

are an important endogenous signaling phospholipids involved in a variety of important processes, including cell migration, cell proliferation, inflammation and angiogenesis. Decreased LPC plasma level in cancer was also observed in previous study and was associated with body weight loss and increased inflammation. Level of these compounds is inversely correlated with C-reactive protein levels in plasma (CRP)[38]. LPCs were found to be disturbed in several diseases including cancer. Previous metabolomic studies have reported lower level of PC(34:4), LysoPC(20:3) and LPC(P-18:0) in plasma of patients with ovarian cancer (EOC) compared to control[39]. Zhang et al.[40] have reported that LPC(14:0) was down-regulated in patients with recurrent EOC. Lower level of lysophospholipids have been associated with high activity of specific cell-surface G protein-coupled receptors which may cause apoptosis. Tan et al.[41] observed significantly lower of LPC(14:0) in the serum of patients with colorectal cancer compared with healthy controls. LPC(18:1), LPC(18:2) and LPC(18:3) were significantly decreasing in plasma of patients with colorectal cancer compared with healthy controls[42,43]. Lee et al.[32] showed that the levels of LPC(18:2) were lower in plasma samples of patients with colorectal cancer and higher in plasma samples of patients with liver, gastric, lung and thyroid compared to those of healthy control individuals using UHPLC-MS/MS. LPC(18:2) was also found in lower level in plasma of patients with ovarian cancer compared to the control group[36]. Previous metabolomic studies have demonstrated that LysoPC(18:1), LysoPC(20:3) were

No	Metabolites	Formula	*m/z*^{a}	RT [s]	pTa versus control		pT1 versus control		pT2 versus control	
					VIP^b	FC^c	VIP^b	FC^c	VIP^b	FC^c
1	Alpha-hydroxyisobutyric acid^{d,e}	$C_4H_8O_3$	87.0439	49.21	–	–	1.20	2.66	1.05	3.92
2	Valeric acid^{d,e,f}	$C_5H_{10}O_2$	103.0753	132.22	1.90	0.41	1.99	0.41	2.05	0.40
3	Creatinine^{d,e,f}	$C_4H_7N_3O$	114.0661	21.28	–	–	–	–	1.48	2.02
4	Epsilon-caprolactam^{d,e,f,g}	$C_6H_{11}NO$	114.0914	114.47	1.28	2.30	1.51	2.33	1.34	2.46
5	4-Heptanone^{d,e,f}	$C_7H_{14}O$	115.1116	206.71	1.96	0.23	1.99	0.25	2.05	0.23
6	3-Ethylphenol^{d,f,g}	$C_8H_{10}O$	123.0803	122.87	1.88	0.36	1.94	0.35	1.95	0.35
7	D-Limonene^{d,f}	$C_{10}H_{16}$	137.1324	143.88	1.86	0.30	1.74	0.33	1.87	0.28
8	3,5,5-Trimethyl-2-cyclohexen-1-one^{d,f,g}	$C_9H_{14}O$	139.1116	193.16	2.00	0.17	2.11	0.17	2.17	0.17
9	Thymol^{d,e,f}	$C_{10}H_{14}O$	151.1116	204.15	1.91	0.39	1.82	0.41	1.84	0.40
10	Perillyl alcohol^{d,f}	$C_{10}H_{16}O$	153.1273	210.29	2.03	0.25	2.20	0.26	2.31	0.24
11	Methyl 2-octynoate^{d,f,g}	$C_9H_{14}O_2$	155.1065	177.72	1.89	0.31	1.99	0.32	2.23	0.29
12	1-Acetylindole^{d,f,g}	$C_{10}H_9NO$	160.0757	131.14	1.78	2.09	1.75	2.19	1.70	2.08
13	Umbelliferone^{d,f,g}	$C_9H_6O_3$	163.0389	182.05	1.84	0.49			2.06	0.46
14	1-Phenyl-1-pentanone^{d,f,g}	$C_{11}H_{14}O$	163.1116	200.50	1.94	0.33	2.04	0.36	2.04	0.37
15	4,7-Dimethyl-1,3-benzothiazol-2-ylamine^{d,f,g}	$C_9H_{10}N_2S$	179.0638	142.04	–	–	1.82	2.02	–	–
16	Benzophenone^{d,f,g}	$C_{13}H_{10}O$	183.0809	226.43	1.56	2.00	1.45	2.14	–	–
17	L-Acetylcarnitine^{d,e,f}	$C_9H_{17}NO_4$	204.1230	22.91	1.46	2.15	1.48	2.37	1.53	2.81
18	Aureonitol^{d,f,g}	$C_{13}H_{18}O_2$	207.1378	173.22	1.97	0.20	2.00	0.22	2.11	0.20
19	4,4,7a-trimethyl-3a,5,6,7-tetrahydro-3*H*-indene-1-carboxylic acid^{d,f,g}	$C_{13}H_{20}O_2$	209.1534	197.75	1.89	0.40	1.87	0.42	1.99	0.38
20	7-Epi-Jasmonic acid^{d,f,g}	$C_{12}H_{18}O_3$	211.1328	160.86	1.97	0.19	2.03	0.20	1.99	0.21
21	Cys-Pro^{d,f,g}	$C_8H_{14}N_2O_3S$	219.0797	91.87	1.03	2.34	–	–	–	–
22	Pro-Leu^{d,f,g}	$C_{11}H_{20}N_2O_3$	229.1546	46.53	–	–	–	–	1.14	2.35
23	Alantolactone^{d,f,g}	$C_{15}H_{20}O_2$	233.1535	194.63	1.95	0.23	1.99	0.25	1.94	0.27
24	Curcumol^{d,f,g}	$C_{15}H_{24}O_2$	237.1848	226.69	1.12	0.23				
25	Isovalerylcarnitine^{d,e,f}	$C_{12}H_{23}NO_4$	246.1697	121.55	1.16	2.18	1.11	2.49	1.07	2.45
26	Linoleic acid^{d,f}	$C_{18}H_{32}O_2$	281.2473	258.56	1.59	2.35	1.53	2.62	1.49	2.73
27	Elaidic acid^{d,f}	$C_{18}H_{34}O_2$	283.2629	278.39	1.87	3.35	2.02	3.86	1.73	2.91
28	PE(P-16:0e/0:0)^{d,f,g}	$C_{21}H_{44}NO_6P$	438.2977	267.49	1.59	0.49	1.95	0.39	2.08	0.36
29	Cefazolin^{d,f,g}	$C_{14}H_{14}N_8O_4S_3$	455.0371	135.59	–	–	1.02	288.76	1.30	62.93
30	LysoPE(P-18:0/0:0)^{d,f,g}	$C_{23}H_{48}NO_6P$	466.3288	294.22	1.72	0.39	1.90	0.34	2.16	0.28
31	LysoPC(14:0/0:0)^{d,f,g}	$C_{22}H_{46}NO_7P$	468.3080	236.23	–	–	–	–	1.96	0.33
32	LysoPC(P-18:0)^{d,g}	$C_{26}H_{54}NO_6P$	508.3756	294.32	–	–	–	–	1.60	0.48
33	LysoPC(18:2)^{d,f,g}	$C_{26}H_{50}NO_7P$	520.3393	246.39	–	–	–	–	1.80	0.44
34	LysoPC(20:3)^{d,f,g}	$C_{28}H_{52}NO_7P$	546.3545	259.45	–	–	1.57	0.45	1.76	0.39
35	LysoPC(22:5)^{d,f,g}	$C_{30}H_{52}NO_7P$	570.3546	255.47	–	–	–	–	1.48	0.45
36	PC(16:1/16:1)^{d,g}	$C_{40}H_{76}NO_8P$	730.5380	312.51	–	–	1.61	0.15	–	–
37	PC(16:0/18:3)^{d,g}	$C_{42}H_{78}NO_8P$	756.5535	313.85	–	–	1.19	0.42	–	–

Table 3. Differential metabolites for discrimination between pTa, pT1 and pT2 BC patients and NCs (p value < 0.05; FDR < 0.05; VIP > 1; FC < 0.5 and > 2). ^{a} Experimental monoisotopic mass; ^{b}VIP scores derived from OPLS-DA model; ^{c}fold change between cancer and control serum calculated from the abundance mean values for each group—cancer-to-normal ratio; ^{d}the metabolites identified by high precursor mass accuracy; ^{e}the metabolites identified by matching retention time; ^{f}the metabolites identified by matching isotopic pattern; ^{g}the metabolites identified by matching MS/MS fragment spectra; AUC: area under the curve; FC: fold change; FDR: false discovery rate; *m/z*: mass-to-charge ratio; pT1 and pTa—high risk non-muscle invasive bladder cancer; pT2—muscle invasive bladder cancer; RT: retention time; VIP: variable influence on projection.

down-regulated in patients with ovarian cancer. Four of these compounds including LPC(14:0), LPC(18:3), LPC(20:3), LPC(22:5) were previously related to kidney injury. Metabolic profiling of plasma from patients with cancer cachexia revealed significantly lower levels of LPC(14:0), LPC(P-18:0), LPC(18:2), LPC(20:3), LPC(22:5) and LPE(18:0) compared to healthy controls[44]. Three of these six LPC including LPC(18:1), LPC(18:3), LPC(22:5) we identified previously at lower levels in serum of patients with thyroid carcinoma[45]. To our knowledge, only one lipid out of the ten most differentiating both groups cancer and control we indicated has been previously associated with bladder cancer. Tan et al.[18] indicated slightly higher level of LPC(18:2) in serum of patients with BC compared to controls using UHPLC-Q-ToF MS.

Lower levels of four prenol lipids including perillyl alcohol, D-limonene, thymol, alantolactone were found in serum of BC compared to controls. These monoterpenoids commonly occurring in many plants are known

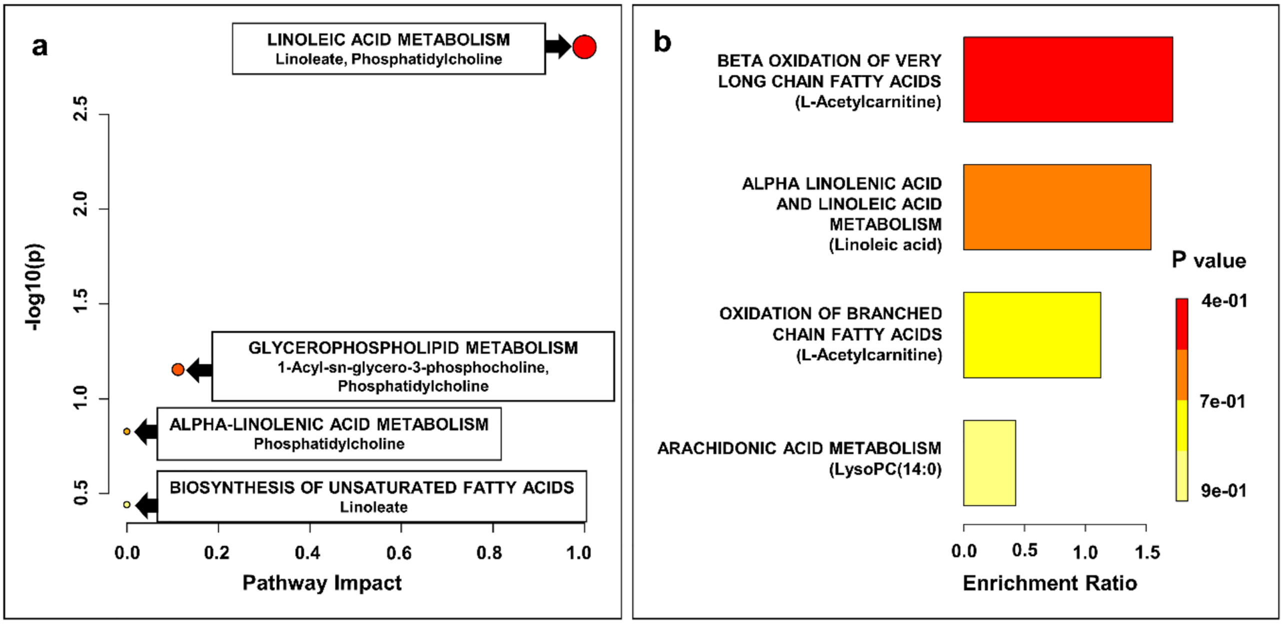

Figure 4. Results of pathway topology analysis of selected statistically significant metabolites in BC. A Pathway analysis based on KEGG (**a**); bubble area donating to the impact of each pathway with color representing the significance from highest in red to lowest in white; (**b**) Quantitative enrichment analysis based on SMPDB.

for their anti-tumor, antioxidant, anti-inflammatory and anti-fungal activity. Thymol and limonene have been shown to inhibit bladder cancer cell proliferation and induces these cells apoptosis[46,47].

We found that serum levels of metabolites: L-acetylcarnitine, linoleic acid and elaidic acid were higher and three others: valeric acid and 7-epi-jasmonic acid lower in BC patients compared to NCs. The levels of linoleic and elaidic acid were also found as significantly higher in patients with colorectal cancer[48]. Increased serum activity of acetylcarnitine have been previously pointed out as a potential tumor biomarkers[49,50]. Acetylcarnitine is a naturally occurring acetic acid ester of carnitine, important in mitochondrial tricarboxylic acid (TCA) cycle activity. Increased urine levels of this compound have previously been reported in patients with BC[51]. Elevation of acetylcarnitine may be an indication of decreased carbon flow into the TCA cycle or excess production of acetyl-CoA[52]. Previous studies revealed elevated urine level of acetylcarnitine and isovalerylcarnitine in BC patients compared to controls[53,54]. However, the association between isovalerylcarnitine and bladder cancer has not yet been explained.

In order to apply the correct treatment regimens for BC patients, in addition to indicating the neoplasm, it is necessary to precisely and accurately indicate the stage and grade of this cancer. In total, 23 differential metabolites were identified as potential marker for discriminating between LG and HG BC patients and NCs. Among these metabolites, 18 metabolites were the common characteristic of both LG and HG BC patients. Three metabolites including lysoPC(20:3), PE(P-16:0e/0:0) and 2(4H)-benzofuranone, 6-Hydroxy-4,4,7a-trimethyl-5,6,7,7a-tetrahydrobenzofuran-2(4*H*)-one were identified in much higher level only in the serum of patients with HG BC, while four metabolites including 3-hexanone, diethylene glycol 2-ethylhexyl ether, elaidic acid, umbelliferone were found in significant higher level only in the serum of patients with LG BC patients.

In total, 38 differential metabolites were identified as potential marker for discriminating between pTa, pT1 and pT2 BC patients and NCs. Among these metabolites, 22 metabolites were the common to all three stages of BC. Two metabolites including Cys-Pro and curcumol were identified in much higher levels only in the serum of patients with pTa BC, while two metabolites including LysoPC(20:3) and alpha-hydroxyisobutyric acid were found in significant higher level only in the serum of patients with pT1 BC patients. Moreover, five metabolites including norcamphor, creatinine, dihydrojasmone, pro-leu, palmitoleoyl ethanolamide were found in significant higher level only in the serum of patients with pT2 BC patients.

We demonstrate that ultra-high-resolution mass spectrometry is a powerful tool for the characterization of the serum metabolome differences in BC. Twenty-seven potentially robust metabolic biomarkers were identified for 100 tumor serum samples from patients with BC patients after comparison against 100 healthy controls owing to the excellent predictive ability of AUC > 0.99. We also identified twenty-three metabolites that might be used as potential biomarkers to distinguish LG and HG and thirty-seven metabolites that may serve to differentiate between the pTa/pT1 and pT2 stages of BC. Our results suggest that differential serum metabolite profiles and can help identify patients with BC compared with NCs, with significant discriminating power between different stages and grades of bladder cancer. Our findings, may potentially provide facile and less invasive diagnostic methodology for detection of different stages and grades of bladder cancer and recurrent disease management. In the future, a new class of biomarkers of BC could contribute to development of non-invasive, highly specific and sensitive diagnostic tests that could be employed to aid the detection of new tumors and also predict recurrences.

Data availability

The data that support the findings of this study is available from the corresponding author upon reasonable request.

Received: 12 June 2022; Accepted: 31 August 2022

References

1. Sung, H. *et al.* Global Cancer Statistics 2020: GLOBOCAN Estimates of Incidence and Mortality Worldwide for 36 Cancers in 185 Countries. *CA. Cancer J. Clin.* **71**, 209–249 (2021).
2. Robins, D. J. *et al.* Mp86-17 the 2017 American joint committee on cancer eighth edition cancer staging manual: changes in staging guidelines for cancers of the kidney, renal pelvis and ureter, bladder, and urethra. *J. Urol.* **197**, e1163 (2017).
3. Troisi, J. *et al.* A serum metabolomic signature for the detection and grading of bladder cancer. *Appl. Sci.* **11**, 2835 (2021).
4. Lee, H. H. & Ham, W. S. Perioperative immunotherapy in muscle-invasive bladder cancer. *Transl. Cancer Res.* **9**, 6546–6553 (2020).
5. Yang, Q. *et al.* Metabolomics biotechnology, applications, and future trends: a systematic review. *RSC Adv.* **9**, 37245–37257 (2019).
6. Raja, G., Jung, Y., Jung, S. H. & Kim, T. J. 1H-NMR-based metabolomics for cancer targeting and metabolic engineering—a review. *Process Biochem.* **99**, 112–122 (2020).
7. Liu, X. *et al.* LC-MS-based plasma metabolomics and lipidomics analyses for differential diagnosis of bladder cancer and renal cell carcinoma. *Front. Oncol.* **10**, 717 (2020).
8. Pan, Z. & Raftery, D. Comparing and combining NMR spectroscopy and mass spectrometry in metabolomics. *Anal. Bioanal. Chem.* **387**, 525–527 (2007).
9. Ng, K., Stenzl, A., Sharma, A. & Vasdev, N. Urinary biomarkers in bladder cancer: A review of the current landscape and future directions. *Urol. Oncol. Semin. Orig. Investig.* **39**, 41–51 (2021).
10. Batista, R. *et al.* Biomarkers for bladder cancer diagnosis and surveillance: A comprehensive review. *Diagnostics* **10**, 39 (2020).
11. Walsh, M. C., Brennan, L., Malthouse, P. G., Roche, H. M. & Gibney, M. J. Effect of acute dietary standardization on the urinary, plasma, and salivary metabolomic profiles of healthy humans 13. *Am. J. Clin. Nutr.* **84**, 531–539 (2006).
12. Gupta, A. *et al.* NMR-derived targeted serum metabolic biomarkers appraisal of bladder cancer: A pre- and post-operative evaluation. *J. Pharm. Biomed. Anal.* **183**, 113134 (2020).
13. Bansal, N. *et al.* Low- and high-grade bladder cancer determination via human serum-based metabolomics approach. *J. Proteome Res.* **12**, 5839–5850 (2013).
14. Cao, M., Zhao, L., Chen, H., Xue, W. & Lin, D. NMR-based metabolomic analysis of human bladder cancer. *Anal. Sci.* **28**, 451–456 (2012).
15. Amara, C. S. *et al.* Serum metabolic profiling identified a distinct metabolic signature in bladder cancer smokers: A key metabolic enzyme associated with patient survival. *Cancer Epidemiol. Biomarkers Prev.* **28**, 770–781 (2019).
16. Vantaku, V. *et al.* Large-scale profiling of serum metabolites in African American and European American patients with bladder cancer reveals metabolic pathways associated with patient survival. *Cancer* **125**, 921–932 (2019).
17. Sahu, D., Lotan, Y., Wittmann, B., Neri, B. & Hansel, D. E. Metabolomics analysis reveals distinct profiles of nonmuscle-invasive and muscle-invasive bladder cancer. *Cancer Med.* **6**, 2106–2120 (2017).
18. Tan, G. *et al.* Three serum metabolite signatures for diagnosing low-grade and high-grade bladder cancer. *Sci. Rep.* **7**, 1–11 (2017).
19. Lin, L. *et al.* LC-MS based serum metabonomic analysis for renal cell carcinoma diagnosis, staging, and biomarker discovery. *J. Proteome Res.* **10**, 1396–1405 (2011).
20. Zhou, Y. *et al.* The development of plasma pseudotargeted GC-MS metabolic profiling and its application in bladder cancer. *Anal. Bioanal. Chem.* **408**, 6741–6749 (2016).
21. Lepara, Z. *et al.* Serum malondialdehyde (MDA) level as a potential biomarker of cancer progression for patients with bladder cancer. *Rom. J. Intern. Med.* **58**, 146–152 (2020).
22. Lin, L. *et al.* LC-MS-based serum metabolic profiling for genitourinary cancer classification and cancer type-specific biomarker discovery. *Proteomics* **12**, 2238–2246 (2012).
23. MassBank of North America. Available at: https://mona.fiehnlab.ucdavis.edu/. Accessed: 8th June 2022
24. Mass Spectrometry Data Center, NIST. *ass Spectral Library* Available at: https://chemdata.nist.gov/. Accessed 1st April 2022.
25. Pang, Z. *et al.* MetaboAnalyst 50: Narrowing the gap between raw spectra and functional insights. *Nucleic Acids Res.* **49**, W388–W396 (2021).
26. Ho, S. Y., Phua, K., Wong, L. & Bin Goh, W. W. Extensions of the external validation for checking learned model interpretability and generalizability. *Patterns* **1**, 100129 (2020).
27. Okuda, S. *et al.* KEGG Atlas mapping for global analysis of metabolic pathways. *Nucleic Acids Res.* **36**, W423–W426 (2008).
28. Han, J., Li, Q., Chen, Y. & Yang, Y. Recent metabolomics analysis in tumor metabolism reprogramming. *Front. Mol. Biosci.* **8**, 763902 (2021).
29. Besiroglu, H. Lipid metabolism profiling and bladder cancer. *Metabolomics Open Access* **5**, 1–4 (2015).
30. Wolrab, D., Jirásko, R., Chocholoušková, M., Peterka, O. & Holčapek, M. Oncolipidomics: Mass spectrometric quantitation of lipids in cancer research. *TrAC Trends Anal. Chem.* **120**, 10 (2019).
31. Lu, Y. *et al.* Comparison of hepatic and serum lipid signatures in hepatocellular carcinoma patients leads to the discovery of diagnostic and prognostic biomarkers. *Oncotarget* **9**, 5032 (2018).
32. Lee, G. B., Lee, J. C. & Moon, H. Plasma lipid profile comparison of five different cancers by nanoflow ultrahigh performance liquid chromatography-tandem mass spectrometry. *Anal Chim Acta* https://doi.org/10.1016/j.aca.2019.02.021 (2019).
33. Wang, X. *et al.* A novel human phosphatidylethanolamine-binding protein resists tumor necrosis factor α-induced apoptosis by inhibiting mitogen-activated protein kinase pathway activation and phosphatidylethanolamine externalization*. *J. Biol. Chem.* **279**, 45855–45864 (2004).
34. Wang, X. *et al.* Silencing of human phosphatidylethanolamine-binding protein 4 sensitizes breast cancer cells to tumor necrosis factor-alpha-induced apoptosis and cell growth arrest. *Clin. Cancer Res.* **11**, 7545–7553 (2005).
35. Yao, Y. *et al.* Exogenous phosphatidylethanolamine induces apoptosis of human hepatoma HepG2 cells via the bcl-2/bax pathway. *World J. Gastroenterol.* **15**, 1751 (2009).
36. Yagi, T. *et al.* Challenges and inconsistencies in using lysophosphatidic acid as a biomarker for ovarian cancer. *Cancers* **11**, 520 (2019).
37. Ravipati, S., Baldwin, D. R., Barr, H. L., Fogarty, A. W. & Barrett, D. A. Plasma lipid biomarker signatures in squamous carcinoma and adenocarcinoma lung cancer patients. *Metabolomics* **11**, 1600–1611 (2015).
38. Taylor, L. A., Arends, J., Hodina, A. K., Unger, C. & Massing, U. Plasma lyso-phosphatidylcholine concentration is decreased in cancer patients with weight loss and activated inflammatory status. *Lipids Health Dis.* **6**, 1–8 (2007).
39. Li, J. *et al.* Distinct plasma lipids profiles of recurrent ovarian cancer by liquid chromatography-mass spectrometry. *Oncotarget* **8**, 46834 (2017).

40. Zhang, F. *et al.* The predictive and prognostic values of serum amino acid levels for clear cell renal cell carcinoma. *Urol. Oncol. Semin. Orig. Investig.* **35**, 392–400 (2017).
41. Tan, B. *et al.* Metabonomics identifies serum metabolite markers of colorectal cancer. *J. Proteome Res.* https://doi.org/10.1021/pr400337b (2013).
42. Shen, S. *et al.* A plasma lipidomics strategy reveals perturbed lipid metabolic pathways and potential lipid biomarkers of human colorectal cancer. *J. Chromatogr. B* **1068–1069**, 41–48 (2017).
43. Zhao, Z. *et al.* Plasma lysophosphatidylcholine levels: potential biomarkers for colorectal cancer. *J Clin Oncol* **25**, 2696–2701 (2007).
44. Cala, M. P. *et al.* Multiplatform plasma fingerprinting in cancer cachexia: a pilot observational and translational study. *J. Cachexia. Sarcopenia Muscle* **9**, 348–357 (2018).
45. Yao, Z. *et al.* Serum metabolic profiling and features of papillary thyroid carcinoma and nodular goiter. *Mol. Biosyst.* **7**, 2608–2614 (2011).
46. Li, Y. *et al.* Thymol inhibits bladder cancer cell proliferation via inducing cell cycle arrest and apoptosis. *Biochem. Biophys. Res. Commun.* **491**, 530–536 (2017).
47. Ye, Z., Liang, Z., Mi, Q. & Guo, Y. Limonene terpenoid obstructs human bladder cancer cell (T24 cell line) growth by inducing cellular apoptosis, caspase activation, G2/M phase cell cycle arrest and stops cancer metastasis. *JBUON* **25**, 280–285 (2020).
48. Wang, X., Wang, J., Rao, B. & Deng, L. I. Gut flora profiling and fecal metabolite composition of colorectal cancer patients and healthy individuals. *Exp. Ther. Med.* **13**, 2848–2854 (2017).
49. Nizioł, J. *et al.* Metabolomic study of human tissue and urine in clear cell renal carcinoma by LC-HRMS and PLS-DA. *Anal. Bioanal. Chem.* **410**, 3859–3869 (2018).
50. Ganti, S. *et al.* Urinary acylcarnitines are altered in human kidney cancer. *Int. J. Cancer* **130**, 2791–2800 (2012).
51. Wittmann, B. M. *et al.* Bladder cancer biomarker discovery using global metabolomic profiling of urine. *PLoS ONE* **9**, e115870 (2014).
52. Schroeder, M. A. *et al.* The cycling of acetyl-coenzyme A through acetylcarnitine buffers cardiac substrate supply: A hyperpolarized 13C magnetic resonance study. *Circ. Cardiovasc. Imaging* **5**, 201–209 (2012).
53. Jin, X. *et al.* Diagnosis of bladder cancer and prediction of survival by urinary metabolomics. *Oncotarget* **5**, 1635–1645 (2014).
54. Rodrigues, D. *et al.* Biomarkers in bladder cancer: A metabolomic approach using in vitro and ex vivo model systems. *Int. J. Cancer* **139**, 256–268 (2016).

Acknowledgements

Research was supported mainly by National Science Centre (Poland), research project SONATA Number UMO-2018/31/D/ST4/00109.

Author contributions

J.N.: Conceptualization, Methodology, Formal analysis, Investigation, Resources, Data Curation, Writing—Original draft, Writing—Review & Editing, Visualization, Supervision, Project administration, Funding acquisition, K.O: Investigation, Resources; Writing—Original draft; A.P.: Investigation; Data Curation; A.K.: Investigation, Data Curation; A.O.: Resources; T.O.: Resources; T.R.: Methodology, Resources, Data Curation, Writing—Review & Editing, Supervision.

Competing interests

The authors declare no competing interests.

Additional information

Supplementary Information The online version contains supplementary material available at https://doi.org/10.1038/s41598-022-19576-9.

Correspondence and requests for materials should be addressed to J.N.